ON NUMERICAL SIMULATION OF TAYLOR–COUETTE FLOW AND STATE SELECTION IN TAYLOR VORTEX FLOW

A thesis submitted in accordance with the regulations to Monash University in fulfullment of the requirements for the degree of Doctor of Philosophy

by

John Rigopoulos
B.Sc. (Hons), M.Sc.

Department of Mechanical Engineering
Monash University
Victoria, Australia 3168

February, 1998

SUMMARY

This thesis presents the results of a numerical investigation on state selection in Taylor vortex flow. The cylinders were assumed infinite in axial extent and so periodic axial boundary conditions were used. The outer cylinder was assumed stationary. In the numerical experiment, the inner cylinder Reynolds number was linearly increased in time from an initial subcritical value to a final supercritical value over a finite ramp time, and then held fixed at the final value. The final value was assumed to be close to the critical value. The numerical simulations were repeated for different ramp times where the initial conditions, initial and final Reynolds numbers were held fixed. A high aspect ratio was used in order to numerically model the interaction of many discrete axial modes.

Of interest were:

1. the behaviour of the amplitude of the axial modes with ramp time,
2. the change in the preferred axial mode with ramp time,
3. why the axial mode corresponding to the critical wavelength was always preferred when the ramp time was sufficiently long, and
4. how Taylor vortex flow can exhibit final state nonuniqueness.

A linear model was developed which explained the behaviour of the modes in their independent stage of growth. This was based on the assumption that the instantaneous growth rate at a particular instantaneous Reynolds number during the ramp was equal to the growth rate obtained for that Reynolds number held fixed. To first order, a Reynolds number which increases linearly with time leads to a growth rate which increases linearly with time. Hence the logarithm of the amplitude varies quadratically with time during the ramp while the amplitude is small.

When the final Reynolds number is reached after a finite ramp time, in comparison to being reached suddenly, the amplitude of each mode is delayed from reaching high amplitudes.

This delay is mode-dependent and has a lowest-to-highest ordering corresponding to the lowest-to-highest ordering of the critical Reynolds number for each mode. The delay is also linearly dependent to the ramp time. Thus, when the ramp time is increased the delay gives an increasing bias in the order at which the modes reach high amplitudes. In turn this leads to a change in the preferred mode with ramp time.

When the ramp time is sufficiently long, the order at which the modes reach high amplitudes corresponds to the lowest-to-highest ordering of the critical Reynolds number for each mode. The difference in the delay time between modes also increases with ramp time. The lowest critical Reynolds number corresponds to the critical wavelength. Hence, for a sufficiently long ramp time the mode with the critical wavelength will always reach high amplitudes earliest and become the preferred mode.

A dynamical systems approach was used to conceptualise the feature of state nonuniqueness of Taylor vortex flow. Coupled nonlinear amplitude equations were used to account for several of the features observed in the behaviour of the amplitude of modes for different ramp times. One of the nonlinear effects observed was that, prior to the saturation of the preferred mode, the lower modes exhibited a region of rapid growth. It is suggested this happens because the two modes adjacent to the preferred mode resonate with the first harmonic of the preferred mode.

The numerical methods used were operator splitting and spectral methods. In the initial development of the numerical code, two-dimensional driven cavity flow was modelled.

Then, for Taylor vortex flow, the incompressible Navier-Stokes equations were expressed in cylindrical coordinates and axisymmetry was assumed, which reduced the equations to two dimensions. The numerical method was shown to give second-order time accuracy.

The method was extended to three dimensions and a code for Taylor-Couette flow was developed. Periodicity was assumed in the azimuthal direction. Wavy vortex flow was simulated as a test case. Again, second-order time accuracy was demonstrated.

STATEMENT OF ORIGINALITY

This thesis contains no material which has been accepted for the award of a degree or diploma in this or any other university. To the best of the candidate's knowledge and belief, this thesis contains no material previously published or written by another person except where due reference is made in the text of this thesis.

John Rigopoulos

February, 1998.

ACKNOWLEDGEMENTS

The Author wishes to express his thanks to the following people.

My supervisors, Associate Professor J. Sheridan and Dr. M.C. Thompson, for providing excellent technical and administrative support during my candidature.

At Monash University, Department of Mechanical Engineering, the Fluid-dynamics Laboratory for Aeronautical and Industrial Research (FLAIR) group, for organising regular student colloquia which provided a stimulating and productive environment for the critical review of research papers in fluid mechanics; Mr B. Treloar, for attending to the occasional technical difficulties with my computer.

At the CSIRO, Division of Building, Construction and Engineering, Dr. M.C. Welsh for allowing me access to the Division's computer resources during the first three years of my candidature; Dr. K. Liffman for a vector plot program and a contour plot program based on the PGPLOT graphics package; Dr. M.J. Rudman for fruitful discussions and his expertise on Taylor-Couette flow.

My mother, Panagiota, and brother, Nick, for their encouragement and personal support.

Monash University for financial support through a Monash Graduate Scholarship.

Dedicated to my mother Panagiota for her strength, perseverance and devotion to bringing up two sons into the world.

Αυτό είναι γιά 'σένα μαμά

PUBLICATIONS

Rigopoulos, J., Thompson, M.C. and Sheridan, J. 1995 Effect of rate of increase of the inner cylinder speed on selection of the final wavelength in Taylor vortex flow, bound proceedings for the *Twelfth Australasian Fluid Mechanics Conference*, The University of Sydney, December 10 - 15, 1995.

Rigopoulos, J., Sheridan, J. and Thompson, M.C. 1997 Effect of Rate of Increase of the Inner Cylinder Speed on State Selection in Taylor vortex flow, CD-ROM proceedings for the *ASME Fluids Engineering Division Summer Meeting*, Vancouver, British Columbia, Canada, June 22 - 26, 1997.

Rigopoulos, J., Sheridan, J. and Thompson, M.C. 1997 A spectral method for Taylor vortex flow and Taylor-Couette flow, CD-ROM proceedings for the *13th AIAA Computational Fluid Dynamics Conference*, Snowmass, Colorado, USA, June 29 - July 2, 1997.

Rigopoulos, J., Sheridan, J. and Thompson, M.C. 1997 State Selection in Taylor vortex flow, abstract booklet for the *10th Couette-Taylor Workshop*, Paris, France, July 15 - 18, 1997.

Contents

1 Introduction

Taylor-Couette flow, the flow of the fluid between two concentric rotating cylinders, has been studied extensively for over a century. It was, and continues to be, of interest because it is one of the simplest situations for studying instability and transition of fluid flow for varying Reynolds number, and close comparisons between experiments and theory can be made conveniently. Usually the fluid is assumed viscous and incompressible.

Currently, two major areas of research in fluid mechanics are (i) the transition to turbulence and (ii) the study of state selection as a nonlinear problem. Taylor-Couette flow has been used as a test case for both of these areas. This thesis is concerned with the latter, particularly applied to Taylor vortex flow.

The field chosen for study arose from an interest in chaos and nonlinear dynamics. The Taylor-Couette flow problem is attractive because it provides a rich and diverse range of fluid flow structures, as is discussed in Chapter 2. How states are selected and whether these states are unique are questions of significance in fluid mechanics in general. Taylor vortex flow, which is axisymmetric, and therefore two-dimensional, thus provides a relatively "simple" example of a flow which exhibits multiple states at the same Reynolds number.

Some fundamental questions about Taylor vortex flow were posed by Koschmieder (1993).

1. Why is the wavelength of supercritical axisymmetric vortices independent of the Taylor number and equal to the critical wavelength when the Taylor number is increased slowly from subcritical values ?

2. Why can supercritical axisymmetric vortices be nonunique ?

To investigate these questions, we considered a numerical experiment whereby the inner cylinder speed was linearly increased in time from an initial subcritical value to a final supercritical value, over a finite ramp time, and then held fixed at the final speed. The numerical simulations were repeated for different ramp times but for the same initial

conditions and the same initial and final speeds. To clarify the behaviour of the modes with different ramp time, it was necessary to simulate Taylor vortex flow with a large aspect ratio, twenty times the gap size. This allowed us to study the independent growth and subsequent nonlinear interaction of many discrete axisymmetric modes. Computer simulations of Taylor vortex flow with such a large aspect ratio was possible on a high-end workstation.

The numerical method was based on operator splitting and spectral methods. Such approaches had previously been successfully applied to the Taylor-Couette cylindrical geometry by Marcus (1984) and Moser, Moin and Leonard (1983).

In industry, Taylor-Couette vessels with axial through-flow are being used to study the global mixing properties of different flow regimes when particles are immersed in the fluid (Rudman(1995)). A computer program that simulates Taylor-Couette flow accurately and efficiently would therefore be of great benefit in predicting the performance of flow regimes with regard to mixing efficiency.

The work described in this thesis can be briefly summarised by the following points.

1. Operator splitting and spectral methods have been used to develop a two-dimensional code to simulate Taylor vortex flow.

2. This two-dimensional code has been used to investigate state selection and nonuniqueness of Taylor vortex flow.

3. A linear model has been developed to explain the behaviour of the amplitude of the modes and how the state selection varies with ramp time.

4. An approach based on dynamical systems has been used to provide a nonlinear model for the nonuniqueness and the process of state selection.

5. Operator splitting and spectral methods have been used to develop a three-dimensional code to simulate Taylor-Couette flow in general. In particular, wavy vortex flow has been simulated.

An outline of the thesis is presented below.

Chapter 2 contains a review of the literature relevant to the study.

Chapter 3 describes the governing equations for Taylor-Couette flow, and Taylor vortex flow and the analytic solution for steady circular Couette flow.

Chapter 4 describes a numerical method for two-dimensional driven cavity flow, based on operator splitting and spectral methods. This was an important step in the development of a code for Taylor vortex flow.

Chapter 5 describes the numerical method used to develop the computer code for Taylor vortex flow. The operator splitting method is designed as a second-order time-accurate scheme. The Poisson and Helmholtz equations are solved using a spectral Tau method.

Chapter 6 describes the results obtained for the amplitudes of the modes for different ramp times. A linear model is used to explain the behaviour of the modes and the change in preferred mode with different ramp time. A nonlinear model is then developed based on a dynamical systems approach.

Chapter 7 describes the numerical method for Taylor-Couette flow, which is three-dimensional. It is an extension of the method used for Taylor vortex flow. Numerical tests are presented showing second-order time-accuracy. Results of a simulation of a wavy vortex flow are presented.

Chapter 8 concludes and makes recommendations for future work.

2 Literature Review

The literature on Taylor-Couette flow is extensive and review articles can be found in DiPrima and Swinney (1985), Stuart (1986) and Koschmieder (1993).

Taylor-Couette flow has been studied from different perspectives in disciplines such as fluid mechanics, chaos, nonlinear dynamics and computational fluid dynamics. The focus in this chapter will be more on Taylor vortex flow, although an overview of different flow regimes will be presented.

2.1 Taylor-Couette flow

A sketch of the Taylor-Couette flow system is shown in Figure 2.1 . The cylindrical coordinate system has axial z, azimuthal ϕ and radial r directions. The velocity components are u_z, u_ϕ and u_r. Consider inner and outer cylinder radii of r_{in} and r_{out} respectively which rotate with corresponding angular velocities Ω_{in} and Ω_{out} respectively. The radius ratio is defined as $\eta = r_{in}/r_{out}$ and the angular velocity ratio is $\mu = \Omega_{out}/\Omega_{in}$. The cylinders can co-rotate or counter-rotate. However, most work has been done with the outer cylinder stationary and only the inner cylinder moving.

We consider a length scale equal to the gapsize $d = r_{out} - r_{in}$. With the velocity scale equal to the inner cylinder speed $r_{in}\Omega_{in}$, the Reynolds number is $Re = r_{in}\Omega_{in}d/\nu$, where ν is the kinematic viscosity of the fluid. As an alternative to Reynolds number, one often defines the Taylor number $\mathcal{T}$, which is a nondimensional measure of rotation rate. Usually one takes $\mathcal{T} = 4\Omega_{in}^2 d^4/\nu^2$. The Taylor number is proportional to the square of the Reynolds number, that is, $\mathcal{T}/\mathcal{T}_c = (Re/Re_c)^2$, where the subscripts denote critical values for the onset of Taylor vortex flow.

The nondimensional height of the cylinders, Γ, is also called the aspect ratio. If the cylinders are finite in axial extent, as they are in real experiments, there will also be end conditions that will apply at the top and bottom end of the annulus. When the cylinders are of infinite height, where the majority of the computational work has been done, one cannot have an infinitely sized computational domain. Here, the Taylor-Couette

flow pattern is assumed periodic in its axial extent and Γ sets the value for the maximum allowed axial wavelength.

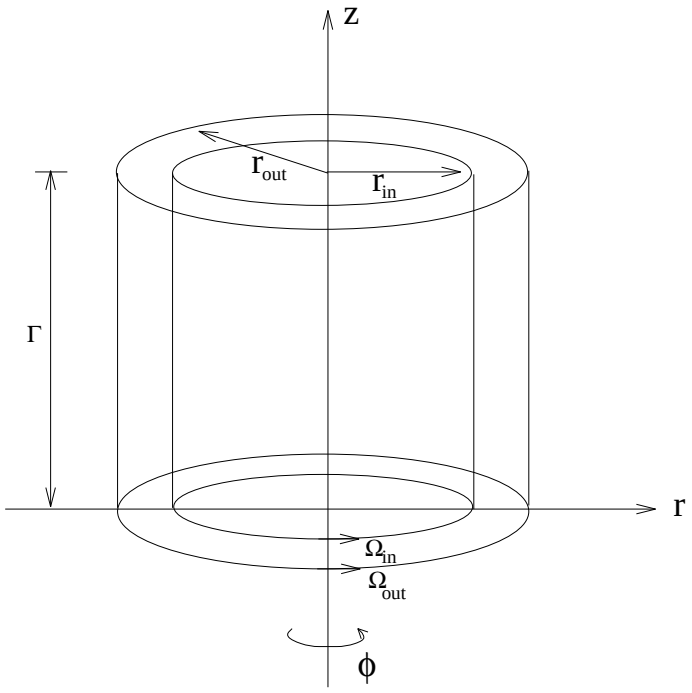

Figure 2.1: A diagram of the Taylor-Couette flow system.

2.2 Transition to turbulence

Andereck et al. (1986), Andereck and Baxter (1988) explored experimentally the rich variety of flows existing in cylindrical Taylor-Couette flow, depending on the inner and outer cylinder Reynolds numbers. They used $\eta = 0.883$ and $\Gamma = 30$. The flow regimes are illustrated in Figure 2.2. The theoretical studies have not kept pace with these experimental observations. The figure demonstrates that the route to turbulence depends in a complex way on the inner and outer cylinder speeds.

For a stationary outer cylinder, as the inner cylinder speed is increased quasi-steadily from rest, Andereck et al. (1986) observed the following series of transitions: circular Couette flow $\rightarrow$ Taylor vortex flow $\rightarrow$ wavy vortex flow $\rightarrow$ modulated wavy flow $\rightarrow$ chaos $\rightarrow$ turbulent Taylor vortex flow.

.

Figure 2.2: Diagram of Re_{in} versus Re_{out} showing the different flow regimes in Taylor-Couette flow obtained experimentally by Andereck et al. (1986) for $\eta = 0.833$.

2.2.1 Steady circular Couette flow

For sufficiently low Re, steady circular Couette flow is observed. This flow has an analytic solution of the form $u_r(z, \phi, r, t) = 0$, $u_\phi(z, \phi, r, t) = V(r)$ and $u_z(z, \phi, r, t) = 0$, where

$$V(r) = Ar + B/r \tag{1}$$

and

$$A = \frac{\Omega_{in}(\mu - \eta^2)}{1 - \eta^2} \qquad\qquad B = \frac{\Omega_{in} r_{in}^2 (1 - \mu)}{1 - \eta^2} \tag{2}$$

2.2.2 Taylor vortex flow

When Re reaches a critical value Re_c, Couette flow becomes unstable with respect to infinitesimal axisymmetric disturbances and Taylor vortex flow forms. This is named after G. I. Taylor (Taylor (1923)) who was first to make a detailed comparison between theory

and experiment of this flow. The instability represents a supercritical steady bifurcation from Couette flow to Taylor vortex flow. At steady state, the flow resembles a series of axisymmetric toroidal vortex cells, which are periodically spaced along the axial direction, each circulating alternately in direction. This is illustrated in Figure 2.3 by the picture on the left. The Taylor vortex flow state is defined by its axial wavelength.

2.2.3 Wavy vortex flow

When Re reaches a second critical value Re_c', Taylor vortex flow becomes unstable with respect to infinitesimal disturbances with azimuthal periodicity and wavy vortex flow forms. This nonaxisymmetric flow was experimentally observed by Taylor but it was Coles (1965) who made an extensive experimental study of wavy vortex flow, through photography and flow visualization. The wavy vortices had a definite frequency and moved with a definite wave velocity in the azimuthal direction. This instability is a time-periodic supercritical bifurcation (a Hopf bifurcation) from Taylor vortex flow to wavy vortex flow. Observed in the proper rotating frame, wavy vortex flow appears steady-state. This is illustrated in Figure 2.3 by the picture on the right. The wavy vortex flow state is defined by its axial wavelength and azimuthal wavenumber.

2.2.4 Modulated wavy vortex flow

When Re reaches a third critical value Re_c'', a second azimuthal wave with a discrete frequency appears, making the flow quasi-periodic. This was noticed by Fenstermacher et al. (1979) who performed laser-Doppler measurements of the periodicity of wavy vortices. The second frequency is incommensurate with the first frequency and it marks the appearance of modulated wavy vortices. It was Gorman and Swinney (1982) who identified this new flow as modulated wavy vortex flow.

.

Figure 2.3: Left picture: Flow visualization of Taylor vortex flow at $\mathcal{T} = 1.16\mathcal{T}_c$. Taken from Koschmieder (1993). The parameters are $\eta = 0.896$ and $\Gamma = 122$. Right picture: Flow visualisation of wavy vortex flow at $\mathcal{T} = 8.49\mathcal{T}_c$. Taken from Koschmieder (1993). The parameters are $\eta = 0.896$, $\Gamma = 122$ and axial wavelength of $\lambda = 2.6$. There are six azimuthal waves.

2.2.5 Chaos and turbulence

Brandstater and Swinney (1987) studied experimentally the transition from quasi-periodic flow to weakly turbulent flow of Taylor-Couette flow with the inner cylinder rotating only. They plotted velocity power spectra, phase space portraits and circle maps to show that the nonperiodic behaviour was deterministic (i.e. chaotic) and could be described by strange attractors. They estimated the onset of chaotic flow at about $11.7Re_c$, after which the dimensions of the flow become noninteger, increasing above the value of 2.0. At this same Reynolds number broadband noise appeared in the power spectrum. The exponential decay of the power spectrum provided additional evidence that the observed nonperiodic behaviour corresponded to low-dimensional deterministic chaos, not stochastic behaviour (which itself would follow a power law). They made the comment that the route to chaos via period doubling, intermittency and the break-up of a 2-torus as described by circle maps did not occur in the Taylor-Couette system. The behaviour of the circle maps of Taylor-Couette flow was apparently quite different from the maps that exhibited frequency locking. In turbulent Taylor vortex flow, the axial periodicity persists in the time-averaged sense.

2.3 Linear stability of steady circular Couette flow

In the analysis of Taylor (1923) the incompressible and axisymmetric Navier-Stokes equations were used. The velocity was set equal to the Couette flow velocity plus the perturbed velocity, $\mathbf{u}'$. After linearization of the resulting disturbance equations, normal mode solutions were sought, of the form

$$u'(z,r,t) = u(r)\cos\left(\frac{2\pi}{\lambda}z\right)e^{\sigma t} \tag{3}$$

$$v'(z,r,t) = v(r)\cos\left(\frac{2\pi}{\lambda}z\right)e^{\sigma t} \tag{4}$$

$$w'(z,r,t) = w(r)\sin\left(\frac{2\pi}{\lambda}z\right)e^{\sigma t} \tag{5}$$

where λ is the axial wavelength and σ is the growth rate of the normal mode. As Taylor vortex flow is not oscillatory, σ is a real number. With some manipulation the disturbance equations are written as an eigenvalue problem, the solution of which gives the growth rate of each mode for the chosen Reynolds number (or Taylor number).

The outer curve in Figure 2.4 describes the variation of critical Reynolds number with axial wavelength of the axisymmetric perturbation. For a particular Re above a minimum critical value, Re_c, there is a linearly unstable band of axial wavelengths. Infinitesimal axisymmetric perturbations with wavelengths in this band will grow exponentially. Outside the band, circular Couette flow is stable and infinitesimal axisymmetric perturbations decay exponentially.

2.4 Moderately supercritical Taylor vortex flow

Coles (1965) conducted experiments for wavy vortex flow. He was able to achieve states with different axial and azimuthal wavenumbers at the same Reynolds number, thus demonstrating nonuniqueness. He found that, in accelerating or decelerating from one Re to another, the rate at which a particular Reynolds number is reached can influence the wavy vortex flow state that appears. Also, if this rate is large enough an hysteresis can result which does not occur for slower rates.

Snyder (1969) subsequently demonstrated nonuniqueness of the axial wavelength in Taylor vortex flow. He conducted an experiment in an apparatus with a large aspect ratio and small gap width. By varying the inner and outer cylinder Reynolds numbers, Re_{in} and Re_{out}, slowly with time via different paths through the critical Reynolds number Re_c, he was able to achieve stable Taylor vortex flows of different wavelengths at the same final Re_{in} and Re_{out}. However, Snyder had experimentally been able to achieve stable Taylor vortex flows for a much smaller band of wavelengths than the band derived from linear theory.

.

Figure 2.4: Stability diagram for Taylor vortex flow for $\eta = 0.727$, $\mu = 0$. Taylor number versus axial wavelength. The solid line is the neutral curve from the linear stability of steady circular Couette flow Chandrasekhar (1961). The dashed line shows the stability boundary from a weakly nonlinear analysis Kogelman and DiPrima (1970). The open circles represent Taylor vortex flow states observed for sudden start experiments Burkhalter and Koschmieder (1974). The filled circles represent Taylor vortex flow states observed for an experiment where the annulus was filled with fluid after inner cylinder was rotating at fixed speed. From Burkhalter and Koschmieder (1974).

Kogelman and DiPrima (1970) undertook an analysis of Taylor vortex flow to third order based on the weakly nonlinear stability theory of Eckhaus (1965). They found that stable Taylor vortex flows are achievable only for wavelengths within a band roughly $1/\sqrt{3}$ times the width of the band from linear theory.

The inner band, shown in Figure 2.4, has inner and outer limits given by

$$\lambda_{nl} = \frac{\lambda_c \lambda_l \sqrt{3}}{\lambda_c + \lambda_l(\sqrt{3} - 1)} \tag{6}$$

where λ_l is the corresponding band limit from linear theory. The critical wavelength λ_c is defined as the wavelength corresponding to a minimum in the critical Reynolds number and takes a value of 2.0 in Figure 2.4. The inner band is called the Eckhaus stable band. Taylor vortex flows with wavelengths outside this band are unstable with respect to axisymmetric perturbations. Kogelman and DiPrima showed that these observations of Snyder lied well within the Eckhaus stable band.

Later, Stuart and DiPrima (1978) analysed the flow using a Landau amplitude equation with a dispersive term which allowed for slow spatial variations in the axial direction. They described the Eckhaus mechanism of instability as being when sideband perturbations resonate with the first harmonic of the fundamental mode of the periodic flow to mutually reinforce each other, leading to an instability.

Burkhalter and Koschmieder (1973) conducted experiments whereby the inner cylinder was increased quasi-steadily from rest and found that the preferred wavelength of the Taylor vortex flow was equal to the critical wavelength, λ_c. Experiments by Burkhalter and Koschmieder (1974) for an inner cylinder impulsively increased from rest showed that the preferred wavelength, λ_s, was smaller than the critical wavelength. This is illustrated in Figure 2.4, where their data are represented by the open circles. Figure 2.5 also shows the variation of preferred axial wavelength with Taylor number for sudden starts.

.

Figure 2.5: Taylor number versus axial wavelength for $\eta = 0.727$. From Burkhalter and Koschmieder (1974).

In addition, stable Taylor vortex flows with wavelengths longer than the critical wavelength were produced by a filling experiment. In these experiments the annulus was filled with fluid when the inner cylinder was rotating at a particular speed.

Koschmieder (1993) stated that stable Taylor vortex flows with preferred wavelengths between λ_s and λ_c can be achieved by applying different inner cylinder acceleration rates to the same final Reynolds number. Thus, Taylor vortex flows with different axial wavelengths within the Eckhaus stable range can be achieved depending on how the experiment is performed.

Nakaya (1974) extended the weakly nonlinear analysis to fifth order for $\eta = 0.5$. The band of stable Taylor vortex flows was found to be narrower than the one derived by Kogelman and DiPrima, but still wider than the range of experimentally observed nonunique flows.

.

Figure 2.6: Stability diagram for stable Taylor vortex flow for $\eta = 0.75$. A plot of $\epsilon = (Re - Re_c)/Re_c$ versus wavenumber q, where q is the critical wavenumber. The dashed curve is the Eckhaus boundary from Kogelman and DiPrima (1970). The solid curve is the nonlinear boundary according to Riecke and Paap (1986). The solid circles show the experimental results for the Eckhaus boundary. The triangles, open circles, and vertical bars near the centre give the band of states selected by spatial ramps of two different slopes in ϵ. From Dominguez-Lerma et al. (1986).

Riecke and Paap (1986) applied a Galerkin procedure to solve the axisymmetric Navier-Stokes equations for the stability of Taylor vortex flow with respect to axisymmetric perturbations. They considered $\eta = 0.892, 0.75$ and 0.5, an infinite cylinder aspect ratio and stationary outer cylinder. For $Re \leq 1.1Re_c$ the band of stable wavenumbers was considerably smaller than predicted from the amplitude expansions of Kogelman and DiPrima, as shown in Figure 2.6.

Dominguez-Lerma et al. (1986) investigated the stability of Taylor vortex flow ex-

perimentally in an apparatus with $\eta = 0.75$ and $\Gamma = 40$. Although quantitatively, the agreement to the numerical results by Riecke and Paap is remarkable, Koschmieder (1993) comments that the experimental uncertainty would have been of the order of at least 1%.

2.5 Wavelength selection criteria

Snyder (1969) described a number of theories of wavenumber selection. These were:

(1) Theories based on Bénard convection.

(2) Models based on the linearised Navier-Stokes equations, already discussed.

(3) Variational methods for the nonlinear problem. For example, selection based on an extremum principle where the criterion is:

(a) minimum total heat transport for the Bénard convection problem,

(b) minimum mean square vertical thermal gradient for the Bénard convection problem,

(c) minimum rate of entropy production,

(d) maximum viscous dissipation,

(e) Coles (1965) suggested that for wavy vortex flow the trajectory of the preferred state corresponds to a path of steepest ascent on a surface of dissipation rate plotted against inner cylinder Reynolds number and wavenumber.

Snyder commented that a common characteristic of the variational principles is that no unique wavenumber is obtained and the principles are not derived directly from the governing equations so it is not known whether any of the above criteria are directly derivable from the governing equations.

(4) Weakly nonlinear models developed from the governing equations. Stuart (1960) developed a perturbation scheme which differed from previous work in that the time variable was included. The notable feature of Stuart's method, pointed out by Segel (1962), was that the final equilibrium state must depend upon the initial state.

DiPrima and Eagles (1977) calculated theoretically the wavenumbers corresponding to maximum amplification rate λ_a and maximum torque λ_t for different radius ratios and

Taylor numbers. The calculations were made for an infinite aspect ratio with the outer cylinder stationary using an analytical, weakly nonlinear approach. Their results contradicted Coles' conjecture with respect to his own experiments. However, they concluded from their own results that it is possible that λ_a or λ_t is a preferred wavenumber. They suggested the problem of final state selection does not require going outside the framework of the Navier-Stokes equations. " Rather, it requires the solution of the initial value problem, or even a succession of initial value problems to match some experiments ".

Benjamin and Mullin (1982) varied the inner cylinder rotation rate and the aspect ratio, keeping the outer cylinder stationary. They argued that the presence of ends in the Taylor-Couette apparatus will always bear crucially on what wavelength is selected, regardless of how long the finite cylinders are. Also, the presence of ends gives rise to a quantisation condition for the possible wavelengths so that only wavelengths corresponding to integer wavenumbers are observed (like a standing wave pattern). As the aspect ratio is increased to infinity the multiplicity of wavenumbers increases to a continuum of possible wavenumbers. The authors describe two types of possible flows: the primary flow, selected by slow (quasi-steady) increases of Reynolds number and secondary flow, selected by other methods e.g. variations of Reynolds number combined with variations of aspect ratio to the same final Reynolds number and aspect ratio. For every given finite aspect ratio, a unique primary flow exists.

2.6 Stability of unsteady circular Couette flow

When the Reynolds number is constant in time the state that develops is a time-periodic state. For time-periodic base states, Floquet theory guarantees the existence of an exponential temporal factor and hence a well-defined growth rate. Linear theory may then be applied in a relatively straightforward fashion. However, in the situation with a linearly ramped inner cylinder one has a time-aperiodic basic state. For time-aperiodic basic states Floquet theory no longer applies.

.

Figure 2.7: $R_{I,c}/R_s$ versus R_0/R_s for $\eta = 0.5$ and $A > 0$. The acceleration rate A labels each curve. R_0 is the initial Reynolds number. —— —— steady-state linear limit, – – – Eagles' enhanced limit for $A = 1.6$. From Neitzel (1982b).

In cases with time-aperiodic states one's attention can be restricted to slowly varying flows to allow the use of the WKBJ approximation, making further assumptions regarding a stability criterion. In the WKBJ approximation the temporal part of the solution is expressed as an exponential function of time. When the inner cylinder speed is increased slowly, Eagles (1974) applied the WKBJ approximation to show that the instantaneous critical Reynolds number is slightly higher than their critical Reynolds numbers in the steady situation. He predicted an increase of approximately 6% for $\eta = 0.5$ and 10% for $\eta = 0.95$.

Alternatively for time-aperiodic states, one can base a stability decision upon some

arbitrary quantity such as a disturbance amplification factor. From this approach, Neitzel (1982b) applied energy-stability theory to unsteady circular Couette flow. He considered the situation of an inner cylinder Reynolds number increased linearly with time from subcritical to supercritical values at different rates, A. His results showed that the instantaneous critical Reynolds number, $R_{I,c}$, increases relative to the steady result, R_s, as A, increases. This is shown in Figure 2.7. For $A = 1.6$ the increase is about 5% for $\eta = 0.5$ compared with 4% for $\eta = 0.95$.

2.7 Amplitude equations

The results from linear theory assume indefinite exponential growth of disturbances. In reality, nonlinear effects will eventually make the growing mode saturate and tend to a steady-state Taylor vortex flow pattern. Landau (1944) replaced the exponential time factor in Equations (3) to (5) with an amplitude time factor $A(t)$. In general, $A(t)$ can be a complex number.

Following Drazin and Reid (1989), $A(t)$ is determined from the Landau equation

$$\frac{dA}{dt} = \sigma A - lA|A|^2 \tag{7}$$

where l is the Landau constant. The analytic solution is

$$|A(t)| = \sqrt{\frac{A_o^2}{\frac{l}{\sigma}A_o^2 + \left(1 - \frac{l}{\sigma}A_o^2\right)\exp(-2\sigma t)}} \tag{8}$$

$$|A| \rightarrow A_e = \sqrt{\frac{\sigma}{l}} \qquad \text{as} \qquad \text{t} \rightarrow \infty \tag{9}$$

where A_e is the equilibrium amplitude.

This equation describes the growth and eventual saturation of the amplitude of a pure mode. Initially the mode grows exponentially and then it self-interacts, generating higher harmonics.

Davey (1962) first made a weakly nonlinear analysis of Taylor vortex flow using an amplitude expansion technique applied to the axisymmetric Navier-Stokes equations. The

amplitude expansion technique was previously used by Stuart (1960) where it was applied to plane Poiseuille flow and by Watson (1960) where it was applied to plane Poiseuille flow and plane Couette flow. Davey derived an amplitude equation of the form given in Equation (7).

Eagles (1971) and DiPrima and Eagles (1977) extended the analysis to fifth order amplitude terms but found no significant differences in the results.

To first order one can write

$$\sigma = K(Re - Re_c) \tag{10}$$

and deduce from Equation (9) that

$$A_e = \sqrt{K(Re - Re_c)/l} \tag{11}$$

This means that the equilibrium amplitude increases in a first approximation as $\sqrt{Re - Re_c}$.

In his theoretical analysis, Davey confirmed this relationship for the wide gap case ($\eta = 0.5$) and outer cylinder at rest.

Despite these agreements Koschmieder (1993) makes the important point that the derivation of the Landau equation in Taylor vortex flow is valid only for two-dimensional, weakly nonlinear flow. In other words, for Reynolds numbers close to the critical. His view is that, in general, the amplitude is unlikely to be the only parameter that determines the characteristics of nonlinear flow.

When more than one mode is considered, an extension can be made to the Landau equation to include coupling terms:

$$\frac{dA_j}{dt} = \sigma_j A_j - l_j A_j |A_j|^2 - \sum_{l \neq j} \alpha_{jl} |A_l|^2 A_j \tag{12}$$

where the subscripts label the modes. The negative sign means that energy is drawn from mode j by mode l. The coefficient α_{jl} is a coupling constant.

The modelling of the behaviour of two coupled generators was discussed by Abarbanel, Rabinovich and Sushchik (1993). The problem has applications in convective flow in a

fluid, electrical circuits, and coupled modes in a laser resonator, for example. The model is often called a two-frequency Van der Pol generator or the kinetic equations. From Equation (12), consider two coupled amplitude equations of the form

$$\frac{dA_1}{dt} = (1 - |A_1|^2 - \alpha_{12}|A_2|^2)A_1 \tag{13}$$

$$\frac{dA_2}{dt} = (1 - |A_2|^2 - \alpha_{21}|A_1|^2)A_2 \tag{14}$$

This model shall be applied in a more general way in Chapter 6.

If it is further assumed that, $\alpha_{12} = \alpha_{21} = 2$. When $\frac{dA_1}{dt} = 0$ and $\frac{dA_2}{dt} = 0$, the equilibrium points are:

(1) $|A_1|^2 = 0$, $|A_2|^2 = 0$

(2) $|A_1|^2 = 0$, $|A_2|^2 = 1$

(3) $|A_1|^2 = 1$, $|A_2|^2 = 0$

(4) $|A_1|^2 = \frac{1}{3}$, $|A_2|^2 = \frac{1}{3}$

In the phase space spanned by $|A_2|^2$ against $|A_1|^2$, the system has two stable equilibrium states, the coordinates of which are given by points (2) and (3). Which of the two states becomes preferred depends on the initial conditions. If the inital amplitude of mode 1 is sufficiently larger than the initial amplitude of mode 2 then after a certain time the system tends to the state given by point (3). In other words, mode 1 survives and suppresses mode 2. So for some initial conditions mode 1 wins and for other initial conditions mode 2 wins. This is what is called mode competition.

When $\alpha_{12} < 1$ and $\alpha_{21} > 1$ mode 1 wins, and when $\alpha_{12} > 1$ and $\alpha_{21} < 1$ mode 2 wins, regardless of the initial conditions. When $\alpha_{12} < 1$ and $\alpha_{21} < 1$ the modes do not affect each other and both modes grow to a finite amplitude.

In an application to the Rayleigh-Bénard thermally driven convection experiment, Abarbanel, Rabinovich and Sushchik (1993) wrote an extension of Equation (12) to the form

$$\frac{dA_j}{dt} = \sigma_j A_j - l_j A_j |A_j|^2 - \sum_{l \neq j} \alpha_{jl} |A_l|^2 A_j + \sum \beta_{lq} A_q^* A_l^* \tag{15}$$

where the asterisk refers to a complex conjugate quantity.

In the quadratic term, the sum is taken over all harmonics which satisfy the resonance condition: $\mathbf{k}_j + \mathbf{k}_q + \mathbf{k}_l = 0$, where $\mathbf{k}$ is the wavevector and the general expression for the temperature or fluid velocity has the form

$$\Phi(\mathbf{r}, t) = \sum_{j=1}^{N} a_j(t) \exp(i(\mathbf{k_j r} - \omega_j t)) + \text{complex conjugate} \tag{16}$$

The coefficient β_{lq} is a coupling constant. The quadratic term models resonant three-wave interactions. Physically, such interactions can occur if the viscosity coefficient is dependent on temperature in a fluid convection. Consider three modes. If initially there is only mode 1 and 2, they will make mode 3 grow to a larger amplitude. Also, If β_{lq} is large enough all three modes will grow simultaneously.

2.8 Computational methods

Taylor (1923) solved the linearised form of the axisymmetric Navier-Stokes equations by expressing the velocity of the perturbation in terms of Bessel functions, where the coefficients where determined via matrix manipulation. By assuming a small gapsize, he represented the exact matrix for the coefficients in terms of approximate expressions for the Bessel functions. He calculated the variation of the value of the critical Reynolds number with different choices of inner and outer cylinder angular velocities and obtained excellent agreement with his experimental results from flow visualization.

Meyer (1967) applied finite differencing to solve the axisymmetric Navier-Stokes equations to simulate Taylor vortex flow. The equations were expressed in terms of stream-function and vorticity. The critical Reynolds number agreed to within 3% of that obtained from linear theory.

Alonso and Macagno (1973) used an alternating direction implicit (ADI) scheme to solve the axisymmetric Navier-Stokes equations which were expressed in terms of tangen-

tial velocity, vorticity and stream function. An infinite cylinder case was assumed with stationary outer cylinder. For $\eta = 0.833$ and for a wide range of Reynolds numbers it was shown that the scheme had a satisfactory rate of convergence and was stable even for a coarse mesh and large time increments.

Liu and Chen (1973) simulated Taylor vortex flow with impulsive starts of the inner cylinder. The axisymmetric Navier-Stokes equations were solved in vorticity-streamfunction notation using explicit finite difference approximations. Random small perturbations were applied in space initially, to more accurately reproduce the development of Taylor vortex flows in a real experiment.

Alziary de Roquefort & Grillaud (1978) computed the Taylor vortex flow for an apparatus with rotating end walls using a finite difference method. The Navier-Stokes equations were expressed in stream function, vorticity and tangential velocity formulation. The scheme involved implicit fractional steps and fast Fourier transforms while upwind differencing was used for the convective terms.

Meyer-Spasche and Keller (1980) traced the bifurcation from circular Couette flow to Taylor vortex flow by solving the steady, axisymmetric Navier-Stokes equations. They used Fourier expansions in the axial direction and a centred finite difference approximation in the radial direction. The discretised equations were solved using a pseudoarclength continuation method; such methods are commonly used to detect bifurcations. Good agreement was obtained for the Torque as a function of Reynolds number between the numerical and experimental results for $\eta = 0.5$ and $\eta = 0.95$.

Spectral methods have been shown to have high accuracy (exponential convergence) and efficiency for a relatively low number of gridpoints, as compared with finite difference methods. The use of spectral methods to solve problems with solid boundaries did not emerge until the late 1970s, when reliable Fourier-Chebyshev algorithms were available. Finite difference methods were not preferred because of the numerical problem of cumulative phase errors, which did not occur with spectral methods.

Marcus, Orszag and Patera (1982) used a pseudo-spectral (or collocation) technique

to simulate Taylor-Couette flow with infinite cylinder length, and finite gap size, fixed outer cylinder and moving inner cylinder. The boundary conditions were assumed to be viscous and no-slip. The velocity was expressed as a Fourier series in the axial direction (due to periodicity), a Fourier series in the azimuthal direction (due to periodicity) and a Chebyshev series in the radial direction (due to the solid boundaries formed by the inner and outer cylinder walls). The velocity was computed by integrating the Navier-Stokes equation in cylindrical coordinates forward in time using a fractional-step time-splitting (or operator splitting) technique. The first step dealt with the nonlinear term and made a second order Adams-Bashforth approximation. The solution of this step was then used in the second step together with an Euler approximation of the pressure term, to obtain a pressure corrected velocity. The pressure was expressed as an inviscid pressure term plus a viscosity-corrected pressure component (Greens function). The inviscid pressure term was determined assuming that the velocity at the second fractional step was divergence free, leading to a Poisson equation, and satisfied the inviscid boundary conditions (that the radial derivative of the inviscid pressure term equalled the radial component of the velocity at the first fractional step at the cylinder walls). The Greens function was evaluated by solving another Poisson-like equation (with right hand side equal to zero), at the end of the viscous step (the final fractional step). It was computed by evaluating a diagonal capacitance matrix once in a pre-processing stage and inverting the capacitance matrix after each viscous step. The use of a Greens function removed the time-splitting errors. The final fractional step was the viscous step which made a Crank-Nicolson approximation of the viscous term. The authors simulated steady-state, periodic and quasi-periodic Taylor-Couette flows and verified that the time-splitting error was less than 10^{-6} for 33 radial collocation points, 32 axial points and 16 azimuthal points (per azimuthal span of $2\pi/6$ radians). Checks were made with results from other researchers on Taylor-Vortex flow for torques and wavespeeds, the later being the more severe test. At small values of the Reynolds number (about $2Re_c$) the boundaries had to treated very carefully. At large Reynolds numbers (about $10Re_c$) the wave speed was insensitive to the exact value of the

Reynolds number.

Moser, Moin and Leonard (1983) developed a spectral method which was classified by Canuto et al (1988) as a Petrov-Galerkin method. The velocity was written as a Fourier series in the azimuthal and axial directions. In the radial direction a spectral expansion was used which inherently satisfied the boundary conditions and the continuity equation. The resulting radial component of velocity contained components which were quasi-orthogonal functions constructed from Chebyshev polynomials. The procedure transformed the three-dimensional Navier-Stokes equation to three independent equations in spectral space containing banded matrices which were efficiently solved at each time step. The pressure term was eliminated from the Navier-Stokes equation. The three equations in spectral space are integrated forward in time by assuming Crank-Nicolson time-differencing for the viscous terms and Adams-Bashforth time-differencing for the nonlinear terms. The procedure was tested with application to Taylor-Couette flow with axisymmetric Taylor vortex flow and wavy vortex flow. In all cases good agreement was obtained with available experimental and theoretical results, although the discretization of the grid was much coarser than in Marcus (1984b).

Marcus (1984a, 1984b) further developed the pseudospectral technique used by Marcus, Orszag and Patera (1982). The difference to that method lay mainly in a different choice of boundary conditions when solving the Poisson equation for the viscous-corrected pressure term. The boundary condition chosen was that the radial derivative of the total pressure was equal to the radial component of velocity at the first fractional step plus the radial component of the diffusion term evaluated after the viscous fractional step, at the cylinder walls. He tested the code by comparing his numerically determined growth rates and wave speeds with linear theory and by comparing his computed torques with experimentally measured values. He used a grid with 33 radial Chebyshev points, 32 axial Fourier points and 32 azimuthal Fourier points. In his code he also used the symmetry characteristics of wavy vortex flow to investigate flows with fixed azimuthal wavenumber. He used his code to study Taylor vortex flows and wavy vortex flows by computing energy,

angular momentum, torque, wave speed, energy dissipation rate, enstrophy, and energy and enstrophy spectra. Using these results he argued that the azimuthal travelling waves are a secondary instability caused by the strong radial motion in the outflow boundaries of the Taylor vortices and are not shear instabilities associated with inflection points of the azimuthal flow. The travelling wave mixes together the fluid in the cores of neighbouring Taylor vortices and thereby creates nonaxisymmetric vortical motions in the (z, ϕ) plane centred at the outflow and inflow boundaries. Marcus also commented that time splitting does not cause appreciable error in pipe flow, but does cause a large error in Taylor-Couette flow. This is because the forcing terms for Taylor-Couette flow are at the radial boundaries while in pipe flow the radial boundaries are rather unimportant. The use of supercomputers made it possible to extend the simulations of wavy vortex flows to fairly large Reynolds numbers. The computations were in excellent agreement with experiments for the critical Reynolds number for the onset of wavy vortex flow and the angular velocities of the waves. Coughlin and Marcus (1991, 1992a, 1992b) used their method to simulate modulated wavy vortex flow.

Street and Hussaini (1991) developed two numerical methods to study Taylor-Couette flow with a fixed outer cylinder and a finite length to gap ratio. The first was a time-split spectral collocation scheme, used in both axisymmetric and three-dimensional time accurate forms. The second was a staggered mesh scheme. In the time-split scheme, Chebyshev series were used in the radial and axial directions (due to solid boundaries) and Fourier series was used in the azimuthal direction (due to periodicity). Collocation was used due to its

1. straightforward treatment of nonlinear terms and boundary conditions,
2. capability to include coordinate stretchings, and
3. ability to solve the resulting discrete equations rapidly.

Coordinate stretching was used in the radial direction to resolve the large gradients near the inner cylinder. The axial direction was not stretched. In the first fractional step, the nonlinear terms and the diffusion terms were treated together. It involved a third

order Runge-Kutta scheme for the nonlinear terms and Crank-Nicolson for the diffusion terms. In the second and final fractional step, the velocity solution of the first step was used together with a backwards Euler approximation of the pressure term. The pressure was determined from a Poisson equation, assuming the velocity at the second step was divergence free. The boundary conditions for pressure were that the normal component of pressure gradient at the boundaries be zero. The error involved in this specification of boundary conditions was related to the overall time-splitting error of the scheme. Each time step required the solution of nine positive-definite Helmholtz equations with Dirichlet conditions and one Poisson equation with pure Neumann boundary conditions (per Fourier azimuthal mode). A tensor-product decomposition technique was used to solve for the Helmholtz equations in which the eigenvectors of the one-dimensional spectral operators were used to diagonalize the multidimensional operator (see Canuto et al (1988), Haidvogel and Zang (1979), Gottlieb and Orszag (1977)). The Poisson equation was solved using an influence matrix method. These two techniques appear to be the same techniques used by Marcus (1984a, 1984b). Computations were done on a Cray 2 supercomputer with a Chebyshev - Chebyshev - Fourier discretization of $65 \times 45 \times 32$ points, including physical-space stretchings in both Chebyshev directions. Very small time steps were required to keep splitting errors small at high spatial resolution levels.

3 Governing Equations

3.1 Taylor-Couette flow

The Navier-Stokes equations written in cylindrical coordinates are:

$$\frac{\partial u_r}{\partial t} + (\mathbf{u}.\nabla)u_r - \frac{{u_\phi}^2}{r} = -\frac{1}{\rho}\frac{\partial P}{\partial r} + \nu\left(\nabla^2 u_r - \frac{u_r}{r^2} - \frac{2}{r^2}\frac{\partial u_\phi}{\partial \phi}\right) \tag{1}$$

$$\frac{\partial u_\phi}{\partial t} + (\mathbf{u}.\nabla)u_\phi + \frac{u_r u_\phi}{r} = -\frac{1}{\rho}\frac{1}{r}\frac{\partial P}{\partial \phi} + \nu\left(\nabla^2 u_\phi - \frac{u_\phi}{r^2} + \frac{2}{r^2}\frac{\partial u_r}{\partial \phi}\right) \tag{2}$$

$$\frac{\partial u_z}{\partial t} + (\mathbf{u}.\nabla)u_z = -\frac{1}{\rho}\frac{\partial P}{\partial z} + \nu\nabla^2 u_z \tag{3}$$

which are subject to the incompressibility constraint

$$\nabla.\mathbf{u} = 0 \tag{4}$$

where $u_r(z,\phi,r,t)$, $u_\phi(z,\phi,r,t)$ and $u_z(z,\phi,r,t)$ are the radial, azimuthal and axial components of velocity, respectively. Also, $P(z,\phi,r,t)$ is the pressure.

The equations are solved in an annular domain ($r_{in} \leq r \leq r_{out}$, $0 \leq \phi \leq 2\pi$, $0 \leq z \leq \Gamma$) with periodic boundary conditions in the axial (z) direction and azimuthal (ϕ) direction, and the radial velocity boundary conditions of $r_{in}\Omega_{in}$ at the inner cylinder and $r_{out}\Omega_{out}$ at the outer cylinder. The radius ratio is defined as $\eta = r_{in}/r_{out}$ and the angular velocity ratio as $\mu = \Omega_{out}/\Omega_{in}$. Then $\mu = 0$ if the outer cylinder is stationary. The periodic height of the cylinders, Γ, defines the aspect ratio.

A transformation from r to r' is made using $r' = r/\alpha - \gamma$ where the length scale $\alpha = (r_{out} - r_{in})/2$ and $\gamma = (\eta + 1)/(1 - \eta)$. This is done because use will be made of the Chebyschev polynomials to model the radial variation in velocity and pressure. The variable z is therefore transformed to z' using $z' = z/\alpha$. The variable ϕ is unchanged. Also, define the velocity scale as $r_{in}\Omega_{in}$ and the pressure scale as $\rho(r_{in}\Omega_{in})^2$. The Reynolds

number is then $Re = \Omega_{in} r_{in}(r_{out} - r_{in})/2\nu$ which is used to substitute in the nondimensional form of the equations for ν. The annular domain is then defined by ($-1 \leq r' \leq 1$, $0 \leq \phi \leq 2\pi$, $0 \leq z' \leq \Gamma'$). The time scale is $\alpha/(\Omega_{in} r_{in})$.

The commonly used length scale in Taylor-Couette flow is the gap size, whereas for the purposes of our computational method half the gap size has been chosen. In this thesis, nondimensionalised input parameters and results will always be presented with respect to a length scale equal to the gapsize. To translate results obtained with a length scale equal to the gap size to results obtained with half the gap size, the following were considered. The Reynolds number and the scales of time, aspect ratio and axial wavelength are half those defined using a length scale equal to the gap size. Consequently, the scales for axial wavenumber and growth rate are twice those defined using a length scale equal to the gap size.

Therefore, the nondimensional values for the length variables (including axial wavelength and aspect ratio) and time variable are twice those defined using a length scale equal to the gap size. Also, the nondimensional values for axial wavenumber and growth rate are half those defined using a length scale equal to the gap size. The primes are dropped on all variables, understanding them to be nondimensional from now on.

The form of the equations are then

$$\frac{\partial u_r}{\partial t} = N_r(\mathbf{u}) - \frac{\partial P}{\partial r} + \frac{1}{Re} L_r(\mathbf{u}) \tag{5}$$

$$\frac{\partial u_\phi}{\partial t} = N_\phi(\mathbf{u}) - \frac{1}{r+\gamma}\frac{\partial P}{\partial \phi} + \frac{1}{Re} L_\phi(\mathbf{u}) \tag{6}$$

$$\frac{\partial u_z}{\partial t} = N_z(\mathbf{u}) - \frac{\partial P}{\partial z} + \frac{1}{Re} L_z(\mathbf{u}) \tag{7}$$

subject to the incompressibility constraint

$$\frac{u_r}{r+\gamma} + \frac{\partial u_r}{\partial r} + \frac{1}{r+\gamma}\frac{\partial u_\phi}{\partial \phi} + \frac{\partial u_z}{\partial z} = 0 \tag{8}$$

The non-linear operators N_r, N_ϕ, N_z are

$$N_r(\mathbf{u}) = -u_r\frac{\partial u_r}{\partial r} - \frac{u_\phi}{r+\gamma}\frac{\partial u_r}{\partial \phi} - u_z\frac{\partial u_r}{\partial z} + \frac{{u_\phi}^2}{r+\gamma} \tag{9}$$

$$N_\phi(\mathbf{u}) = -u_r\frac{\partial u_\phi}{\partial r} - \frac{u_\phi}{r+\gamma}\frac{\partial u_\phi}{\partial \phi} - u_z\frac{\partial u_\phi}{\partial z} - \frac{u_r u_\phi}{r+\gamma} \tag{10}$$

$$N_z(\mathbf{u}) = -u_r\frac{\partial u_z}{\partial r} - \frac{u_\phi}{r+\gamma}\frac{\partial u_z}{\partial \phi} - u_z\frac{\partial u_z}{\partial z} \tag{11}$$

and the linear operators L_r, L_ϕ, L_z are

$$L_r(\mathbf{u}) = \frac{1}{r+\gamma}\frac{\partial u_r}{\partial r} + \frac{\partial^2 u_r}{\partial r^2} + \frac{1}{(r+\gamma)^2}\frac{\partial^2 u_r}{\partial \phi^2} - \frac{2}{(r+\gamma)^2}\frac{\partial u_\phi}{\partial \phi} + \frac{\partial^2 u_r}{\partial z^2} - \frac{u_r}{(r+\gamma)^2} \tag{12}$$

$$L_\phi(\mathbf{u}) = \frac{1}{r+\gamma}\frac{\partial u_\phi}{\partial r} + \frac{\partial^2 u_\phi}{\partial r^2} + \frac{1}{(r+\gamma)^2}\frac{\partial^2 u_\phi}{\partial \phi^2} + \frac{2}{(r+\gamma)^2}\frac{\partial u_r}{\partial \phi} + \frac{\partial^2 u_\phi}{\partial z^2} - \frac{u_\phi}{(r+\gamma)^2} \tag{13}$$

$$L_z(\mathbf{u}) = \frac{1}{r+\gamma}\frac{\partial u_z}{\partial r} + \frac{\partial^2 u_z}{\partial r^2} + \frac{1}{(r+\gamma)^2}\frac{\partial^2 u_z}{\partial \phi^2} + \frac{\partial^2 u_z}{\partial z^2} \tag{14}$$

The radial boundary conditions become:

$$u_r(z,\phi,-1,t) = 1 \qquad \text{and} \qquad u_r(z,\phi,1,t) = \mu/\eta \tag{15}$$

3.2 Taylor vortex flow

For axisymmetry, all derivatives with respect to the azimuthal variable are zero, which reduces the equations to:

$$\frac{\partial u_r}{\partial t} = N_r(\mathbf{u}) - \frac{\partial P}{\partial r} + \frac{1}{Re}L_r(\mathbf{u}) \tag{16}$$

$$\frac{\partial u_\phi}{\partial t} = N_\phi(\mathbf{u}) + \frac{1}{Re} L_\phi(\mathbf{u}) \tag{17}$$

$$\frac{\partial u_z}{\partial t} = N_z(\mathbf{u}) - \frac{\partial P}{\partial z} + \frac{1}{Re} L_z(\mathbf{u}) \tag{18}$$

subject to the incompressibility constraint

$$\frac{u_r}{r+\gamma} + \frac{\partial u_r}{\partial r} + \frac{\partial u_z}{\partial z} = 0 \tag{19}$$

The velocity components are $u_r(z,r,t)$, $u_\phi(z,r,t)$ and $u_z(z,r,t)$. Also $P(z,r,t)$ is the pressure.

The non-linear operators N_r, N_ϕ, N_z are

$$N_r(\mathbf{u}) = -u_r \frac{\partial u_r}{\partial r} - u_z \frac{\partial u_r}{\partial z} + \frac{{u_\phi}^2}{r+\gamma} \tag{20}$$

$$N_\phi(\mathbf{u}) = -u_r \frac{\partial u_\phi}{\partial r} - u_z \frac{\partial u_\phi}{\partial z} - \frac{u_r u_\phi}{r+\gamma} \tag{21}$$

$$N_z(\mathbf{u}) = -u_r \frac{\partial u_z}{\partial r} - u_z \frac{\partial u_z}{\partial z} \tag{22}$$

and the linear operators L_r, L_ϕ, L_z are

$$L_r(\mathbf{u}) = \frac{1}{r+\gamma}\frac{\partial u_r}{\partial r} + \frac{\partial^2 u_r}{\partial r^2} + \frac{\partial^2 u_r}{\partial z^2} - \frac{u_r}{(r+\gamma)^2} \tag{23}$$

$$L_\phi(\mathbf{u}) = \frac{1}{r+\gamma}\frac{\partial u_\phi}{\partial r} + \frac{\partial^2 u_\phi}{\partial r^2} + \frac{\partial^2 u_\phi}{\partial z^2} - \frac{u_\phi}{(r+\gamma)^2} \tag{24}$$

$$L_z(\mathbf{u}) = \frac{1}{r+\gamma}\frac{\partial u_z}{\partial r} + \frac{\partial^2 u_z}{\partial r^2} + \frac{\partial^2 u_z}{\partial z^2} \tag{25}$$

These equations are solved in a rectangular domain ($-1 \leq r \leq 1,\ 0 \leq z \leq \Gamma$) with periodic boundary conditions in the axial direction and radial velocity boundary conditions of

$$u_r(z,-1,t) = 1 \qquad \text{and} \qquad u_r(z,1,t) = \mu/\eta \tag{26}$$

3.3 Steady circular Couette flow

For sufficiently low Reynolds number, steady circular Couette flow is obtained with an analytic solution $u_r(z,\phi,r,t) = 0$, $u_\phi(z,\phi,r,t) = V(r)$ and $u_z(z,\phi,r,t) = 0$, where

$$V(r) = Ar + B/r \tag{27}$$

and

$$A = \frac{\Omega_{in}(\mu - \eta^2)}{1-\eta^2} \qquad \text{and} \qquad B = \frac{\Omega_{in} r_{in}^2 (1-\mu)}{1-\eta^2} \tag{28}$$

The nondimensional form of this solution is

$$V(r) = A[(1-\eta)r + \eta + 1] + B\frac{1}{(1-\eta)r + \eta + 1} \tag{29}$$

where

$$A = \frac{\mu - \eta^2}{2\eta(1-\eta^2)} \qquad \text{and} \qquad B = \frac{2\eta(1-\mu)}{1-\eta^2} \tag{30}$$

4 Two-dimensional Driven Cavity Flow

As an intermediate step before dealing with the numerical method for Taylor vortex flow, a numerical method for the flow of the fluid in a two-dimensional, square, driven cavity is described and validated with numerical tests. The numerical method for two-dimensional driven cavity flow is simpler to implement because the equations are in Cartesian coordinates. For validation purposes, the essential features of the numerical tests are the location and strength of various vortices inside the cavity which are known to arise at certain values of Reynolds number.

4.1 Governing equations

The Navier-Stokes equations written in primitive variable form are:

$$\frac{\partial \mathbf{u}}{\partial t} = -(\mathbf{u}.\nabla)\mathbf{u} - \frac{1}{\rho}\nabla P + \nu\nabla^2\mathbf{u} \tag{1}$$

subject to the incompressibility constraint

$$\nabla.\mathbf{u} = 0 \tag{2}$$

where for two-dimensional flows $\mathbf{u} = u(x, y, t)\mathbf{x} + v(x, y, t)\mathbf{y}$.

We consider a square domain Ω ($|x| \leq L$, $|y| \leq L$) where a constant x component of velocity, U, is at the top boundary otherwise the components of velocity around the boundary of the domain are zero. Choosing a length scale of L and a velocity scale of U, the Reynolds number is $Re = UL/\nu$.

The results will be compared to results by Ghia et al. (1982). The length scale and hence Reynolds number here are half the corresponding values defined by Ghia et al. That is, $Re = Re_G/2$ where the G subscript stands for the value defined by Ghia et al.

The nondimensional form of the boundary conditions (on the boundary $\partial\Omega$) are

$$u(x,y,t) = \begin{cases} 1 & \text{if } y = 1 \\ 0 & \text{elsewhere on } \partial\Omega \end{cases} \tag{3}$$

$$v(x,y,t) = 0 \qquad \text{on } \partial\Omega \tag{4}$$

4.2 Operator splitting method

The operator splitting procedure treats the time-advancement of the non-linear term, the pressure term and the viscous terms separately. The velocity is advanced from time step l to time step $l+1$ using three fractional steps. From Karniadakis, Israeli and Orszag (1991), an operator splitting scheme shall be applied which has first-order time-accuracy.

The first fractional step accounts for the non-linear term and uses an explicit, second order Adams-Bashforth approximation :

$$u^{l+\frac{1}{3}} = u^l - \Delta t \left[\frac{3}{2} \left(u^l \frac{\partial u}{\partial x}^l + v^l \frac{\partial u}{\partial y}^l \right) - \frac{1}{2} \left(u^{l-1} \frac{\partial u}{\partial x}^{l-1} + v^{l-1} \frac{\partial u}{\partial y}^{l-1} \right) \right] \tag{5}$$

$$v^{l+\frac{1}{3}} = v^l - \Delta t \left[\frac{3}{2} \left(u^l \frac{\partial v}{\partial x}^l + v^l \frac{\partial v}{\partial y}^l \right) - \frac{1}{2} \left(u^{l-1} \frac{\partial v}{\partial x}^{l-1} + v^{l-1} \frac{\partial v}{\partial y}^{l-1} \right) \right] \tag{6}$$

The second fractional step is due to the pressure term contribution:

$$u^{l+\frac{2}{3}} = u^{l+\frac{1}{3}} - \Delta t \frac{\partial P}{\partial x}^{l+1} \tag{7}$$

$$v^{l+\frac{2}{3}} = v^{l+\frac{1}{3}} - \Delta t \frac{\partial P}{\partial y}^{l+1} \tag{8}$$

These are explicit forward Euler approximations. The pressure P^{l+1} is solved using the Poisson equation:

$$\frac{\partial^2 P}{\partial x^2}^{l+1} + \frac{\partial^2 P}{\partial y^2}^{l+1} = \frac{1}{\Delta t} \left(\frac{\partial u}{\partial x}^{l+1/3} + \frac{\partial v}{\partial y}^{l+1/3} \right) \tag{9}$$

which is obtained by applying the incompressibility constraint on $\mathbf{u}^{l+2/3}$ and applying Equations (7) and (8).

A further assumption is that $\mathbf{u}^{l+2/3}$ satisfies the prescribed boundary conditions (Equations (3) and (4)) in the directions normal to the boundaries:

$$\text{At} \qquad x = \pm 1, \qquad u^{l+2/3} = u_{\partial\Omega} = \begin{cases} 1 & \text{for } y = 1 \\ 0 & \text{for } -1 \leq y < 1 \end{cases} \tag{10}$$

$$\text{At} \qquad y = \pm 1, \qquad v^{l+2/3} = v_{\partial\Omega} = 0 \tag{11}$$

From Equations (7) and (8), Neumann boundary conditions are imposed on the square boundary:

$$\frac{\partial P}{\partial x}^{l+1} = \frac{1}{\Delta t}(u^{l+1/3} - u_{\partial\Omega}) \qquad \text{at } x = \pm 1 \tag{12}$$

$$\frac{\partial P}{\partial y}^{l+1} = \frac{1}{\Delta t}(v^{l+1/3} - v_{\partial\Omega}) \qquad \text{at } y = \pm 1 \tag{13}$$

The third fractional step is the viscous step:

$$u^{l+1} = u^{l+\frac{2}{3}} + \frac{1}{Re}\Delta t \left(\frac{\partial^2 u}{\partial x^2}^{l+1} + \frac{\partial^2 u}{\partial y^2}^{l+1} \right) \tag{14}$$

$$v^{l+1} = v^{l+\frac{2}{3}} + \frac{1}{Re}\Delta t \left(\frac{\partial^2 v}{\partial x^2}^{l+1} + \frac{\partial^2 v}{\partial y^2}^{l+1} \right) \tag{15}$$

where an implicit, backwards Euler approximation is made. Equations (14) and (15) are each in the form of an Helmholtz equation, with the Dirichlet boundary conditions that u^{l+1} and v^{l+1} take the boundary values of velocity defined by Equations (3) and (4).

4.3 Spectral method

A Tau spectral method will be described that solves:

(1) the Poisson equation for the pressure in the pressure step using Neumann boundary conditions, and,

(2) the Helmholtz equations for the two velocity components in the viscous step using Dirichlet boundary conditions.

4.3.1 Poisson solver

The Poisson equation for the pressure $P(x, y)$ at each time step, has the form

$$\frac{\partial^2 P}{\partial x^2} + \frac{\partial^2 P}{\partial y^2} = F(x, y) \tag{16}$$

where the Neumann boundary conditions have the form

$$\frac{\partial P}{\partial x} = \alpha(y) \qquad \text{at } x = -1 \tag{17}$$

$$\frac{\partial P}{\partial x} = \beta(y) \qquad \text{at } x = 1 \tag{18}$$

$$\frac{\partial P}{\partial y} = \chi(x) \qquad \text{at } y = 1 \tag{19}$$

$$\frac{\partial P}{\partial y} = \psi(x) \qquad \text{at } y = -1 \tag{20}$$

A Chebyshev-Chebyshev expansion of a function $P(x, y)$ is

$$P(x, y) = \sum_{n=0}^{N} \sum_{m=0}^{N} a_{nm} T_n(x) T_m(y) \tag{21}$$

where the Chebyshev polynomial is

$$T_n(x) = \cos(n \arccos x) \tag{22}$$

and there are $N + 1$ points in the x direction and $N + 1$ points in the y direction.

From Gottlieb and Orszag (1977), Equation (16) in spectral form can be written as

$$\frac{1}{c_n} \sum_{\substack{p = n+2 \\ p+n \text{ even}}}^{N} p(p^2 - n^2) a_{pm} + \frac{1}{c_m} \sum_{\substack{q = m+2 \\ q+m \text{ even}}}^{N} q(q^2 - m^2) a_{nq} = F_{nm} \tag{23}$$

for $0 \leq n \leq N-2$ and $0 \leq m \leq N-2$ where $c_0 = 2$ and $c_n = 1$ for $n \geq 1$. This can be written in matrix form as:

$$A \begin{pmatrix} a_{00} & a_{01} & \dots & a_{0,N-2} \\ a_{10} & a_{11} & \dots & a_{1,N-2} \\ \vdots & \vdots & \vdots & \vdots \\ a_{N-2,0} & a_{N-2,1} & \dots & a_{N-2,N-2} \\ a_{N-1,0} & a_{N-1,1} & \dots & a_{N-1,N-2} \\ a_{N,0} & a_{N,1} & \dots & a_{N,N-2} \end{pmatrix}$$

$$+ \qquad \begin{pmatrix} a_{00} & a_{01} & \dots & a_{0,N-2} & a_{0,N-1} & a_{0,N} \\ a_{10} & a_{11} & \dots & a_{1,N-2} & a_{1,N-1} & a_{1,N} \\ \vdots & \vdots & \vdots & \vdots & \vdots & \vdots \\ a_{N-2,0} & a_{N-2,1} & \dots & a_{N-2,N-2} & a_{N-2,N-1} & a_{N-2,N} \end{pmatrix} A^T$$

$$= \qquad \begin{pmatrix} F_{00} & F_{01} & \dots & F_{0,N-2} \\ F_{10} & F_{11} & \dots & F_{1,N-2} \\ \vdots & \vdots & \vdots & \vdots \\ F_{N-2,0} & F_{N-2,1} & \dots & F_{N-2,N-2} \end{pmatrix}$$

where A is the $N-1 \times N+1$ matrix:

$$\begin{pmatrix} 0 & 0 & 2^3/2 & 0 & 4^3/2 & 0 & \dots & N^3/2 \\ 0 & 0 & 0 & 3(3^2-1^2) & 0 & 5(5^2-1^1) & \dots & 0 \\ 0 & 0 & 0 & 0 & 4(4^2-2^2) & 0 & \dots & N(N^2-2^2) \\ 0 & 0 & 0 & 0 & 0 & 5(5^2-3^2) & \dots & 0 \\ \vdots & \vdots & \vdots & \vdots & \vdots & \vdots & \vdots & \vdots \\ 0 & 0 & 0 & 0 & 0 & 0 & \dots & N(N^2-(N-2)^2) \end{pmatrix}$$

The one-dimensional Chebyshev approximation of a function $\alpha(y)$ is

$$\alpha(y) = \sum_{m=0}^{N} \alpha_m T_m(y) \tag{24}$$

The spectral expressions for $a_{nm}^{(1,0)}$ and $a_{nm}^{(0,1)}$, i.e.

$$a_{nm}^{(1,0)} = \frac{2}{c_n} \sum_{\substack{p=n+1 \\ p+n \text{ odd}}}^{N} p a_{pm} \tag{25}$$

and

$$a_{nm}^{(0,1)} = \frac{2}{c_m} \sum_{\substack{q=m+1 \\ q+m \text{ odd}}}^{N} q a_{nq} \tag{26}$$

The spectral form of the boundary conditions then are

$$\sum_{n=0}^{N} a_{nm}^{(1,0)} (-1)^{n+1} = \sum_{n=0}^{N} (-1)^n n^2 a_{nm} = \alpha_m \tag{27}$$

$$\sum_{n=0}^{N} a_{nm}^{(1,0)} = \sum_{n=0}^{N} n^2 a_{nm} = \beta_m \tag{28}$$

for $0 \leq m \leq N$, and

$$\sum_{m=0}^{N} a_{nm}^{(0,1)} = \sum_{m=0}^{N} m^2 a_{nm} = \chi_n \tag{29}$$

$$\sum_{m=0}^{N} a_{nm}^{(0,1)} (-1)^{m+1} = \sum_{m=0}^{N} (-1)^m m^2 a_{nm} = \psi_n \tag{30}$$

for $0 \leq n \leq N$.

Adding and subtracting Equations (27) and (28) we get:

$$\sum_{\substack{n=0 \\ n\ odd}}^{N} n^2 a_{nm} = \frac{1}{2}(\beta_m + \alpha_m) = \eta_m \tag{31}$$

$$\sum_{\substack{n=0 \\ n\ even}}^{N} n^2 a_{nm} = \frac{1}{2}(\beta_m - \alpha_m) = \theta_m \tag{32}$$

for $0 \leq m \leq N$, and adding and subtracting Equations (29) and (30) we get:

$$\sum_{\substack{m=0 \\ m\ odd}}^{N} m^2 a_{nm} = \frac{1}{2}(\chi_n + \psi_n) = \delta_n \tag{33}$$

$$\sum_{\substack{m=0 \\ m\ even}}^{N} m^2 a_{nm} = \frac{1}{2}(\chi_n - \psi_n) = \zeta_n \tag{34}$$

for $0 \leq n \leq N$.

In the first term on the left hand side of the matrix Equation (23), we substitute Equation (31) to eliminate the coefficients $a_{N-1,m}$, and Equation (32) to eliminate the coefficients $a_{N,m}$, for $0 \leq m \leq N-2$. In the second term on the left hand side of the matrix Equation (23), we substitute Equation (33) to eliminate the coefficients $a_{n,N-1}$, and Equation (34) to eliminate the coefficients $a_{n,N}$ for $0 \leq n \leq N-2$. Subsequently we obtain a matrix equation in terms of the coefficients a_{nm} for $0 \leq n, m \leq N-2$, of the form:

$$Aa + aA^T = f \tag{35}$$

where the matrices A, a and f are $(N-1) \times (N-1)$. The matrix f is

$$f = F - Q - S \tag{36}$$

where Q and S are the $(N-1) \times (N-1)$ matrices with elements

$$Q_{nm} = \begin{cases} \frac{N^2-n^2}{NC_n}\theta_m & \text{for } n \text{ even} \\ \frac{(N-1)^2-n^2}{(N-1)C_n}\eta_m & \text{for } n \text{ odd} \end{cases} \tag{37}$$

$$S_{nm} = \begin{cases} \frac{N^2-m^2}{NC_m}\zeta_n & \text{for } m \text{ even} \\ \frac{(N-1)^2-m^2}{(N-1)C_m}\delta_n & \text{for } m \text{ odd} \end{cases} \tag{38}$$

The matrix A does not have the upper triangular structure that the matrix A has. It is a general matrix with alternating zero and non-zero elements. Now that the matrix equation (35) represents a system with $(N-1)^2$ equations in $(N-1)^2$ unknowns, we can solve for the unknowns by the following procedure.

Firstly, diagonalize the matrix A to get the eigenvalues Λ and corresponding eigenvectors e:

$$Ae = e\Lambda \tag{39}$$

where e and Λ are $(N-1) \times (N-1)$ arrays. Then by using the transformations $f = eg$ and $a = eb$, Equation (35) becomes

$$\Lambda b + bA^T = g \tag{40}$$

where g and b are $(N-1) \times (N-1)$ arrays. The transformed matrix equation (40) can now easily be solved for b by taking

$$b_k = g_k[\lambda_k I + A^T]^{-1} \tag{41}$$

for $k = 0, 1, ..., N-2$, where b_k and g_k are the k^{th} row of elements of b and g respectively, and λ_k is the k^{th} eigenvalue of matrix A. Once b_{nm} are calculated, a_{nm} can be determined

from $a = eb$ and the boundary conditions (Equations (31) to (34)) for $0 \leq m, n \leq N$. A Chebyshev-Chebyshev inverse transform of a_{nm} will give the solution for $P(x, y)$.

4.3.2 Helmholtz solver

The Helmholtz equation for a component of velocity $W(x, y)$ at each time step, has the form

$$\frac{\partial^2 W}{\partial x^2} + \frac{\partial^2 W}{\partial y^2} - \lambda W = F(x, y) \tag{42}$$

where the Dirichlet boundary conditions have the form

$$W(-1, y) = \alpha(y) \tag{43}$$

$$W(1, y) = \beta(y) \tag{44}$$

$$W(x, 1) = \chi(x) \tag{45}$$

$$W(x, -1) = \psi(x) \tag{46}$$

Equation (42) in spectral form is similar to matrix Equation (23) but with the term $-\lambda a_{nm}$ (for $0 \leq n, m \leq N - 2$) added in the left hand side where a_{nm} are the spectral coefficients for $W(x, y)$.

Using the boundary conditions (Equations (43) to (46)) we have

$$\sum_{n=0}^{N} a_{nm}(-1)^n = \alpha_m \tag{47}$$

$$\sum_{n=0}^{N} a_{nm} = \beta_m \tag{48}$$

for $0 \leq m \leq N$, and

$$\sum_{m=0}^{N} a_{nm} = \chi_n \tag{49}$$

$$\sum_{m=0}^{N} a_{nm}(-1)^m = \psi_n \tag{50}$$

for $0 \leq n \leq N$.

Adding and subtracting Equations (47) and (48) we get:

$$\sum_{\substack{n=0 \\ n\ even}}^{N} a_{nm} = \frac{1}{2}(\beta_m + \alpha_m) = \eta_m \tag{51}$$

$$\sum_{\substack{n=0 \\ n\ odd}}^{N} a_{nm} = \frac{1}{2}(\beta_m - \alpha_m) = \theta_m \tag{52}$$

for $0 \leq m \leq N$. Adding and subtracting Equations (49) and (50) we get:

$$\sum_{\substack{m=0 \\ m\ even}}^{N} a_{nm} = \frac{1}{2}(\chi_n + \psi_n) = \delta_n \tag{53}$$

$$\sum_{\substack{m=0 \\ m\ odd}}^{N} a_{nm} = \frac{1}{2}(\chi_n - \psi_n) = \zeta_n \tag{54}$$

for $0 \leq n \leq N$.

In the spectral matrix form of the Helmholtz equation we substitute Equation (51) to eliminate the coefficients $a_{N,m}$, and Equation (52) to eliminate the coefficients $a_{N-1,m}$, for $0 \leq m \leq N-2$. Also, we substitute Equation (53) to eliminate $a_{n,N}$, and Equation (54) to eliminate the coefficients $a_{n,N-1}$ for $0 \leq n \leq N-2$. Subsequently the matrix equation is of the form:

$$Aa + aA^T - \lambda a = f \tag{55}$$

where A, a and f are $(N-1) \times (N-1)$. The elements of A are not the same as those in the Poisson equation case but are still alternating zero and non-zero elements.

The array f is

$$f = F - Q - S \tag{56}$$

where Q and S are the $(N-1) \times (N-1)$ matrices with elements:

$$Q_{nm} = \begin{cases} \frac{N(N^2-n^2)}{C_n}\eta_m & \text{for } n \text{ even} \\ \frac{(N-1)((N-1)^2-n^2)}{C_n}\theta_m & \text{for } n \text{ odd} \end{cases} \tag{57}$$

$$S_{nm} = \begin{cases} \frac{N(N^2-m^2)}{C_m}\delta_n & \text{for } m \text{ even} \\ \frac{(N-1)((N-1)^2-m^2)}{C_m}\zeta_n & \text{for } m \text{ odd} \end{cases} \tag{58}$$

Applying the same transformations as for the Poisson equation case, we get:

$$\Lambda b + bA^T - \lambda b = g \tag{59}$$

which can easily be solved for b by taking

$$b_k = g_k[(\lambda_k - \lambda)I + A^T]^{-1} \tag{60}$$

for $k = 0, 1, ..., N-2$, where b_k and g_k are the k^{th} row of elements of b and g respectively, and λ_k is the k^{th} eigenvalue of matrix A. Once b_{nm} are calculated, a_{nm} can be determined from $a = eb$ and the boundary conditions (Equations (51) to (54)) for $0 \leq m, n \leq N$. A double Chebyshev inverse transform of a_{nm} will give the solution for $W(x, y)$.

4.3.3 Preprocessing calculations

The method calculates the $N-1$ arrays $[\lambda_k I + A^T]^{-1}$ for the Poisson solver and the $N-1$ arrays $[(\lambda_k - \lambda)I + A^T]^{-1}$ for the Helmholtz solver, once, in a pre-processing step.

4.4 Spatial oscillations

It is well known that when spectral methods are used to solve differential equations spatial oscillations are obtained if the gridspacing is not small enough to resolve the gradients in the solution. The use of jump discontinuous boundary conditions, such as in the case of driven cavity flow, therefore produces spatial oscillations for any number of gridpoints since the infinite gradient is never resolved.

One way of overcoming this problem is apply smoother Dirichlet boundary conditions for the Helmholtz solver for $u(x, y)$ used in the viscous step. For example, Ku, Hirsh and Taylor (1987) replaced the top boundary condition with the discrete variation $u(x, 1) = 0, 0.3, 1, ..., 1, 0.3, 0$ and Shen (1991) used the continuous variation $u(x, 1) = (1 - x^2)^2$. Such treatments of the boundary condition have resulted in more resolved solutions as the number of gridpoints was increased. In smoothing the discontinuous boundary conditions one has to be careful not to smooth it too much otherwise the solution may be significantly different to the true solution. This appears to be the case with Shen's treatment, where the effective Reynolds number is larger than if discontinuous boundary conditions were used. In this case, a distinction was made between the Classical Driven Cavity Flow where discontinuous boundary conditions were used, and Regularized Driven Cavity Flow where Shen's smoothed boundary conditions were used.

4.5 Results and comparisons

The treatment of $u(x, 1)$ by Shen was considerably different to the classical (discontinuous) boundary conditions so that no quantitative comparison to, say, the results of Ghia et al. could be made. It is necessary to keep the same profile for the velocity at the top boundary as the number of gridpoints is increased in order to make it possible to resolve the flow with a sufficient number of gridpoints. Therefore rather than using Ku et al.'s approach it was decided to use the top velocity profile $u(x, 1) = 1 - \exp(-20(1 - x^2))$, which has a high but resolvable gradient near the top two corners of the cavity.

A simulation was considered to have reached steady state when

$$\left|u^l - u^{l-1}\right|_{max} < 1 \times 10^{-8} \tag{61}$$

was satisfied.

Consider the relations $u = \frac{\partial \psi}{\partial y}$ and $v = -\frac{\partial \psi}{\partial x}$ where $\psi(x, y)$ is the streamfunction. The Poisson equation is:

$$\frac{\partial^2 \psi}{\partial x^2} + \frac{\partial^2 \psi}{\partial y^2} = \frac{\partial u}{\partial y} - \frac{\partial v}{\partial x} \tag{62}$$

which, together with the Dirichlet boundary conditions of $\psi = 0$ everywhere on the boundary of the domain, was used to calculate the streamfunction. A Tau method was used to solve the Poisson equation of the type described in Section 4.3.2 with $\lambda = 0$.

In the calculation the streamfunctions of particular interest were: the minimum value of streamfunction for the Primary (P) vortex, the maximum values of streamfunction for the 1^{st} Bottom Left (BL) and 1^{st} Bottom Right (BR) secondary vortices and, when possible, the minimum values of streamfunction for the 2^{nd} Bottom Left (BL) and 2^{nd} Bottom Right (BR) secondary vortices.

The spectral interpolation form of the Chebyshev-Chebyshev approximation to streamfunction:

$$\psi(x, y) = \sum_{n=0}^{N} \sum_{m=0}^{N} \psi_{nm} T_n(x) T_m(y) \tag{63}$$

was used to calculate extrema in ψ and their locations for fine grid variations in x and y.

The flow was simulated till steady state for Reynolds numbers (Re_G) of 100, 400 and 1000. For each Reynolds number several different numbers of gridpoints and time spacings were tried. In Tables 4.1 to 4.3, when it was possible, the location of the centres of the primary and secondary vortices and the corresponding streamfunction values were calculated. These calculations were then compared to those from Ghia et al., who use a coupled implicit multigrid (CSI–MG) method and provided high Reynolds number fine mesh flow solutions for the driven cavity flow problem. They provided streamfunction

solutions to five decimal place accuracy. The tables demonstrate that the computed values converge to the results by Ghia et al. as the gridspacing and timespacing are reduced. (In the tables, I.C. stands for initial conditions in the interior of the domain.)

Figures 4.1 to 4.15 consist of: (1) Velocity vector plots and streamfunction plots for the primary and secondary vortices, and, (2) graphs of the horizontal component of velocity through the vertical centreline and the vertical component of velocity through the horizontal centreline, plotted against the results from Ghia et al.

Figures 4.1 to 4.3 highlight the numerical problem of spatial oscillations when insufficient grid resolution is used. This is most noticeable near the top two corners of Figure 4.1 where the sizes of the vectors alternate in sequence in the y direction. These spatial oscillations are not present when more gridpoints are used, as illustrated in Figures 4.4 to 4.6. Figures 4.9, 4.12 and 4.15 also show good agreement with results by Ghia et al.

The run for $Re = 100$ with a 49×49 grid and $\Delta t = 0.01$ took about 6.4 hours of CPU time to reach steady state. The driven cavity flow simulations where made on a Silicon Graphics Indy R3000 Workstation. The run for $Re = 400$ with a 65×65 grid and $\Delta t = 0.01$ took about 8 hours of CPU time. The run for $Re = 1000$ with a 65×65 grid and $\Delta t = 0.01$ took about 15.5 hours of CPU time to reach steady state. In the latter two examples, the initial conditions were taken from solutions to coarser grids in order to reduce the overall computation time.

Another test of the code was to demonstrate exponential convergence of the spectral method. This was done by keeping Δt fixed and increasing the number of gridpoints. The test case was for the analytic solution

$$u_{an} = -\cos(x)\sin(y)\exp(-2t/Re) \tag{64}$$

$$v_{an} = \sin(x)\cos(y)\exp(-2t/Re) \tag{65}$$

$$p_{an} = -\frac{1}{4}(\cos(2x) + \cos(2y)) \exp(-4t/Re) \tag{66}$$

The value for $|u - u_{an}|$ was recorded after a fixed time for various values of Δt. From this, Figure 4.16 demonstrates the first-order time-accuracy of the (classical) operator splitting method.

Vortex	Property	Ghia *et al.*	17×17 grid	17×17 grid
P	ψ_{min}	-0.103423	-0.099099	-0.103683
	Location x, y	0.6172, 0.7344	0.6165, 0.7465	0.6157, 0.7369
1^{st} BR	ψ_{max}	1.25374×10^{-5}		
	Location x, y	0.9453, 0.0625		
1^{st} BL	ψ_{max}	1.74877×10^{-6}		
	Location x, y	0.0313, 0.0391		
Δt			0.1	0.01
I.C.			zero	zero
FIGS.				7.4 to 7.6

Vortex	Property	25×25 grid	25×25 grid	33×33 grid
P	ψ_{min}	-0.098772	-0.103011	-0.098737
	Location x, y	0.6187, 0.7471	0.6161, 0.7386	0.6189, 0.7471
1^{st} BR	ψ_{max}	3.0387×10^{-5}	1.44557×10^{-5}	2.97096×10^{-5}
	Location x, y	0.9376, 0.0802	0.9550, 0.0563	0.9385, 0.0726
1^{st} BL	ψ_{max}	1.229×10^{-5}		1.10433×10^{-5}
	Location x, y	0.0301, 0.0743		0.0395, 0.0468
Δt		0.1	0.01	0.1
I.C.		zero	zero	zero
FIGS.			7.9.1 to 7.9.3	

Vortex	Property	33×33 grid	49×49 grid	49×49 grid
P	ψ_{min}	-0.102966	-0.102962	-0.103474
	Location x, y	0.6163, 0.7385	0.6162, 0.7385	0.6160, 0.7375
1^{st} BR	ψ_{max}	1.5132×10^{-5}	1.5020×10^{-5}	1.35271×10^{-5}
	Location x, y	0.9427, 0.0668	0.9417, 0.0635	0.9463, 0.0619
1^{st} BL	ψ_{max}	3.1244×10^{-6}	2.9945×10^{-6}	2.22989×10^{-6}
	Location x, y	0.0283, 0.0423	0.0358, 0.0373	0.0277, 0.0338
Δt		0.01	0.01	0.001
I.C.		zero	zero	solution from 49×49 grid with $\Delta t = 0.01$
FIGS.			7.18.4 to 7.18.6	

Table 4.1: Properties of Primary and Secondary Vortices for $Re_G = 100$

Vortex	Property	Ghia *et al.*	33×33 grid	65×65 grid
P	ψ_{min}	-0.113909	-0.113095	-0.113024
	Location x, y	0.5547, 0.6055	0.5549, 0.6068	0.5547, 0.6068
1^{st} BR	ψ_{max}	6.42352×10^{-4}	6.43051×10^{-4}	6.54073×10^{-4}
	Location x, y	0.8906, 0.1250	0.8869, 0.1256	0.8843, 0.1234
1^{st} BL	ψ_{max}	1.41951×10^{-5}	1.39134×10^{-5}	1.48628×10^{-5}
	Location x, y	0.0508, 0.0469	0.0559, 0.0451	0.0513, 0.0475
2^{nd} BR	ψ_{min}	-1.86595×10^{-8}		-1.281×10^{-7}
	Location x, y	0.9922, 0.0078		0.9905, 0.0091
2^{nd} BL	ψ_{min}	-7.67738×10^{-10}		
	Location x, y	0.0039, 0.0039		
Δt			0.01	0.01
I.C.			zero	solution from 33×33 grid and $\Delta t = 0.01$ and linear interpolation
FIGS.				7.24.4 to 7.24.6

Table 4.2: Properties of Primary and Secondary Vortices for $Re_G = 400$

Vortex	Property	Ghia *et al.*	33×33 grid	65×65 grid
P	ψ_{min}	-0.117929	-0.118103	-0.117767
	Location x, y	0.5313, 0.5625	0.5308, 0.5650	0.5310, 0.5660
1^{st} BR	ψ_{max}	1.75102×10^{-3}	1.73405×10^{-3}	1.72787×10^{-3}
	Location x, y	0.8594, 0.1094	0.8616, 0.1112	0.8632, 0.1125
1^{st} BL	ψ_{max}	2.31129×10^{-4}	2.25550×10^{-4}	2.25203×10^{-4}
	Location x, y	0.0859, 0.0781	0.0888, 0.0728	0.0831, 0.0777
2^{nd} BR	ψ_{min}	-9.31929×10^{-8}		-1.56805×10^{7}
	Location x, y	0.9922, 0.0078		0.9910,0.0088
Δt			0.01	0.01
I.C.			zero	solution from 33×33 grid $\Delta t = 0.01$ and linear interpolation
FIGS.				7.30.1 to 7.30.3

Table 4.3: Properties of Primary and Secondary Vortices for $Re_G = 1000$

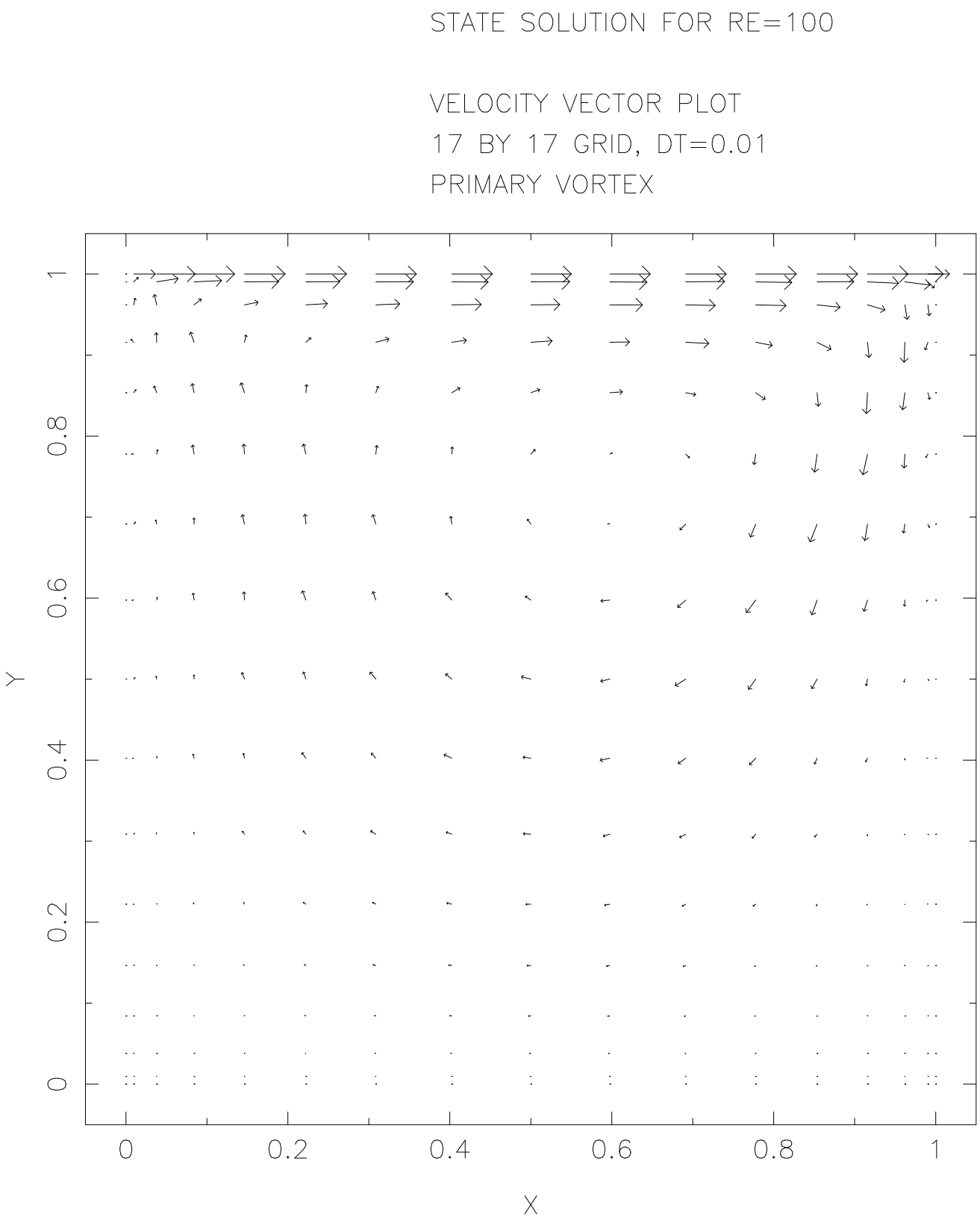

Figure 4.1: Velocity vectors for $Re_G = 100$ using a 17×17 grid and $\Delta t = 0.01$.

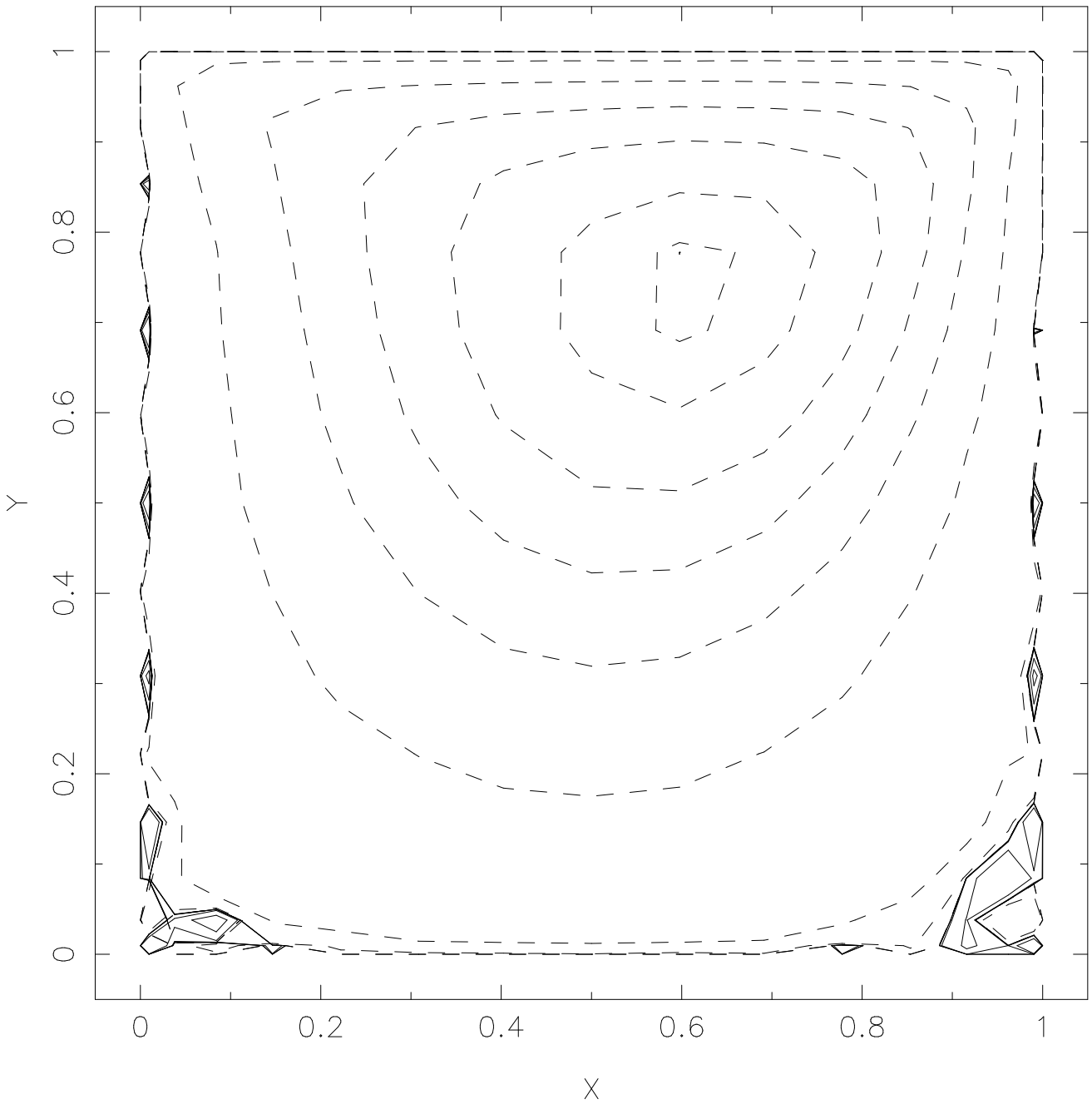

Figure 4.2: Streamlines for $Re_G = 100$ using a 17×17 grid and $\Delta t = 0.01$.

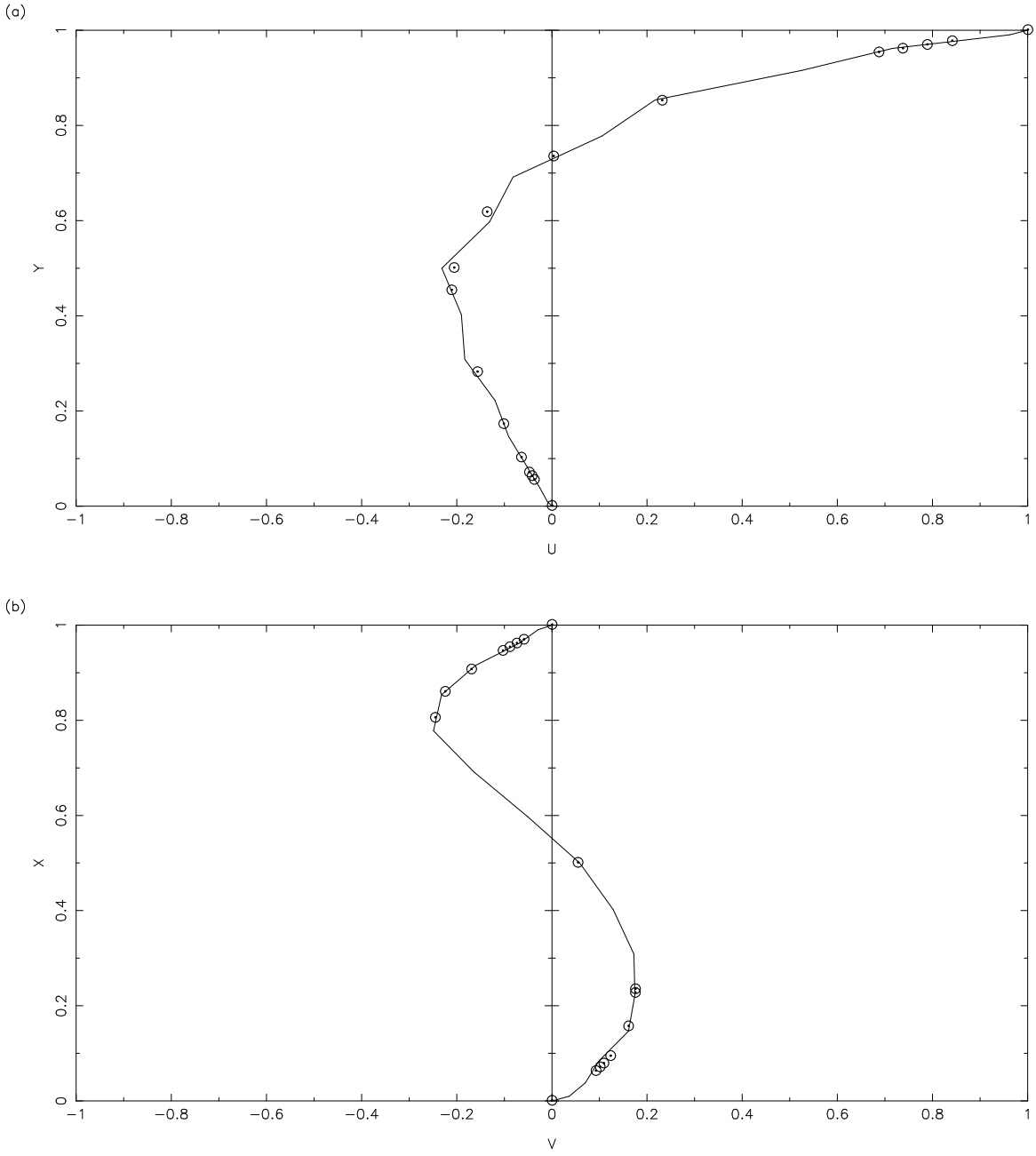

FIGURE 7.6: (a) HORIZONTAL COMPONENT OF VELOCITY THROUGH VERTICAL CENTERLINE
(b) VERTICAL COMPONENT OF VELOCITY THROUGH HORIZONTAL CENTERLINE

CIRCLED POINTS REPRESENT DATA FROM GHIA

17 BY 17 GRID, DT=0.01

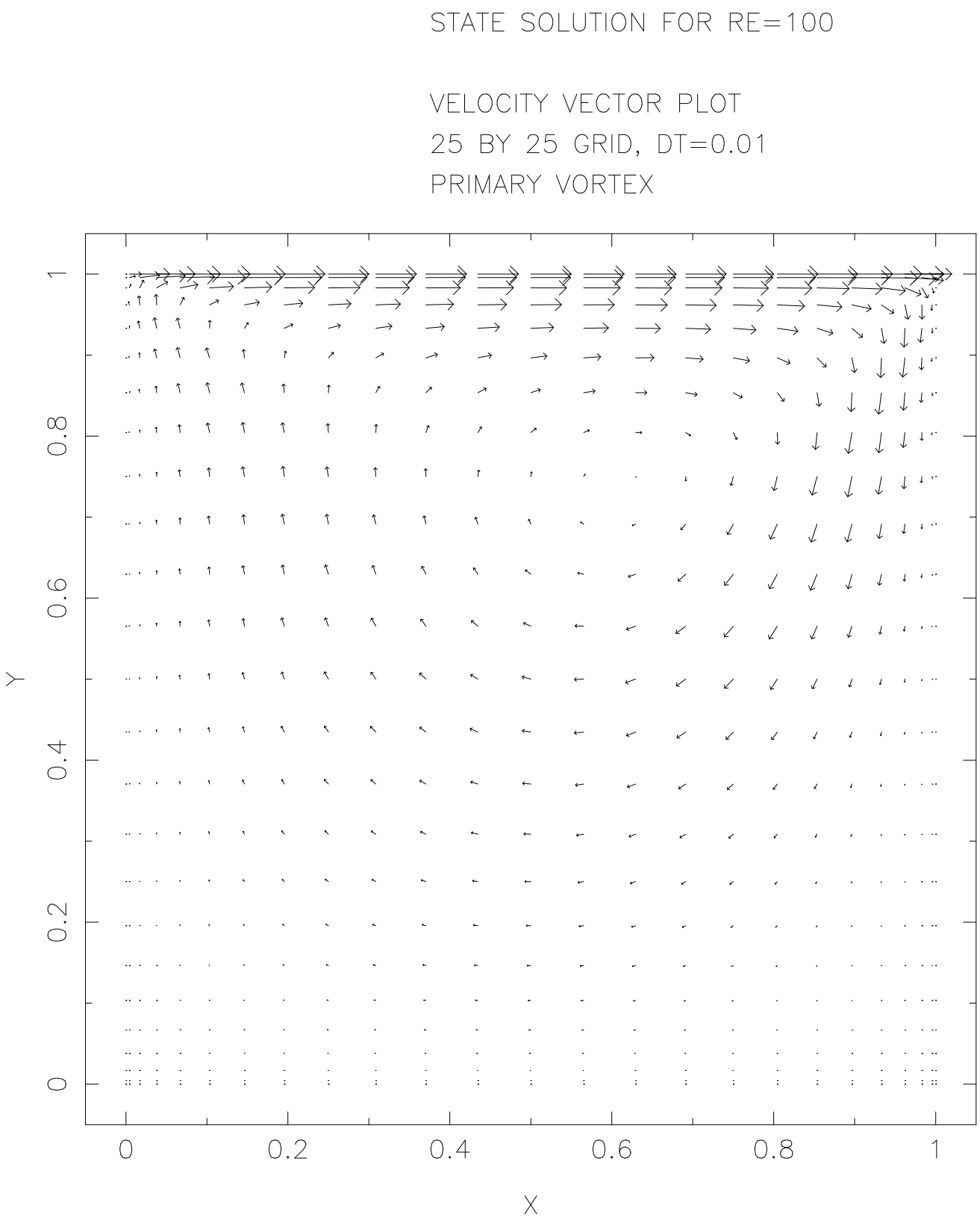

Figure 4.4: Velocity vectors for $Re_G = 100$ using a 25×25 grid and $\Delta t = 0.01$.

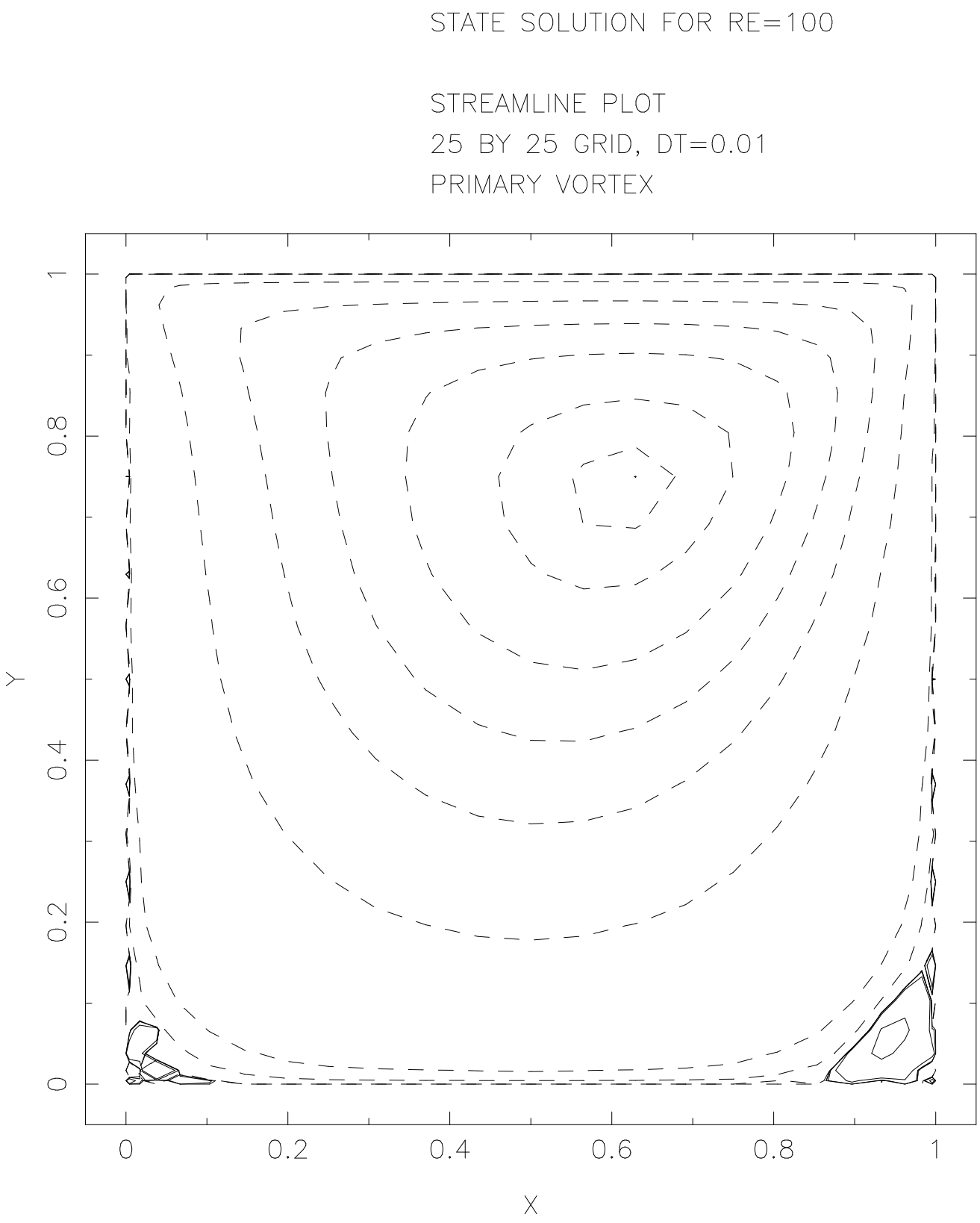

Figure 4.5: Streamlines for $Re_G = 100$ using a 25×25 grid and $\Delta t = 0.01$.

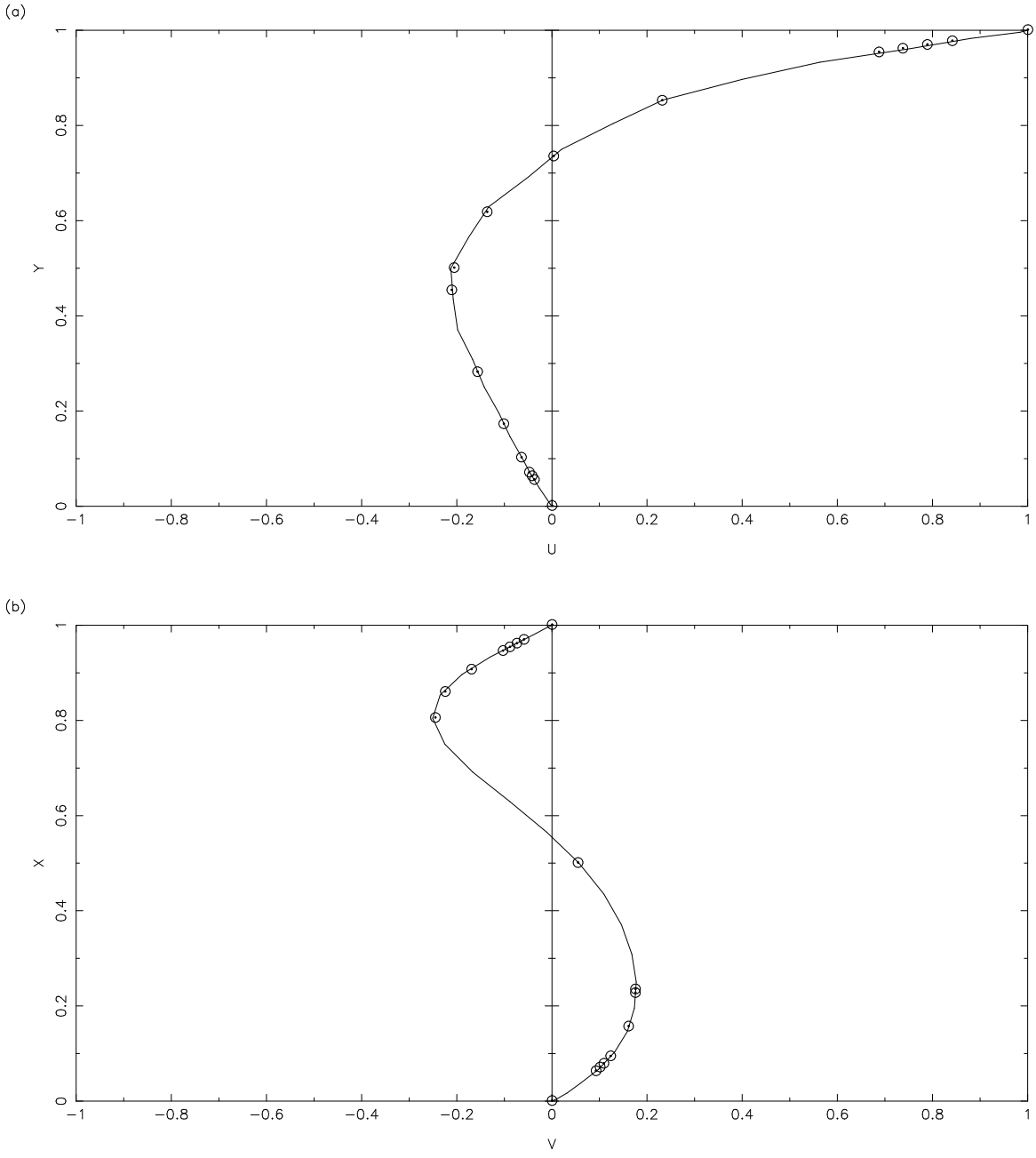

FIGURE 7.9.3: (a) HORIZONTAL COMPONENT OF VELOCITY THROUGH VERTICAL CENTERLINE
(b) VERTICAL COMPONENT OF VELOCITY THROUGH HORIZONTAL CENTERLINE

CIRCLED POINTS REPRESENT DATA FROM GHIA

25 BY 25 GRID, DT=0.01

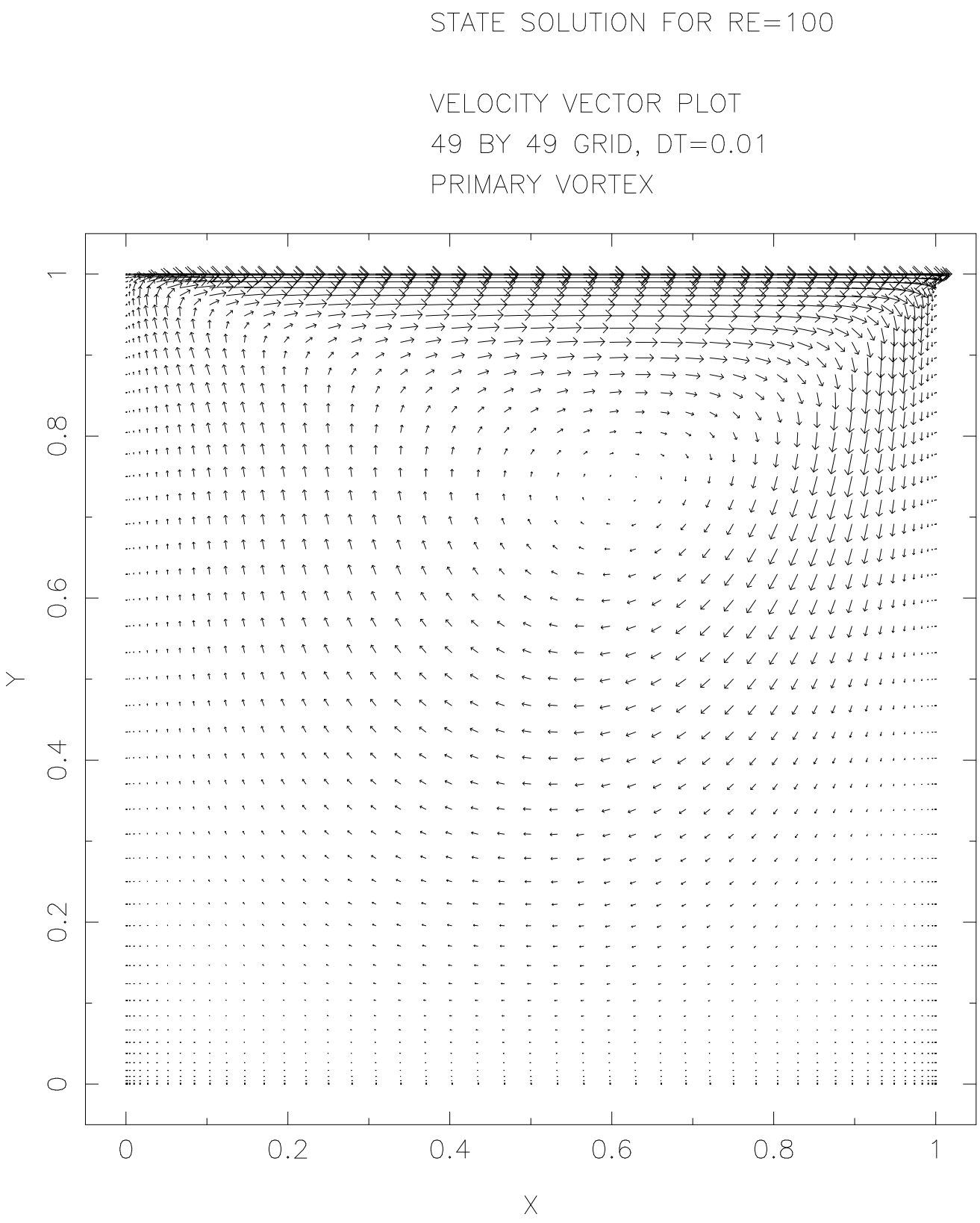

Figure 4.7: Velocity vectors for $Re_G = 100$ using a 49×49 grid and $\Delta t = 0.01$.

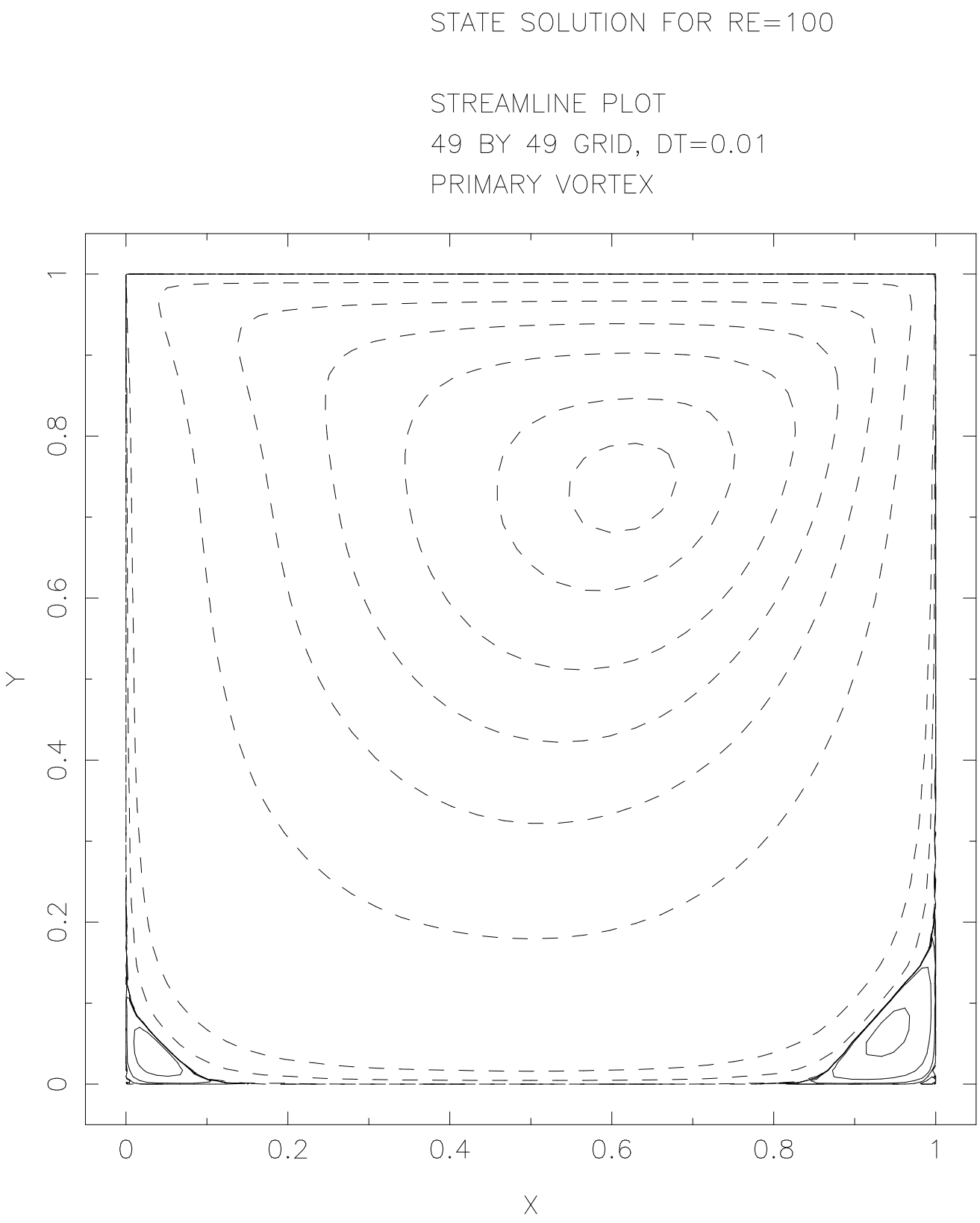

Figure 4.8: Streamlines for $Re_G = 100$ using a 49×49 grid and $\Delta t = 0.01$.

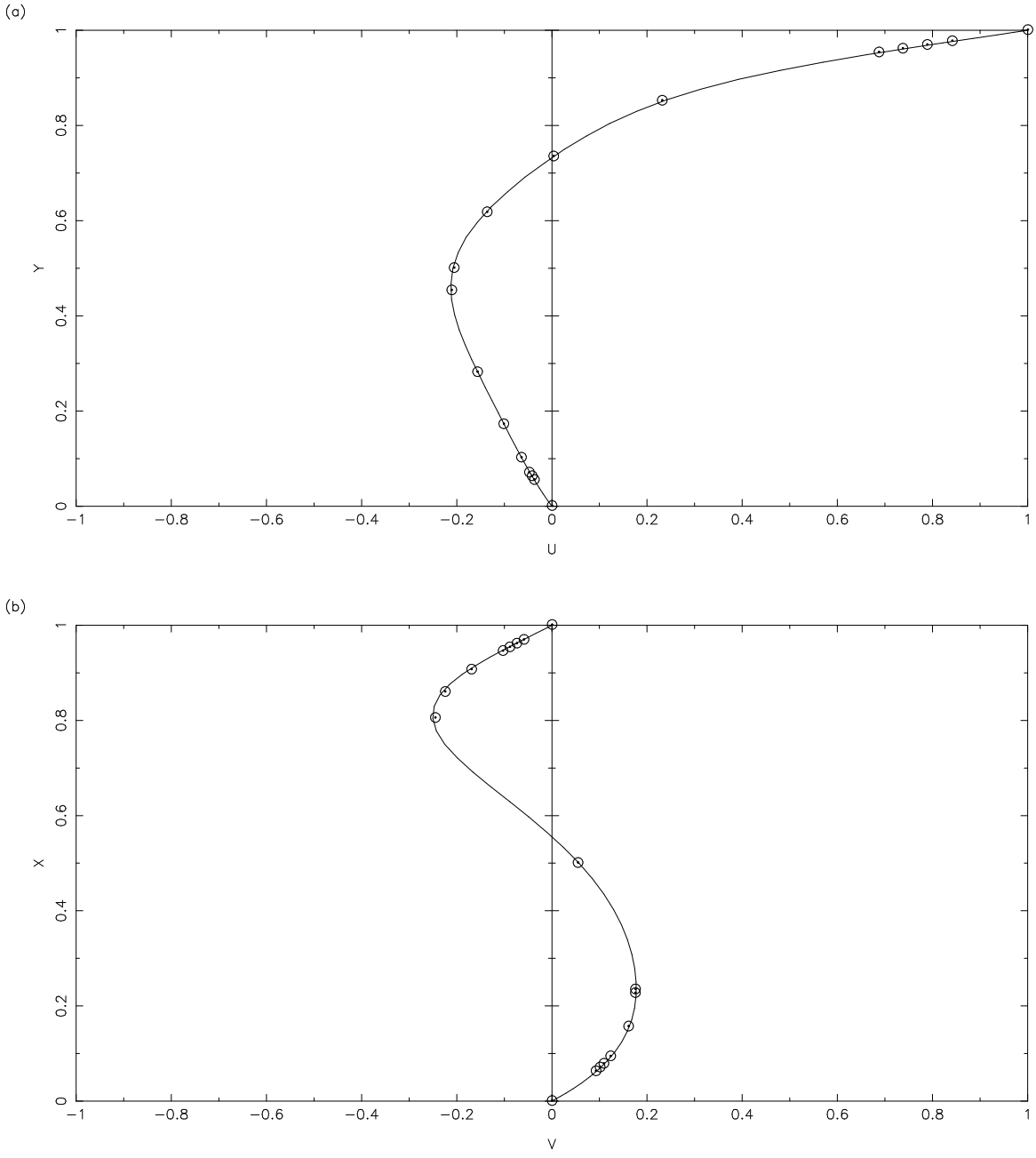

FIGURE 7.18.6: (a) HORIZONTAL COMPONENT OF VELOCITY THROUGH VERTICAL CENTERLINE
(b) VERTICAL COMPONENT OF VELOCITY THROUGH HORIZONTAL CENTERLINE

CIRCLED POINTS REPRESENT DATA FROM GHIA

49 BY 49 GRID, DT = 0.01, RE = 100

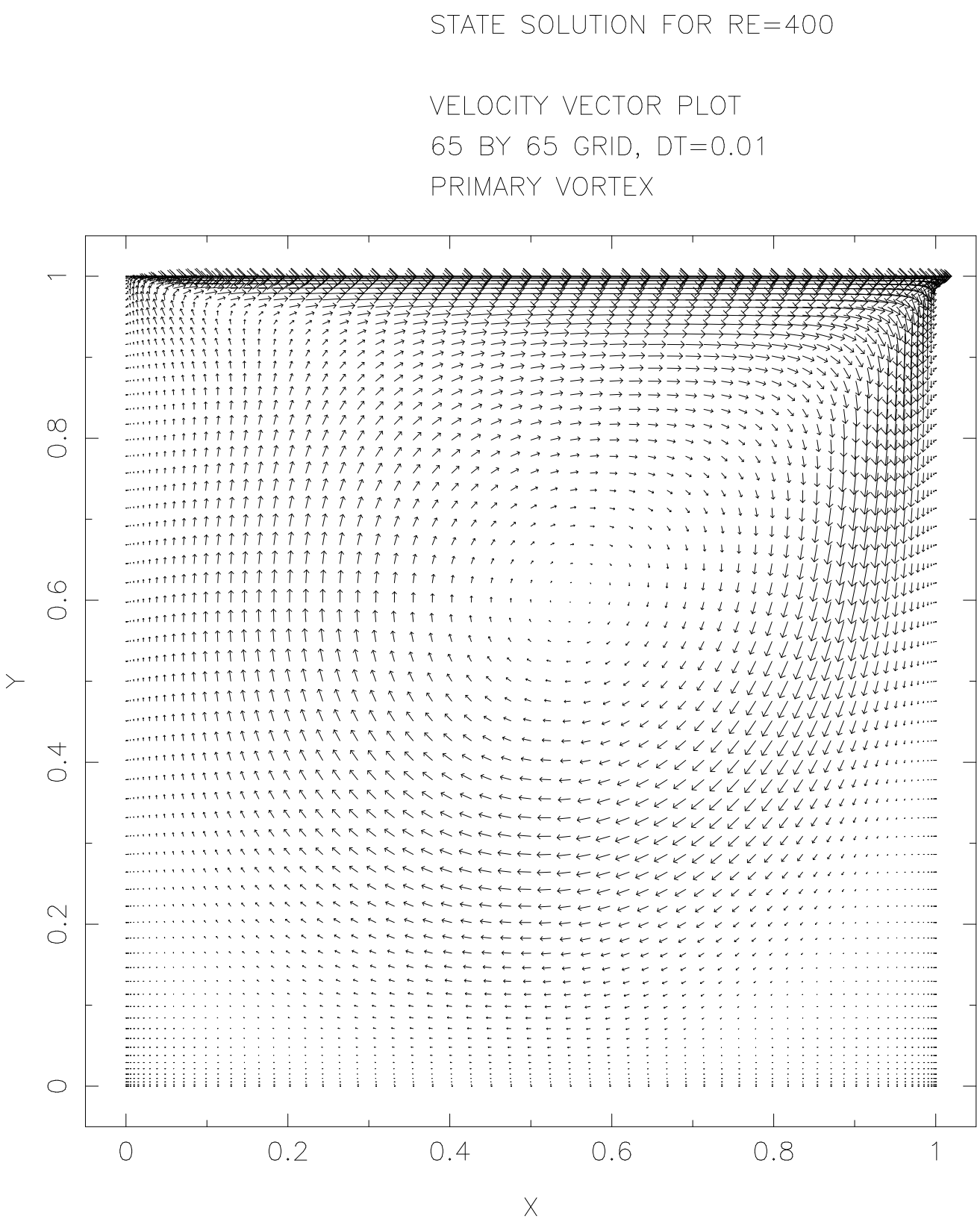

Figure 4.10: Velocity vectors for $Re_G = 400$ using a 65×65 grid and $\Delta t = 0.01$.

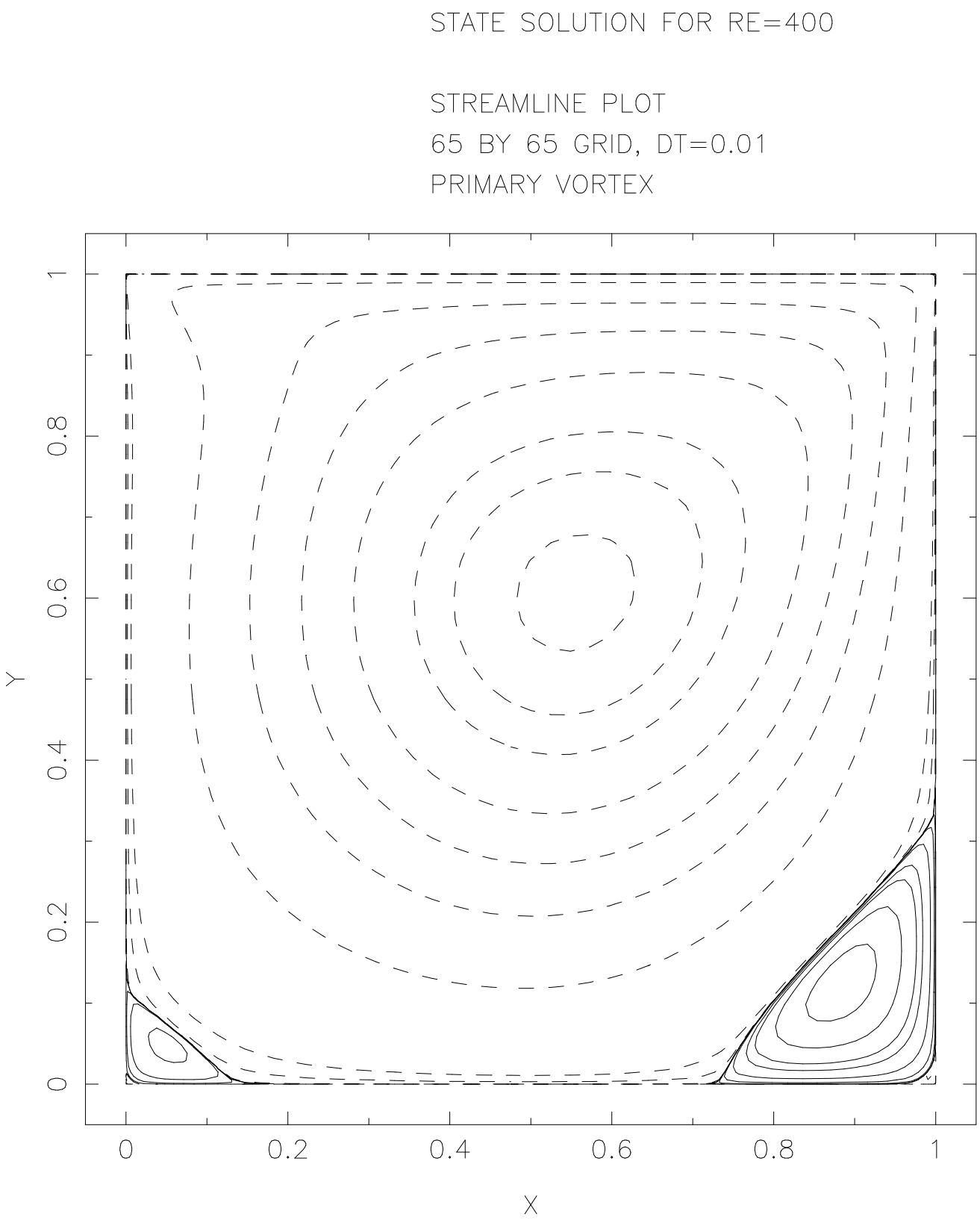

Figure 4.11: Streamlines for $Re_G = 400$ using a 65×65 grid and $\Delta t = 0.01$.

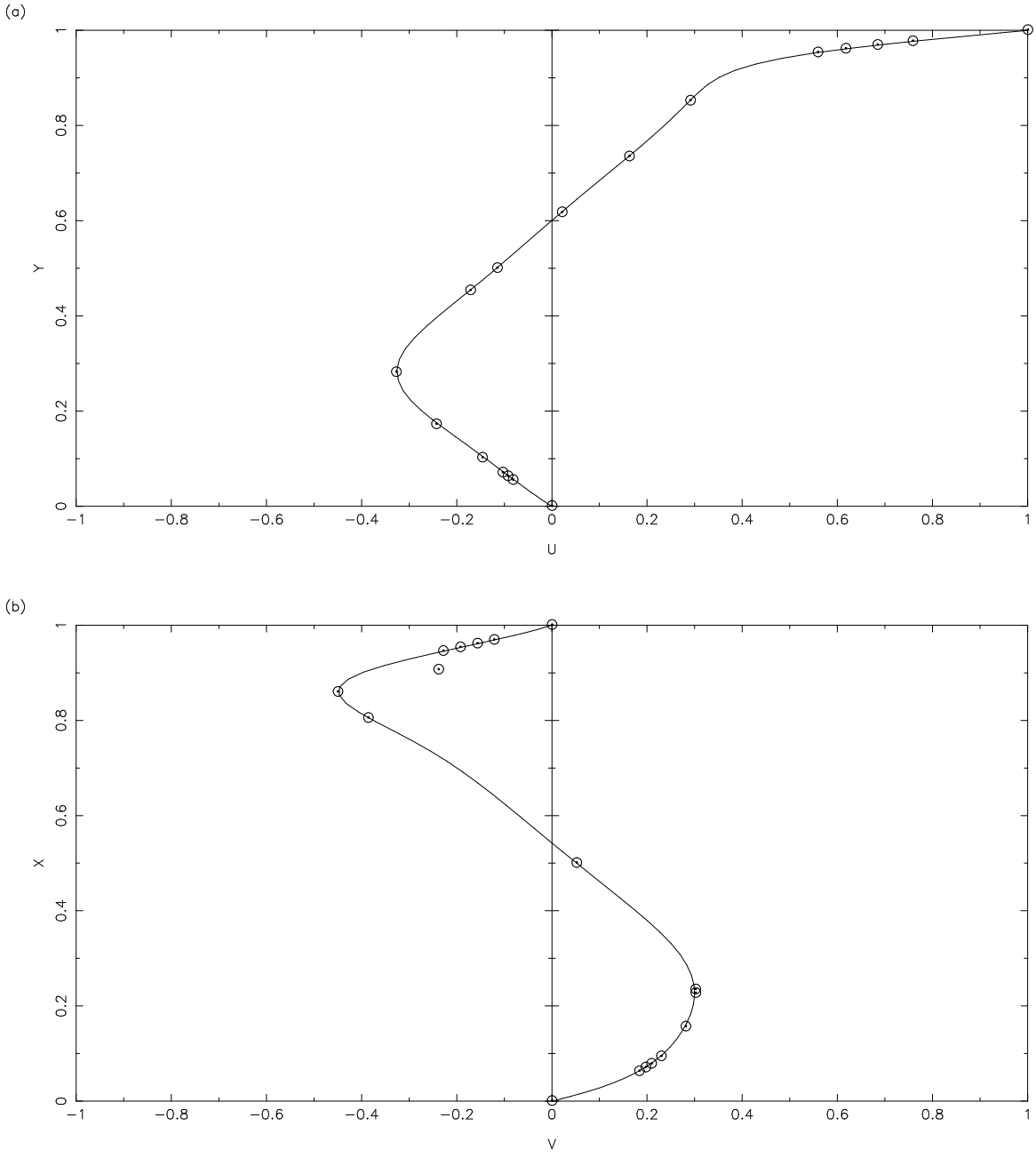

FIGURE 7.24.6: (a) HORIZONTAL COMPONENT OF VELOCITY THROUGH VERTICAL CENTERLINE
(b) VERTICAL COMPONENT OF VELOCITY THROUGH HORIZONTAL CENTERLINE

CIRCLED POINTS REPRESENT DATA FROM GHIA

65 BY 65 GRID, DT = 0.01, RE = 400

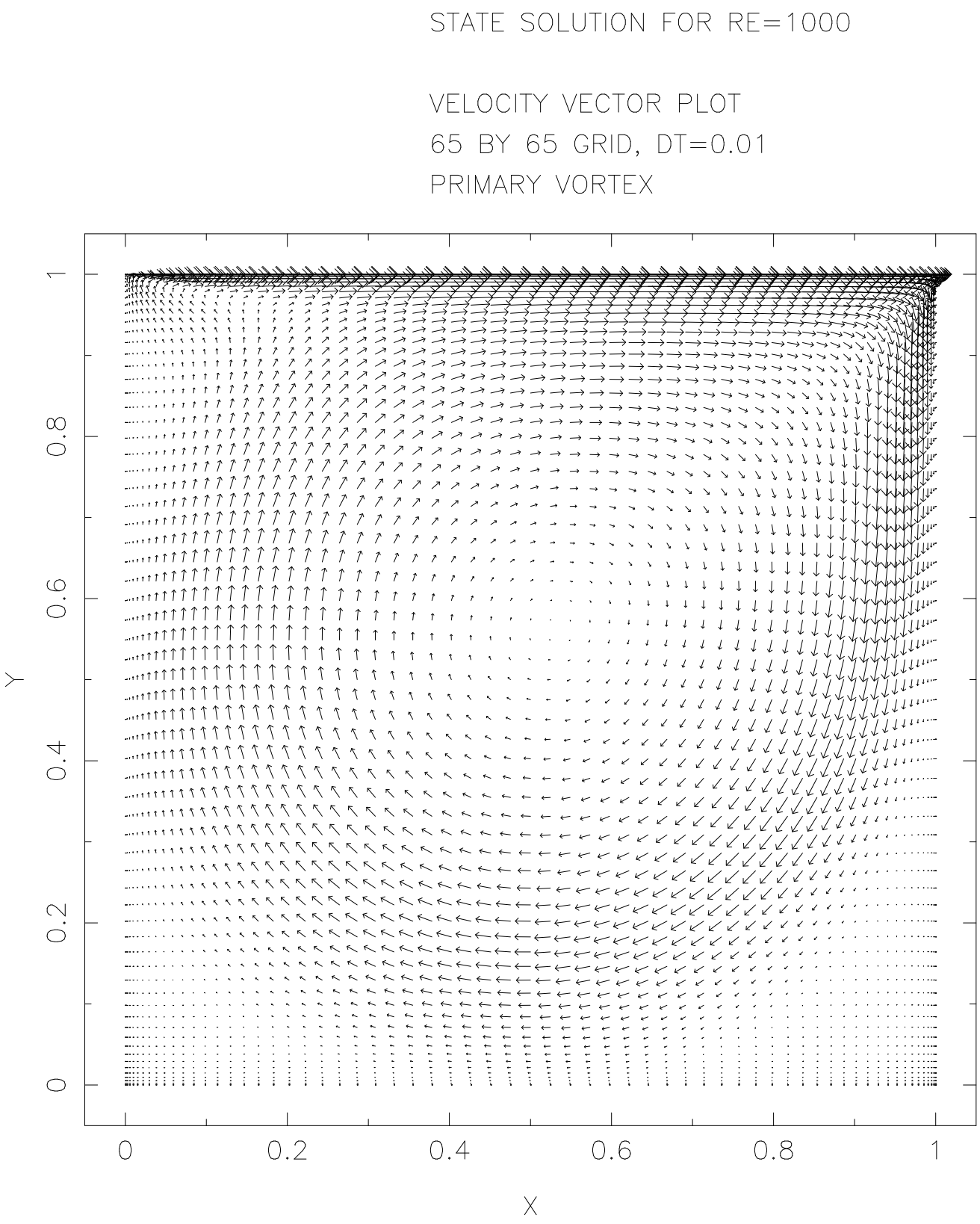

Figure 4.13: Velocity vectors for $Re_G = 1000$ using a 65×65 grid and $\Delta t = 0.01$.

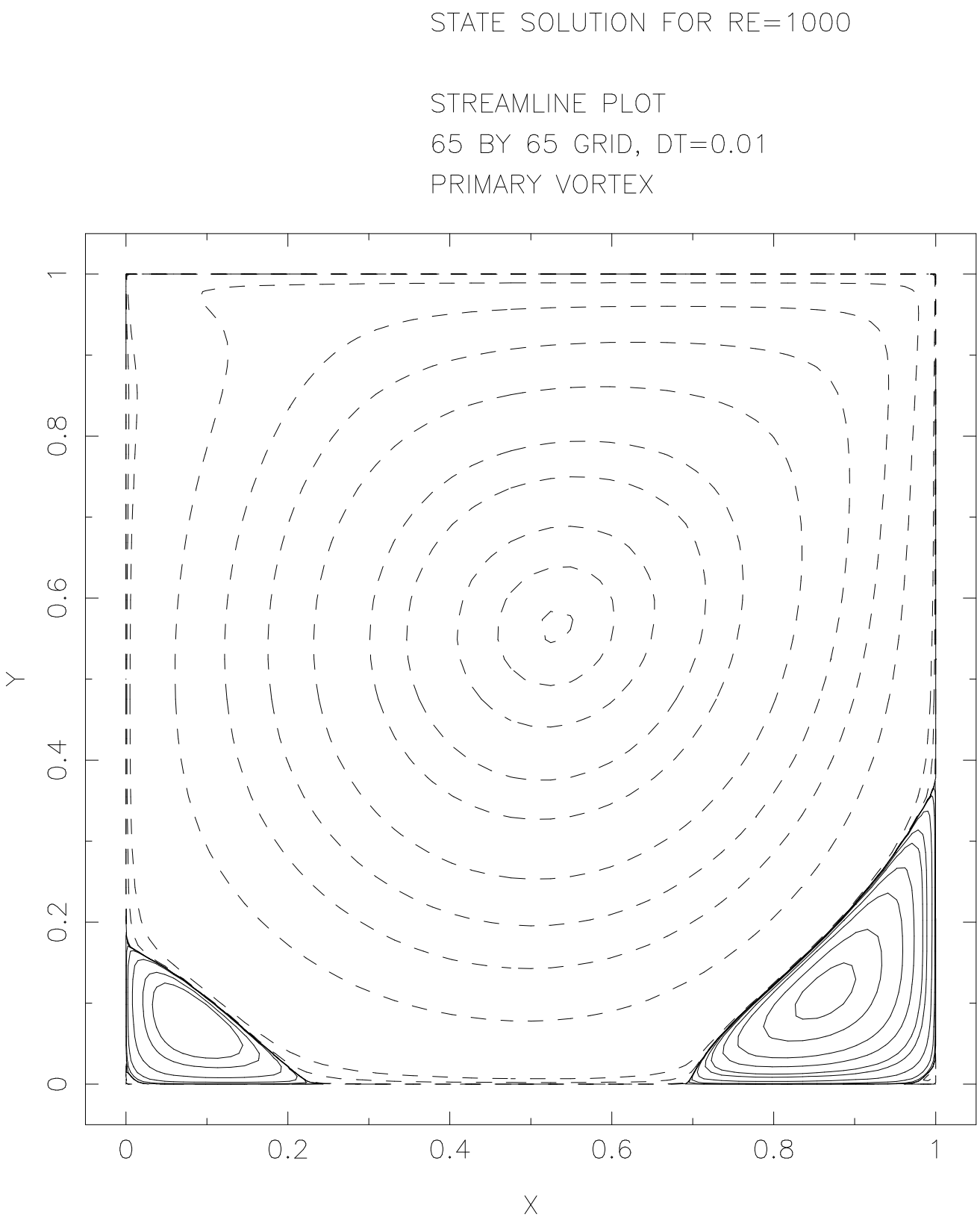

Figure 4.14: Streamlines for $Re_G = 1000$ using a 65×65 grid and $\Delta t = 0.01$.

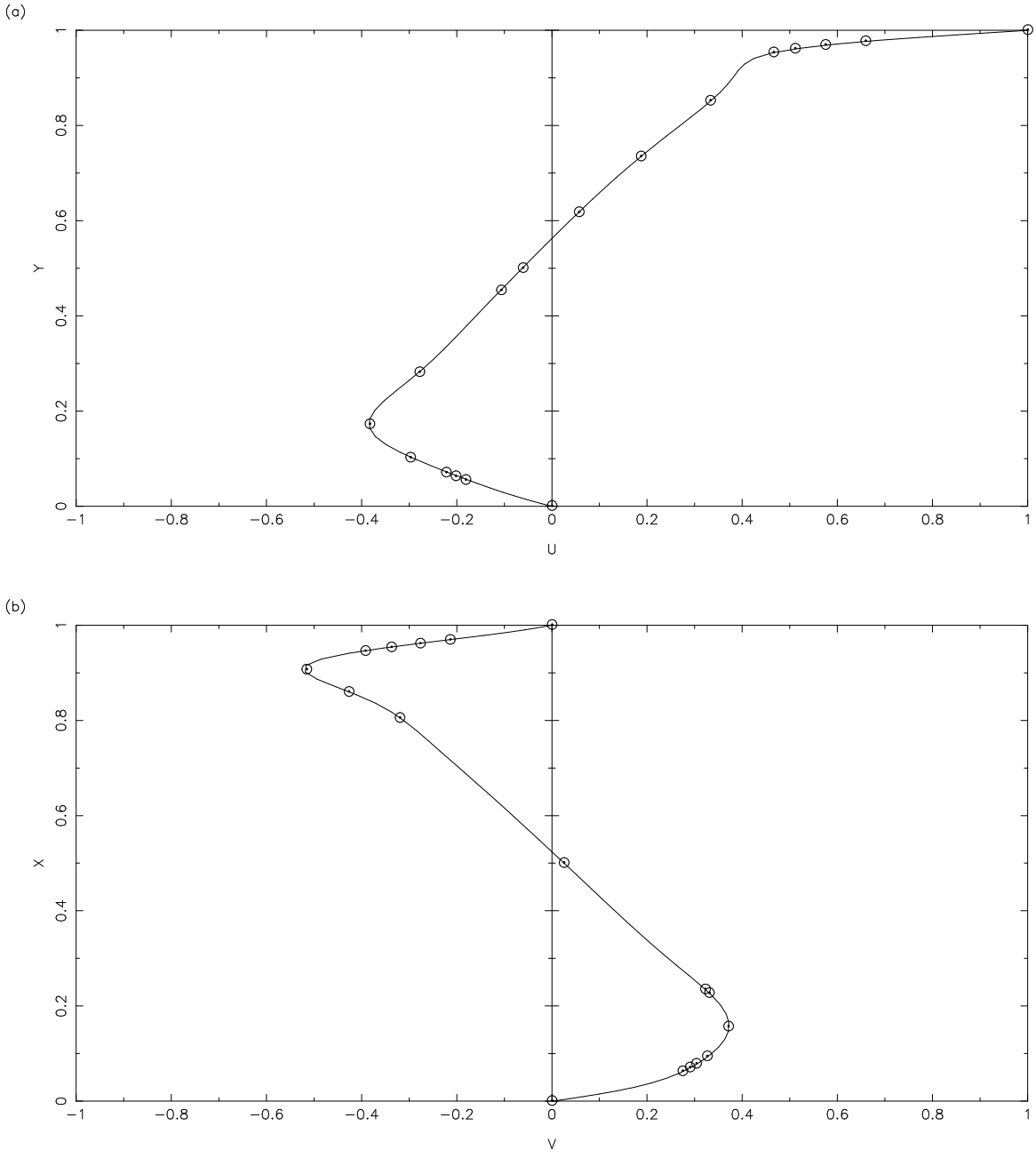

FIGURE 7.24.6: (a) HORIZONTAL COMPONENT OF VELOCITY THROUGH VERTICAL CENTERLINE
(b) VERTICAL COMPONENT OF VELOCITY THROUGH HORIZONTAL CENTERLINE

CIRCLED POINTS REPRESENT DATA FROM GHIA

65 BY 65 GRID, DT = 0.01, RE = 400

.

Figure 4.16: $Log_e|u - u_{an}|$ versus $Log_e \Delta t$ at a point in the domain for $Re_G = 0.1$, and a 25×25 grid.

Figure 4.3: $Re_G = 100$ using a 17×17 grid and $\Delta t = 0.01$.
(a) Horizontal component of velocity through vertical centreline.
(b) Vertical component of velocity through horizontal centreline.

Circled points represent data from Ghia et al. (1982)

Figure 4.6: $Re_G = 100$ using a 25×25 grid and $\Delta t = 0.01$.
(a) Horizontal component of velocity through vertical centreline.
(b) Vertical component of velocity through horizontal centreline.

Circled points represent data from Ghia et al. (1982)

Figure 4.9: $Re_G = 100$ using a 49×49 grid and $\Delta t = 0.01$.
(a) Horizontal component of velocity through vertical centreline.
(b) Vertical component of velocity through horizontal centreline.

Circled points represent data from Ghia et al. (1982)

Figure 4.12: $Re_G = 400$ using a 65×65 grid and $\Delta t = 0.01$.
(a) Horizontal component of velocity through vertical centreline.
(b) Vertical component of velocity through horizontal centreline.

Circled points represent data from Ghia et al. (1982)

Figure 4.15: $Re_G = 1000$ using a 65×65 grid and $\Delta t = 0.01$.
(a) Horizontal component of velocity through vertical centreline.
(b) Vertical component of velocity through horizontal centreline.

Circled points represent data from Ghia et al. (1982)

5 Numerical Method for Taylor Vortex Flow

An operator splitting approach will be used. In such an approach each of the discrete spatial operators is treated separately, which effectively reduces the computational cost in the numerical solution of the Navier-Stokes equations. Due to the success of the Tau spectral method in simulating driven cavity flow, it was decided to apply this approach in modelling Taylor vortex flow.

5.1 The classical splitting scheme

The operator splitting procedure treats the non-linear term, the pressure term and the viscous terms in the Navier-Stokes equations, separately. The velocity is advanced from time step l to time step $l+1$ using three fractional steps. A classical operator splitting scheme which has first-order temporal accuracy for velocity will now be described, following a general operator splitting procedure described by Karniadakis et al. (1991). We proceed with the equations for Taylor vortex flow described in Chapter 3.

The first fractional step accounts for the nonlinear term and uses an explicit, second-order Adams-Bashforth approximation :

$$u_r^{l+\frac{1}{3}} = u_r^l + \Delta t \left(\frac{3}{2} N_r(\mathbf{u}^l) - \frac{1}{2} N_r(\mathbf{u}^{l-1}) \right) \tag{1}$$

$$u_\phi^{l+\frac{1}{3}} = u_\phi^l + \Delta t \left(\frac{3}{2} N_\phi(\mathbf{u}^l) - \frac{1}{2} N_\phi(\mathbf{u}^{l-1}) \right) \tag{2}$$

$$u_z^{l+\frac{1}{3}} = u_z^l + \Delta t \left(\frac{3}{2} N_z(\mathbf{u}^l) - \frac{1}{2} N_z(\mathbf{u}^{l-1}) \right) \tag{3}$$

The second fractional step is due to the pressure term contribution:

$$u_r^{l+\frac{2}{3}} = u_r^{l+\frac{1}{3}} - \Delta t \frac{\partial P^{l+1}}{\partial r} \tag{4}$$

$$u_\phi^{l+\frac{2}{3}} = u_\phi^{l+\frac{1}{3}} \tag{5}$$

$$u_z^{l+\frac{2}{3}} = u_z^{l+\frac{1}{3}} - \Delta t \frac{\partial P}{\partial z}^{l+1} \tag{6}$$

These are explicit forward Euler approximations. The pressure P^{l+1} is solved using the Poisson equation:

$$\begin{aligned} \frac{1}{r+\gamma}\frac{\partial P}{\partial r}^{l+1} &+ \frac{\partial^2 P}{\partial r^2}^{l+1} + \frac{\partial^2 P}{\partial z^2}^{l+1} \\ &= \frac{1}{\Delta t}\left(\frac{1}{r+\gamma}u_r^{l+1/3} + \frac{\partial u_r}{\partial r}^{l+1/3} + \frac{\partial u_z}{\partial z}^{l+1/3}\right) \end{aligned} \tag{7}$$

which is obtained by applying the incompressibility constraint (Equation (19) in Chapter (3)) at time step $l + 2/3$ and using Equations (4) and (6). Multiplying both sides of Equation (7) by $r + \gamma$ we get:

$$\begin{aligned} \frac{\partial P}{\partial r}^{l+1} &+ (r+\gamma)\frac{\partial^2 P}{\partial r^2}^{l+1} + (r+\gamma)\frac{\partial^2 P}{\partial z^2}^{l+1} \\ &= \frac{1}{\Delta t}\left(u_r^{l+1/3} + (r+\gamma)\frac{\partial u_r}{\partial r}^{l+1/3} + (r+\gamma)\frac{\partial u_z}{\partial z}^{l+1/3}\right) \end{aligned} \tag{8}$$

The solution of Equation (8) is convenient because the spectral form of the operator $r + \gamma$ can be easily derived analytically.

A further assumption is that $\mathbf{u}^{l+2/3}$ satisfies the prescribed boundary conditions in the directions normal to the boundaries (cylinder walls):

$$u_r^{l+2/3}(z, \pm 1, t) = 0 \tag{9}$$

From Equation (4), this implies that Neumann boundary conditions can be imposed:

$$\frac{\partial P}{\partial r}^{l+1} = \frac{1}{\Delta t} u_r^{l+1/3} \qquad \text{at } r = \pm 1 \tag{10}$$

Periodicity in the pressure is assumed in the axial direction.

The third fractional step is the viscous step:

$$u_r^{l+1} = u_r^{l+\frac{2}{3}} + \frac{\Delta t}{Re} L_r(\mathbf{u}^{l+1}) \tag{11}$$

$$u_\phi^{l+1} = u_\phi^{l+\frac{2}{3}} + \frac{\Delta t}{Re} L_\phi(\mathbf{u}^{l+1}) \tag{12}$$

$$u_z^{l+1} = u_z^{l+\frac{2}{3}} + \frac{\Delta t}{Re} L_z(\mathbf{u}^{l+1}) \tag{13}$$

where an implicit, backwards Euler approximation is made. Equations (11) to (13) are each in the form of an Helmholtz equation. We multiply both sides of Equations (11) and (12) by $(r+\gamma)^2$ and both sides of Equation (13) by $r+\gamma$ to get:

$$\begin{aligned} (r+\gamma)\frac{\partial u_r}{\partial r}^{l+1} &+ (r+\gamma)^2 \frac{\partial^2 u_r}{\partial r^2}^{l+1} + (r+\gamma)^2 \frac{\partial^2 u_r}{\partial z^2}^{l+1} - \left(\frac{Re}{\Delta t}(r+\gamma)^2 + 1\right) u_r^{l+1} \\ &= -\left(\frac{Re}{\Delta t}(r+\gamma)^2 + 1\right) u_r^{l+2/3} \end{aligned} \tag{14}$$

$$\begin{aligned} (r+\gamma)\frac{\partial u_\phi}{\partial r}^{l+1} &+ (r+\gamma)^2 \frac{\partial^2 u_\phi}{\partial r^2}^{l+1} + (r+\gamma)^2 \frac{\partial^2 u_\phi}{\partial z^2}^{l+1} - \left(\frac{Re}{\Delta t}(r+\gamma)^2 + 1\right) u_\phi^{l+1} \\ &= -\left(\frac{Re}{\Delta t}(r+\gamma)^2 + 1\right) u_\phi^{l+2/3} \end{aligned} \tag{15}$$

$$\begin{aligned} \frac{\partial u_z}{\partial r}^{l+1} &+ (r+\gamma)\frac{\partial^2 u_z}{\partial r^2}^{l+1} + (r+\gamma)\frac{\partial^2 u_z}{\partial z^2}^{l+1} - \frac{Re}{\Delta t}(r+\gamma) u_z^{l+1} \\ &= -\frac{Re}{\Delta t}(r+\gamma) u_z^{l+2/3} \end{aligned} \tag{16}$$

Again, Equations (14) to (16) are convenient because the spectral form of the operators $r+\gamma$ and $(r+\gamma)^2$ can be easily derived analytically. The Helmholtz equations can each be solved with the following respective Dirichlet boundary conditions:

$$u_r^{l+1}(z,\pm 1,t) = 0 \tag{17}$$

$$u_\phi^{l+1}(z,-1,t) = 1 \qquad \text{and} \qquad u_\phi^{l+1}(z,1,t) = \mu/\eta \tag{18}$$

$$u_z^{l+1}(z,\pm 1,t) = 0 \tag{19}$$

Periodic boundary conditions are assumed in the axial direction for each of these velocity components.

5.2 Higher order splitting schemes

Following Karniadakis et al. (1991), the non-linear terms are approximated via an explicit scheme, for example, a J_e-order scheme from the Adams-Bashforth family as follows,

$$u_r^{l+1/3} = u_r^l + \Delta t \sum_{q=0}^{J_e-1} \beta_q N_r(\mathbf{u}^{l-q}) \tag{20}$$

$$u_\phi^{l+1/3} = u_\phi^l + \Delta t \sum_{q=0}^{J_e-1} \beta_q N_\phi(\mathbf{u}^{l-q}) \tag{21}$$

$$u_z^{l+1/3} = u_z^l + \Delta t \sum_{q=0}^{J_e-1} \beta_q N_z(\mathbf{u}^{l-q}) \tag{22}$$

For a 2^{nd} order Adams Bashforth scheme ($J_e = 2$), $\beta_0 = \frac{3}{2}$ and $\beta_1 = -\frac{1}{2}$, as in Equations (1) to (3). For a 3^{rd} order Adams Bashforth scheme ($J_e = 3$), $\beta_0 = \frac{23}{12}$, $\beta_1 = -\frac{4}{3}$ and $\beta_2 = \frac{5}{12}$.

The linear (viscous) terms are approximated via an implicit scheme, for example, a J_i-order scheme from the Adams-Moulton family as follows

$$u_r^{l+1} = u_r^{l+\frac{2}{3}} + \frac{\Delta t}{Re}\sum_{q=0}^{J_i-1}\gamma_q L_r(\mathbf{u}^{l+1-q}) \tag{23}$$

$$u_\phi^{l+1} = u_\phi^{l+\frac{2}{3}} + \frac{\Delta t}{Re}\sum_{q=0}^{J_i-1}\gamma_q L_\phi(\mathbf{u}^{l+1-q}) \tag{24}$$

$$u_z^{l+1} = u_z^{l+\frac{2}{3}} + \frac{\Delta t}{Re}\sum_{q=0}^{J_i-1}\gamma_q L_z(\mathbf{u}^{l+1-q}) \tag{25}$$

For a 1^{st} order Adams-Moulton scheme ($J_i = 1$, i.e. Backward-Euler), $\gamma_0 = 1$, as in Equations (11) to (13). For a 2^{nd} order Adams-Moulton scheme ($J_i = 2$, i.e. Crank-Nicolson), $\gamma_0 = \frac{1}{2}$ and $\gamma_1 = \frac{1}{2}$.

If a weighted approximation (with $J_i = 2$) is used for the linear terms then $\gamma_0 = \frac{1}{2} + \theta$ and $\gamma_1 = \frac{1}{2} - \theta$, where θ is a weighting parameter. For example, $\theta = \frac{1}{2}$ corresponds to a Backward-Euler approximation ($J_i = 1$) and $\theta = 0$ corresponds to a Crank-Nicolson approximation ($J_i = 2$).

From Equations (23) to (25), the Helmholtz equations for the three components of velocity in the viscous step become

$$\begin{aligned}
& (r+\gamma)\frac{\partial u_r}{\partial r}^{l+1} + (r+\gamma)^2\frac{\partial^2 u_r}{\partial r^2}^{l+1} + (r+\gamma)^2\frac{\partial^2 u_r}{\partial z^2}^{l+1} \\
- & \left(\frac{1}{\gamma_0}\frac{Re}{\Delta t}(r+\gamma)^2 + 1\right) u_r^{l+1} = -\left(\frac{1}{\gamma_0}\frac{Re}{\Delta t}(r+\gamma)^2 + 1\right) u_r^{l+2/3} \\
- & \frac{1}{\gamma_0}\sum_{q=1}^{J_i-1}\gamma_q\left[(r+\gamma)\frac{\partial u_r}{\partial r} + (r+\gamma)^2\frac{\partial^2 u_r}{\partial r^2} + (r+\gamma)^2\frac{\partial^2 u_r}{\partial z^2} - u_r\right]^{(l+1-q)}
\end{aligned} \tag{26}$$

$$\begin{aligned}
& (r+\gamma)\frac{\partial u_\phi}{\partial r}^{l+1} + (r+\gamma)^2\frac{\partial^2 u_\phi}{\partial r^2}^{l+1} + (r+\gamma)^2\frac{\partial^2 u_\phi}{\partial z^2}^{l+1} \\
- & \left(\frac{1}{\gamma_0}\frac{Re}{\Delta t}(r+\gamma)^2 + 1\right) u_\phi^{l+1} = -\left(\frac{1}{\gamma_0}\frac{Re}{\Delta t}(r+\gamma)^2 + 1\right) u_\phi^{l+2/3} \\
- & \frac{1}{\gamma_0}\sum_{q=1}^{J_i-1}\gamma_q\left[(r+\gamma)\frac{\partial u_\phi}{\partial r} + (r+\gamma)^2\frac{\partial^2 u_\phi}{\partial r^2} + (r+\gamma)^2\frac{\partial^2 u_\phi}{\partial z^2} - u_\phi\right]^{(l+1-q)}
\end{aligned} \tag{27}$$

$$
\begin{aligned}
& \frac{\partial u_z}{\partial r}^{l+1} + (r+\gamma)\frac{\partial^2 u_z}{\partial r^2}^{l+1} + (r+\gamma)\frac{\partial^2 u_z}{\partial z^2}^{l+1} \\
- & \frac{1}{\gamma_0}\frac{Re}{\Delta t}(r+\gamma)u_z^{l+1} = -\frac{1}{\gamma_0}\frac{Re}{\Delta t}(r+\gamma)u_z^{l+2/3} \\
- & \frac{1}{\gamma_0}\sum_{q=1}^{J_i-1}\gamma_q\left[\frac{\partial u_z}{\partial r} + (r+\gamma)\frac{\partial^2 u_z}{\partial r^2} + (r+\gamma)\frac{\partial^2 u_z}{\partial z^2}\right]^{(l+1-q)}
\end{aligned}
\tag{28}
$$

If $J_i = 1$ and $\gamma_0 = 1$ then Equations (26) to (28) become Equations (14) to (16).

In the pressure step Equation (8) is solved subject to higher order pressure boundary conditions. That is, instead of using Equation (10) we use an explicit J_p-order scheme,

$$
\frac{\partial P}{\partial r}^{l+1} = \sum_{q=0}^{J_p-1}\beta_q\left[-\frac{1}{Re}\left(\nabla\times(\nabla\times\mathbf{u})\right)_r + N_r(\mathbf{u})\right]^{(l-q)} \tag{29}
$$

which becomes

$$
\frac{\partial P}{\partial r}^{l+1} = \sum_{q=0}^{J_p-1}\beta_q\left[\frac{1}{Re}\left(\frac{\partial^2 u_r}{\partial z^2} - \frac{\partial^2 u_z}{\partial z\partial r}\right) - \left(u_r\frac{\partial u_r}{\partial r} + u_z\frac{\partial u_r}{\partial z} - \frac{{u_\phi}^2}{r+\gamma}\right)\right]^{(l-q)} \tag{30}
$$

Equation (30) is used to set the Neumann boundary conditions at $r = \pm 1$. The pressure is assumed to be periodic in the axial direction.

For $J_p = 0$ we obtain zero on the right hand side of Equation (30) which is the same result that would be obtained with Equation (10). A scheme with a $J_p = 0$ treatment of the pressure boundary conditions and any value for J_e and J_i is called a classical splitting scheme. For $J_p = 1$, e.g. Forward-Euler, $\beta_0 = 1$ and for higher J_p we can choose β_q to correspond to the Adams-Bashforth family of approximations.

From Karniadakis et al. (1991), a zeroth order time treatment of the pressure boundary conditions is expected to produce first order time accuracy in velocity. Similarly, a first order time treatment of the pressure boundary conditions is expected to produce second order time accuracy in velocity.

Here, a splitting scheme labelled as (J_e, J_p, J_i) denotes that the nonlinear terms are to J_e-order, the pressure boundary conditions are to J_p-order and the viscous terms are to J_i-order.

5.3 Spectral methods

A Tau spectral method will be described which has a Fourier approximation in the axial direction (z) and a Chebyshev approximation in the radial (r) direction that solves the:

(1) Poisson equation for the pressure in the pressure step using Neumann boundary conditions in r and periodic boundary conditions in z,

(2) Helmholtz equation for the radial and azimuthal velocity components in the viscous step using Dirichlet boundary conditions in r and periodic boundary conditions in z, and,

(3) Helmholtz equation for the axial velocity component in the viscous step using Dirichlet boundary conditions in r and periodic boundary conditions in z.

5.3.1 Spatial discretisation of the grid

A discrete Fourier-Chebyshev approximation of a function $P(z,r)$ is

$$P(z,r) = \sum_{m=-M/2}^{M/2-1} \sum_{n=0}^{N} P_{mn} T_n(r) \exp(imz) \tag{31}$$

where the Chebyshev polynomial is

$$T_n(r) = \cos(n \cos^{-1} r) \tag{32}$$

In the radial direction there are $N+1$ Chebyshev-Gauss-Lobatto points defined by

$$r_j = \cos(\pi j/N) \qquad \text{for} \quad j = 0, ..., N \tag{33}$$

where $-1 \leq r \leq 1$. The distribution of these points becomes denser as $r \to \pm 1$.

In the axial direction there are M equidistant points defined by

$$z_j = \frac{2\pi}{M} j \qquad \text{for} \quad j = 0, ..., M-1 \tag{34}$$

In Equation (34), 2π radians corresponds to an aspect ratio length of Γ. Therefore, an equivalent form of a Fourier-Chebyshev approximation of a function $P(z,r)$ is

$$P(z,r) = \sum_{m=-M/2}^{M/2-1} \sum_{n=0}^{N} P_{mn} T_n(r) \exp\left(i \frac{2\pi m}{\Gamma} z\right) \tag{35}$$

where the axial direction has M equidistant points defined by

$$z_j = \frac{\Gamma}{M} j \qquad \text{for} \quad j = 0, ..., M-1 \tag{36}$$

From Equation (35), the allowed discrete axial wavenumbers are given by

$$\kappa_m = \frac{2\pi}{\Gamma} m \qquad \text{for} \quad m = 0, ..., M/2-1 \tag{37}$$

That is, the allowed discrete axial wavelengths are given by

$$\lambda_m = \frac{\Gamma}{m} \qquad \text{for} \quad m = 1, ..., M/2-1 \tag{38}$$

From Equation (38), the largest possible discrete axial wavelength is equal in magnitude to the aspect ratio and the smallest possible discrete axial wavelength is in magnitude about a factor $M/2$ smaller than the aspect ratio.

5.3.2 Spectral operator for variable coefficients

A function $u(r)$ expressed in terms of Chebyshev polynomials is

$$u(r) = \sum_{n=0}^{N} u_n T_n(r) \tag{39}$$

where

$$T_n(r) = \cos(n \cos^{-1} r) \tag{40}$$

and the subscript denotes Chebyshev transform coefficient index. From Canuto et al. (1988) there is the expression

$$(uv)_n = \frac{1}{2}\sum_{p+q=n} u_p v_q + \frac{1}{2}\sum_{|p-q|=n} u_p v_q \tag{41}$$

If $u(r) = r + \gamma$ then $u_0 = \gamma$, $u_1 = 1$ and $u_n = 0$ for $n \geq 2$. Also, if $u(r) = (r+\gamma)^2$ then $u_0 = \gamma^2 + 1/2$, $u_1 = 2\gamma$, $u_2 = 1/2$ and $u_n = 0$ for $n \geq 3$. By substituting this information into Equation (41) the spectral form of the operator for $(r+\gamma)$ is then the $(N+1)\times(N+1)$ tridiagonal matrix C, where

$$C_{pq} = \begin{cases} \gamma & \text{for } p = q \\ 1/2 & \text{for } p = q+1 \text{ and } p \leq N-1 \\ 1/2 & \text{for } p = q-1 \text{ and } p \geq 1 \\ 1 & \text{for } p = q-1 \text{ and } p = 0 \\ 0 & \text{otherwise} \end{cases} \tag{42}$$

where $0 \leq p \leq N$ and $0 \leq q \leq N$. Also, the spectral form of the operator $(r+\gamma)^2$ is the $(N+1)\times(N+1)$ pentadiagonal matrix C^2, where

$$C^2_{pq} = \begin{cases} \gamma^2 + 1/2 & \text{for } p = q \text{ and } p = 0,\ 2 \leq p \leq N-2 \\ \gamma^2 + 3/4 & \text{for } p = q \text{ and } p = 1 \\ \gamma^2 + 1/4 & \text{for } p = q \text{ and } p = N-1 \\ \gamma^2 & \text{for } p = q \text{ and } p = N \\ 2\gamma & \text{for } p = q-1 \text{ and } p = 0 \\ \gamma & \text{for } p = q-1 \text{ and } p \geq 1 \\ 1/2 & \text{for } p = q-2 \text{ and } p = 0 \\ 1/4 & \text{for } p = q-2 \text{ and } p \geq 1 \\ \gamma & \text{for } p = q+1 \text{ and } p \leq N-1 \\ 1/4 & \text{for } p = q+2 \text{ and } p \leq N-1 \\ 0 & \text{otherwise} \end{cases} \tag{43}$$

5.3.3 Poisson solver for pressure

The Poisson equation for the pressure $P(z,r)$ at each time step, has the form

$$\frac{\partial P}{\partial r} + (r+\gamma)\frac{\partial^2 P}{\partial r^2} + (r+\gamma)\frac{\partial^2 P}{\partial z^2} = F(z,r) \tag{44}$$

where the Neumann boundary conditions have the form

$$\frac{\partial P}{\partial r} = \alpha(z) \qquad \text{at } r = -1 \tag{45}$$

$$\frac{\partial P}{\partial r} = \beta(z) \qquad \text{at } r = 1 \tag{46}$$

Equation (44) in matrix form in spectral space can be written as

$$PD + (PD^2 + \Lambda P)C = F \tag{47}$$

where P and F are $M \times (N+1)$ matrices. The spectral coefficients P_{mn} and F_{mn} are complex numbers in general.

D is the $(N+1) \times (N+1)$ matrix with elements defined by

$$D_{pq} = \begin{cases} \frac{2}{c_q} p & \text{for } p \geq q+1 \text{ and } p+q \text{ odd} \\ 0 & \text{otherwise} \end{cases} \tag{48}$$

where $0 \leq p \leq N$ and $0 \leq q \leq N$. The coefficients $c_0 = 2$, $c_q = 1$, for $1 \leq q \leq N-1$ and $c_N = 2$.

D^2 is the $(N+1) \times (N+1)$ matrix with elements defined by

$$D^2_{pq} = \begin{cases} \frac{1}{c_q} p(p^2 - q^2) & \text{for } p \geq q+2 \text{ and } p+q \text{ even} \\ 0 & \text{otherwise} \end{cases} \tag{49}$$

where $0 \leq p \leq N$ and $0 \leq q \leq N$.

Λ is a diagonal $M \times M$ matrix with elements

$$\Lambda_{jk} = \begin{cases} -j^2 & \text{for } j = k \\ 0 & \text{otherwise} \end{cases} \tag{50}$$

where the Fourier indices j and k take the ordering described above.

The spectral form of the boundary conditions can be written as:

$$\sum_{n=0}^{N} n^2 P_{R,mn} = \beta_{R,m} \tag{51}$$

$$\sum_{n=0}^{N} (-1)^{n+1} n^2 P_{R,mn} = \alpha_{R,m} \tag{52}$$

$$\sum_{n=0}^{N} n^2 P_{I,mn} = \beta_{I,m} \tag{53}$$

$$\sum_{n=0}^{N} (-1)^{n+1} n^2 P_{I,mn} = \alpha_{I,m} \tag{54}$$

for $-M/2 \leq m \leq M/2 - 1$. The subscripts R and I denote real and imaginary components.

Adding and subtracting Equations (51) and (52) we get:

$$\sum_{n=0,\ n\ odd}^{N} n^2 P_{R,mn} = \frac{1}{2}(\beta_{R,m} + \alpha_{R,m}) = \eta_{R,m} \tag{55}$$

$$\sum_{n=0,\ n\ even}^{N} n^2 P_{R,mn} = \frac{1}{2}(\beta_{R,m} - \alpha_{R,m}) = \theta_{R,m} \tag{56}$$

Adding and subtracting Equations (53) and (54) we get:

$$\sum_{n=0,\ n\ odd}^{N} n^2 P_{I,mn} = \frac{1}{2}(\beta_{I,m} + \alpha_{I,m}) = \eta_{I,m} \tag{57}$$

$$\sum_{n=0,\ n\ even}^{N} n^2 P_{I,mn} = \frac{1}{2}(\beta_{I,m} - \alpha_{I,m}) = \theta_{I,m} \tag{58}$$

for $-M/2 \leq m \leq M/2 - 1$.

In the matrix Equation (47) we substitute Equation (55) and (57) to eliminate the complex coefficients $P_{m,N-1}$ and Equation (56) and (58) to eliminate the complex coefficients $P_{m,N}$, for $-M/2 \leq m \leq M/2-1$. Subsequently we obtain the matrix equation

$$PB + (PB^2 + \Lambda P)C = f \tag{59}$$

where now P takes the range $-M/2 \leq m \leq M/2-1$, $0 \leq n \leq N-2$ of its original definition, C is the portion $0 \leq p \leq N-2$, $0 \leq q \leq N-2$ of its original definition and Λ is the same. The matrices B and B^2 are both $(N-1) \times (N-1)$ where

$$B_{pq} = \begin{cases} \frac{-2p^2}{(N-1)c_q} & \text{for } p \leq q-1,\ q \text{ even},\ p \text{ odd} \\ \frac{2p}{c_q}\left(1 - \frac{p}{N-1}\right) & \text{for } p \geq q+1,\ q \text{ even},\ p \text{ odd} \\ \frac{-2p^2}{Nc_q} & \text{for } p \leq q-1,\ q \text{ odd},\ p \text{ even} \\ \frac{2p}{c_q}\left(1 - \frac{p}{N}\right) & \text{for } p \geq q+1,\ q \text{ odd},\ p \text{ even} \\ 0 & \text{otherwise} \end{cases} \tag{60}$$

and

$$B^2_{pq} = \begin{cases} \frac{-p^2((N-1)^2-q^2)}{(N-1)c_q} & \text{for } p \leq q,\ q \text{ odd},\ p \text{ odd} \\ \frac{p}{c_q}\left(p^2 - q^2 - \frac{p((N-1)^2-q^2)}{N-1}\right) & \text{for } p \geq q+2,\ q \text{ odd},\ p \text{ odd} \\ \frac{-p^2(N^2-q^2)}{Nc_q} & \text{for } p \leq q,\ q \text{ even},\ p \text{ even} \\ \frac{p}{c_q}\left(p^2 - q^2 - \frac{p(N^2-q^2)}{N}\right) & \text{for } p \geq q+2,\ q \text{ even},\ p \text{ even} \\ 0 & \text{otherwise} \end{cases} \tag{61}$$

where $0 \leq p \leq N-2$ and $0 \leq q \leq N-2$. The matrices B and B^2 do not have the lower triangular structure that the matrices D and D^2 respectively have. They are general matrices with alternating zero and non-zero elements.

The matrix f has real and imaginary components

$$f_R = F_R - Q_R - S_R C \tag{62}$$

and

$$f_I = F_I - Q_I - S_I C \tag{63}$$

where Q and S are $M \times (N-1)$ matrices with components

$$Q_{R,mn} = \begin{cases} \frac{2}{(N-1)c_n}\eta_{R,m} & \text{for } n \text{ even} \\ \frac{2}{Nc_n}\theta_{R,m} & \text{for } n \text{ odd} \end{cases} \tag{64}$$

$$Q_{I,mn} = \begin{cases} \frac{2}{(N-1)c_n}\eta_{I,m} & \text{for } n \text{ even} \\ \frac{2}{Nc_n}\theta_{I,m} & \text{for } n \text{ odd} \end{cases} \tag{65}$$

$$S_{R,mn} = \begin{cases} \frac{N^2-n^2}{Nc_n}\theta_{R,m} & \text{for } n \text{ even} \\ \frac{(N-1)^2-n^2}{(N-1)c_n}\eta_{R,m} & \text{for } n \text{ odd} \end{cases} \tag{66}$$

$$S_{I,mn} = \begin{cases} \frac{N^2-n^2}{Nc_n}\theta_{I,m} & \text{for } n \text{ even} \\ \frac{(N-1)^2-n^2}{(N-1)c_n}\eta_{I,m} & \text{for } n \text{ odd} \end{cases} \tag{67}$$

Equation (59) represents a system with $M \times (N-1)$ equations in the $M \times (N-1)$ complex unknowns, P_{mn}. The solution is determined by taking

$$P_{R,k} = f_{R,k}[B + (B^2 + \lambda_k I_{N-1})C]^{-1} \tag{68}$$

$$P_{I,k} = f_{I,k}[B + (B^2 + \lambda_k I_{N-1})C]^{-1} \tag{69}$$

for $-M/2 \leq k \leq M/2 - 1$, where $P_{R,k}$, $P_{I,k}$ and $f_{R,k}$, $f_{I,k}$ are the k^{th} row of the real and imaginary component elements of P and f respectively, and λ_k is the k^{th} diagonal element of matrix Λ. I_{N-1} is the $(N-1) \times (N-1)$ identity matrix.

As it stands, the matrix $[B + (B^2 + \lambda_k I_{N-1})C]$ is not invertible for $k = 0$. In this instance, it was decided to set the element $[B + (B^2 + \lambda_0 I_{N-1})C]_{0,0}$ to a constant (unity) for $k = 0$. The solution for $P(z, r)$ will only be defined to within a constant, which does not of itself play a role in the Navier Stokes equations, since it is the pressure gradient that is required.

Once the P_{mn} are calculated for $-M/2 \leq m \leq M/2-1$ and $0 \leq n \leq N-2$, the P_{mn} for $-M/2 \leq m \leq M/2-1$ and $n = N-1, N$ can be determined using Equations (55) to (58). A Fourier-Chebyshev inverse transform of P_{mn} will give the solution for $P(z,r)$.

5.3.4 Helmholtz solver for radial and azimuthal components of velocity

The Helmholtz equation for the radial and azimuthal components of velocity at each time step, each have the form

$$(r+\gamma)\frac{\partial U}{\partial r} + (r+\gamma)^2\frac{\partial^2 U}{\partial r^2} + (r+\gamma)^2\frac{\partial^2 U}{\partial z^2} - \left(\frac{Re}{\Delta t}(r+\gamma)^2 + 1\right)U = F(z,r) \tag{70}$$

where the Dirichlet boundary conditions have the form

$$U(z,-1) = \alpha(z) \tag{71}$$

$$U(z,1) = \beta(z) \tag{72}$$

and periodic boundary conditions are assumed in the axial direction.

Equation (70) in matrix form in spectral space can be written as

$$U(DC + D^2C^2 - I_{N+1}) + \left(\Lambda - \frac{Re}{\Delta t}I_M\right)UC^2 = F \tag{73}$$

The matrices D, D^2 and C in Equation (73) are the same as those defined for Equation (47). Here, I_{N+1} is the $(N+1)\times(N+1)$ identity matrix and I_M is the $M \times M$ identity matrix. The matrix U contains the spectral coefficients U_{mn} of the velocity function $U(z,r)$.

The spectral form of the boundary conditions can be written as:

$$\sum_{n=0}^{N} U_{R,mn} = \beta_{R,m} \tag{74}$$

$$\sum_{n=0}^{N} (-1)^n U_{R,mn} = \alpha_{R,m} \tag{75}$$

$$\sum_{n=0}^{N} U_{I,mn} = \beta_{I,m} \tag{76}$$

$$\sum_{n=0}^{N} (-1)^n U_{I,mn} = \alpha_{I,m} \tag{77}$$

for $-M/2 \leq m \leq M/2 - 1$.

Adding and subtracting Equations (74) and (75) we get:

$$\sum_{n=0,\ n\ even}^{N} U_{R,mn} = \frac{1}{2}(\beta_{R,m} + \alpha_{R,m}) = \eta_{R,m} \tag{78}$$

$$\sum_{n=0,\ n\ odd}^{N} U_{R,mn} = \frac{1}{2}(\beta_{R,m} - \alpha_{R,m}) = \theta_{R,m} \tag{79}$$

Adding and subtracting Equations (76) and (77) we get:

$$\sum_{n=0,\ n\ even}^{N} U_{I,mn} = \frac{1}{2}(\beta_{I,m} + \alpha_{I,m}) = \eta_{I,m} \tag{80}$$

$$\sum_{n=0,\ n\ odd}^{N} U_{I,mn} = \frac{1}{2}(\beta_{I,m} - \alpha_{I,m}) = \theta_{I,m} \tag{81}$$

for $-M/2 \leq m \leq M/2 - 1$.

In the matrix Equation (73) we substitute Equations (79) and (81) to eliminate the complex coefficients $U_{m,N-1}$ and Equations (78) and (80) to eliminate the complex coefficients $U_{m,N}$, for $-M/2 \leq m \leq M/2 - 1$. Subsequently, we obtain the matrix equation

$$U(BC + B^2C^2 - I_{N-1}) + \left(\Lambda - \frac{Re}{\Delta t} I_M\right) UC^2 = f \tag{82}$$

The matrices C and C^2 take the range $0 \leq p \leq N-2$, $0 \leq q \leq N-2$ of their original definitions. I_{N-1} is the $(N-1) \times (N-1)$ identity matrix. The matrices B and B^2 are both $(N-1) \times (N-1)$ where

$$B_{pq} = \begin{cases} \frac{-2(N-1)}{c_q} & \text{for } p \leq q-1,\ q \text{ even},\ p \text{ odd} \\ \frac{2}{c_q}(p-(N-1)) & \text{for } p \geq q+1,\ q \text{ even},\ p \text{ odd} \\ \frac{-2N}{c_q} & \text{for } p \leq q-1,\ q \text{ odd},\ p \text{ even} \\ \frac{2}{c_q}(p-N) & \text{for } p \geq q+1,\ q \text{ odd},\ p \text{ even} \\ 0 & \text{otherwise} \end{cases} \tag{83}$$

and

$$B^2_{pq} = \begin{cases} \frac{-(N-1)((N-1)^2-q^2)}{c_q} & \text{for } p \leq q,\ q \text{ odd},\ p \text{ odd} \\ \frac{1}{c_q}(p(p^2-q^2)-(N-1)((N-1)^2-q^2)) & \text{for } p \geq q+2,\ q \text{ odd},\ p \text{ odd} \\ \frac{-N(N^2-q^2)}{c_q} & \text{for } p \leq q,\ q \text{ even},\ p \text{ even} \\ \frac{1}{c_q}(p(p^2-q^2)-N(N^2-q^2)) & \text{for } p \geq q+2,\ q \text{ even},\ p \text{ even} \\ 0 & \text{otherwise} \end{cases} \tag{84}$$

where $0 \leq p \leq N-2$ and $0 \leq q \leq N-2$. The matrices B and B^2 do not have the lower triangular structure that the matrices D and D^2 respectively have. They are general matrices with alternating zero and non-zero elements.

The matrix f has real and imaginary components given by

$$f_R = F_R - Q_R C - S_R C^2 \tag{85}$$

and

$$f_I = F_I - Q_I C - S_I C^2 \tag{86}$$

where Q and S are $M \times (N-1)$ matrices with components

$$Q_{R,mn} = \begin{cases} \frac{2(N-1)}{c_n}\theta_{R,m} & \text{for } n \text{ even} \\ \frac{2N}{c_n}\eta_{R,m} & \text{for } n \text{ odd} \end{cases} \tag{87}$$

$$Q_{I,mn} = \begin{cases} \frac{2(N-1)}{c_n}\theta_{I,m} & \text{for } n \text{ even} \\ \frac{2N}{c_n}\eta_{I,m} & \text{for } n \text{ odd} \end{cases} \tag{88}$$

$$S_{R,mn} = \begin{cases} \frac{N(N^2-n^2)}{c_n}\eta_{R,m} & \text{for } n \text{ even} \\ \frac{(N-1)((N-1)^2-n^2)}{c_n}\theta_{R,m} & \text{for } n \text{ odd} \end{cases} \tag{89}$$

$$S_{I,mn} = \begin{cases} \frac{N(N^2-n^2)}{c_n}\eta_{I,m} & \text{for } n \text{ even} \\ \frac{(N-1)((N-1)^2-n^2)}{c_n}\theta_{I,m} & \text{for } n \text{ odd} \end{cases} \tag{90}$$

Equation (82) represents a system with $M \times (N-1)$ equations in the $M \times (N-1)$ complex unknowns, U_{mn}, determined from

$$U_{R,k} = f_{R,k}\left[BC + B^2C^2 - I_{N-1} + \left(\lambda_k - \frac{Re}{\Delta t}\right) I_{N-1}C^2\right]^{-1} \tag{91}$$

$$U_{I,k} = f_{I,k}\left[BC + B^2C^2 - I_{N-1} + \left(\lambda_k - \frac{Re}{\Delta t}\right) I_{N-1}C^2\right]^{-1} \tag{92}$$

for $-M/2 \leq k \leq M/2-1$, where $U_{R,k}$, $U_{I,k}$ and $f_{R,k}$, $f_{I,k}$ are the k^{th} row of the real and imaginary component elements of U and f respectively, and λ_k is the k^{th} diagonal element of matrix Λ. I_{N-1} is the $(N-1) \times (N-1)$ identity matrix. Once the U_{mn} are calculated for $-M/2 \leq m \leq M/2-1$ and $0 \leq n \leq N-2$, the U_{mn} for $-M/2 \leq m \leq M/2-1$ and $n = N-1, N$ can be determined using Equations (78) to (81). A Fourier-Chebyshev inverse transform of U_{mn} will give the solution for $U(z,r)$.

5.3.5 Helmholtz solver for axial component of velocity

The Helmholtz equation for the axial component of velocity $W(z,r)$ in the viscous step has the form

$$\frac{\partial W}{\partial r} + (r+\gamma)\frac{\partial^2 W}{\partial r^2} + (r+\gamma)\frac{\partial^2 W}{\partial z^2} - \frac{Re}{\Delta t}(r+\gamma)W = F(z,r) \tag{93}$$

where the Dirichlet boundary conditions have the form

$$W(z,-1) = \alpha(z) \tag{94}$$

$$W(z,1) = \beta(z) \tag{95}$$

and periodic boundary conditions are assumed in the axial direction.

Equation (93) in matrix form in spectral space can be written as

$$W(D + D^2 C) + \left(\Lambda - \frac{Re}{\Delta t} I_M\right) WC = F \tag{96}$$

The matrices D, D^2, C, Λ and I_M in Equation (96) are the same as those defined for Equation (73). The matrix W contains the complex spectral coefficients W_{mn} of the axial velocity.

The spectral form of the boundary conditions can be written as:

$$\sum_{n=0}^{N} W_{R,mn} = \beta_{R,m} \tag{97}$$

$$\sum_{n=0}^{N} (-1)^n W_{R,mn} = \alpha_{R,m} \tag{98}$$

$$\sum_{n=0}^{N} W_{I,mn} = \beta_{I,m} \tag{99}$$

$$\sum_{n=0}^{N} (-1)^n W_{I,mn} = \alpha_{I,m} \tag{100}$$

for $-M/2 \leq m \leq M/2 - 1$.

Adding and subtracting Equations (97) and (98) we get:

$$\sum_{n=0,\ n\ even}^{N} W_{R,mn} = \frac{1}{2}(\beta_{R,m} + \alpha_{R,m}) = \eta_{R,m} \tag{101}$$

$$\sum_{n=0,\ n\ odd}^{N} W_{R,mn} = \frac{1}{2}(\beta_{R,m} - \alpha_{R,m}) = \theta_{R,m} \tag{102}$$

Adding and subtracting Equations (99) and (100) we get:

$$\sum_{n=0,\ n\ even}^{N} W_{I,mn} = \frac{1}{2}(\beta_{I,m} + \alpha_{I,m}) = \eta_{I,m} \tag{103}$$

$$\sum_{n=0,\ n\ odd}^{N} W_{I,mn} = \frac{1}{2}(\beta_{I,m} - \alpha_{I,m}) = \theta_{I,m} \tag{104}$$

for $-M/2 \leq m \leq M/2 - 1$.

In to the matrix Equation (96) are substituted Equations (102) and (104) to eliminate the complex coefficients $W_{m,N-1}$ and Equations (101) and (103) to eliminate the complex coefficients $W_{m,N}$, for $-M/2 \leq m \leq M/2-1$. Subsequently we obtain the matrix equation

$$W(B + B^2C) + \left(\Lambda - \frac{Re}{\Delta t} I_M\right) WC = f \tag{105}$$

The matrices C, B, B^2 and I_M are the same as those defined for Equation (82). The matrix f has real and imaginary components

$$f_R = F_R - Q_R - S_R C \tag{106}$$

and

$$f_I = F_I - Q_I - S_I C \tag{107}$$

where Q and S are $M \times (N-1)$ matrices with components

$$Q_{R,mn} = \begin{cases} \frac{2(N-1)}{c_n}\theta_{R,m} & \text{for } n \text{ even} \\ \frac{2N}{c_n}\eta_{R,m} & \text{for } n \text{ odd} \end{cases} \tag{108}$$

$$Q_{I,mn} = \begin{cases} \frac{2(N-1)}{c_n}\theta_{I,m} & \text{for } n \text{ even} \\ \frac{2N}{c_n}\eta_{I,m} & \text{for } n \text{ odd} \end{cases} \tag{109}$$

$$S_{R,mn} = \begin{cases} \frac{N(N^2-n^2)}{c_n}\eta_{R,m} & \text{for } n \text{ even} \\ \frac{(N-1)((N-1)^2-n^2)}{c_n}\theta_{R,m} & \text{for } n \text{ odd} \end{cases} \tag{110}$$

$$S_{I,mn} = \begin{cases} \frac{N(N^2-n^2)}{c_n}\eta_{I,m} & \text{for } n \text{ even} \\ \frac{(N-1)((N-1)^2-n^2)}{c_n}\theta_{I,m} & \text{for } n \text{ odd} \end{cases} \tag{111}$$

Equation (105) represents a system with $M \times (N-1)$ equations in the $M \times (N-1)$ complex unknowns, W_{mn}, determined from

$$W_{R,k} = f_{R,k}\left[B + B^2C + \left(\lambda_k - \frac{Re}{\Delta t}\right) I_{N-1}C\right]^{-1} \tag{112}$$

$$W_{I,k} = f_{I,k}\left[B + B^2C + \left(\lambda_k - \frac{Re}{\Delta t}\right) I_{N-1}C\right]^{-1} \tag{113}$$

for $-M/2 \le k \le M/2-1$, where $W_{R,k}$, $W_{I,k}$ and $f_{R,k}$, $f_{I,k}$ are the k^{th} row of the real and imaginary component elements of W and f respectively, and λ_k is the k^{th} diagonal element of matrix Λ. I_{N-1} is the $(N-1)\times(N-1)$ identity matrix. Once the W_{mn} are calculated for $-M/2 \le m \le M/2-1$ and $0 \le n \le N-2$, the W_{mn} for $-M/2 \le m \le M/2-1$ and $n = N-1, N$ can be determined using Equations (101) to (104). A Fourier-Chebyshev inverse transform of W_{mn} will give the solution for $W(z,r)$.

5.4 Preprocessing calculations

The matrices D, D^2, C and C^2 are calculated once in a pre-processing step. The matrices B and B^2 are calculated once for Dirichlet boundary conditions and once for Neumann boundary conditions in a pre-processing step.

Then we calculate

(1) the M inversions $[B + (B^2 + \lambda_k I_{N-1})C]^{-1}$ for the Poisson solver,

(2) the M inversions $[BC+B^2C^2-I_{N-1}+\left(\lambda_k-\frac{Re}{\Delta t}\right)I_{N-1}C^2]^{-1}$ for the Helmholtz solver for the radial and azimuthal components of velocity, and

(3) the M inversions $[B+B^2C+\left(\lambda_k-\frac{Re}{\Delta t}\right)I_{N-1}C]^{-1}$ for the Helmholtz solver for the axial component of velocity,

all done once, in a preprocessing step.

5.5 Numerical tests

The code for Taylor vortex flow was validated by comparison of exponential growth rates and velocity profiles against the published results of other researchers.

5.5.1 Comparison of growth rates

We compared our results for the exponential growth rate of a Taylor vortex flow to that recorded by Marcus (1984a). The parameters in the case studied were $\eta = 0.5$, $\mu = 0$, $Re = 74.924$ and $\Gamma = \lambda = 1.9877208$. The critical Reynolds number from linear theory is $Re_{crit} = 68.225$, as determined by Chandrasekhar (1961). The corresponding exponential growth rate computed by Marcus was $\sigma = 0.035636$.

The growth rate was calculated using the radial component of velocity evaluated at the centre of the domain, $u_r(t)$, and

$$\sigma = \frac{1}{\Delta t}\log_e(u_r(t+\Delta t)/u_r(t)) \tag{114}$$

where the velocity was measured in the linear stage of growth of the axisymmetric mode.

The initial conditions that were used were equal to the Couette flow plus a random perturbation of the order 1.0×10^{-4}.

Consider the relations

$$u_r = \frac{\partial \psi}{\partial z} \tag{115}$$

and

$$u_z = -\frac{1}{r+\gamma}\frac{\partial((r+\gamma)\psi)}{\partial r} \tag{116}$$

where $\psi(z,r)$ is the streamfunction. We can write the Helmholtz equation

$$(r+\gamma)\frac{\partial\psi}{\partial r} + (r+\gamma)^2\frac{\partial^2\psi}{\partial r^2} + (r+\gamma)^2\frac{\partial^2\psi}{\partial z^2} - \psi = (r+\gamma)^2\left[\frac{\partial u_r}{\partial z} - \frac{\partial u_z}{\partial r}\right] \tag{117}$$

to be solved subject to Dirichlet boundary conditions of $\psi = 0$ at $r = \pm 1$ and periodic boundary conditions in z. A Tau method was used to solve this Helmholtz equation, of the type described in Section 5.3.4 (and setting $Re = 0$ since the term with the factor $Re/\Delta t$ in Equation (70) does not play a role in Equation (117)).

The interpolation form of the Fourier-Chebyshev approximation to streamfunction:

$$\psi(z,r) = \sum_{m=-M/2}^{M/2-1}\sum_{n=0}^{N}\psi_{mn}T_n(r)\exp(imz) \tag{118}$$

was used to calculated ψ for a finer grid variation in z and r, so that a smoother streamline plot could be obtained.

In Figure 5.1, the steady state solution is shown in the form of a velocity vector plot for a 32×33 grid and $\Delta t = 0.1$. In Figure 5.2 is shown a graph of the streamfunction. Coles (1965) described Taylor vortex flow as a kind of gyroscopic precession in the fluid. In Figure 5.3 is a three-dimensional perspective view along the axial direction, showing the precessional nature of the particle paths traced by the moving fluid. The paths spiral around a toroidal surface.

The code took about 7.5 CPU minutes for 1500 timesteps (i.e. 0.3 CPU seconds per timestep) for a 16×17 grid and 39.5 CPU minutes for 1500 timesteps (i.e. 1.58 CPU seconds per timestep) for a 32×33 grid. These values are for an SGI R3000 Workstation.

We considered different operator splitting schemes of order (J_e, J_p, J_i) for different values of Δt. Tables 5.1 to 5.4 demonstrate convergence to the result by Marcus as the order of time-accuracy of each fractional step is improved. There was virtually no improvement in our computed growth rates when finer grids of 32×33 was used, meaning that a 16×17

grid gave good spatial resolution for the test case considered.

Figure 5.4 shows that the (J_e, J_p, J_i) order schemes $(2, 0, 1)$, $(2, 1, 1)$ and $(2, 2, 1)$ effectively have first-order time-accuracy because the slope has a value of about one.

In Figure 5.4, the scheme $(2, 1, 2)$ has second-order time accuracy as the slope is about two. Solutions for larger timespacings were not possible for the $(2, 1, 2)$ scheme as numerical error in the form of temporal oscillations were present.

Karniadakis et al. (1991) showed that the use of the Crank-Nicolson scheme in the viscous step may lead to instabilities for large time steps. This type of instability is also referred to as a short-wave instability. They described its occurrence for an operator splitting spectral element application to two-dimensional Stokes Channel Flow and Grooved Channel Flow. The use of the unsymmetrically weighted approximation in the viscous step was found to introduce damping and resulted in a more stable scheme.

For his applications to three-dimensional Taylor-Couette flow, Marcus (1984a) used a Backward-Euler approximation in the viscous step rather than a Crank-Nicolson method to avoid what he describes as a numerical neutrally stable oscillation that can occur at large wavenumbers. He reports that the final accuracy will be of the order $O((\Delta t)^2,\ \Delta t/Re)$ where Re is the Reynolds number. However, since his calculations were done for values of $Re > 100$ his method was then effectively second order. For smaller Reynolds numbers the $O(\Delta t/Re)$ error would especially become more significant compared to the $O((\Delta t)^2$ error for a Backward-Euler scheme.

We now consider a higher order scheme which can be varied between the $(2, 1, 1)$ scheme and the $(2, 1, 2)$ scheme. As discussed in Section 5.2, this can be achieved by using a weighted approximation over two time steps for the viscous terms with a weighting factor θ, henceforth referred to as a θ-method. In Table 5.5 a summary of results is presented for σ using a scheme with J_e=2, J_p=1 and a θ-method for the viscous terms. The accuracy improved as θ was reduced from the value $\theta = 0.5$, but for values close to $\theta = 0$ the time dependent solution exhibited temporal oscillations.

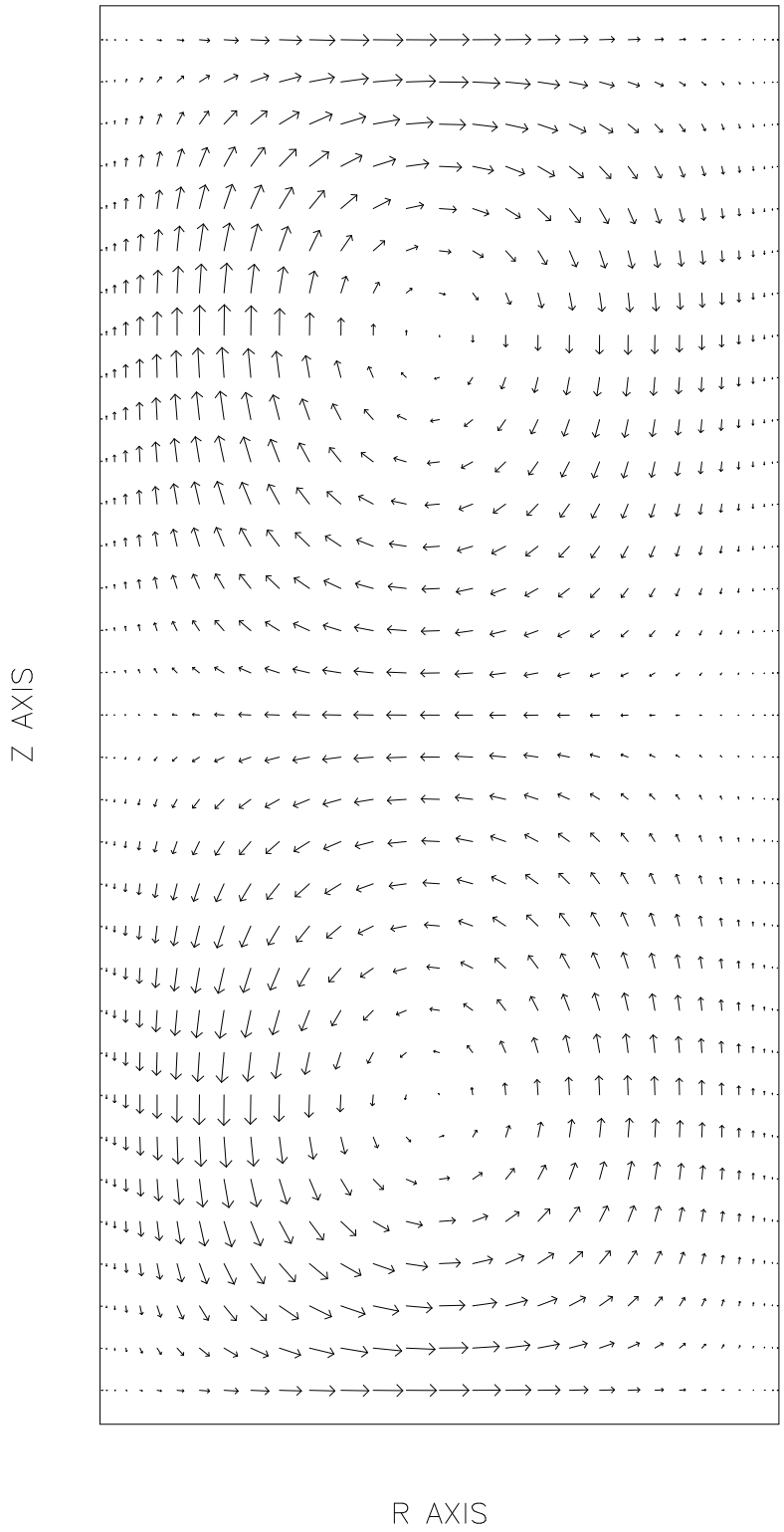

Figure 5.1: Velocity vectors using a 32×33 grid and $\Delta t = 0.1$.

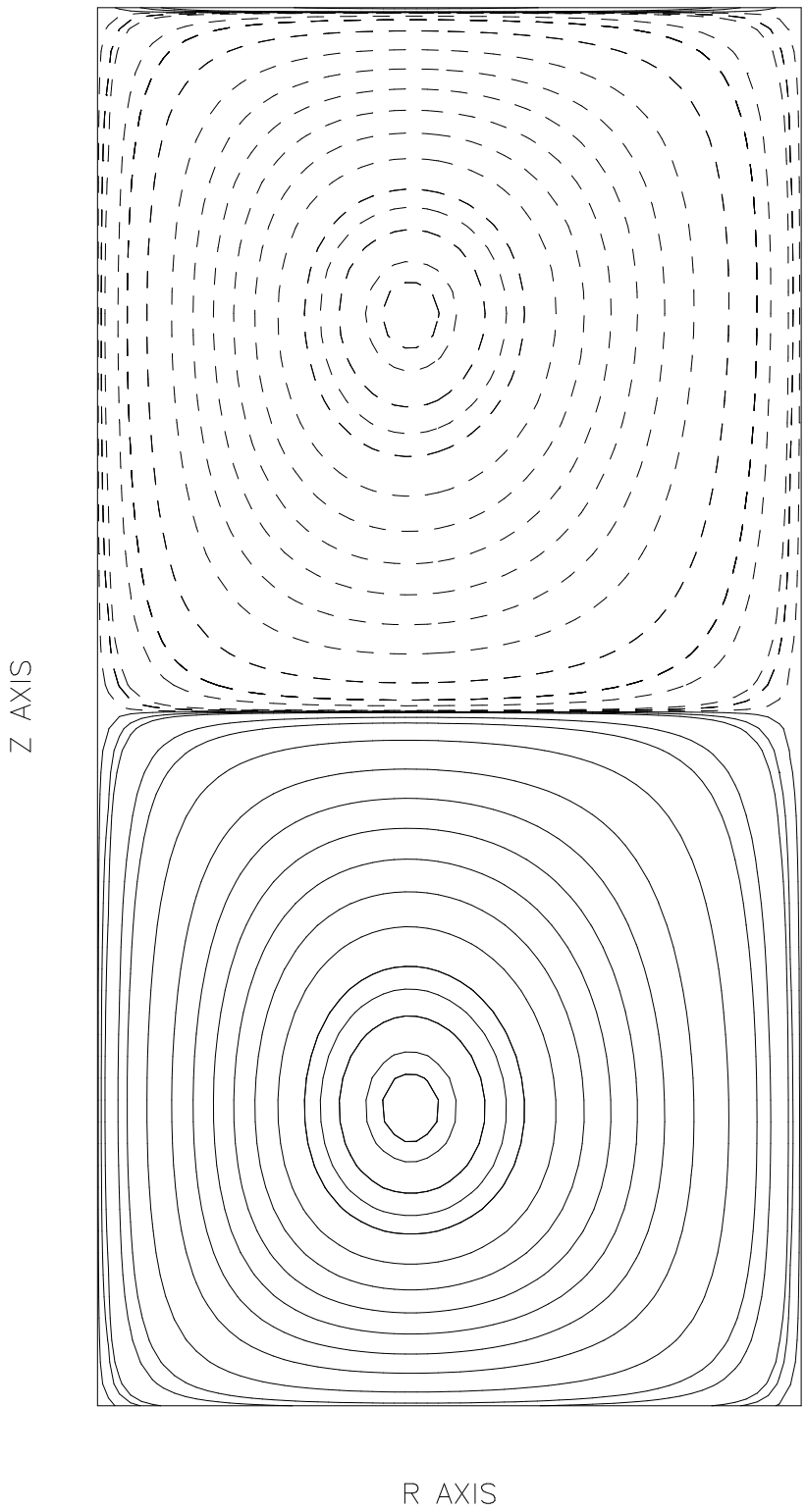

Figure 5.2: Streamfunction plot for a 32×33 grid and $\Delta t = 0.1$.

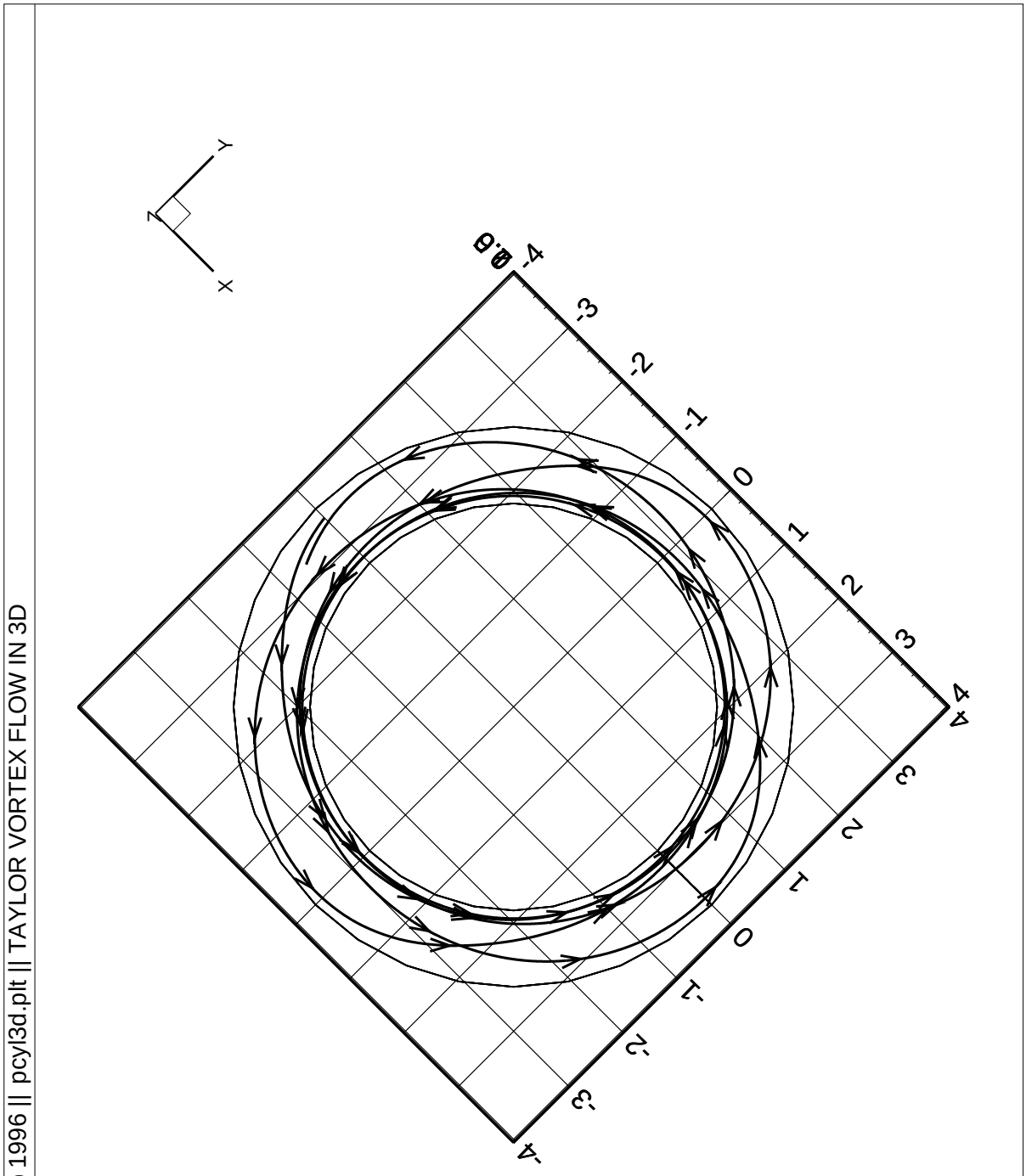

Figure 5.3: View of particle paths viewed along the axial direction showing precessional motion.

J_e	2	2	2
J_p	0	1	2
J_i	1	1	1
σ for 16×17 grid	0.069351	0.033320	0.032980

Table 5.1: Results for $\Delta t = 1.0$.

J_e	2	2	2	2	2
J_p	0	1	2	1	2
J_i	1	1	1	2	2
σ for 16×17 grid	0.040518	0.035333	0.035329	0.035649	0.035644
σ for 32×33 grid		0.035332	0.035328		

Table 5.2: Results for $\Delta t = 0.1$.

J_e	2	2	2
J_p	0	1	2
J_i	1	1	1
σ for 16×17 grid	0.036141	0.035612	0.035613

Table 5.3: Results for $\Delta t = 0.01$.

J_e	2	2
J_p	0	0
J_i	1	1
Δt	0.005	0.001
σ for 16×17 grid	0.035874	
σ for 32×33 grid		0.035695

Table 5.4: Other results.

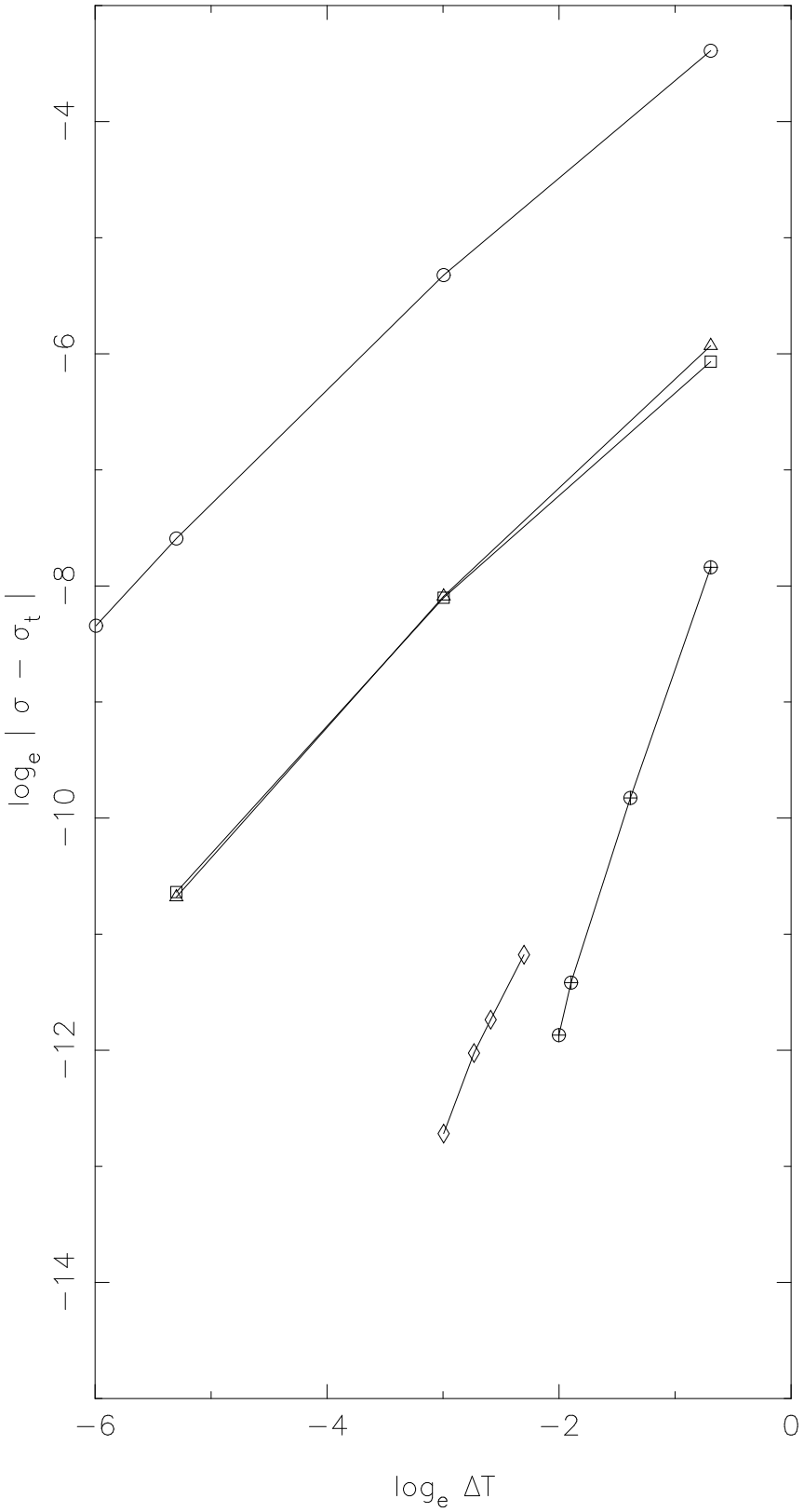

Figure 5.4: Time-accuracy of different operator splitting schemes.

First-order: ◯ : (2,0,1), □ : (2,1,1), △ : (2,2,1).

Second-order: ◇ : (2,1,2), ⊕ : (2,1,$\theta = 0.0125$).

Figure 5.5 shows how the size of the temporal oscillations increased as θ approached zero, making estimates of the growth rate unreliable for those cases. This result suggests that an optimum value of θ exists which gives sufficiently high accuracy and a tolerable level of stability.

θ	0	0.001	0.005	0.0125	0.025
J_i	2				
σ	oscillates	oscillates	0.035640	0.035635	0.035628
θ	0.05	0.1	0.2	0.4	0.5
J_i					1
σ	0.035616	0.035585	0.035521	0.035395	0.035332

Table 5.5: Results for σ for a 32×33 grid, $\Delta t = 0.05$ and different values of θ. The value by Marcus was 0.035636.

In Figure 5.4, the scheme $(2, 1, \theta = 0.0125)$ has second-order time-accuracy. Therefore, with an appropriate choice of θ one can obtain second-order time-accuracy for timespacings which are larger than those possible from using a $(2, 1, 2)$ scheme.

From Karniadakis et al. (1991), if the nonlinear terms are expressed as

$$\vec{N}(\vec{u}) = -\frac{1}{2}[(\vec{u}.\nabla)\vec{u} + \nabla.(\vec{u}\vec{u})] \qquad (= -(\vec{u}.\nabla)\vec{u}) \tag{119}$$

this is known as a skew-symmetric form. The expression $\nabla.(\vec{u}\vec{u})$ is in dyadic tensor notation. The non-linear terms in this case become

$$N_r(\vec{u}) = -\frac{1}{2}\left[u_r\frac{\partial u_r}{\partial r} + u_z\frac{\partial u_r}{\partial z} - 2\frac{{u_\phi}^2}{r+\gamma} + \frac{u_r^2}{r+\gamma} + \frac{\partial(u_r^2)}{\partial r} + \frac{\partial(u_r u_z)}{\partial z}\right] \tag{120}$$

$$N_\phi(\vec{u}) = -\frac{1}{2}\left[u_r\frac{\partial u_\phi}{\partial r} + u_z\frac{\partial u_\phi}{\partial z} + 3\frac{u_r u_\phi}{r+\gamma} + \frac{\partial(u_r u_\phi)}{\partial r} + \frac{\partial(u_\phi u_z)}{\partial z}\right] \tag{121}$$

$$N_z(\vec{u}) = -\frac{1}{2}\left[u_r\frac{\partial u_z}{\partial r} + u_z\frac{\partial u_z}{\partial z} + \frac{u_r u_z}{r+\gamma} + \frac{\partial(u_r u_z)}{\partial r} + \frac{\partial(u_z^2)}{\partial z}\right] \tag{122}$$

The latter terms in Equations (120) to (122) are kept in conservative form. The skew-symmetric form of the nonlinear terms is often preferred because it minimizes aliasing effects. The nonlinear terms were expressed in skew-symmetric form and some of the above runs were repeated. No difference was found between these results and the corresponding ones in Table 5.5, indicating that aliasing is not a problem with the code. Aliasing error depends on Re. Here, the discrete system is still subject to aliasing error, but for small Re the affected modes are strongly damped.

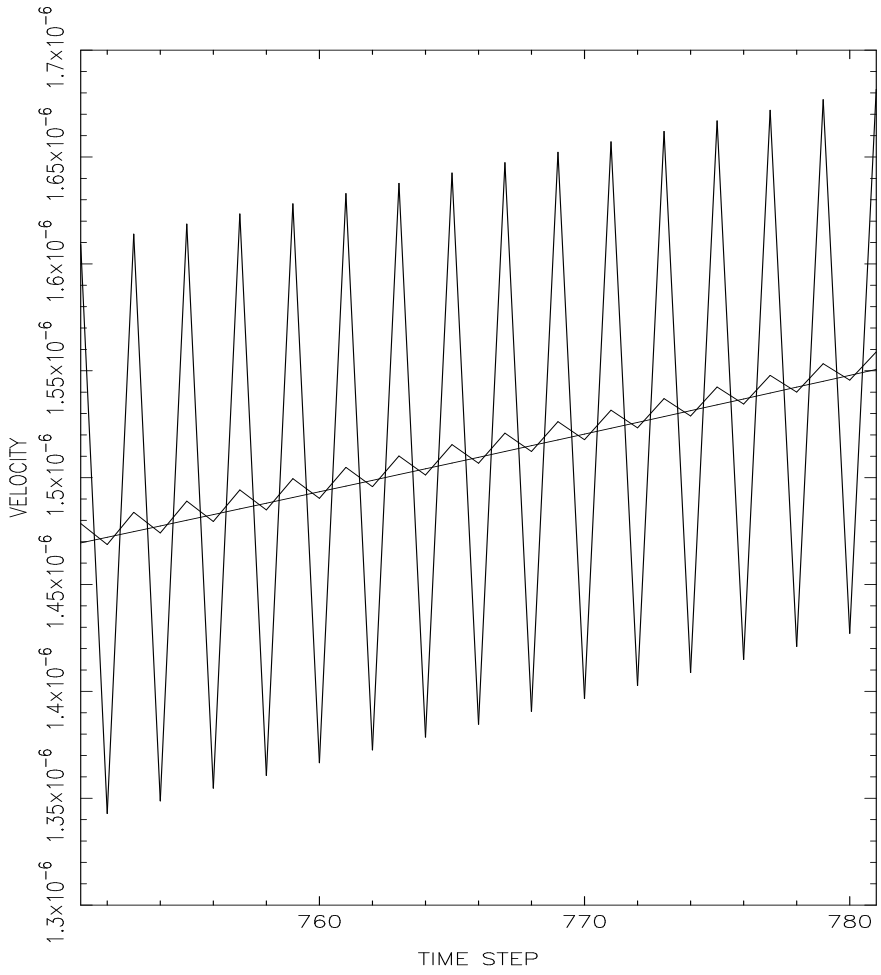

Figure 5.5: The computed velocity during a specific time step interval in the initial exponential growth stage of the Taylor vortices, for three values of θ. The velocity was taken as the radial velocity in the middle of the domain. The straight line is for $\theta = 0.005$. The greatest oscillation occurred for $\theta = 0$. The smaller oscillation occurred for $\theta = 0.001$.

A test was also made for $\Gamma = \lambda = 2.026834$, $\eta = 0.5$, $\mu = 0.11765$ and $Re = Re_{crit} = 82.557$ which has the theoretical value of $\sigma_t = 0$. Using a 16×17 grid with $\Delta t = 0.1$ and $\theta = 0.5$ the result was $\sigma = 0.000106$. A repeat run with a 32×33 grid gave the same result.

Another test was made for $\Gamma = \lambda = 2.008691$, $\eta = 0.95$, $\mu = 0$ and $Re = Re_{crit} = 184.99$ which has the theoretical value of $\sigma_t = 0$. The result by Marcus was $\sigma_t = 5.16 \times 10^{-4}$. A run with a 16×17 grid, $\Delta t = 0.1$ and $\theta = 0.5$ gave $\sigma = 3.32 \times 10^{-6}$ A 32×33 grid gave the same result.

The discrepancies between our results and the results by Marcus can be considered unimportant because they are much less than the three decimal place accuracy of our results.

5.5.2 Comparison of velocities

From Chandrasekhar (1961) the following information was taken: $\eta = 0.5$, $\mu = -0.363636$, $\kappa = 3.9$, $Re_{crit} = 91.55$. This example is for counter-rotating cylinders. Runs were done for $Re = 100$ and $\Gamma = \lambda = 2\pi/\kappa = 1.6110732$.

The velocity values of the steady state solution were compared to those obtained from an independent finite element code developed by Dr Mark Thompson. This code used a grid with 30×30 points and quadratic polynomials. The solution from this code is expected to be accurate to not more than about three decimal places in the velocity. Nevertheless, it will be used here to indicate whether or not the code developed for this thesis and described above gives a vastly different result.

For a 16×17 grid, $\Delta t = 0.1$ and $\theta = 0.5$ the velocity vector plot and streamline plot are shown in Figure 5.6. Figure 5.7 shows the velocity vector plot and streamline plot for a 32×33 grid, $\Delta t = 0.1$ and $\theta = 0.5$. Comparison of the streamline plots in Figures 5.6 and 5.7 indicates that good spatial resolution is attained with a 16×17 grid in the case being studied.

Firstly, some observations are made. it can be seen in Figure 5.6 that there is a pair

of counter-rotating vortices and a pair of much weaker counter-rotating vortices separated by a curved nodal surface. This nodal surface is actually only vertical when Re is very close to Re_{crit}, as observed by Taylor (1923). The curved nodal surface approaches a vertical nodal surface as the Reynolds number approaches the critical Reynolds number from above.

In the streamline plots, the dashed curves represent clockwise rotating vortices and solid curves represent anticlockwise rotating vortices. Thus, there are essentially two types of boundaries, the strong outflow jet boundary (at for example $z = 0$ and $z = \Gamma$) and the weaker inflow jet boundary (at for example $z = \Gamma/2$).

On the left hand sides of Figures 5.8, 5.9 and 5.10 we plot the axial velocity through a horizontal line at a value of z corresponding to 0.50124, the axial span of a clockwise rotating Taylor Vortex cell. On the right hand sides of Figures 5.8, 5.9 and 5.10 we plot the radial velocity through the vertical centreline. In Figure 5.8 we use a 16×17 grid, $\Delta t = 0.1$ and $\theta = 0.5$. In Figure 5.9 a 32×33 grid, $\Delta t = 0.1$ and $\theta = 0.5$ are used. In Figure 5.10 a 16×17 grid, $\Delta t = 0.1$ and $\theta = 0.1$ are used. The circled points (representing results from the code developed here) appear to fit the curve (representing results from the finite element code) reasonably well. The circled points also appear to be consistently in the same location with respect to the curve for each of the three figures, indicating again that good spatial resolution can be attained with a 16×17 grid.

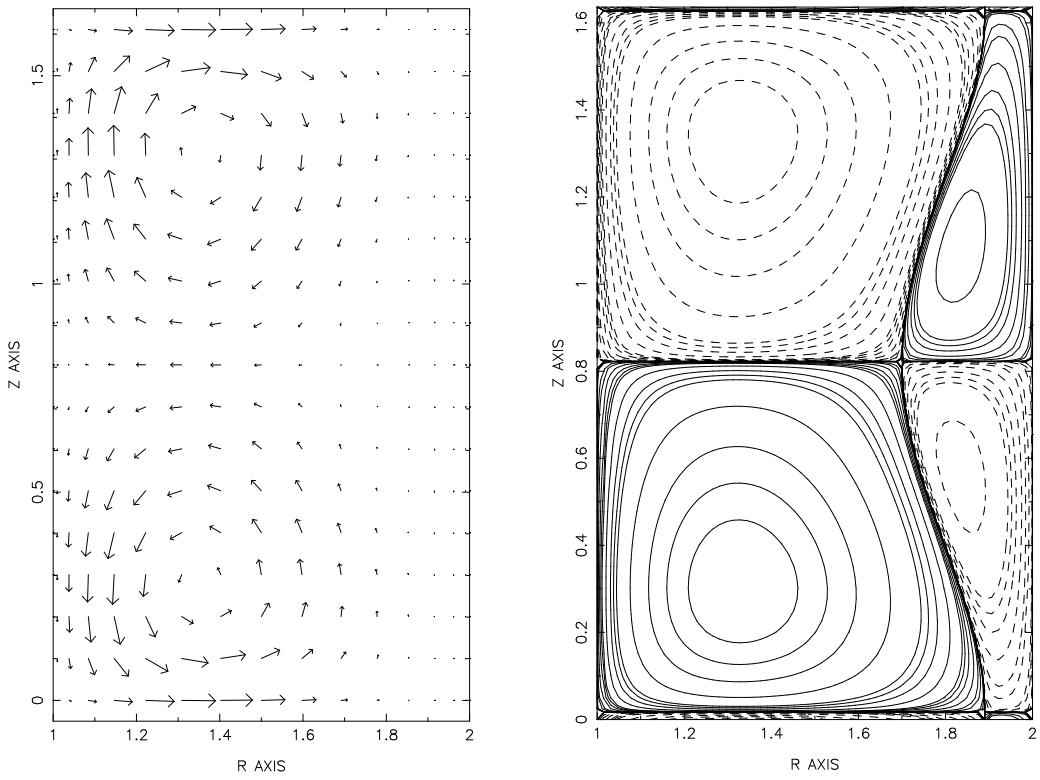

Figure 5.6: Velocity vectors and streamfunction. 16×17 grid, $\Delta t = 0.1$, $\theta = 0.5$

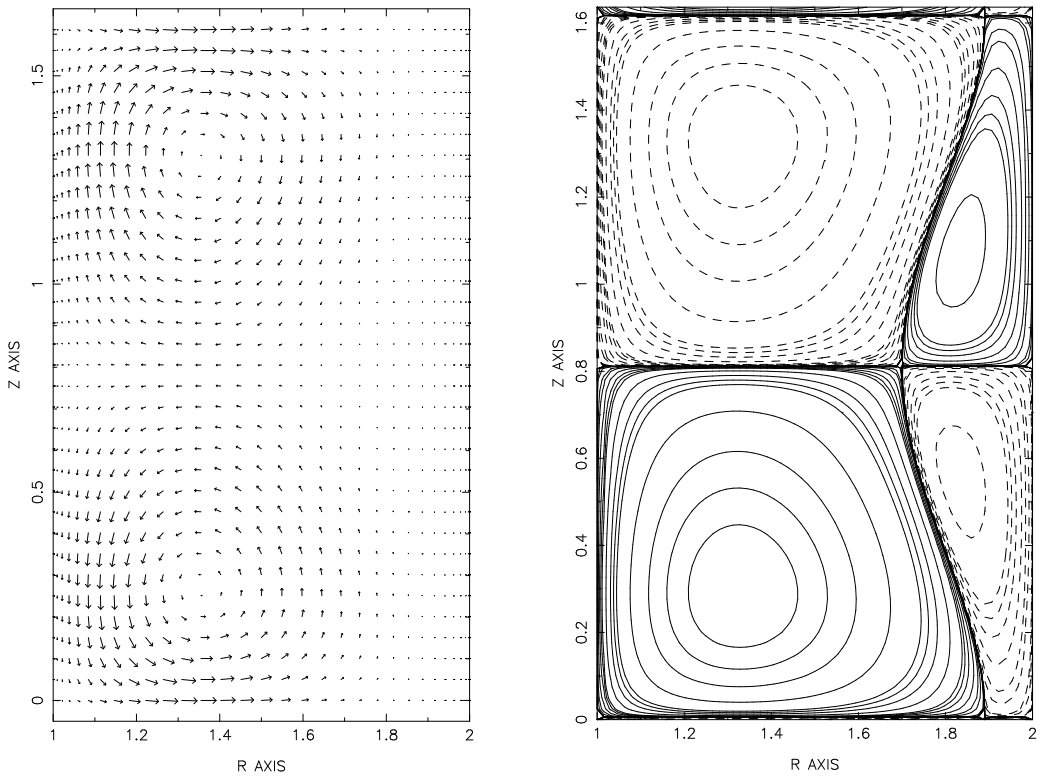

Figure 5.7: Velocity vectors and streamfunction. 32×33 grid, $\Delta t = 0.1$, $\theta = 0.5$

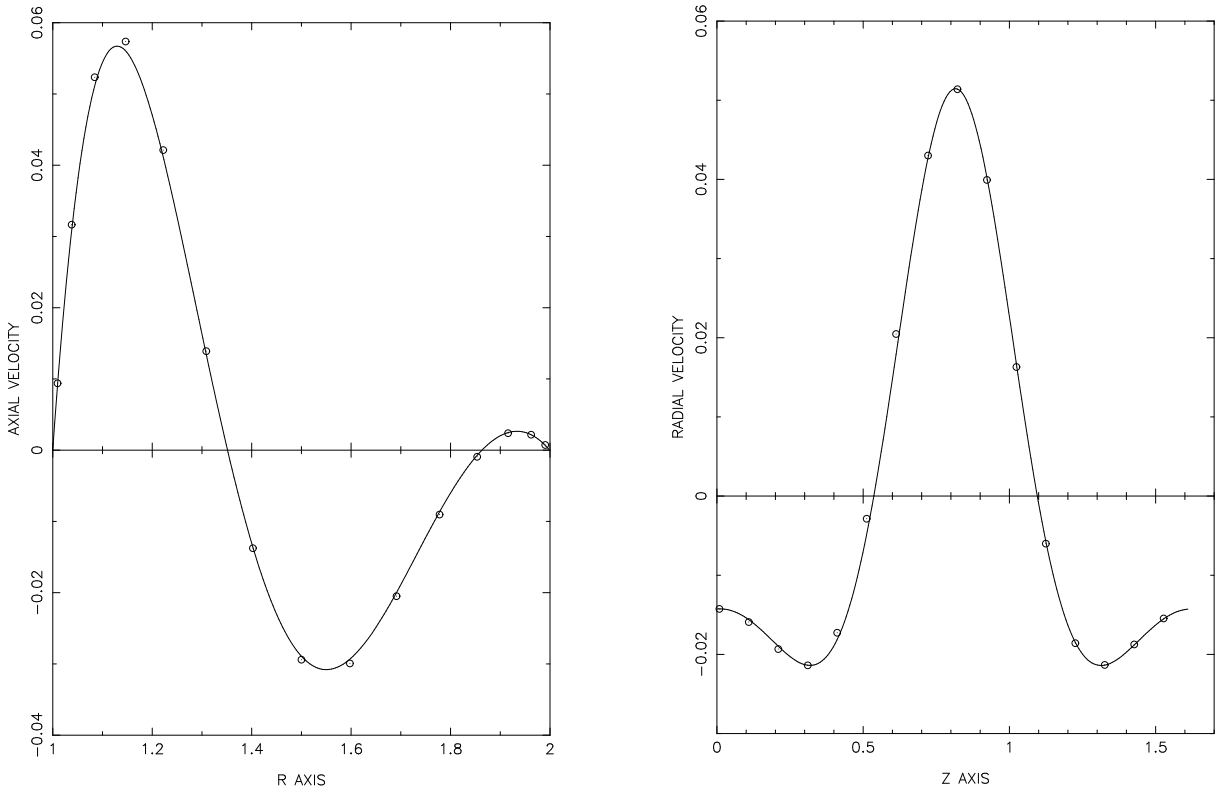

Figure 5.8: (Left) Axial velocity through a horizontal line at a value of z corresponding to 0.50124 the axial span of a clockwise rotating Taylor Vortex cell. (Right) Radial velocity through the vertical centreline. The circled points represent results from the spectral code developed here and the solid line represents results from a finite element code. Spectral code numerical paramters: 16×17 grid, $\Delta t = 0.1$ and $\theta = 0.5$

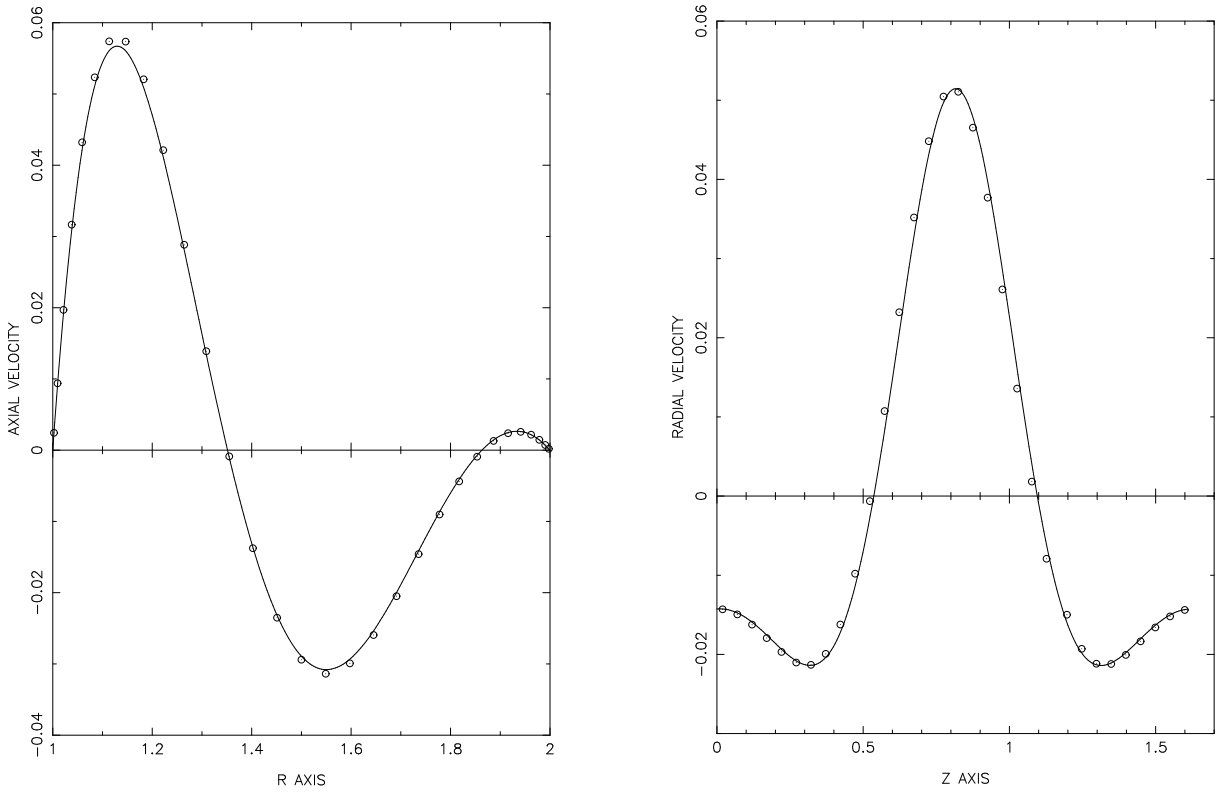

Figure 5.9: (Left) Axial velocity through a horizontal line at a value of z corresponding to 0.50124 the axial span of a clockwise rotating Taylor Vortex cell. (right) Radial velocity through the vertical centreline. The circled points represent results from the spectral code developed here and the solid line represents results from a finite element code. Spectral code numerical paramters: 32×33 grid, $\Delta t = 0.1$ and $\theta = 0.5$

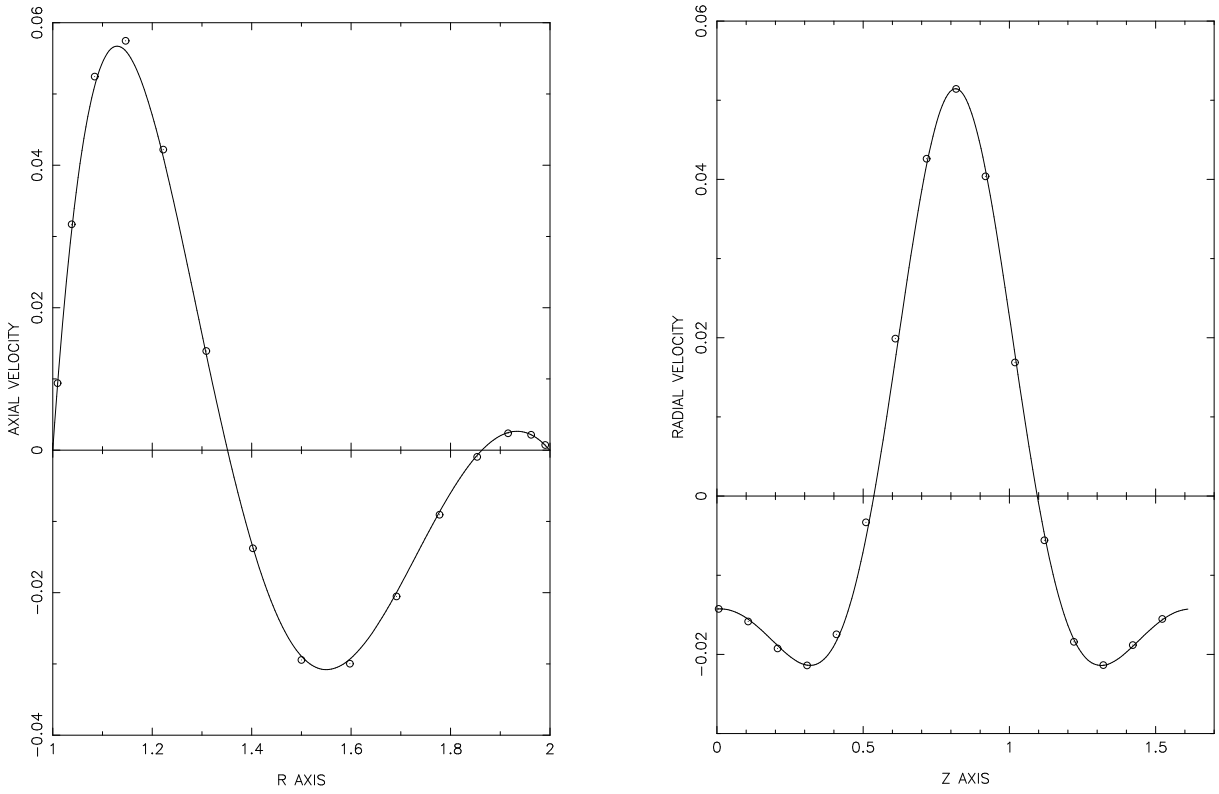

Figure 5.10: (Left) Axial velocity through a horizontal line at a value of z corresponding to 0.50124 the axial span of a clockwise rotating Taylor Vortex cell. (Right) Radial velocity through the vertical centreline. The circled points represent results from the spectral code developed here and the solid line represents results from a finite element code. Spectral code numerical paramters: 16×17 grid, $\Delta t = 0.1$ and $\theta = 0.1$

6 Behaviour Of The Amplitude Of The Modes

Consider the situation of an infinite aspect ratio where the outer cylinder is stationary. As described by Koschmieder (1993), the axial wavelength of the Taylor vortices depends on the rate at which the inner cylinder Reynolds number is increased from an initial subcritical value to a final supercritical value. If the final Reynolds number is moderately supercritical then for impulsive increases the selected wavelength is less than the critical wavelength predicted from linear stability theory. When the acceleration rate is decreased the selected wavelength increases and approaches the critical wavelength. This was illustrated by the sudden start and quasi-steady increase experiments of Burkhalter and Koschmieder (1974) in Figure 2.4. When the inner cylinder Reynolds number is increased at a sufficiently slow rate the selected wavelength is the critical wavelength.

Some fundamental questions about state selection for Taylor vortex flow were posed by Koschmieder (1993).

- An explanation is needed as to why the wavelength of supercritical axisymmetric vortices is independent of the Taylor number and equal to the critical wavelength when the Taylor number is increased slowly from subcritical values.

- Also, an explanation is needed as to why supercritical axisymmetric vortices can be nonunique.

To gain insight into the evolution of the amplitude of the axial modes with different ramp time, it was decided to simulate Taylor vortex flow numerically with a large aspect ratio. This allowed us to study the independent growth and subsequent nonlinear interaction of many discrete axisymmetric modes.

6.1 The numerical experiments

We considered an inner cylinder Reynolds number which was linearly increased in time from an initial subcritical value Re_i to a final supercritical value Re_f over a ramp time T, and then kept constant at Re_f. The value of Re_f was taken as only slightly in excess of

Re_c because the nonlinear behaviour is not as complicated and thus the nonlinear terms in the amplitude equations are easier to determine. In the example that will be considered, $Re_f/Re_c = \sqrt{2}$. A number of different simulations were conducted for fixed Re_i, Re_f and different T. In each simulation, initial conditions of circular Couette flow plus a random perturbation of the order 10^{-4} was applied. A random perturbation was applied because this is typical of what occurs in a physical experiment. The random number generation sequence was kept the same for each simulation to ensure that initial conditions were reproducible.

The nondimensional time, t, is related to the time in units of inner cylinder revolutions, t_{rev}, via

$$t_{rev} = \frac{1}{2\pi}\left(\frac{1}{\eta} - 1\right)\frac{Re(t)}{Re_i}t \tag{1}$$

where

$$Re(t) = \begin{cases} Re_i + \frac{Re_f - Re_i}{T}t & \text{if } t \leq T \\ Re_f & \text{if } t > T \end{cases} \tag{2}$$

In terms of inner cylinder revolutions, the ramp time is

$$T_{rev} = \frac{1}{2\pi}\left(\frac{1}{\eta} - 1\right)\frac{Re_f}{Re_i}T \tag{3}$$

We calculated the magnitude of the amplitude of each mode, $|A_\lambda(t)|$ from the Fourier transform of the radial component of velocity at the radial centre of the gap,

$$|A_\lambda(t)| = \sqrt{\hat{u}_r^2(r_c, m, t)_{real} + \hat{u}_r^2(r_c, m, t)_{imag}} \tag{4}$$

and the representation in terms of a discrete Fourier expansion together with the finite aspect ratio means that the allowable wavelengths are restricted to

$$\lambda = \Gamma/m \qquad \text{for} \qquad m = 1, ..., M/2 - 1 \tag{5}$$

where m is the axial Fourier index.

There was a slight discrepancy between the initial amplitude of the Fourier modes, centred at a value of about e^{-14} (or 8.3×10^{-7}), and the magnitude of the perturbation (10^{-4}). The random numbers were defined to lie between 0 and 1. So, the mean value of the perturbation was 5.0×10^{-5}, which was the amplitude of the $m = 0$ mode. The perturbation was not divergence free.

6.2 Input data

The following choice of parameter values was made: $\eta = 0.727$, $\mu = 0$, $Re_i = 70$, $Re_f = 116.67$. Koschmieder (1993) presented results of minimum critical Reynolds number and critical wavelength versus radius ratio. Using linear interpolation, the critical wavelength and Reynolds number were calculated to be $\lambda_c = 2.00286$ and $Re_{c,\lambda_c} = 82.79$ for radius ratio $\eta = 0.727$. The aspect ratio $\Gamma = 20.0286$ was set to be ten times larger than λ_c. This gave a wide range of possible modes and good definition of wavelengths near critical.

Using Equation (5), in the vicinity of λ_c we have the following allowed discrete wavelengths: 1.54066, 1.66905, 1.82078, 2.00286, 2.2254 which correspond to 13, 12, 11, 10 and 9 pairs of vortices within the domain respectively.

The numerical parameters were set to $M = 324$, $N = 33$ and $\Delta t = 0.1$. These parameters were chosen after extensive testing to ensure that they supplied sufficient spatial resolution. However, for the faster ramps Δt had to be reduced by up to an order of magnitude for a short initial period of time in the simulation. This was done to adequately resolve the initial stage of fast decay due to viscous damping.

6.3 Results and discussion

It is evident from Figure 6.1 that, for sudden starts, the amplitude of each mode did not begin to grow exponentially. There was a short initial period of time of decay of the modes. Liu and Chen (1973) attributed this initial decay to viscous damping. During this time the base flow, being the circular Couette flow, is unsteady. Once the the base flow

becomes steady the amplitude of the modes begin to grow exponentially.

In Figures 6.2 to 6.15 we plot $|A_\lambda(t)|$ for different ramp times T for five modes in the vicinity of the mode with the critical wavelength. The inset graphs in Figures 6.2 to 6.9 show a close-up of the region where the modes interact. Figures 6.13 to 6.15 show that λ_c is preferred for sufficiently long ramp times. In Figure 6.2, for sudden starts the preferred wavelength $\lambda = 1.66905$ is less than λ_c. The selected wavelength changes from 1.66905 to 1.82078 to 2.00286 for progressively longer ramp times. The wavelengths of these three Taylor vortex flow states lie within the Eckhaus stable band. This trend agrees with the observed behaviour from physical experiments reported by Koschmieder (1993).

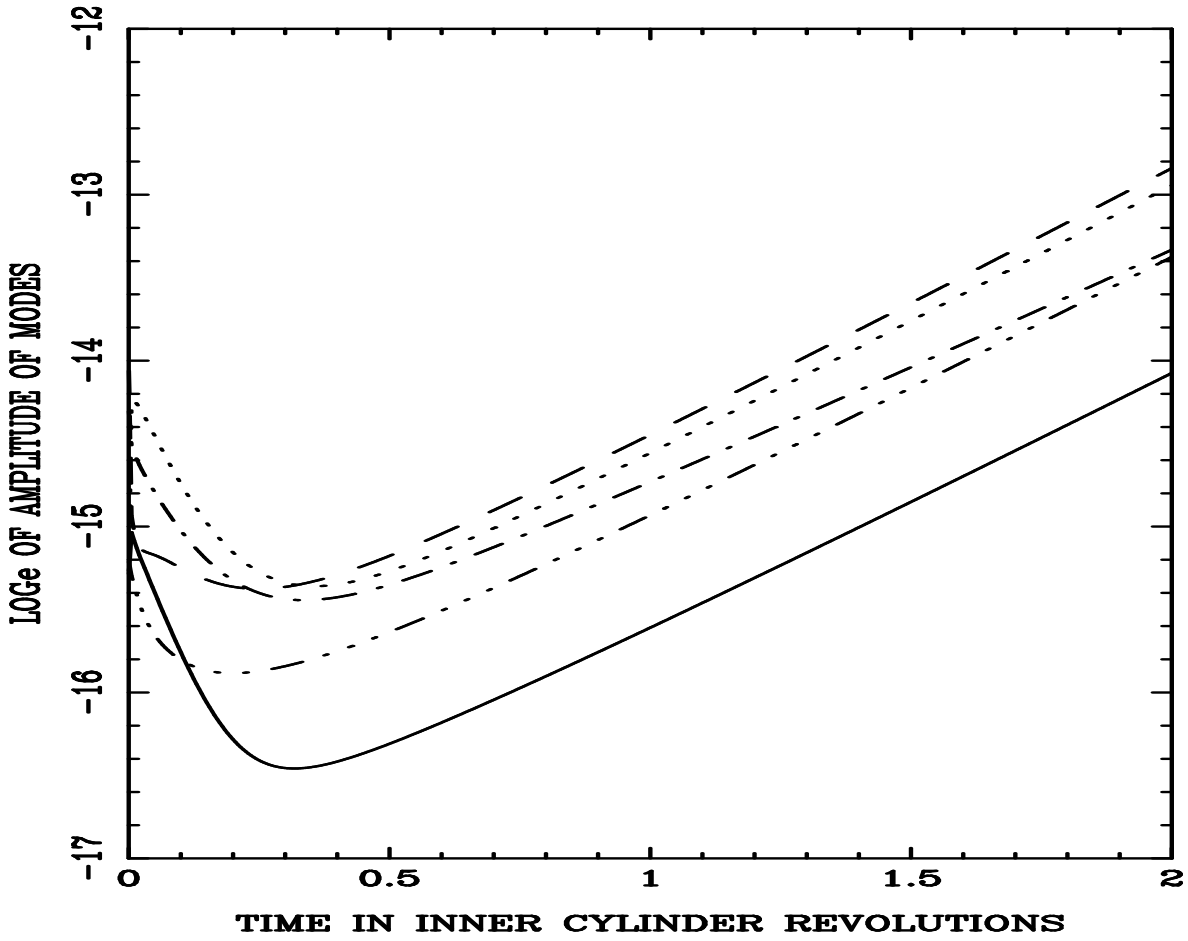

Figure 6.1: $|A_\lambda(t)|$ for sudden starts ($T = 0$).

Modes: $\cdot - \cdot - \cdot$ $\lambda = 2.2254$, ——— $\lambda_c = 2.00286$, $- - - -$ $\lambda = 1.82078$,

$\cdots\cdots\cdot$ $\lambda = 1.66905$, $- \cdots -$ $\lambda = 1.54066$

Simulations with different pseudo-random sequences had initial amplitudes for each mode which were different, centred at a value of about e^{-14} (or 8.3×10^{-7}). As a result, the behaviour of the amplitudes of the modes was different for different pseudo-random sequences. The ramp time to produce a changed preferred wavelength was different for different pseudo-random sequences.

In Figure 6.16 to 6.20 are plots of instantaneous growth rate versus instantaneous Reynolds number during the Reynolds number ramp for five different modes. The inset graphs show a close-up of the intersections on the Reynolds number axis. The effect due to the unsteady base flow is also noticeable for fast rates of increase in Re. This effect shows up as a deviation from the linear relationship between σ and Re. As the rate of increase of Re is slowed down, the base flow becomes steady earlier in terms of Reynolds number and this deviation less pronounced.

Figures 6.21 to 6.23 each have plots of the instantaneous growth rate versus instantaneous Reynolds number during the Reynolds number ramp for three different ramp times. For sufficiently slow rates of increase the σ versus Re profile converges to a straight line that starts from Re_i. This linear relationship between σ versus Re has a gradient and an Re intercept which is different for each mode. In the graphs for longer ramp times the points in the last portion of the Reynolds number ramp were not used because the modes interacted nonlinearly there.

Figures 6.21 to 6.23 for $T = 99.61$ demonstrate that, for sufficiently slow rates of increase of Re, the instantaneous growth rate at a particular Re during a ramp is equal to the growth rate when Re is held fixed at that particular value. The results by Eagles (1977) and Neitzel (1982), who studied the stability of unsteady circular Couette flow, indicate that this behaviour would gradually break down as the acceleration rate is increased to large values. As shown in Figures 6.21 to 6.23, the linear relationship between growth rate and Reynolds number is pushed more to the right of the Re axis. Hence, the instantaneous critical Reynolds numbers for each mode increase with larger acceleration rates, shown in the inset graphs of Figures 6.20, 6.19, 6.18 and 6.17. For example, Figure 6.20 shows that

when $T = 99.61$, the critical Reynolds number for λ_c is 82.8, agreeing with the result 82.79 from Koschmieder (1993), obtained by keeping the value of Re fixed. In contrast, Figure 6.17 shows that for $T = 4.98$ the instantaneous critical Reynolds number for λ_c is increased by about 3%.

With a grid size of 324×33, on an SGI R3000 the code took about 3.6 CPU seconds per time step. The total computation time to produce the results for Figure 6.15, for example was about 7.15 CPU hours.

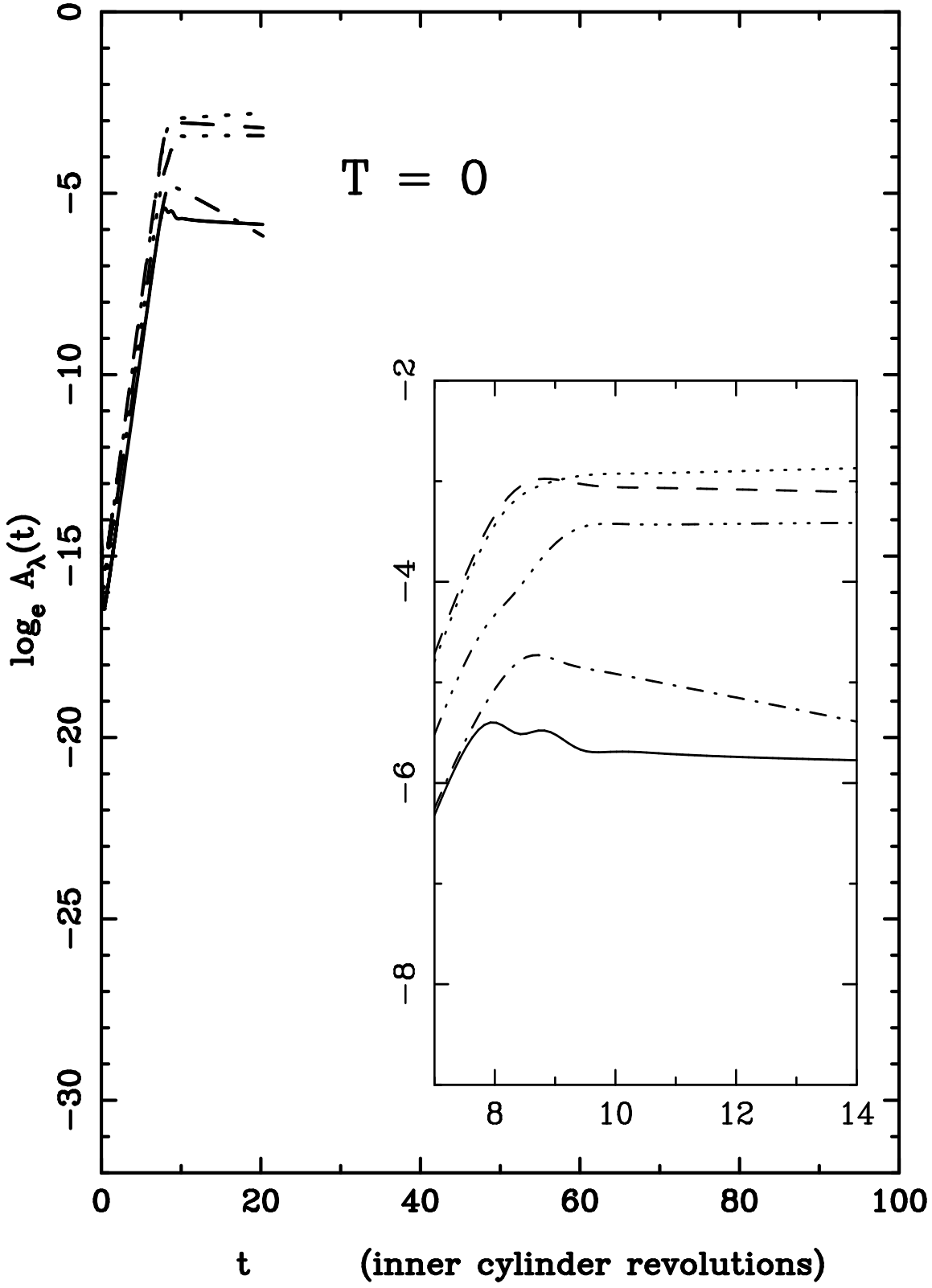

Figure 6.2: $A_\lambda(t)$ for ramp times $T = 0$. Modes: $\cdot - \cdot - \cdot$ $\lambda = 2.2254$, ———

$\lambda_c = 2.00286$, $- - - - \ \lambda = 1.82078$, $\cdots\cdots\cdot \ \lambda = 1.66905$, $- \cdots - \ \lambda = 1.54066$

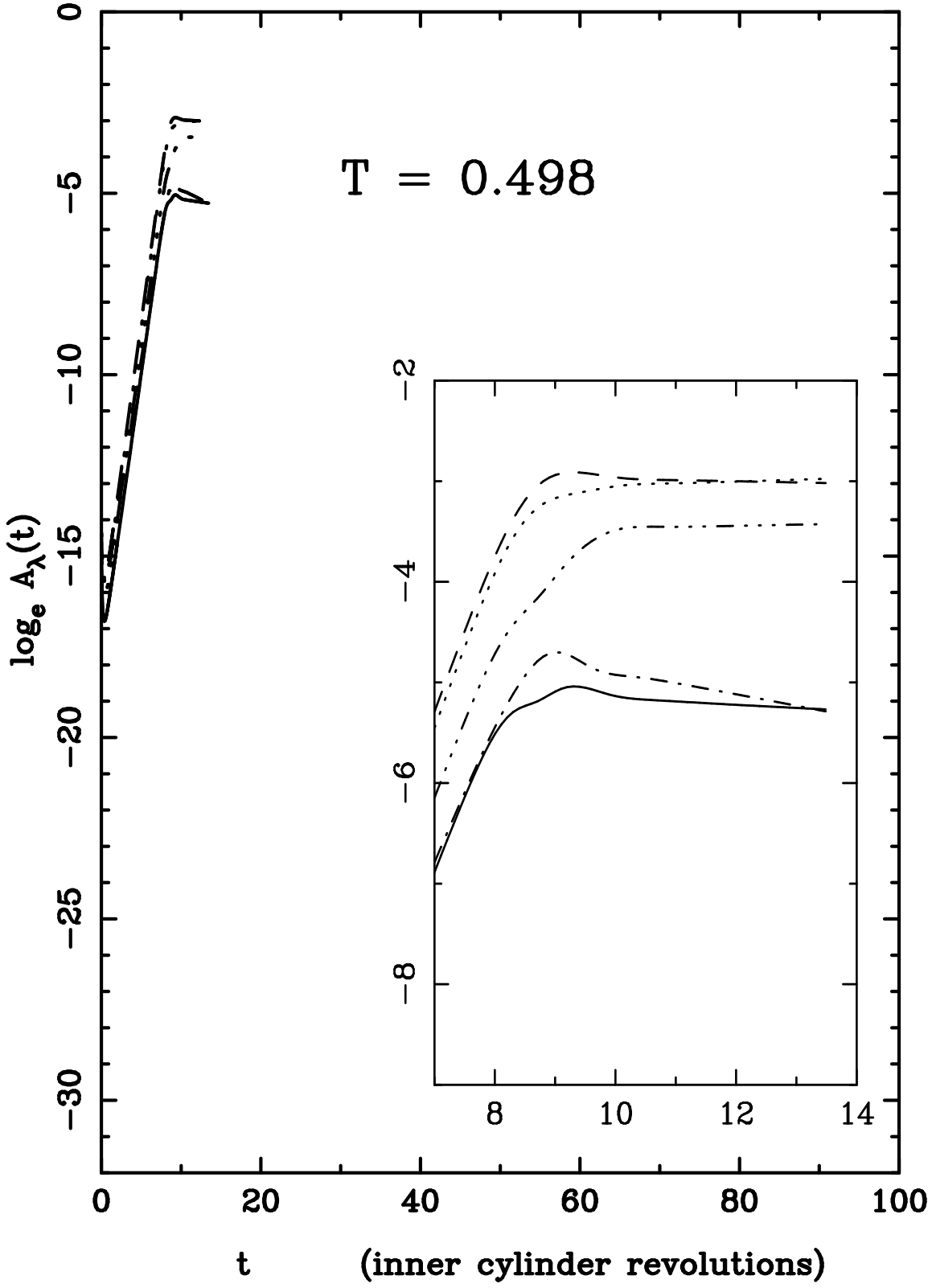

Figure 6.3: $A_\lambda(t)$ for ramp times $T = 0.498$. Modes: $\cdot - \cdot - \cdot$ $\lambda = 2.2254$, ———

$\lambda_c = 2.00286$, $- - - -$ $\lambda = 1.82078$, $\cdots\cdots\cdot$ $\lambda = 1.66905$, $- \cdots -$ $\lambda = 1.54066$

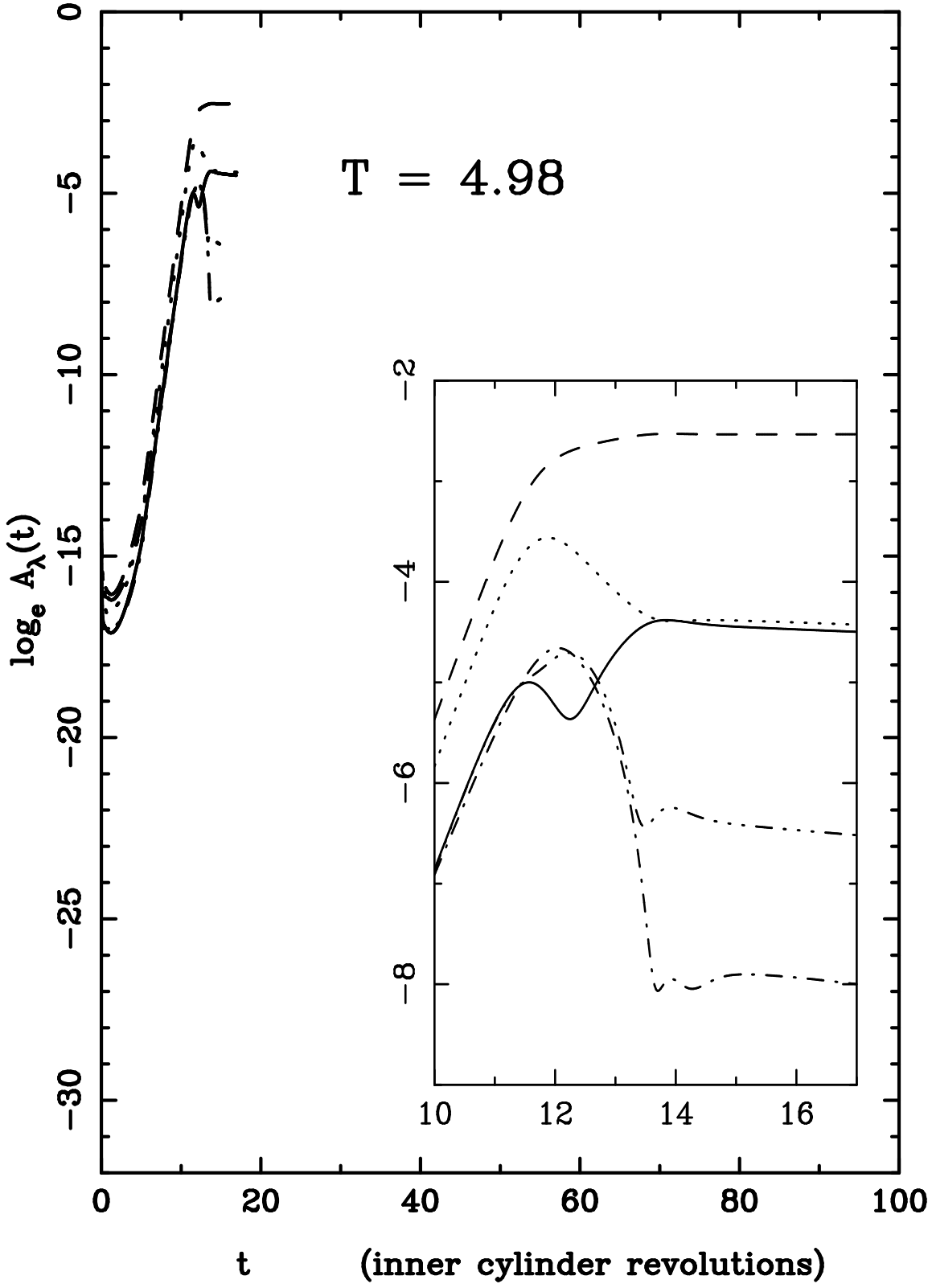

Figure 6.4: $A_\lambda(t)$ for ramp times $T = 4.98$. Modes: · – · – · $\lambda = 2.2254$, ———

$\lambda_c = 2.00286$, $- - - -$ $\lambda = 1.82078$, $\cdots\cdots\cdot$ $\lambda = 1.66905$, $- \cdots -$ $\lambda = 1.54066$

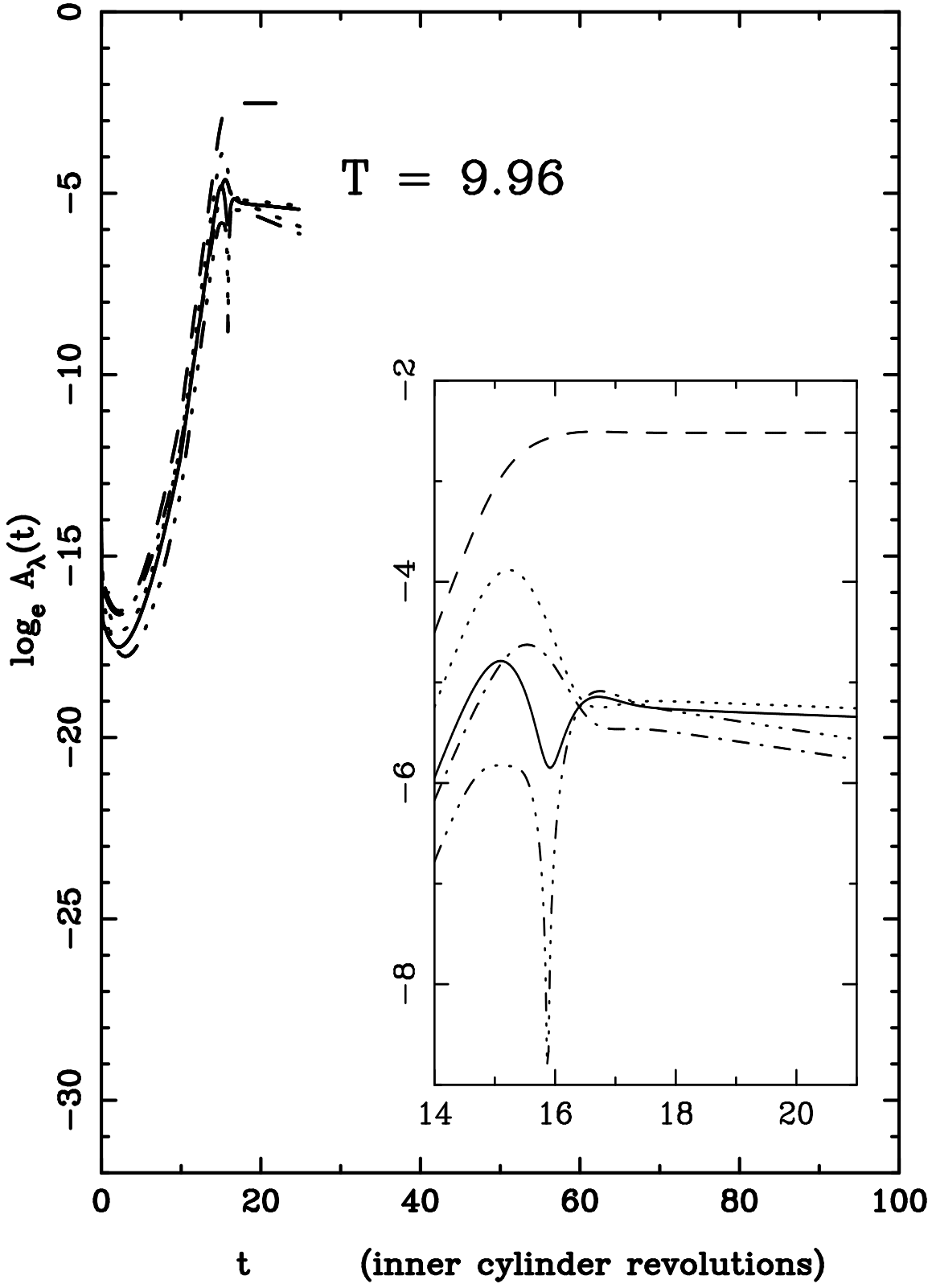

Figure 6.5: $A_\lambda(t)$ for ramp times $T = 9.96$. Modes: $\cdot - \cdot - \cdot$ $\lambda = 2.2254$, ———

$\lambda_c = 2.00286$, $- - - - \ \lambda = 1.82078$, $\cdots\cdots\cdot \ \lambda = 1.66905$, $- \cdots - \ \lambda = 1.54066$

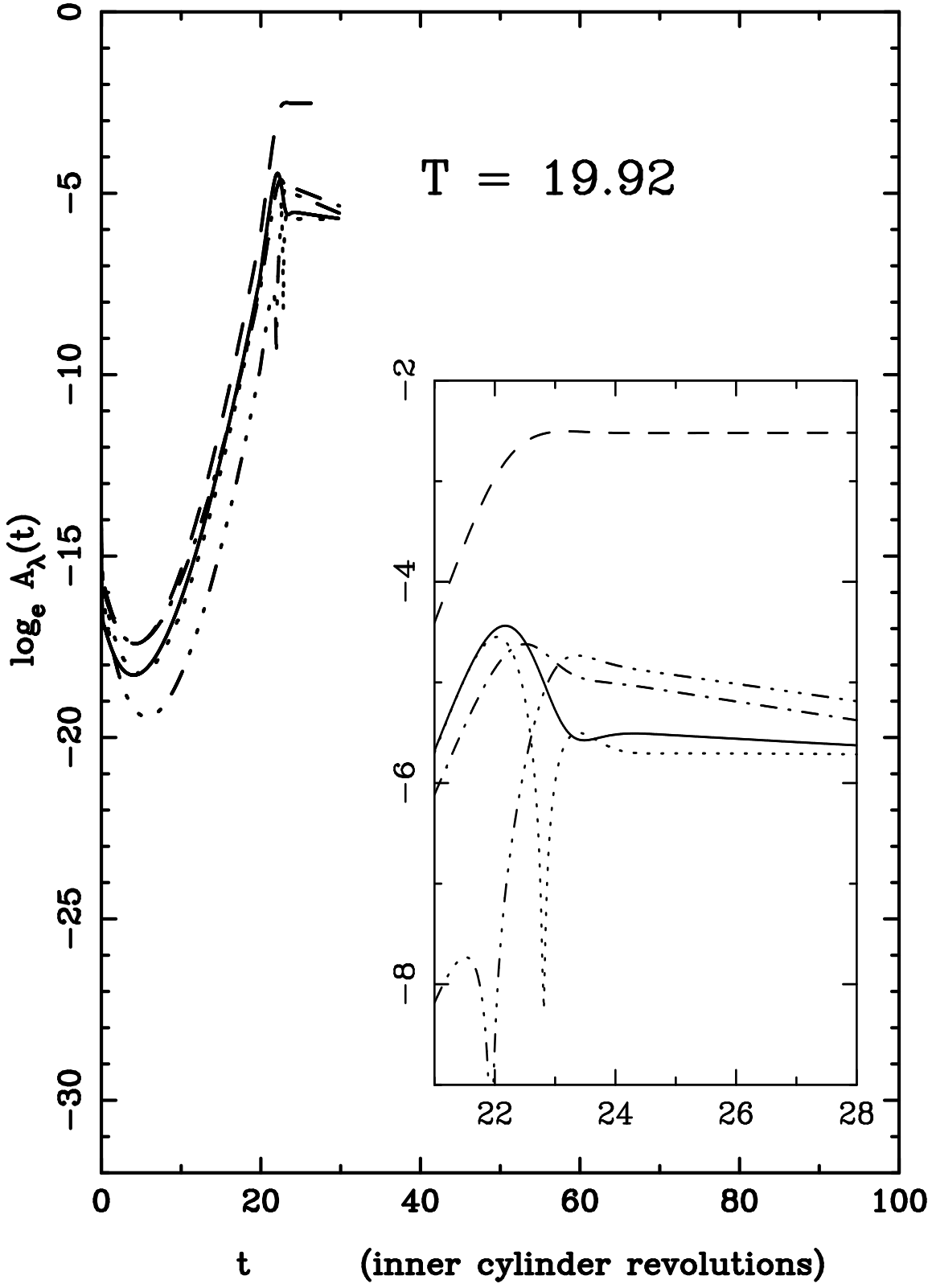

Figure 6.6: $A_\lambda(t)$ for ramp times $T = 19.92$. Modes: · – · – · $\lambda = 2.2254$, ———

$\lambda_c = 2.00286$, $----$ $\lambda = 1.82078$, $\cdots\cdots\cdots$ $\lambda = 1.66905$, $-\cdots-$ $\lambda = 1.54066$

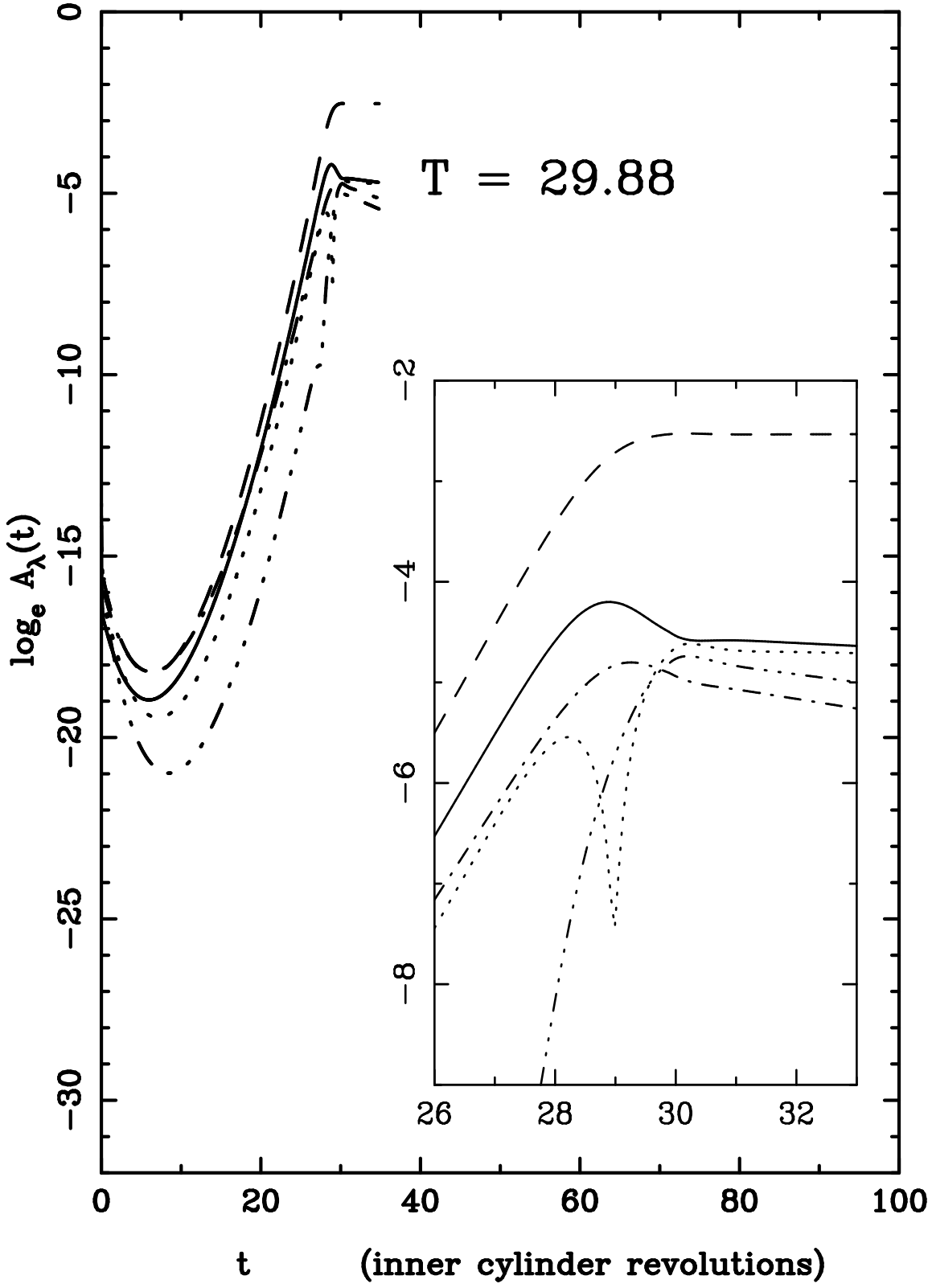

Figure 6.7: $A_\lambda(t)$ for ramp times $T = 29.88$. Modes: $\cdot - \cdot - \cdot$ $\lambda = 2.2254$, ———

$\lambda_c = 2.00286$, $- - - -$ $\lambda = 1.82078$, $\cdots\cdots\cdot$ $\lambda = 1.66905$, $- \cdots -$ $\lambda = 1.54066$

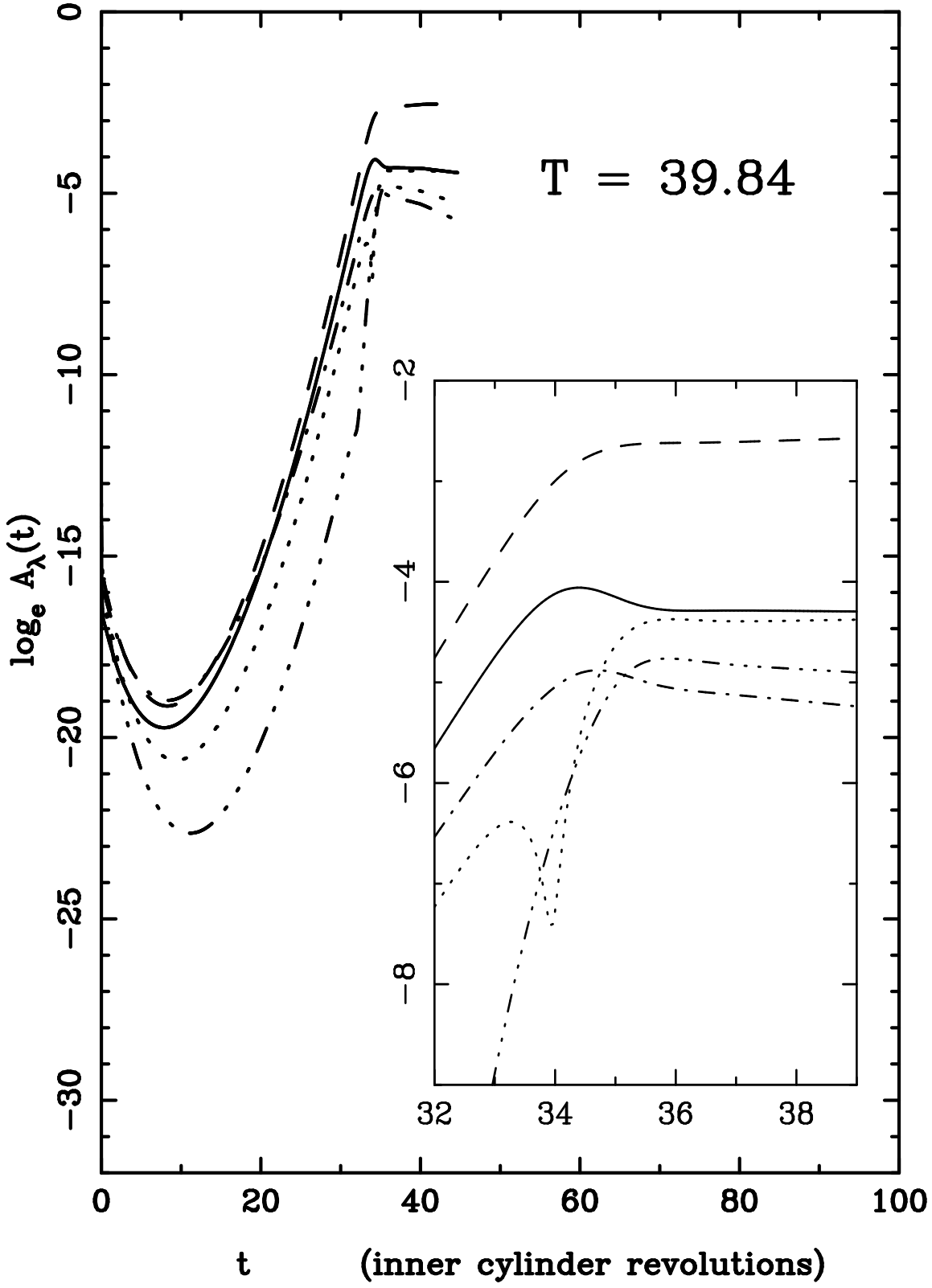

Figure 6.8: $A_\lambda(t)$ for ramp times $T = 39.84$. Modes: · – · – · $\lambda = 2.2254$, ———

$\lambda_c = 2.00286$, $----$ $\lambda = 1.82078$, $\cdots\cdots\cdots$ $\lambda = 1.66905$, $-\cdots-$ $\lambda = 1.54066$

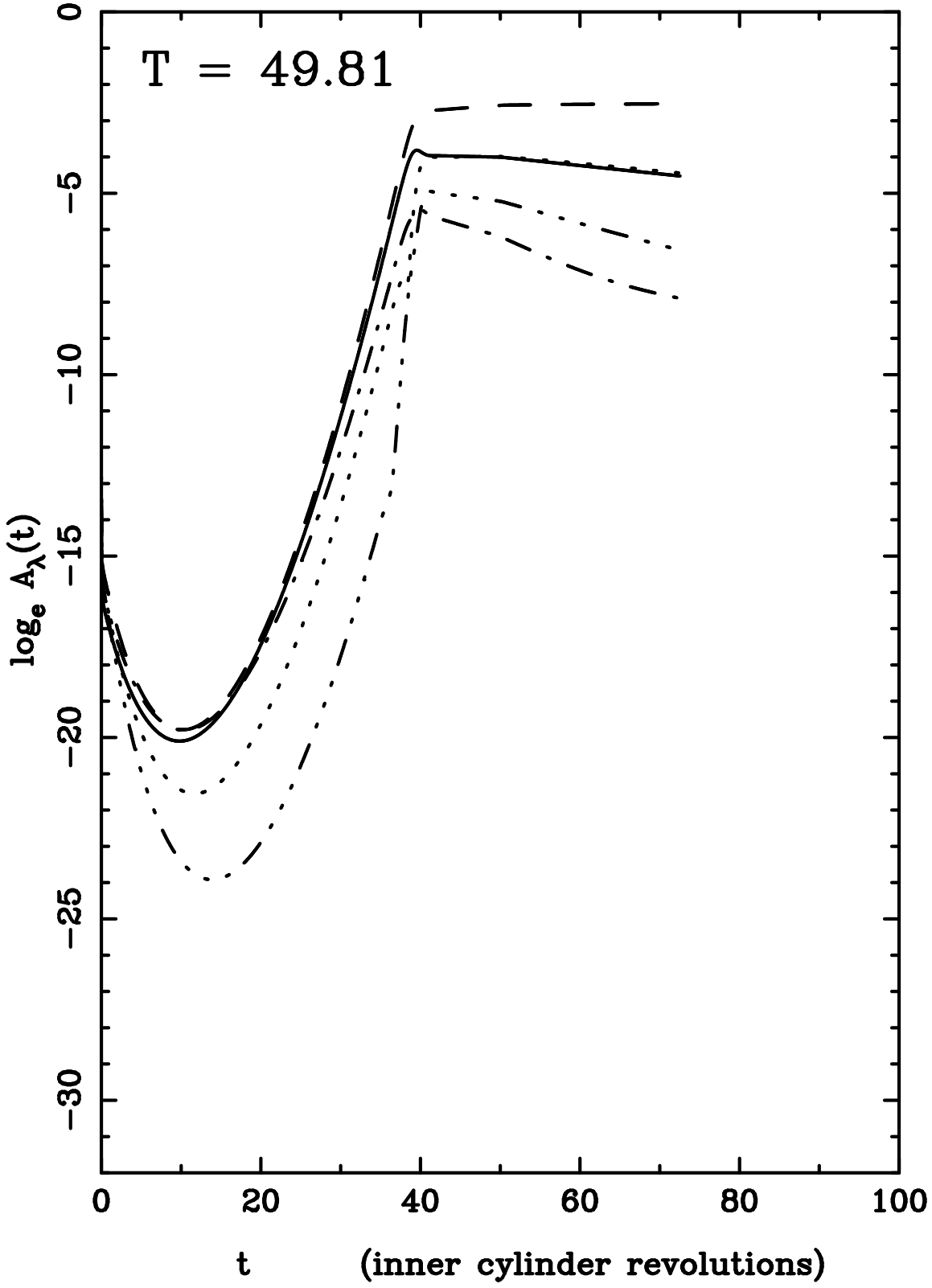

Figure 6.9: $A_\lambda(t)$ for ramp times $T = 49.81$. Modes: $\cdot - \cdot - \cdot$ $\lambda = 2.2254$, ———

$\lambda_c = 2.00286$, $- - - -$ $\lambda = 1.82078$, $\cdots\cdots\cdot$ $\lambda = 1.66905$, $- \cdots -$ $\lambda = 1.54066$

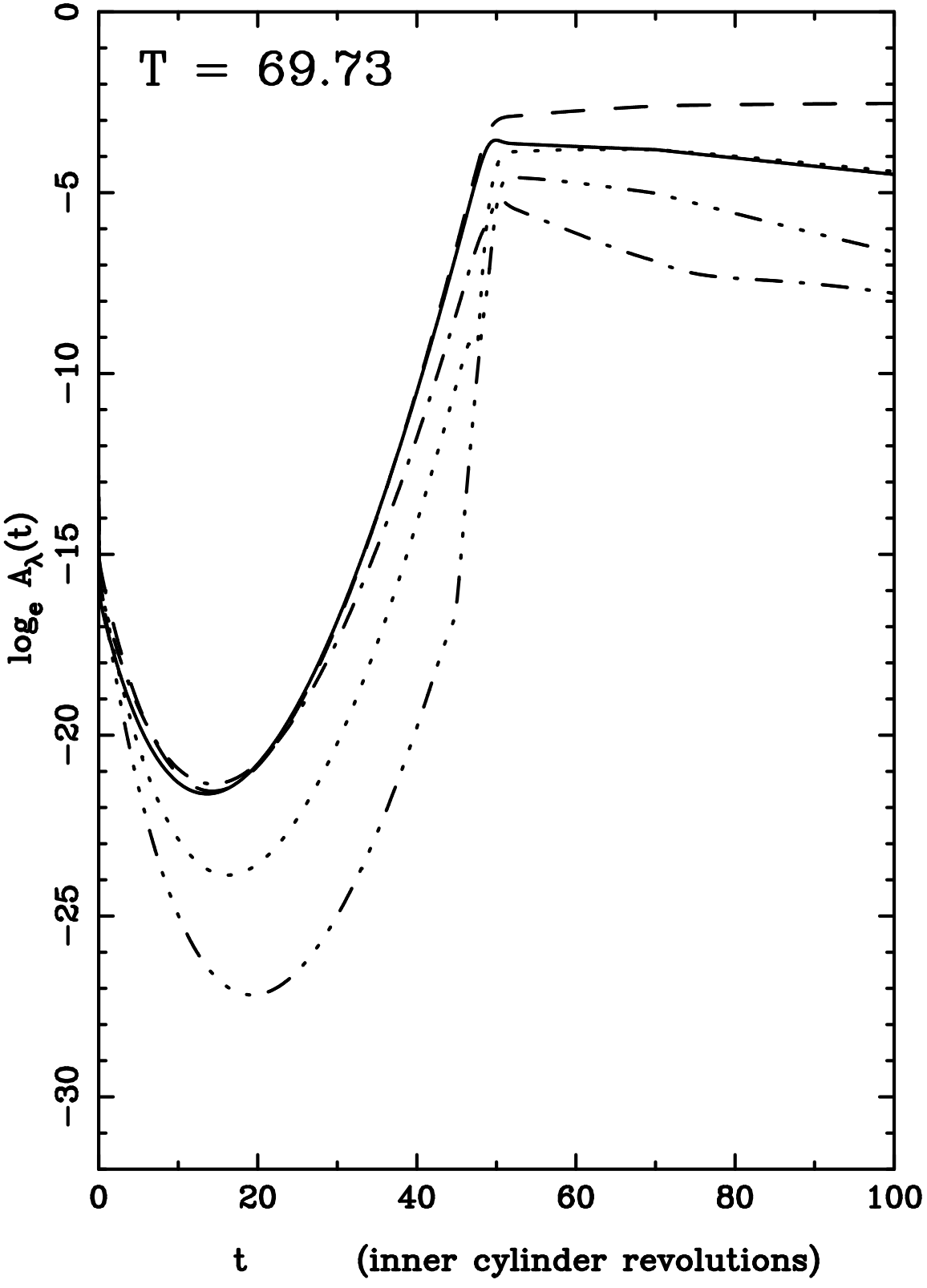

Figure 6.10: $A_\lambda(t)$ for ramp times $T = 69.73$. Modes: $\cdot - \cdot - \cdot$ $\lambda = 2.2254$, ———

$\lambda_c = 2.00286$, $- - - - \ \lambda = 1.82078$, $\cdots\cdots\cdot \ \lambda = 1.66905$, $- \cdots - \ \lambda = 1.54066$

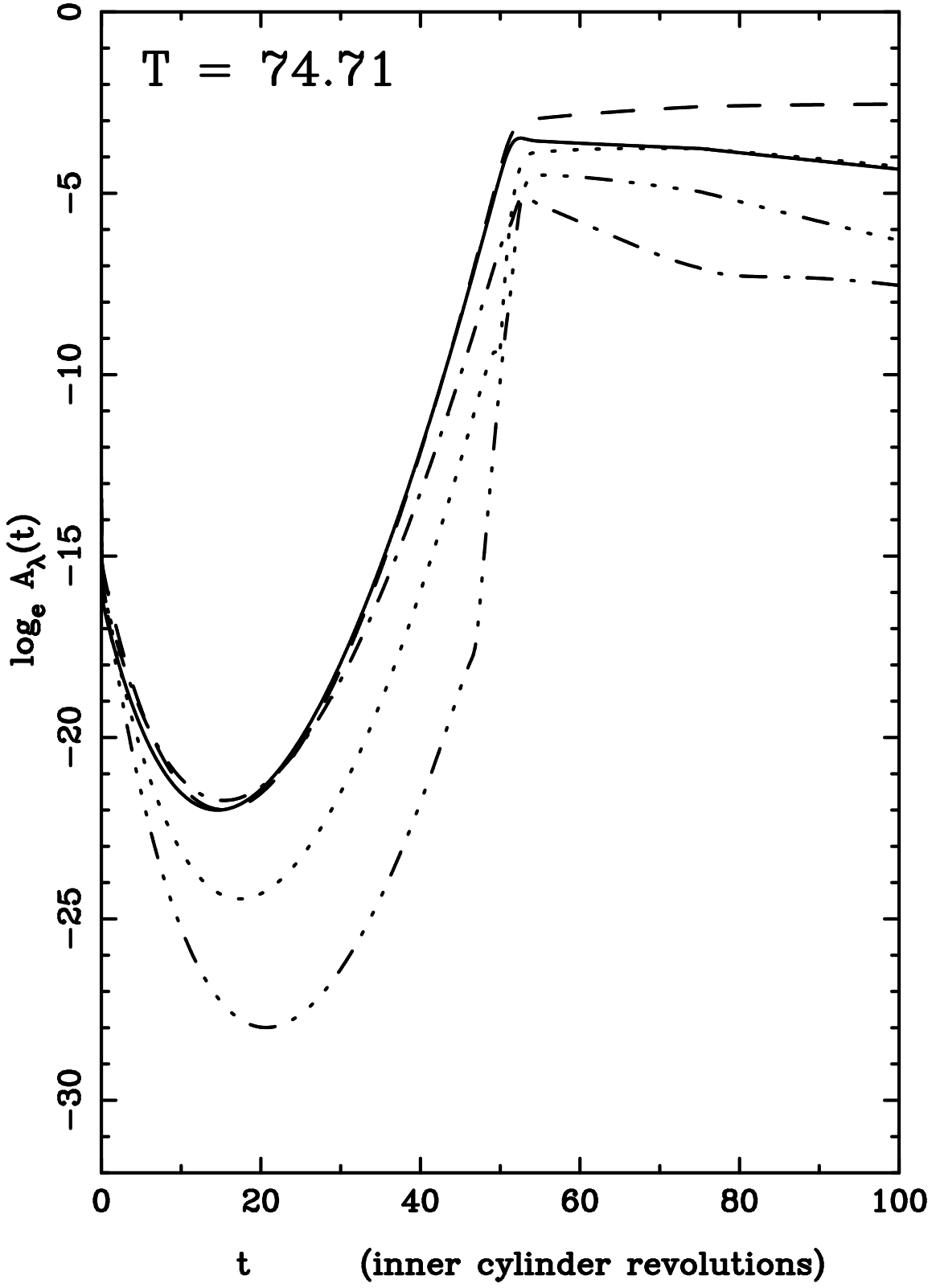

Figure 6.11: $A_\lambda(t)$ for ramp times $T = 74.71$. Modes: $\cdot - \cdot - \cdot$ $\lambda = 2.2254$, ———

$\lambda_c = 2.00286$, $- - - - \ \lambda = 1.82078$, $\cdots\cdots\cdot \ \lambda = 1.66905$, $- \cdots - \ \lambda = 1.54066$

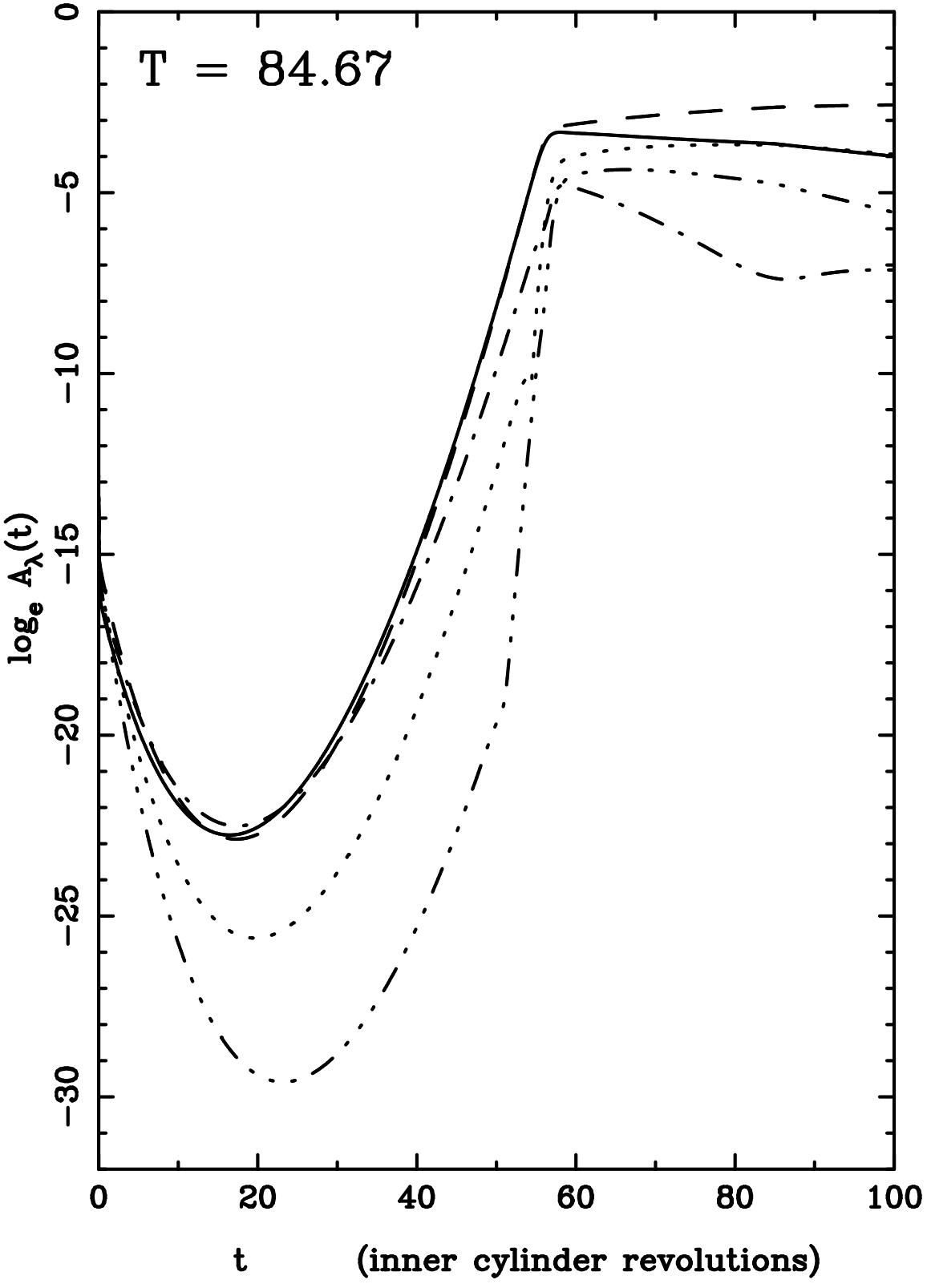

Figure 6.12: $A_\lambda(t)$ for ramp times $T = 84.67$. Modes: $\cdot - \cdot - \cdot$ $\lambda = 2.2254$, ———

$\lambda_c = 2.00286$, $- - - - \ \lambda = 1.82078$, $\cdots\cdots\cdot \ \lambda = 1.66905$, $- \cdots - \ \lambda = 1.54066$

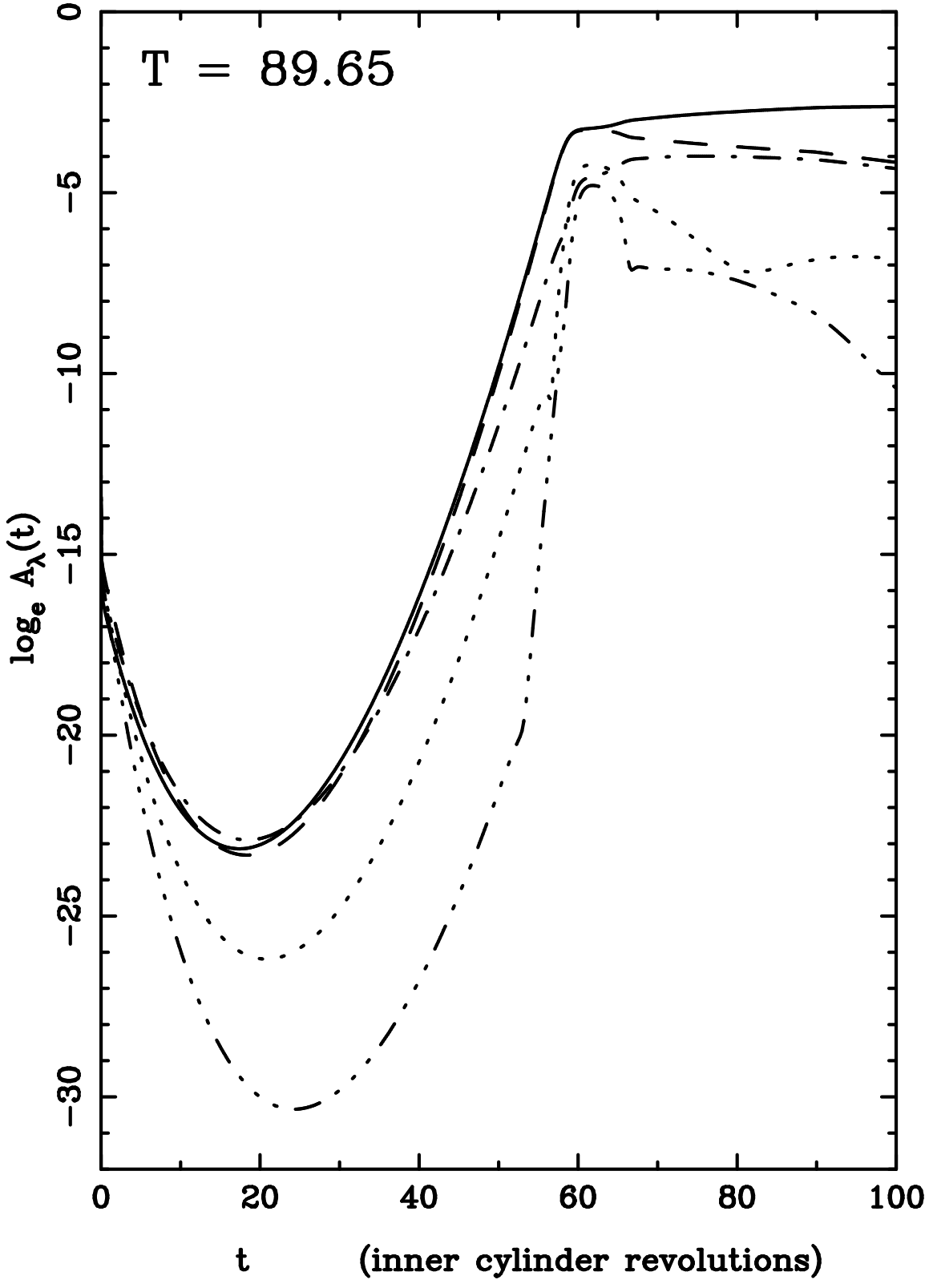

Figure 6.13: $A_\lambda(t)$ for ramp times $T = 89.65$. Modes: $\cdot - \cdot - \cdot$ $\lambda = 2.2254$, ———

$\lambda_c = 2.00286$, $- - - - \ \lambda = 1.82078$, $\cdots\cdots\cdot \ \lambda = 1.66905$, $- \cdots - \ \lambda = 1.54066$

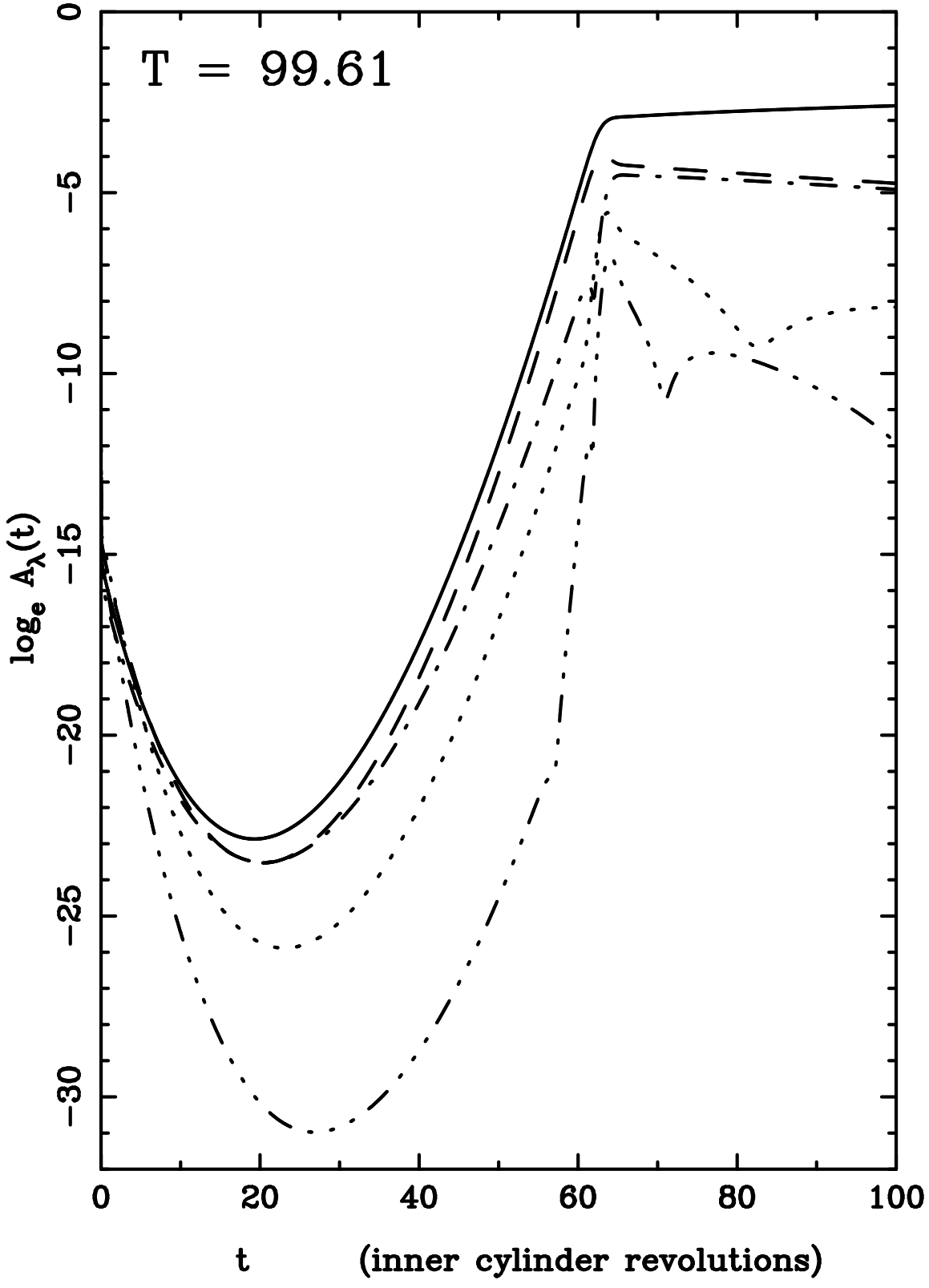

Figure 6.14: $A_\lambda(t)$ for ramp times $T = 99.61$. Modes: $\cdot - \cdot - \cdot$ $\lambda = 2.2254$, ———

$\lambda_c = 2.00286$, $- - - -$ $\lambda = 1.82078$, $\cdots\cdots\cdot$ $\lambda = 1.66905$, $- \cdots -$ $\lambda = 1.54066$

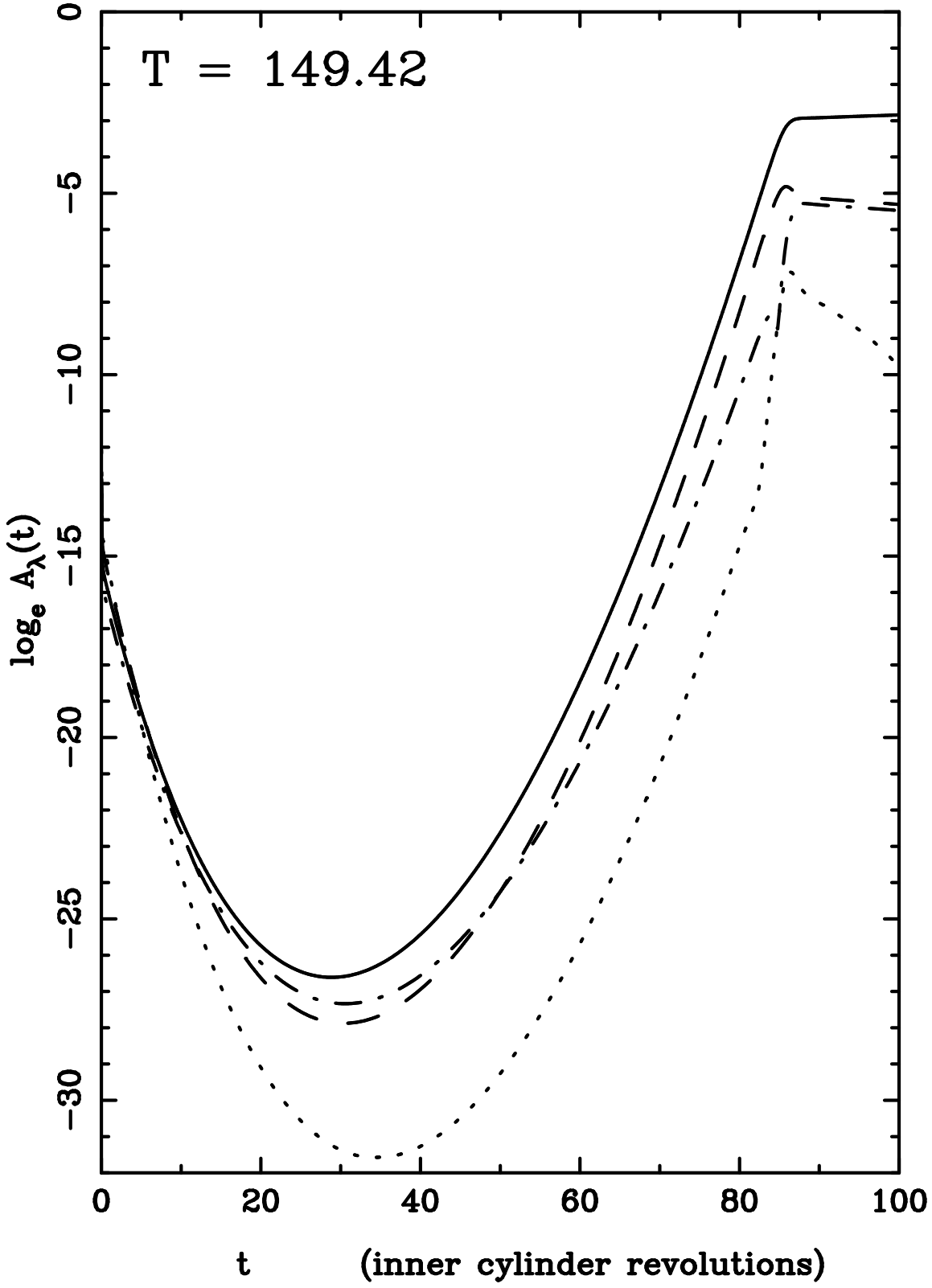

Figure 6.15: $A_\lambda(t)$ for ramp times $T = 149.42$. Modes: $\cdot - \cdot - \cdot$ $\lambda = 2.2254$, ———

$\lambda_c = 2.00286$, $- - - - \ \lambda = 1.82078$, $\cdots\cdots\cdot \ \lambda = 1.66905$, $- \cdots - \ \lambda = 1.54066$

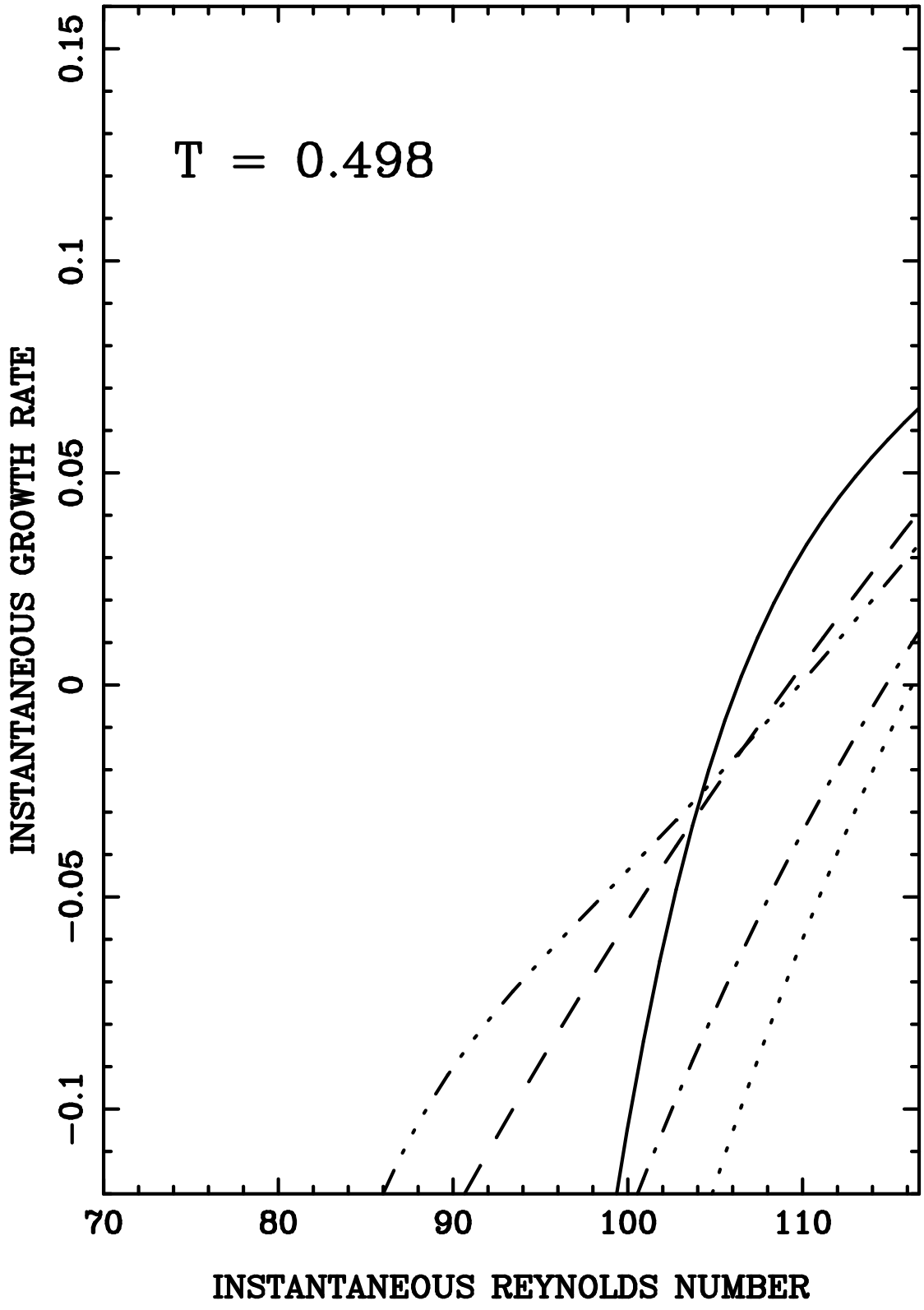

Figure 6.16: Instantaneous $\sigma_\lambda(t)$ versus instantaneous $Re(t)$ for $T = 0.498$.

Modes: $\cdot - \cdot - \cdot \quad \lambda = 2.2254$, ——— $\lambda_c = 2.00286$, $- - - - \lambda = 1.82078$,

$\cdots\cdots\cdot \lambda = 1.66905$, $- \cdots - \lambda = 1.54066$

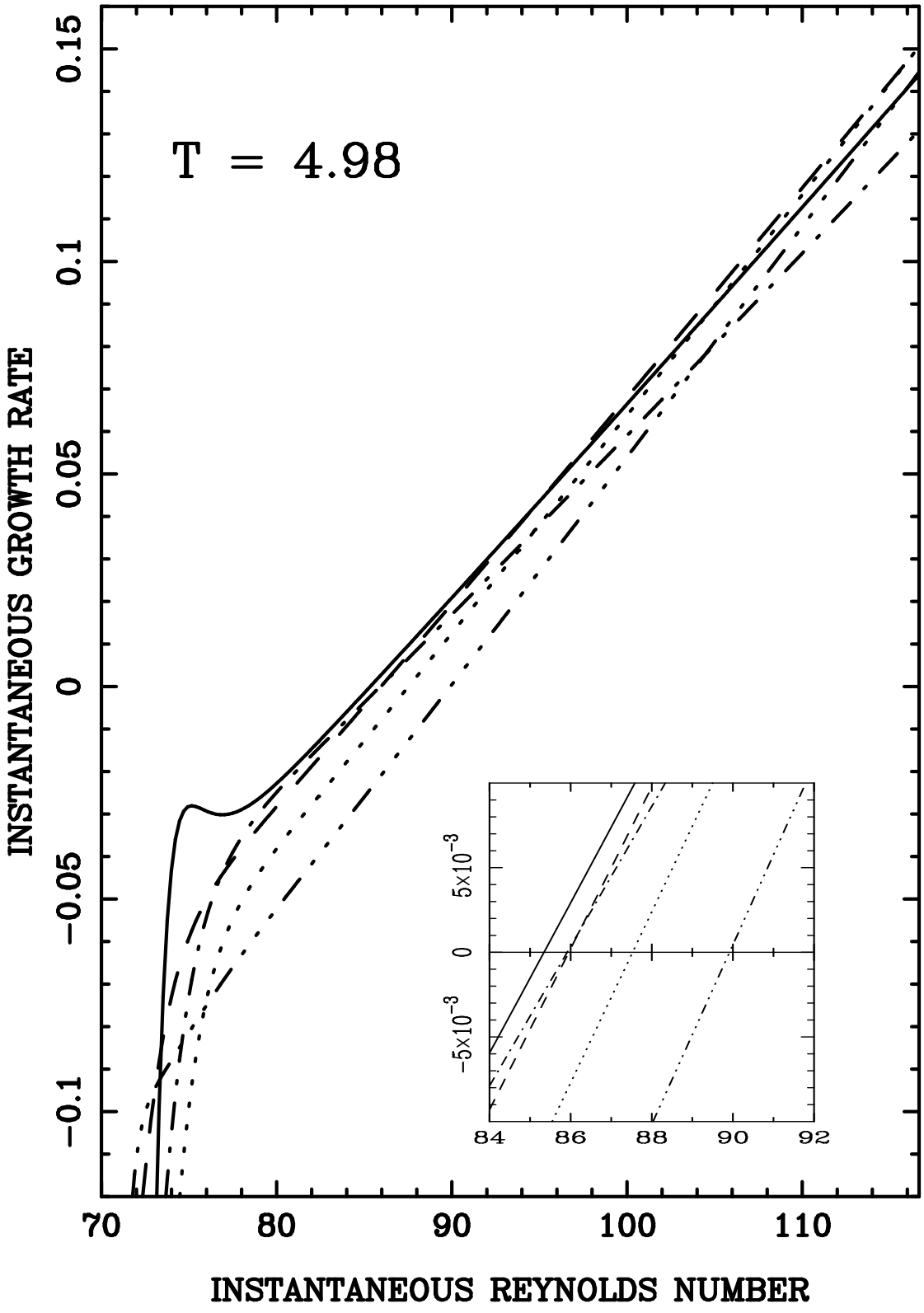

Figure 6.17: Instantaneous $\sigma_\lambda(t)$ versus instantaneous $Re(t)$ for $T = 4.98$.

Modes: $\cdot - \cdot - \cdot \quad \lambda = 2.2254$, ——— $\lambda_c = 2.00286$, $- - - - \lambda = 1.82078$,

$\cdots\cdots\cdot \lambda = 1.66905$, $- \cdots - \lambda = 1.54066$

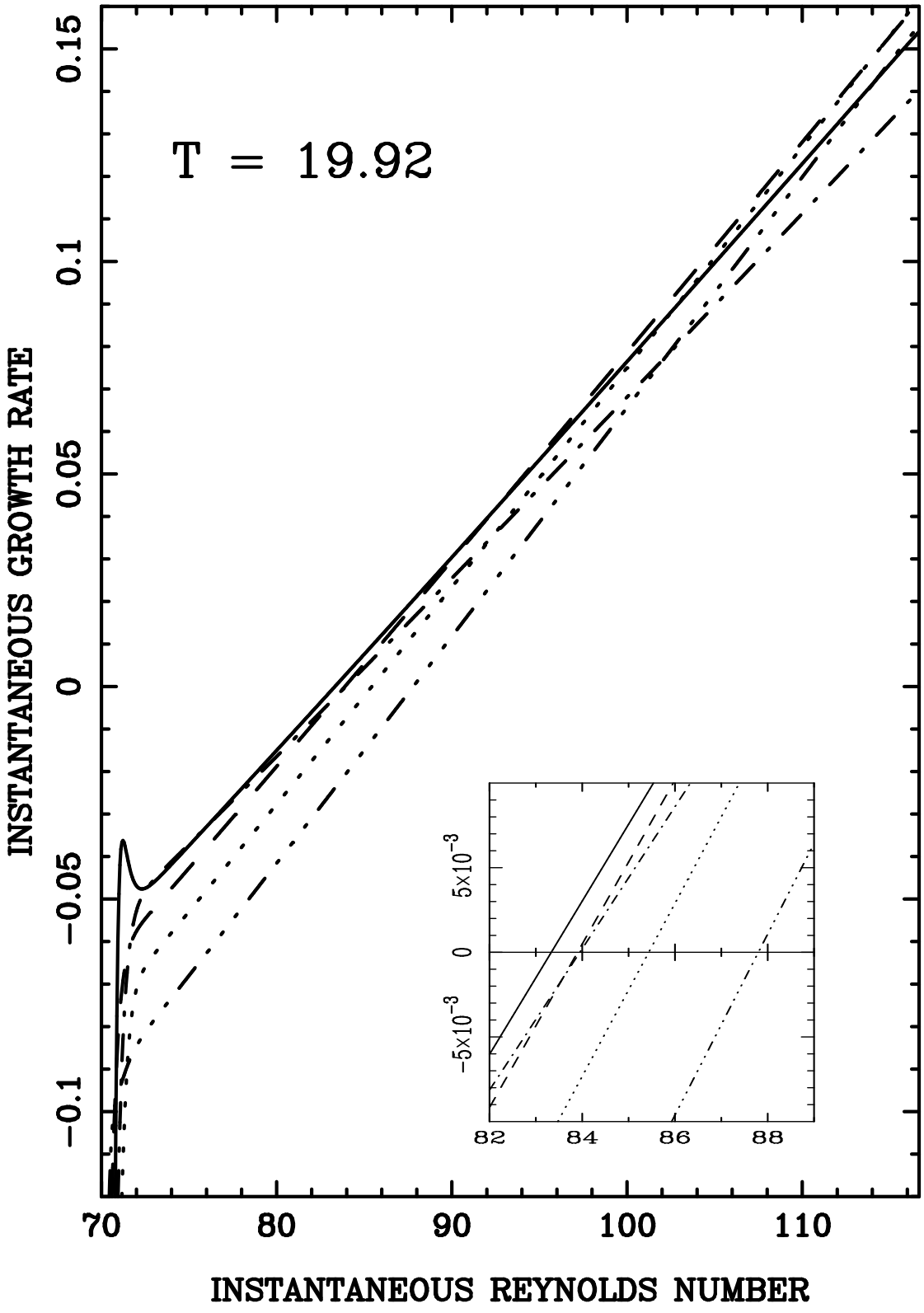

Figure 6.18: Instantaneous $\sigma_\lambda(t)$ versus instantaneous $Re(t)$ for $T = 19.92$.

Modes: $\cdot - \cdot - \cdot \quad \lambda = 2.2254$, ——— $\lambda_c = 2.00286$, $- - - - \lambda = 1.82078$,

$\cdots\cdots\cdot \lambda = 1.66905$, $- \cdots - \lambda = 1.54066$

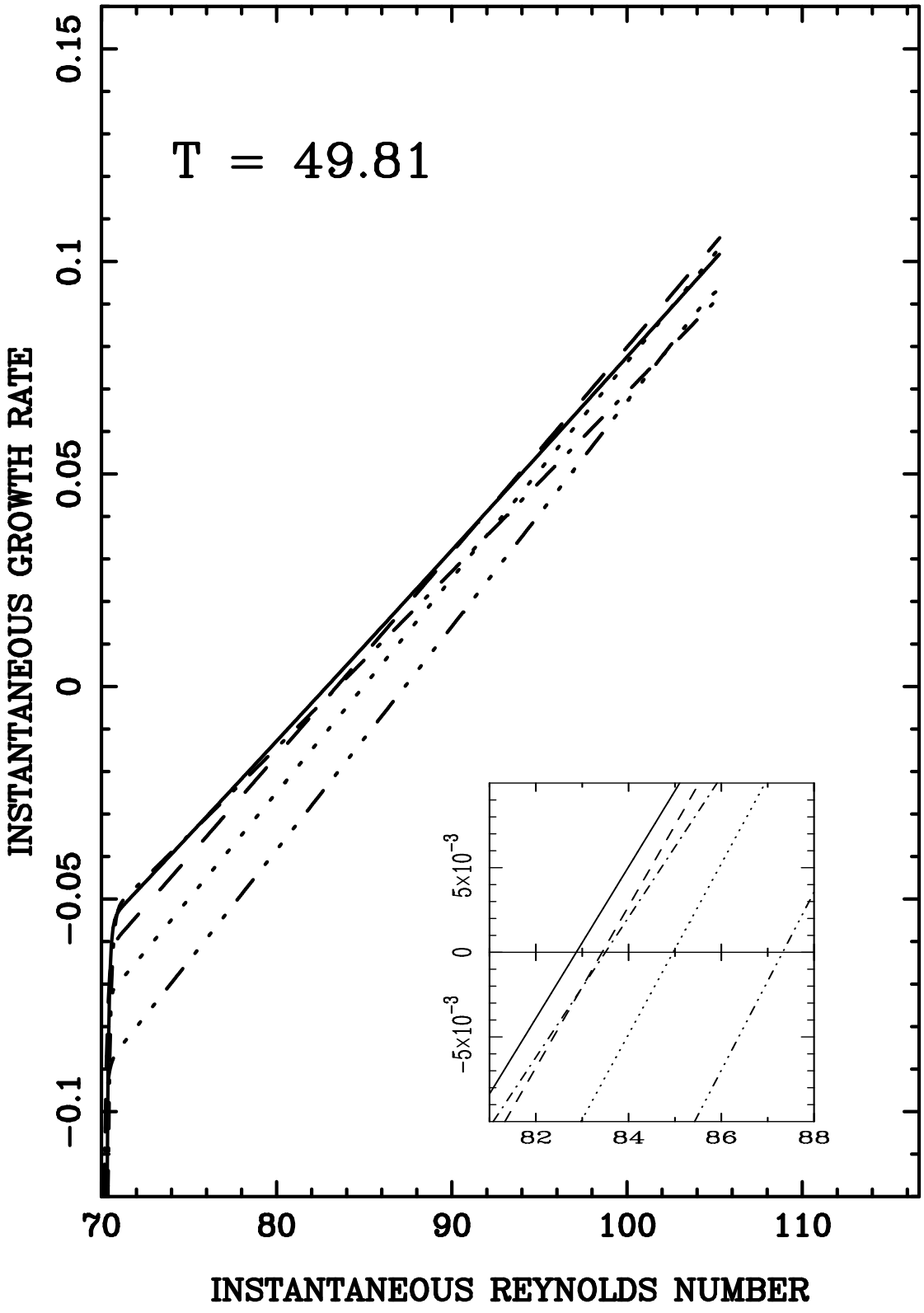

Figure 6.19: Instantaneous $\sigma_\lambda(t)$ versus instantaneous $Re(t)$ for $T = 49.81$.

Modes: $\cdot - \cdot - \cdot \quad \lambda = 2.2254$, ——— $\lambda_c = 2.00286$, $- - - - \lambda = 1.82078$,

$\cdots\cdots\cdot \lambda = 1.66905$, $- \cdots - \lambda = 1.54066$

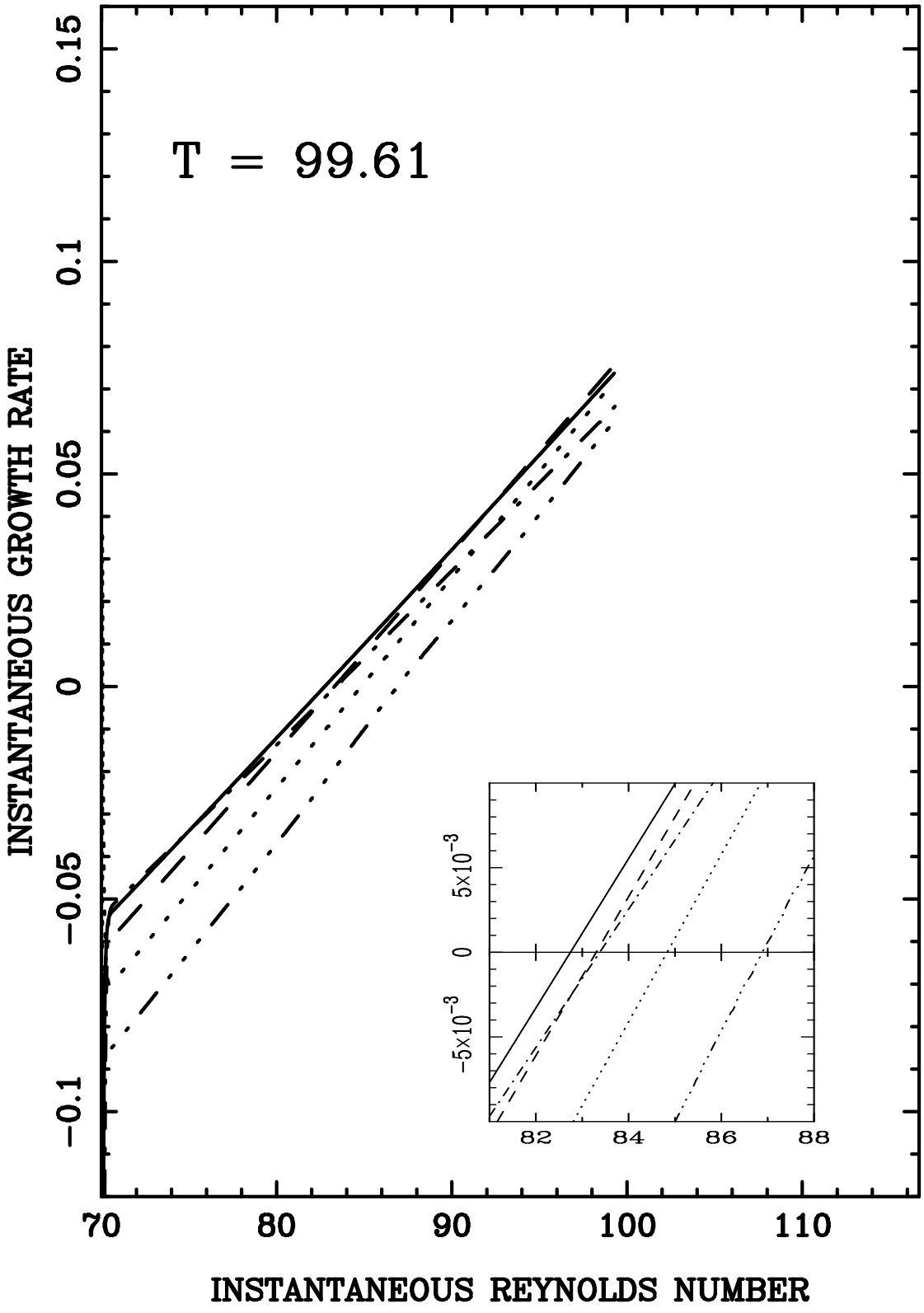

Figure 6.20: Instantaneous $\sigma_\lambda(t)$ versus instantaneous $Re(t)$ for $T = 99.61$.

Modes: $\cdot - \cdot - \cdot \quad \lambda = 2.2254$, ——— $\lambda_c = 2.00286$, $- - - - \lambda = 1.82078$,

$\cdots\cdots\cdot \lambda = 1.66905$, $- \cdots - \lambda = 1.54066$

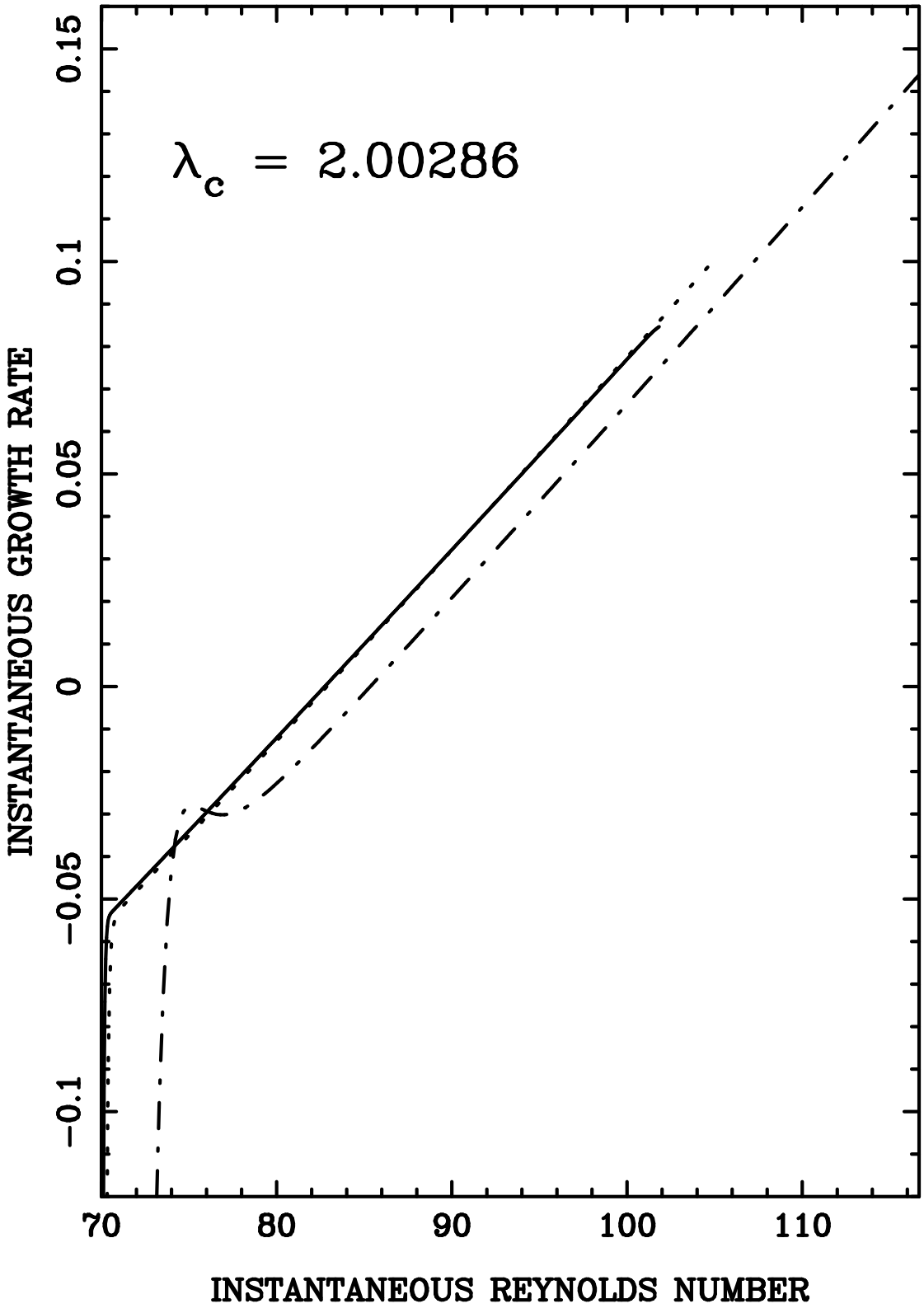

Figure 6.21: Instantaneous $\sigma_\lambda(t)$ versus instantaneous $Re(t)$ for $\lambda_c = 2.00286$.

Ramp times: $\cdot - \cdot - \cdot \quad T = 4.98$, $\cdots\cdots\cdot\ T = 49.81$, ——— $T = 99.61$.

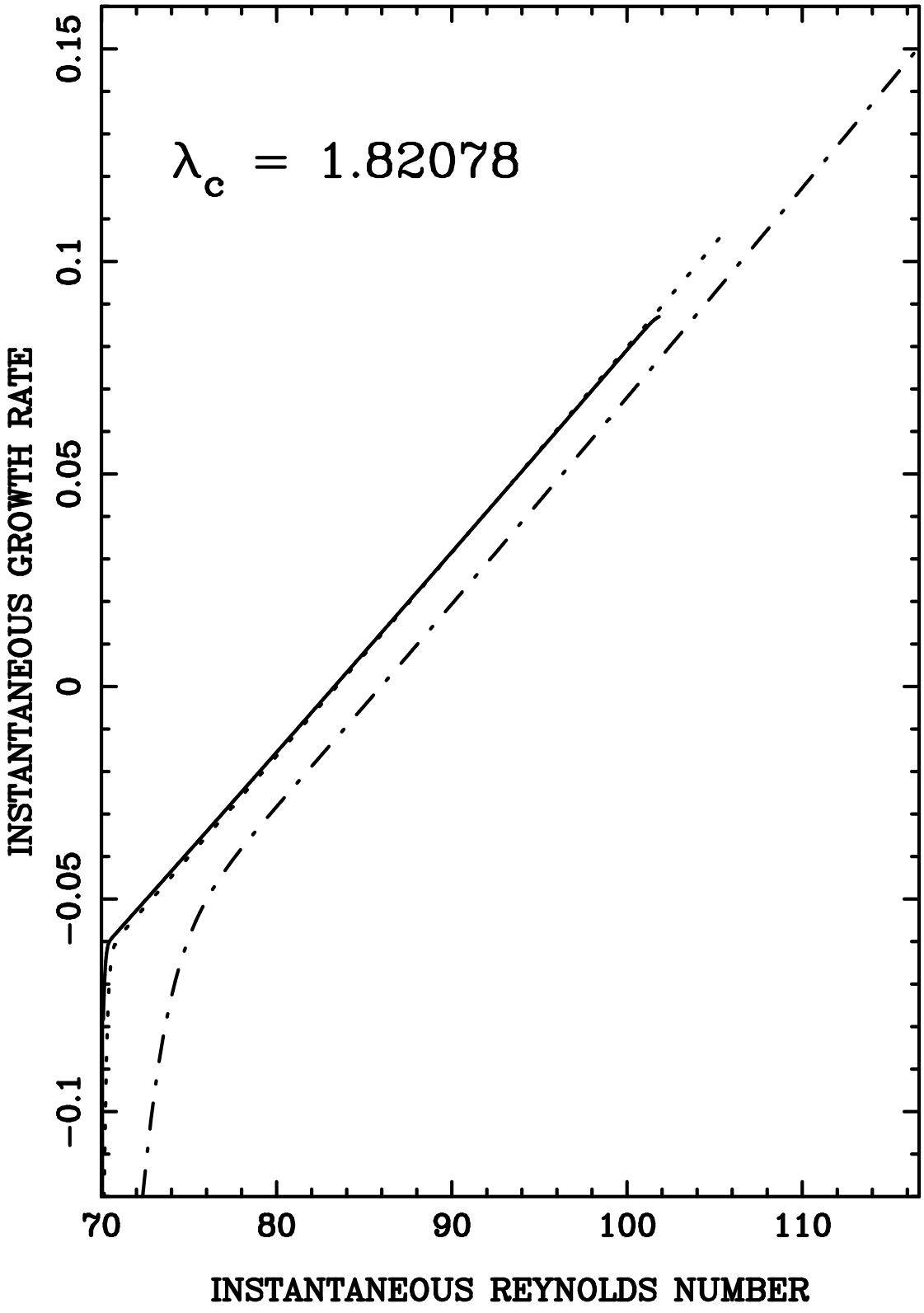

Figure 6.22: Instantaneous $\sigma_\lambda(t)$ versus instantaneous $Re(t)$ for $\lambda = 1.82078$.

Ramp times: $\cdot - \cdot - \cdot \quad T = 4.98$, $\cdots\cdots\cdot\ T = 49.81$, ——— $T = 99.61$.

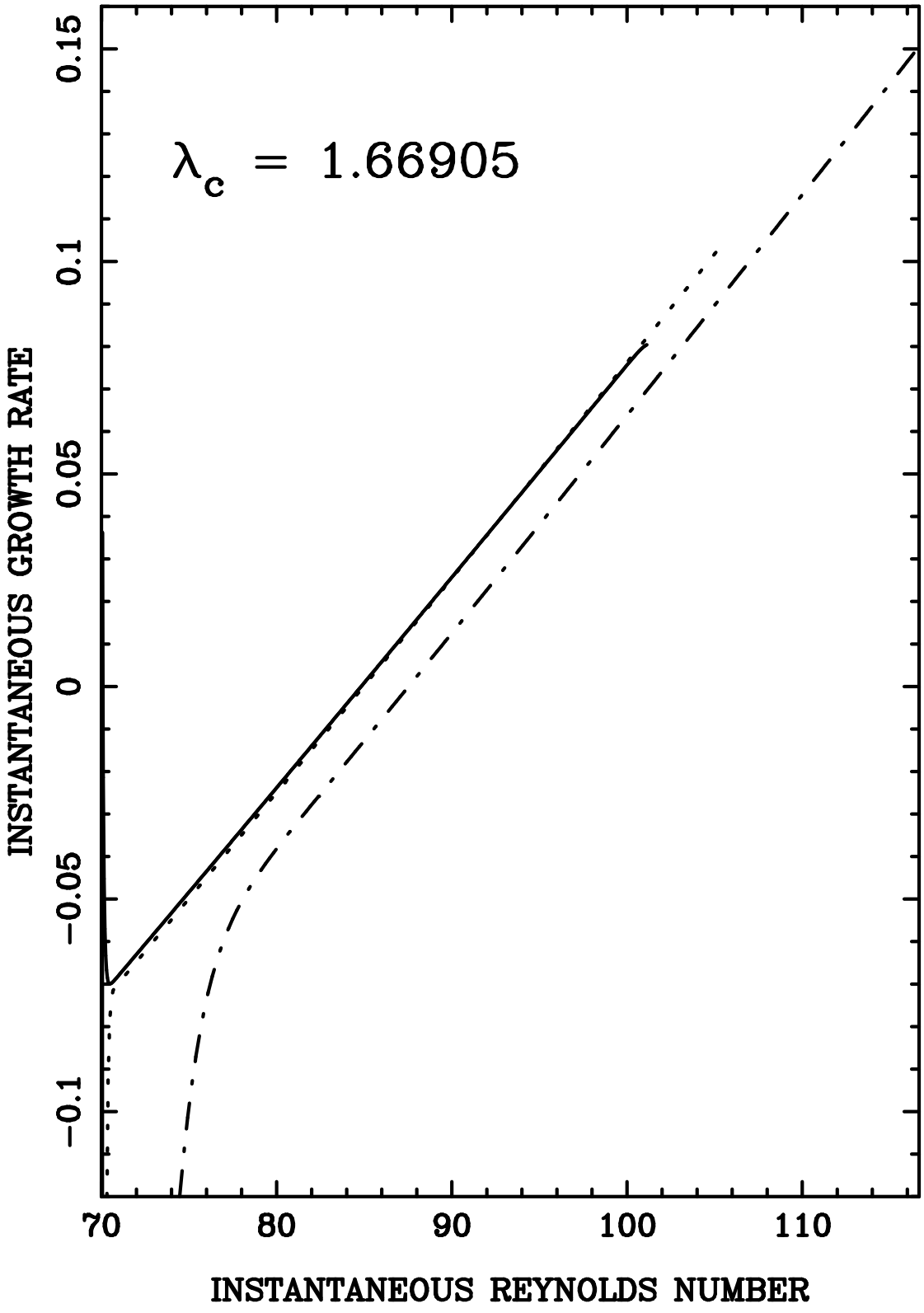

Figure 6.23: Instantaneous $\sigma_\lambda(t)$ versus instantaneous $Re(t)$ for $\lambda = 1.66905$.

Ramp times: $\cdot - \cdot - \cdot \quad T = 4.98$, $\cdots\cdots\cdot\ T = 49.81$, ——— $T = 99.61$.

6.4 Linear model

If the initial perturbation is expressed as a weighted sum of eigenfunctions of the linearized form of the equations, then the weighting factors assign a value for the initial amplitude $A_\lambda(0)$ for each mode. This amplitude $A_\lambda(0)$ would strictly apply at a point in time after which the base flow becomes steady and the modes begin their independent stage of growth. However, in our model the effect of the unsteady base flow will be neglected.

6.4.1 Constant *Re*

If the $A_\lambda(0)$ are small, each mode will either grow or decay exponentially, depending on whether the wavelength is inside or outside the amplification band predicted from linear stability theory.

As the modes grow independently of each other, for a constant Reynolds number we can write

$$A_\lambda(t) = A_\lambda(0)e^{\sigma_\lambda t} \tag{6}$$

Here, the amplitude $A_\lambda(t)$ is equivalent to the exponential growth factor in Equations (3) to (5) in Chapter 2. Equation (6) is the solution to the Landau equation in its simplest form

$$\frac{dA_\lambda}{dt} = \sigma_\lambda A_\lambda \tag{7}$$

In Figures 6.21 to 6.23, when T is increased (or the acceleration of Re is decreased) σ_λ approaches a linear relationship to Re. From Drazin and Reid (1989), the growth rate can be written as linearly proportional to Reynolds number, provided it is not too far from the critical Reynolds number. Assigning the critical Reynolds number and cofactor of proportionality, K, with mode-dependency, we have

$$\sigma_\lambda = K_\lambda(Re - Re_{c,\lambda}) + O((Re - Re_{c,\lambda})^2) \tag{8}$$

In Figures 6.17 to 6.20, the lines of σ_λ versus Re intersect each other. Therefore the value of the slope, K_λ, can be different for each mode. Which mode has the greatest growth rate depends on the value of Re. Indeed, the ordering of the growth rates of each mode, greatest to smallest, varies with Re. Figures 6.17 to 6.20 show that in the linear part of the plot, $K_{\lambda_{13}} > K_{\lambda_{12}} > K_{\lambda_{11}} > K_{\lambda_{10}} > K_{\lambda_9}$. That is, K_λ increases with decreasing λ.

The values of K_λ and $Re_{c,\lambda}$ could be determined from a linear stability analysis. Alternatively, results from a sufficiently long ramp time can be used, for example $T = 99.61$ in Figure 6.20. Subsequently, Equation (8) can be used to predict the values of σ_λ for each mode as a function of Re.

6.4.2 Linearly increasing $Re(t)$

It will be assumed that the instantaneous growth rate $\sigma_\lambda(t)$ at a particular Re during a ramp is equal to the growth rate when Re is held fixed at that particular value. As discussed earlier, this assumption is in practice valid for sufficiently slow rates of increase of Re, so that the base flow becomes steady very early during the Re ramp.

We can formally integrate Equation (7) to give

$$A_\lambda(t) = A_\lambda(0) e^{\left(\int_0^t \sigma_\lambda(t')dt'\right)} \tag{9}$$

where from Equation (8),

$$\sigma_\lambda(t) = K_\lambda(Re(t) - Re_{c,\lambda}) \tag{10}$$

The linear ramp is defined to start from $t = 0$. The ramp function $Re(t)$ can be defined as

$$Re(t) = \begin{cases} Re_i + \frac{dRe}{dt}t & \text{if } t \leq T \\ Re_f & \text{if } t > T \end{cases} \tag{11}$$

where the ramp rate is

$$\frac{dRe}{dt} = \frac{Re_f - Re_i}{T} \tag{12}$$

According to Equation (11), a sudden start is equivalent to a having a constant $Re = Re_f$.

In terms of the instantaneous exponential growth rate we have,

$$\sigma_\lambda(t) = \begin{cases} -\sigma_{o,\lambda} + C_\lambda t & \text{if } t \leq T \\ \sigma_{f,\lambda} & \text{if } t > T \end{cases} \tag{13}$$

where

$$\sigma_{o,\lambda} = -K_\lambda(Re_i - Re_{c,\lambda}) \tag{14}$$

and

$$\sigma_{f,\lambda} = K_\lambda(Re_f - Re_{c,\lambda}) \tag{15}$$

A consequence of using an Re ramp rate is that each mode has a particular rate of change of growth rate C_λ, where

$$C_\lambda = K_\lambda \frac{dRe}{dt} \tag{16}$$

The solution of Equation (9) after substitution of Equation (13) for $\sigma_\lambda(t)$ gives

$$A_\lambda(t) = \begin{cases} A_\lambda(0) e^{-\sigma_{o,\lambda} t + \frac{1}{2} C_\lambda t^2} & \\ & \text{for } t \leq T \\ A_\lambda(0) e^{\frac{1}{2}(\sigma_{f,\lambda} - \sigma_{o,\lambda})T + \sigma_{f,\lambda}(t-T)} & \\ & \text{for } t > T \end{cases} \tag{17}$$

The log of the amplitude of the modes will therefore vary quadratically in time during the ramping stage. During the linear ramp in Reynolds number the instantaneous growth rate for a mode increases linearly from an initial negative value through zero to a final positive value. Therefore during the ramp the log of the amplitude of the mode decays quadratically to some minimum amplitude then grows quadratically to a higher amplitude. These features agree with the behaviour of the modes in their independent stage of growth shown in Figures 6.2 to 6.15.

Now, consider the time, t^*_λ it takes for the amplitude of each mode λ to grow to a particular higher amplitude A^*. Then, from Equation (17) we get

$$t^*_\lambda = \frac{1}{\sigma_{f,\lambda}} \ln\left(\frac{A^*}{A_\lambda(0)}\right) + \frac{T}{2}\left(1 + \frac{\sigma_{o,\lambda}}{\sigma_{f,\lambda}}\right) \tag{18}$$

For simplicity of the argument, let us assume the initial amplitudes of the modes are the same so that no particular mode is favoured initially. This would be the case if the initial perturbation was constructed as an equally weighted sum of the linear eigenfunctions of each mode.

Consider the right hand side of Equation (18). The first term represents the time it takes for each mode to reach A^* for impulsive starts, $t^*_{\lambda,impulse}$. The second term represents an additional time delay, $t^*_{\lambda,ramp}$, for each mode due to the ramp.

Now $t^*_{\lambda,impulse}$ has a shortest-to-longest ordering for each mode according to the highest-to-lowest ordering of the final exponential growth rates $\sigma_{f,\lambda}$ for each mode. This follows from factor $1/\sigma_{f,\lambda}$ in the first term. The values of $\sigma_{f,\lambda}$ as a function of Re_f are given by Equation (15).

Also, $t^*_{\lambda,ramp}$ has a shortest-to-longest ordering corresponding to the lowest-to-highest ordering of the critical Reynolds number $Re_{c,\lambda}$ for each mode. This follows from the factor

$$\frac{\sigma_{o,\lambda}}{\sigma_{f,\lambda}} = \frac{Re_{c,\lambda} - Re_i}{Re_f - Re_{c,\lambda}} \tag{19}$$

in the second term which has a smallest-to-largest ordering corresponding to the lowest-to-highest ordering of the critical Reynolds number $Re_{c,\lambda}$ for each mode. The values $Re_{c,\lambda}$ are given by the neutral stability curve from linear stability analysis, as illustrated by the outer curve in Figure 2.4. The highest-to-lowest ordering of $\sigma_{f,\lambda}$ is not the same as the lowest-to-highest ordering of $Re_{c,\lambda}$.

When the ramp time is increased from the impulsive start situation ($T = 0$) to the situation with very slow increases (T very large), $t^*_{\lambda,ramp}$ becomes progressively more significant in relation to $t^*_{\lambda,impulsive}$. The shortest-to-longest ordering of t^*_λ gradually changes from the highest-to-lowest ordering of $\sigma_{f,\lambda}$ to the lowest-to-highest ordering of $Re_{c,\lambda}$.

For sufficiently large ramp times the shortest-to-longest ordering of t^*_λ will always be according to the lowest-to-highest ordering of $Re_{c,\lambda}$. The smallest value being $t^*_{\lambda_c}$. These features are observed in Figures 6.14 and 6.15, for $T = 99.61$ and $T = 149.42$ in the portion of the independent stage of growth before nonlinear effects occur.

As the ramp time is increased further, the mode with the critical wavelength will grow to A^* progressively earlier than the other modes. In this sense, the critical wavelength is being increasingly favoured, above all other modes.

6.5 Nonlinear effects

Suppose the discrepancy due to the unsteady base flow is disregarded. One can redefine t^*_λ as the time it would take a pure mode perturbation with wavelength λ to grow to an amplitude A^*_λ where nonlinear self-interaction begins (eventually leading to saturation of the mode). Then $t^*_{\lambda,ramp}$ represents the delay time for mode λ to grow to A^*_λ. The change in the ordering of t^*_λ with ramp time influences which state will be preferred at steady state.

From Figure 6.2, $\lambda = 1.66905$ is the preferred mode when $T = 0$. In Figure 6.4 for $T = 4.98$, the delay time for $\lambda = 1.66905$ is sufficiently greater than the delay time for $\lambda = 1.82078$ so the $\lambda = 1.82078$ mode has time to self-interact and approach the form of a steady state Taylor vortex flow. Consequently the $\lambda = 1.66905$ mode and the remaining modes react as if they are small perturbations to that Taylor vortex flow, and decay. Thereby a stable Taylor vortex flow with $\lambda = 1.82078$ is achieved. The non-preferred modes decay very slowly.

Similarly in Figure 6.14 for $T = 99.61$ the difference in delay time between the $\lambda = 1.82078$ mode and the $\lambda = 2.00286$ mode is great enough so that the $\lambda = 2.00286$ mode has time to self-interact and approach the form of a steady state Taylor vortex flow. Consequently the $\lambda = 1.82078$ mode and the remaining modes react as if they are small perturbations to that Taylor vortex flow, and decay. Thereby a stable Taylor vortex flow with $\lambda = 2.00286$ is achieved.

As the ramp time is increased past $T = 99.61$, the delay time for the $\lambda = 2.00286$ mode will decrease relative to the delay time for the other modes. Thus the $\lambda = 2.00286$ mode will increasingly have more time to self-interact and approach the form of a steady state Taylor vortex flow. This is a partial explanation as to why the mode with the critical wavelength is always preferred when the inner cylinder Reynolds number is increased quasi-steadily from subcritical to supercritical values.

6.6 Nonlinear amplitude equations for sudden starts.

The complicated behaviour of the amplitude of the modes shown in Figures 6.2 to 6.15 demonstrate how difficult it is to mathematically account for every nonlinear effect. However, in this thesis, attention shall be drawn to several nonlinear effects discussed below. A dynamical systems approach is used to provide a physical nonlinear model for the amplitude of the modes.

6.6.1 Amplitude equations for two coupled modes.

Following the model of two-mode Van der Pol generator discussed by Abarbanel, Rabinovich and Sushchik (1993) for convective flow in a fluid, we can express two coupled amplitude equations as:

$$\frac{dA_1}{dt} = \sigma_1 A_1 - l_1 A_1 |A_1|^2 - \alpha_{12} A_1 |A_2|^2 \tag{20}$$

$$\frac{dA_2}{dt} = \sigma_2 A_2 - l_2 A_2 |A_2|^2 - \alpha_{21} A_2 |A_1|^2 \tag{21}$$

where the amplitudes are complex numbers. Here, σ is the growth rate and l is the Landau constant, which are different for each mode. The linear terms on the right hand side of Equations (20) and (21) represent the initial stages of exponential growth of the amplitude of each mode. The second terms represents the nonlinear self-interaction of each mode. The third terms represents the nonlinear interaction between the modes. The second and third terms act to decelerate the growth.

Substituting $A_1 = |A_1| \exp(i\phi_1)$ and $A_2 = |A_2| \exp(i\phi_2)$, where ϕ is the phase, we obtain

$$\frac{d|A_1|^2}{dt} = 2(\sigma_1 - l_1 |A_1|^2 - \alpha_{12} |A_2|^2) |A_1|^2 \tag{22}$$

$$\frac{d|A_2|^2}{dt} = 2(\sigma_2 - l_2 |A_2|^2 - \alpha_{21} |A_1|^2) |A_2|^2 \tag{23}$$

where the coefficients are real numbers.

At steady state, that is, when $\frac{d|A_1|^2}{dt} = 0$ and $\frac{d|A_2|^2}{dt} = 0$, the system has four equilibrium points. In the phase plane of $|A_2|^2$ versus $|A_1|^2$ these have the coordinates:

(1) $|A_1|^2 = 0$, $|A_2|^2 = 0$

(2) $|A_1|^2 = 0$, $|A_2|^2 = \sigma_2 / l_2$

(3) $|A_1|^2 = \sigma_1 / l_1$, $|A_2|^2 = 0$

(4) $|A_1|^2 = (\sigma_1 - \frac{\alpha_{12}\sigma_2}{l_2}) / (l_1 - \frac{\alpha_{21}\alpha_{12}}{l_2})$, $|A_2|^2 = (\sigma_2 - \frac{\alpha_{21}\sigma_1}{l_1}) / (l_2 - \frac{\alpha_{21}\alpha_{12}}{l_1})$

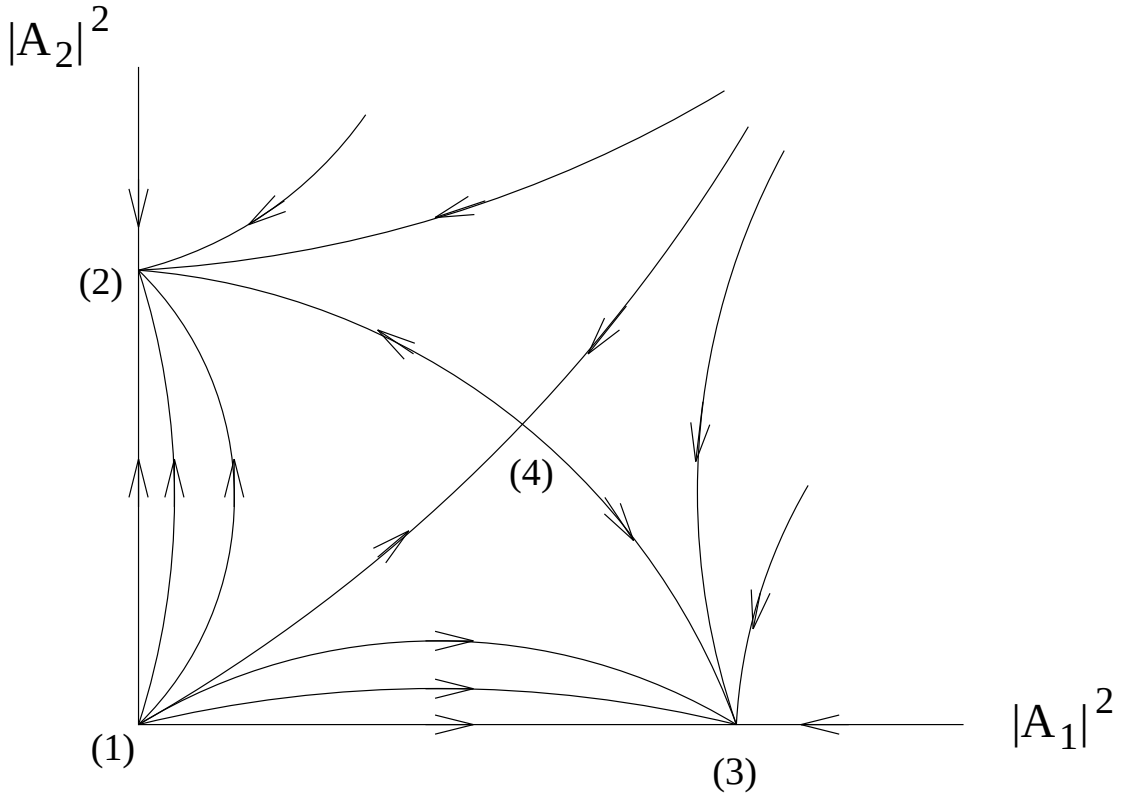

Figure 6.24: Integral curves for strong coupling between modes.

When there is strong coupling between the modes, that is, when $\alpha_{12} > \frac{\sigma_1 l_2}{\sigma_2}$, $\alpha_{12}\alpha_{21} > l_2 l_1$ and $\alpha_{21} > \frac{\sigma_2 l_1}{\sigma_1}$, the integral curves are as shown in Figure 6.24. A particular curve describes the time-dependent path taken in the phase space and the mode reached at steady state. There are two stable equilibrium points, with coordinates given by (2) and (3). The preferred final mode depends on the initial conditions. For some initial conditions the paths tend to the stable point (3) where mode 1 is preferred and mode 2 has decayed to zero. For other initial conditions the paths tend to stable point (2) where mode 2 is preferred and mode 1 has decayed to zero. Thus, when the coupling is strong the two-mode system exhibits nonuniqueness of the final state.

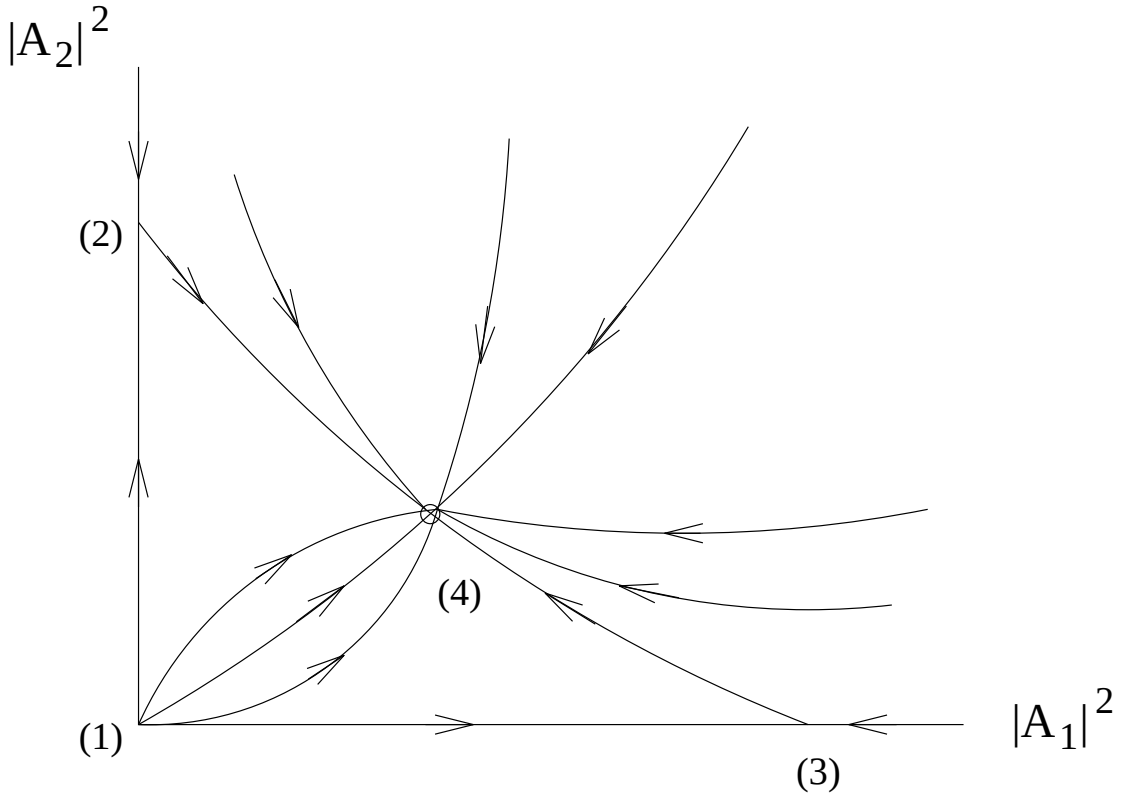

Figure 6.25: Integral curves for weak coupling between modes.

When there is weak coupling between the modes, that is, when $\alpha_{12} < \frac{\sigma_1 l_2}{\sigma_2}$, $\alpha_{12}\alpha_{21} < l_2 l_1$ and $\alpha_{21} < \frac{\sigma_2 l_1}{\sigma_1}$, the integral curves are as shown in Figure 6.25. The two modes do not affect each other much and both evolve to a nonzero final amplitude. This describes the situation of a final state which contains mixed modes, a feature that is not observed in Taylor vortex flow.

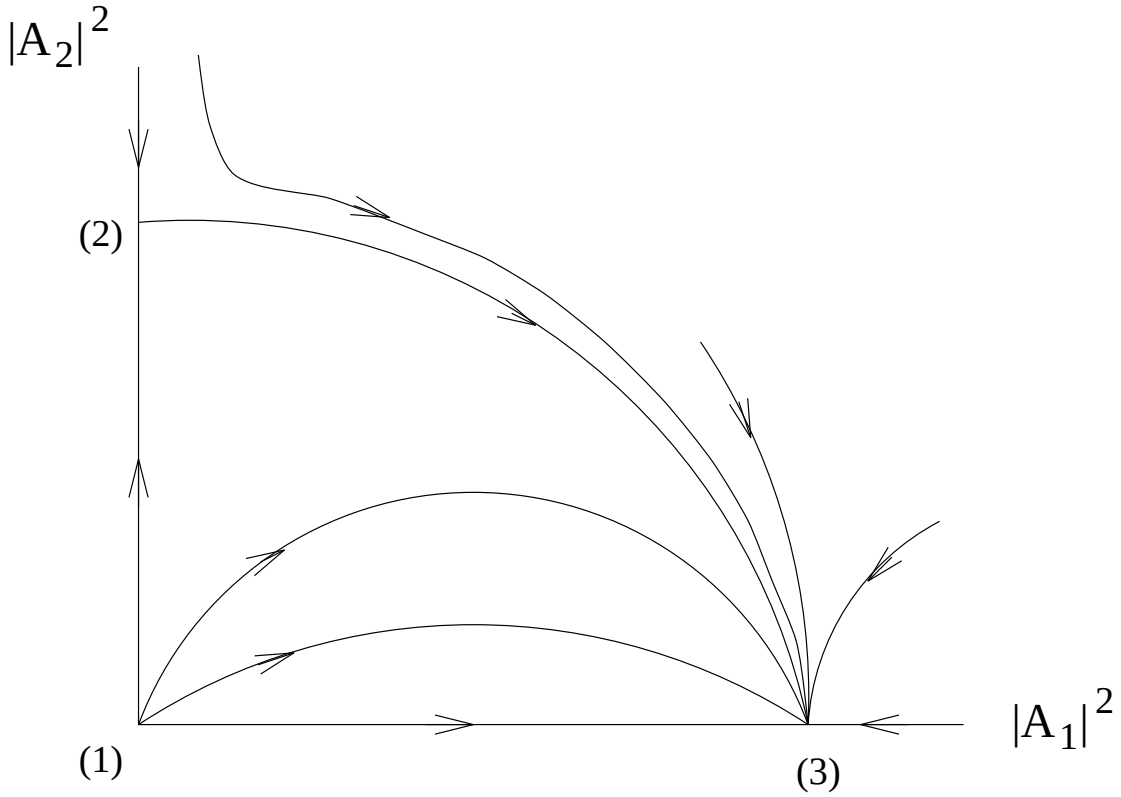

Figure 6.26: Integral curves when mode 1 is unique.

When $\alpha_{12} < \frac{\sigma_1 l_2}{\sigma_2}$, $\alpha_{12}\alpha_{21} > l_2 l_1$ and $\alpha_{21} > \frac{\sigma_2 l_1}{\sigma_1}$, the integral curves are as shown in Figure 6.26. In this case, regardless of the initial conditions, mode 1 is the preferred final mode and mode 2 decays to zero. This represents the case when mode 1 is unique for the two-mode system.

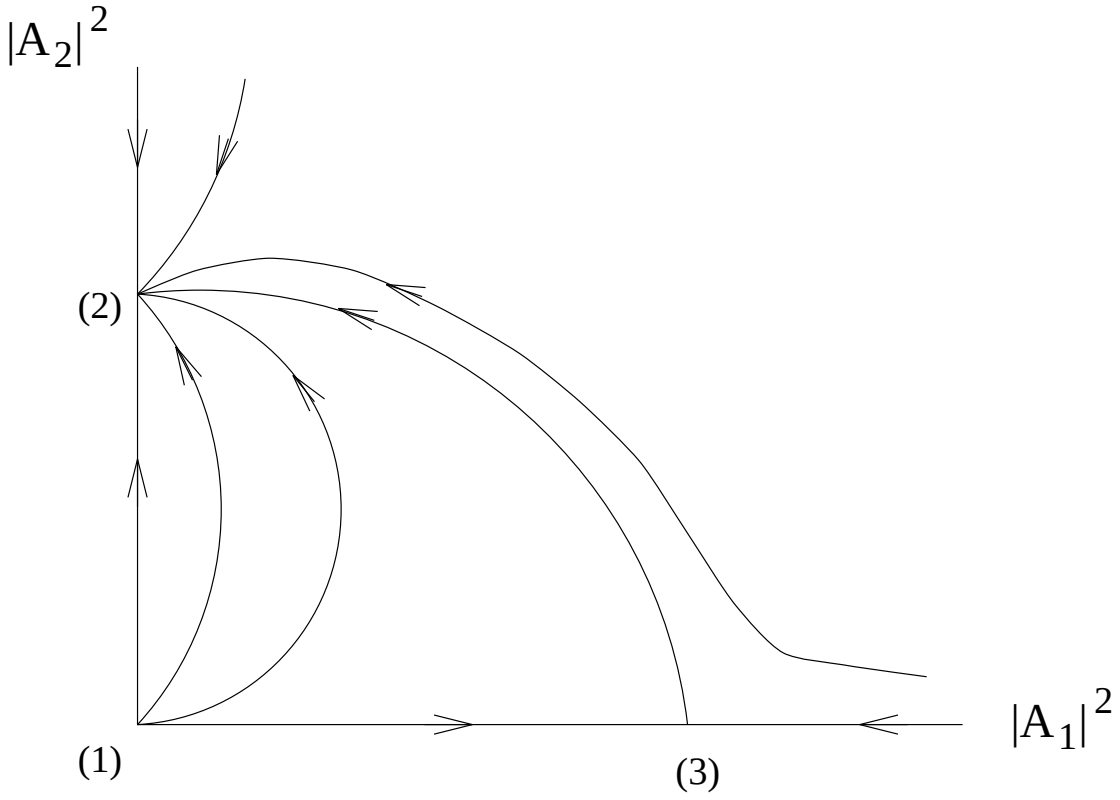

Figure 6.27: Integral curves when mode 2 is unique.

When $\alpha_{12} > \frac{\sigma_1 l_2}{\sigma_2}$, $\alpha_{12}\alpha_{21} > l_2 l_1$ and $\alpha_{21} < \frac{\sigma_2 l_1}{\sigma_1}$, the integral curves are as shown in Figure 6.27. In this case, regardless of the initial conditions, mode 2 is the preferred final mode and mode 1 decays to zero. This represents the case when mode 2 is unique for the two-mode system.

6.6.2 Nonlinear model for N coupled modes.

Extending the nonlinear model to N modes, the amplitudes $A_i(t)$ are described by the amplitude equations

$$\frac{dA_i}{dt} = \sigma_i A_i - l_i A_i |A_i|^2 - \sum_{j=1, j\neq i}^{N} \alpha_{ij} A_i |A_j|^2 \quad \text{for} \quad i = 1, ..., N \tag{24}$$

In Equation (24), σ_i is the growth rate and l_i is the Landau constant for each mode. The linear terms on the right hand side represents the initial stage of exponential growth of the amplitude of each mode. The second terms represents the nonlinear self-interaction of mode i. The third terms represent the nonlinear interaction of mode i with the other modes j.

One can envisage an N-dimensional phase space spanned by $\{\ |A_1|^2, |A_2|^2, ..., |A_N|^2\ \}$. Solving Equation (24) for $\frac{d|A_i|^2}{dt} = 0$ gives the coordinates of all the equilibrium points. In a similar manner to the two-mode system, if in the N-mode system the coupling constants α_{ij} satisfy some set of strong coupling conditions then we obtain N stable equilibrium points in the phase space.

We can now try to perceive the N stable equilibrium points as a model for discrete set of N possible Taylor vortex flows within the Eckhaus stable band. The N-mode system is nonunique because the coupling constants are sufficiently strong, in a similar manner to the 2-mode system. The strong coupling conditions can themselves be viewed as conditions for nonuniqueness of the N-mode system. Which state is preferred depends on the initial conditions. Again, similar to the 2-mode system, there are also conditions for the coupling constants which, when satisfied, would lead to uniqueness of a particular mode.

6.6.3 Resonant three-wave interactions.

The N-mode system of amplitude equations can be improved to

$$\frac{dA_i}{dt} = \sigma_i A_i - l_i A_i |A_i|^2 - \sum_{j=1, j\neq i}^{N} \alpha_{ij} A_i |A_j|^2 + \sum_{j,q} \beta_{jq} A_j^* A_q^* \tag{25}$$

where the quadratic nonlinearity in the last term models resonant three-wave interactions. The index q is taken over all harmonics and is such that the resonance condition is satisfied, namely

$$i + j = q \tag{26}$$

Consider the the Eckhaus mechanism of instability of a Taylor vortex flow with a fundamental mode k and first harmonic $q = 2k$. When there are side-band perturbations with modes i and j such that $i + j = 2k$, these perturbations resonate with the first harmonic and mutually reinforce each other, destabilizing the Taylor vortex flow. However, when we consider a Taylor vortex flow within the Eckhaus stable band, the resonances still occur but they are not strong enough to destabilize the flow.

Resonance effects on many of the modes are also observed in the Figures 6.9 to 6.15 where the Reynolds number was linearly increased in time. In regions of time close and prior to the saturation of the preferred mode, the lower amplitude modes exhibited large accelerations followed by a much slower tendency to decay.

We can illustrate the effect of the quadratic terms with a simple model. Consider amplitude equations for four modes, the initial conditions being such that $A_F(0) \gg A_H(0) \gg A_1(0) \gg A_2(0)$:

$$\frac{d|A_F|}{dt} = \sigma_F |A_F| \tag{27}$$

$$\frac{d|A_H|}{dt} = \sigma_H |A_H| \tag{28}$$

$$\frac{d|A_1|}{dt} = \sigma_1 |A_1| + \beta_{H,2} |A_H| . |A_2| \tag{29}$$

$$\frac{d|A_2|}{dt} = \sigma_2 |A_2| + \beta_{H,1} |A_H| . |A_1| \tag{30}$$

where $|A_F|$, $|A_H|$, $|A_1|$ and $|A_2|$ refer to the magnitudes of the fundamental mode, its first harmonic, a perturbed mode 1 and a perturbed mode 2, respectively. The perturbed modes must satisfy resonance conditions, namely $i_1 + i_2 = i_H$. In Equation (25), the quadratic terms are complex conjugates, whereas in Equations (29) and (30) it was assumed for simplicity that the phases satisfy $\phi_1 + \phi_2 = -\phi_H$ and cancel out.

Initially, mode 2 grows as $\exp(\sigma_2 t)$. When the amplitude of mode 2 is large enough, the quadratic terms will make the amplitude grow as $\exp((\sigma_H + \sigma_1)t)$. As $\sigma_H + \sigma_1 \gg \sigma_2$, at some point in time following the initial exponential growth of mode 2 we begin to see a rapid exponential growth. This is demonstrated in Figure 6.28 with selected values of the coefficients. By inspection of Equation (30), the smaller $|A_2(0)|$ is relative to $|A_H(0)|$ and $|A_1(0)|$, the earlier the rapid exponential growth begins for mode 2.

We can extend the previous simple equations to include cubic coupling terms:

$$\frac{d|A_F|}{dt} = \sigma_F|A_F| - l_F|A_F|^3 \tag{31}$$

$$\frac{d|A_H|}{dt} = \sigma_H|A_H| - l_H|A_H|^3 \tag{32}$$

$$\frac{d|A_1|}{dt} = \sigma_1|A_1| - \alpha_{1,F}|A_1|.|A_F|^2 + \beta_{H,2}|A_H|.|A_2| \tag{33}$$

$$\frac{d|A_2|}{dt} = \sigma_2|A_2| - \alpha_{2,F}|A_2|.|A_F|^2 + \beta_{H,1}|A_H|.|A_1| \tag{34}$$

where a demonstration is shown in Figure 6.29. Again, the region of rapid exponential growth for mode 2 is evident, however, strong coupling of the perturbed modes 1 and 2 to the fundamental mode cause both perturbed modes to decay.

In practise one would expect many quadratic terms in the amplitude equation to account for resonances with different modes and harmonics.

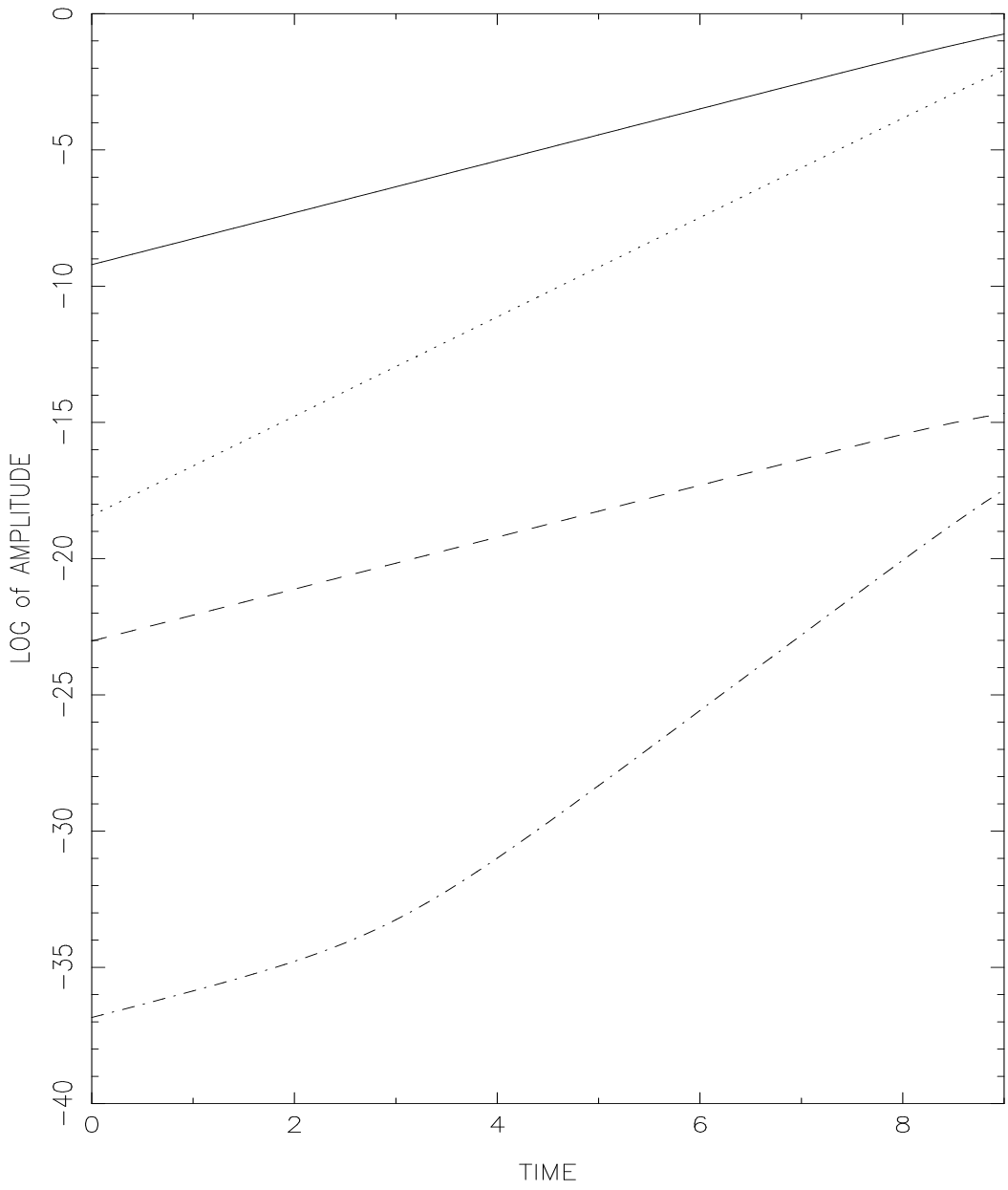

Figure 6.28: A demonstration of $log_e|A|$ versus t for four modes showing the rapid exponential growth of mode 2 following its initial slower exponential growth.

———— fundamental mode, ... first harmonic,

– – – – – perturbation mode 1, – · – · – perturbation mode 2.

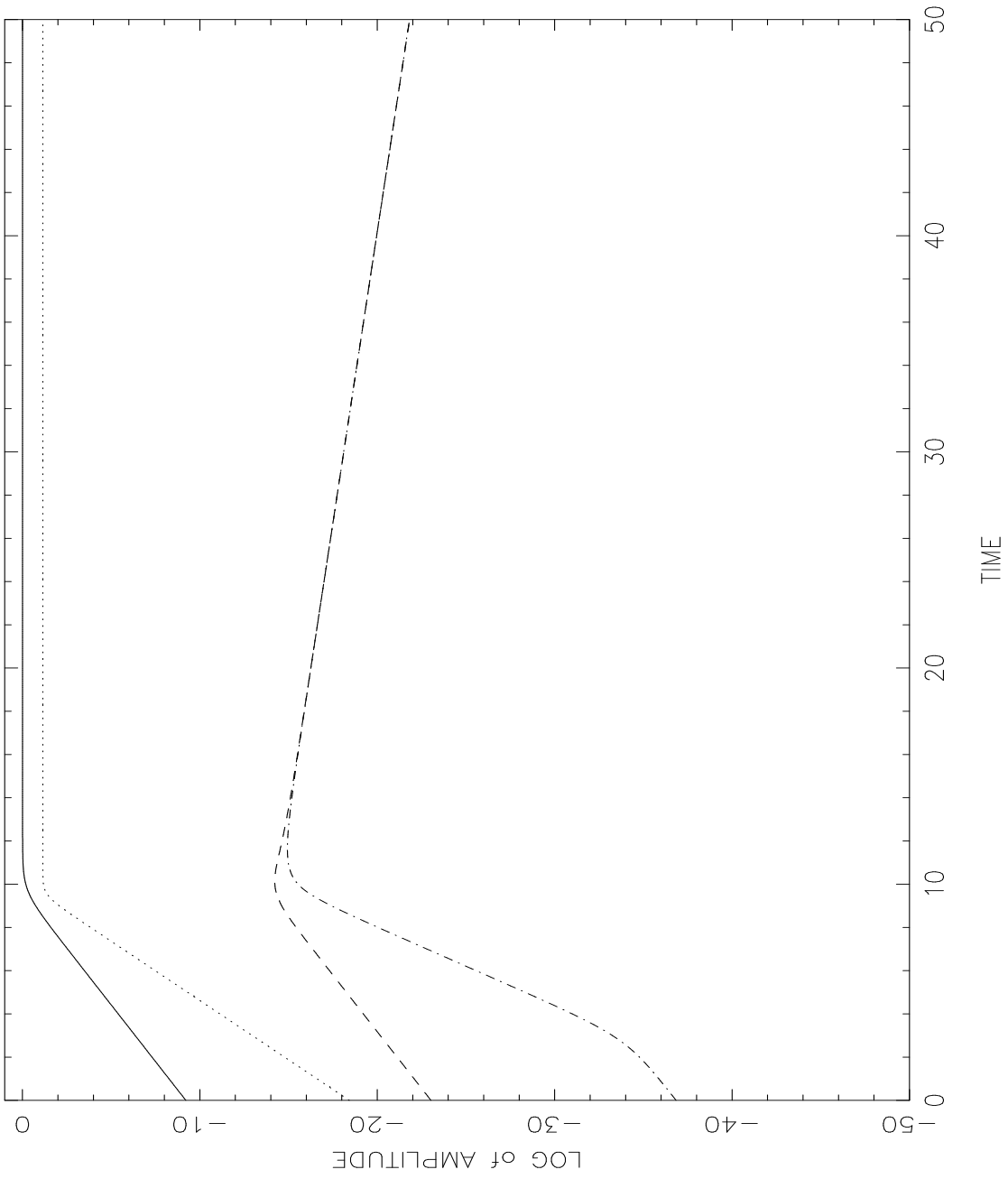

Figure 6.29: A demonstration of $log_e|A|$ versus t for four modes showing nonlinear effects.

———— fundamental mode, ... first harmonic,

– – – – – perturbation mode 1, – · – · – perturbation mode 2.

6.7 Nonlinear amplitude equations for linearly increased $Re(t)$.

In Equation (25), we can replace σ_i with $\sigma_i(t)$, defined by Equation (13). As a first approach we can assume that l_i, α_{ij} and β_{jq} do not vary with Re, although more numerical runs will be needed to determine the degree to which this is valid. However, it is a reasonable assumption considering that the Reynolds number is assumed to be not far from the critical value. In theory therefore, one can use amplitude equations in an attempt to reproduce the behaviour of the amplitude of the modes with ramp time, and compare with the results from numerical simulations.

As a reminder, the aspect ratio was set to $\Gamma = 10\lambda_c$. In the vicinity of λ_c the discrete axial wavelengths 2.2254, 2.00286, 1.82078, 1.66905 and 1.54066 correspond to the modes 9, 10, 11, 12 and 13, respectively.

In Figures 6.9 to 6.12 the preferred mode is mode 11. In these figures, during the ramp the log of the amplitude of mode 12 varies quadratically with time whilst its amplitude is small, followed by a rapid acceleration prior to the saturation of mode 11. It is suggested that this is partly due to the first harmonic ($i_H = 22$) of the fundamental mode ($i_F = 11$) interacting simultaneously with the smaller amplitude modes $i_1 = 10$ and $i_2 = 12$, bringing about a mutual reinforcement or resonance of these two modes (since the condition under which the resonance occurs is satisfied). One also expects mutual reinforcements of modes $i_1 = 9$ and $i_2 = 13$, $i_1 = 8$ and $i_2 = 14$, and so on. These resonances are a result of interactions with the first harmonic of the mode 11. These are also manifested as rapid accelerations prior to the saturation of the fundamental mode.

In Figures 6.14 and 6.15 the preferred mode is mode 10. In these figures, the first harmonic ($i_H = 20$) of the fundamental mode ($i_F = 10$) interacts simultaneously with the smaller amplitude modes $i_1 = 11$ and $i_2 = 9$ bringing about a mutual reinforcement of these two modes. With respect to the first harmonic of mode 10, resonances are also expected for $i_1 = 8$ and $i_2 = 12$, $i_1 = 7$ and $i_2 = 13$, and so on.

It is also noticed that the lower the amplitude of the unpreferred mode, the earlier it

begins to accelerate. This feature is accounted for by the quadratic term in Equation (30) if the lower amplitude mode is i_2.

Although we have discussed resonances with respect to interactions with the first harmonic of the preferred mode there are also contributions to the resonance due to interactions with the first harmonics of the other modes.

6.7.1 Nonuniqueness and uniqueness.

The nonlinear amplitude equations model the behaviour of the amplitude of the modes with ramp time, and the change in preferred mode with ramp time.

Consider the situation of fixed initial conditions and variable ramp time. Using the two-mode system with the quadratic terms ignored for simplicity, we get

$$\frac{dA_{10}}{dt} = \sigma_{10}(t)A_{10} - l_{10}A_{10}|A_{10}|^2 - \alpha_{10,11}A_{10}|A_{11}|^2 \tag{35}$$

$$\frac{dA_{11}}{dt} = \sigma_{11}(t)A_{11} - l_{11}A_{11}|A_{11}|^2 - \alpha_{11,10}A_{11}|A_{10}|^2 \tag{36}$$

where we are modelling modes 10 and 11 in the numerical simulations. Again, mode 10 refers to the mode with the critical wavelength.

The coordinates of the four equilibrium points are similar to those defined in Section 6.6.1, however, they now vary with time during the ramp as do the growth rates. The equilibrium points are given by

(1) $|A_{10}|^2 = 0$, $|A_{11}|^2 = 0$

(2) $|A_{10}|^2 = 0$, $|A_{11}|^2 = \sigma_{11}(t)/l_{11}$

(3) $|A_{10}|^2 = \sigma_{10}(t)/l_{10}$, $|A_{11}|^2 = 0$

(4) $|A_{10}|^2 = (\sigma_{10}(t) - \frac{\alpha_{10,11}}{l_{11}}\sigma_{11}(t))/(l_{10} - \frac{\alpha_{11,10}\alpha_{10,11}}{l_{11}})$

and $|A_{11}|^2 = (\sigma_{11}(t) - \frac{\alpha_{11,10}}{l_{10}}\sigma_{10}(t))/(l_{11} - \frac{\alpha_{11,10}\alpha_{10,11}}{l_{10}})$

The ramp begins at a subcritical Reynolds number where the growth rates for both modes are negative. Initially the only stable state is given by equilibrium point (1). That is, all integral curves in the phase space spanned by $\{|A_{10}|^2, |A_{11}|^2\}$ tend to the point given

by (1). This state represents steady circular Couette flow. As Re increases during the ramp point (1) remains the only stable state as long as Re is subcritical.

As Re exceeds the critical values for modes 10 and 11, in turn, two new stable equilibrium states appear given by points (3) and (2) whilst point (1) becomes an unstable state. Also, equilibrium point (4) appears which is a saddle-point by nature. At this stage in time there is a region in the phase space where integral curves lead to state (3) and a region where integral curves lead to state (2), similar to Figure 6.24. Thus, the two-mode system is exhibiting nonuniqueness.

As Re continues to grow linearly, the growth rates and the coordinates of the points (2), (3) and (4) also grow linearly in the phase space. The two stable states and saddle point therefore continue to exist. For faster ramps the two-mode system continues to exhibit nonuniqueness. However, for slower ramps the integral curve pattern changes in that the region where curves lead to state (3) increases and the region where curves lead to state (2) narrows out. For sufficiently slow ramps all integral curves lead to state (3), rendering this state, which has the critical wavelength, unique. This effect of the ramp on the integral curves was previously explained in terms of a mode-dependent time delay in the growth of each mode.

This argument can be extended to account for an N-mode system in an N-dimensional phase space. As the ramp time is lengthened, more integral curves lead to the state with the critical wavelength than the other states. Thus for sufficiently long ramp times the integral curve pattern will be deformed to the situation where all integral curves lead to the state with the critical wavelength, exhibiting uniqueness.

7 Numerical Method For Taylor-Couette Flow.

The numerical method for Taylor vortex flow was extended to three dimensions in the development of a numerical method for Taylor-Couette flow.

7.1 The classical operator splitting scheme.

The operator splitting procedure treats the non-linear term, the pressure term and the viscous terms separately. The velocity, $\mathbf{u}(z, \phi, r, t)$ is advanced from time step l to time step $l+1$ using three fractional steps. The following is a classical (first order) operator splitting scheme as derived from Karniadakis (1991). We proceed from the equations for Taylor-Couette flow described in Chapter 3.

The first fractional step accounts for the non-linear term and uses an explicit, second order Adams-Bashforth approximation :

$$u_r^{l+\frac{1}{3}} = u_r^l + \Delta t \left(\frac{3}{2} N_r(\mathbf{u}^l) - \frac{1}{2} N_r(\mathbf{u}^{l-1}) \right) \tag{1}$$

$$u_\phi^{l+\frac{1}{3}} = u_\phi^l + \Delta t \left(\frac{3}{2} N_\phi(\mathbf{u}^l) - \frac{1}{2} N_\phi(\mathbf{u}^{l-1}) \right) \tag{2}$$

$$u_z^{l+\frac{1}{3}} = u_z^l + \Delta t \left(\frac{3}{2} N_z(\mathbf{u}^l) - \frac{1}{2} N_z(\mathbf{u}^{l-1}) \right) \tag{3}$$

The second fractional step is due to the pressure term contribution:

$$u_r^{l+\frac{2}{3}} = u_r^{l+\frac{1}{3}} - \Delta t \frac{\partial P}{\partial r}^{l+1} \tag{4}$$

$$u_\phi^{l+\frac{2}{3}} = u_\phi^{l+\frac{1}{3}} - \Delta t \frac{1}{r+\gamma} \frac{\partial P}{\partial \phi}^{l+1} \tag{5}$$

$$u_z^{l+\frac{2}{3}} = u_z^{l+\frac{1}{3}} - \Delta t \frac{\partial P}{\partial z}^{l+1} \tag{6}$$

These are explicit forward Euler approximations. The pressure P^{l+1} is solved using the Poisson equation:

$$\frac{1}{r+\gamma}\frac{\partial P}{\partial r}^{l+1} + \frac{\partial^2 P}{\partial r^2}^{l+1} + \frac{1}{(r+\gamma)^2}\frac{\partial^2 P}{\partial \phi^2}^{l+1} + \frac{\partial^2 P}{\partial z^2}^{l+1}$$
$$= \frac{1}{\Delta t}\left(\frac{1}{r+\gamma}u_r^{l+1/3} + \frac{\partial u_r}{\partial r}^{l+1/3} + \frac{1}{r+\gamma}\frac{\partial u_\phi}{\partial \phi}^{l+1/3} + \frac{\partial u_z}{\partial z}^{l+1/3}\right) \quad (7)$$

which is obtained by applying the incompressibility constraint (Equation (8) in Chapter 3) at time step $l+2/3$ and using Equations (4) to (6). We multiply both sides of Equation (7) by $(r+\gamma)^2$ to get:

$$(r+\gamma)\frac{\partial P}{\partial r}^{l+1} + (r+\gamma)^2\frac{\partial^2 P}{\partial r^2}^{l+1} + \frac{\partial^2 P}{\partial \phi^2}^{l+1} + (r+\gamma)^2\frac{\partial^2 P}{\partial z^2}^{l+1}$$
$$= \frac{1}{\Delta t}\left((r+\gamma)u_r^{l+1/3} + (r+\gamma)^2\frac{\partial u_r}{\partial r}^{l+1/3} + (r+\gamma)\frac{\partial u_\phi}{\partial \phi}^{l+1/3}\right.$$
$$+ \left.(r+\gamma)^2\frac{\partial u_z}{\partial z}^{l+1/3}\right) \quad (8)$$

A further assumption is that $\mathbf{u}^{l+2/3}$ satisfies the prescribed boundary conditions in the directions normal to the boundaries (cylinder walls):

$$u_r^{l+2/3}(z,\phi,\pm 1,t) = 0 \quad (9)$$

From Equation (4), this implies that Neumann boundary conditions can be imposed:

$$\frac{\partial P}{\partial r}^{l+1} = \frac{1}{\Delta t}u_r^{l+1/3} \qquad \text{at } r = \pm 1 \quad (10)$$

Periodicity in the pressure is assumed in the axial and azimuthal directions.

The third fractional step is the viscous step:

$$u_r^{l+1} = u_r^{l+\frac{2}{3}} + \frac{\Delta t}{Re}L_r(\mathbf{u}^{l+1}) \quad (11)$$

$$u_\phi^{l+1} = u_\phi^{l+\frac{2}{3}} + \frac{\Delta t}{Re}L_\phi(\mathbf{u}^{l+1}) \quad (12)$$

$$u_z^{l+1} = u_z^{l+\frac{2}{3}} + \frac{\Delta t}{Re}L_z(\mathbf{u}^{l+1}) \quad (13)$$

where an implicit, backwards Euler approximation is made. Equations (11) to (13) are each in the form of an Helmholtz equation. We multiply both sides of Equations (11) to (13) by $(r+\gamma)^2$ to get:

$$\begin{aligned}&(r+\gamma)\frac{\partial u_r}{\partial r}^{l+1} + (r+\gamma)^2\frac{\partial^2 u_r}{\partial r^2}^{l+1} + \frac{\partial^2 u_r}{\partial \phi^2}^{l+1} - 2\frac{\partial u_\phi}{\partial \phi}^{l+1} + (r+\gamma)^2\frac{\partial^2 u_r}{\partial z^2}^{l+1} \\ - &\left(\frac{Re}{\Delta t}(r+\gamma)^2+1\right)u_r^{l+1} = -\frac{Re}{\Delta t}(r+\gamma)^2 u_r^{l+2/3}\end{aligned} \tag{14}$$

$$\begin{aligned}&(r+\gamma)\frac{\partial u_\phi}{\partial r}^{l+1} + (r+\gamma)^2\frac{\partial^2 u_\phi}{\partial r^2}^{l+1} + \frac{\partial^2 u_\phi}{\partial \phi^2}^{l+1} + 2\frac{\partial u_r}{\partial \phi}^{l+1} + (r+\gamma)^2\frac{\partial^2 u_\phi}{\partial z^2}^{l+1} \\ - &\left(\frac{Re}{\Delta t}(r+\gamma)^2+1\right)u_\phi^{l+1} = -\frac{Re}{\Delta t}(r+\gamma)^2 u_\phi^{l+2/3}\end{aligned} \tag{15}$$

$$\begin{aligned}&(r+\gamma)\frac{\partial u_z}{\partial r}^{l+1} + (r+\gamma)^2\frac{\partial^2 u_z}{\partial r^2}^{l+1} + \frac{\partial^2 u_z}{\partial \phi^2}^{l+1} + (r+\gamma)^2\frac{\partial^2 u_z}{\partial z^2}^{l+1} \\ - &\frac{Re}{\Delta t}(r+\gamma)^2 u_z^{l+1} = -\frac{Re}{\Delta t}(r+\gamma)^2 u_z^{l+2/3}\end{aligned} \tag{16}$$

These Helmholtz equations can each be solved with the following respective Dirichlet boundary conditions:

$$u_r^{l+1}(z,\phi,\pm 1,t) = 0 \tag{17}$$

$$u_\phi^{l+1}(z,\phi,-1,t) = 1 \qquad \text{and} \qquad u_\phi^{l+1}(z,\phi,1,t) = \mu/\eta \tag{18}$$

$$u_z^{l+1}(z,\phi,\pm 1,t) = 0 \tag{19}$$

Periodic boundary conditions is assumed in the axial and azimuthal direction for each of these velocity components.

7.2 Higher order splitting schemes

This section is basically an extension of Section 5.2. The points referring to the values of the coefficients and the order of the scheme for each fractional step also apply here. Following Karniadakis (1991), the non-linear terms are approximated via an explicit scheme, for example, a J_e-order scheme from the Adams-Bashforth family as follows,

$$u_r^{l+1/3} = u_r^l + \Delta t \sum_{q=0}^{J_e-1} \beta_q N_r(\mathbf{u}^{l-q}) \tag{20}$$

$$u_\phi^{l+1/3} = u_\phi^l + \Delta t \sum_{q=0}^{J_e-1} \beta_q N_\phi(\mathbf{u}^{l-q}) \tag{21}$$

$$u_z^{l+1/3} = u_z^l + \Delta t \sum_{q=0}^{J_e-1} \beta_q N_z(\mathbf{u}^{l-q}) \tag{22}$$

The linear (viscous) terms are approximated via an implicit scheme, for example, a J_i-order scheme from the Adams-Moulton family as follows

$$u_r^{l+1} = u_r^{l+\frac{2}{3}} + \frac{\Delta t}{Re} \sum_{q=0}^{J_i-1} \gamma_q L_r(\mathbf{u}^{l+1-q}) \tag{23}$$

$$u_\phi^{l+1} = u_\phi^{l+\frac{2}{3}} + \frac{\Delta t}{Re} \sum_{q=0}^{J_i-1} \gamma_q L_\phi(\mathbf{u}^{l+1-q}) \tag{24}$$

$$u_z^{l+1} = u_z^{l+\frac{2}{3}} + \frac{\Delta t}{Re} \sum_{q=0}^{J_i-1} \gamma_q L_z(\mathbf{u}^{l+1-q}) \tag{25}$$

From Equations (23) to (25), the Helmholtz equations for the three components of velocity in the viscous step become

$$\begin{aligned}
& (r+\gamma)\frac{\partial u_r}{\partial r}^{l+1} + (r+\gamma)^2\frac{\partial^2 u_r}{\partial r^2}^{l+1} + \frac{\partial^2 u_r}{\partial \phi^2}^{l+1} - 2\frac{\partial u_\phi}{\partial \phi}^{l+1} + (r+\gamma)^2\frac{\partial^2 u_r}{\partial z^2}^{l+1} \\
- & \left(\frac{1}{\gamma_0}\frac{Re}{\Delta t}(r+\gamma)^2 + 1\right) u_r^{l+1} = -\frac{1}{\gamma_0}\frac{Re}{\Delta t}(r+\gamma)^2 u_r^{l+2/3} \\
- & \frac{1}{\gamma_0}\sum_{q=1}^{J_i-1}\gamma_q\left[(r+\gamma)\frac{\partial u_r}{\partial r} + (r+\gamma)^2\frac{\partial^2 u_r}{\partial r^2} + \frac{\partial^2 u_r}{\partial \phi^2} - 2\frac{\partial u_\phi}{\partial \phi} + (r+\gamma)^2\frac{\partial^2 u_r}{\partial z^2} - u_r\right]^{(l+1-q)}
\end{aligned}$$

(26)

$$
\begin{aligned}
& (r+\gamma)\frac{\partial u_\phi}{\partial r}^{l+1} + (r+\gamma)^2\frac{\partial^2 u_\phi}{\partial r^2}^{l+1} + \frac{\partial^2 u_\phi}{\partial \phi^2}^{l+1} + 2\frac{\partial u_r}{\partial \phi}^{l+1} + (r+\gamma)^2\frac{\partial^2 u_\phi}{\partial z^2}^{l+1} \\
- & \left(\frac{1}{\gamma_0}\frac{Re}{\Delta t}(r+\gamma)^2+1\right)u_\phi^{l+1} = -\frac{1}{\gamma_0}\frac{Re}{\Delta t}(r+\gamma)^2 u_\phi^{l+2/3} \\
- & \frac{1}{\gamma_0}\sum_{q=1}^{J_i-1}\gamma_q\left[(r+\gamma)\frac{\partial u_\phi}{\partial r} + (r+\gamma)^2\frac{\partial^2 u_\phi}{\partial r^2} + \frac{\partial^2 u_\phi}{\partial \phi^2} + 2\frac{\partial u_r}{\partial \phi} + (r+\gamma)^2\frac{\partial^2 u_\phi}{\partial z^2} - u_\phi\right]^{(l+1-q)}
\end{aligned}
\tag{27}
$$

$$
\begin{aligned}
& (r+\gamma)\frac{\partial u_z}{\partial r}^{l+1} + (r+\gamma)^2\frac{\partial^2 u_z}{\partial r^2}^{l+1} + \frac{\partial^2 u_z}{\partial \phi^2}^{l+1} + (r+\gamma)^2\frac{\partial^2 u_z}{\partial z^2}^{l+1} \\
- & \frac{1}{\gamma_0}\frac{Re}{\Delta t}(r+\gamma)^2 u_z^{l+1} = -\frac{1}{\gamma_0}\frac{Re}{\Delta t}(r+\gamma)^2 u_z^{l+2/3} \\
- & \frac{1}{\gamma_0}\sum_{q=1}^{J_i-1}\gamma_q\left[(r+\gamma)\frac{\partial u_z}{\partial r} + (r+\gamma)^2\frac{\partial^2 u_z}{\partial r^2} + \frac{\partial^2 u_z}{\partial \phi^2} + (r+\gamma)^2\frac{\partial^2 u_z}{\partial z^2}\right]^{(l+1-q)}
\end{aligned}
\tag{28}
$$

In the pressure step Equation (8) is solved subject to higher order pressure boundary conditions. That is, instead of using Equation (10) we use an explicit J_p-order scheme,

$$
\frac{\partial P}{\partial r}^{l+1} = \sum_{q=0}^{J_p-1}\beta_q\left[-\frac{1}{Re}\left(\nabla\times(\nabla\times\mathbf{u})\right)_r + N_r(\mathbf{u})\right]^{(l-q)} \tag{29}
$$

which becomes

$$
\begin{aligned}
\frac{\partial P}{\partial r}^{l+1} &= \sum_{q=0}^{J_p-1}\beta_q\left[\frac{1}{Re}\left(\frac{\partial^2 u_r}{\partial z^2} - \frac{\partial^2 u_z}{\partial z\partial r} - \frac{1}{(r+\gamma)^2}\frac{\partial u_\phi}{\partial \phi} - \frac{1}{r+\gamma}\frac{\partial^2 u_\phi}{\partial \phi\partial r} + \frac{1}{r+\gamma}\frac{\partial^2 u_r}{\partial \phi^2}\right)\right. \\
&- \left.\left(u_r\frac{\partial u_r}{\partial r} + \frac{u_\phi}{r+\gamma}\frac{\partial u_r}{\partial \phi} + u_z\frac{\partial u_r}{\partial z} - \frac{{u_\phi}^2}{r+\gamma}\right)\right]^{(l-q)}
\end{aligned}
\tag{30}
$$

Equation (30) is used to set the Neumann boundary conditions at $r = \pm 1$.

7.3 Spectral methods

A Tau spectral method is described below with a Fourier approximation in the axial direction (z), a Fourier approximation in the azimuthal direction (ϕ) and a Chebyshev approximation in the radial (r) direction, that solves for:

(1) the Poisson equation for the pressure in the pressure step using Neumann boundary conditions in r and periodic boundary conditions in z and ϕ,

(2) the coupled Helmholtz equations for the radial and azimuthal velocity components in the viscous step using Dirichlet boundary conditions in r and periodic boundary conditions in z and ϕ, and,

(3) the Helmholtz equation for the axial velocity component in the viscous step using Dirichlet boundary conditions in r and periodic boundary conditions in z and ϕ.

7.3.1 Spatial discretization of the grid

A discrete Fourier-Fourier-Chebyshev approximation of a function $P(z, \phi, r)$ is

$$P(z,\phi,r) = \sum_{m=-M/2}^{M/2-1} \sum_{l=-L/2}^{L/2-1} \sum_{n=0}^{N} P_{mln} T_n(r) \exp(il\phi) \exp(imz) \tag{31}$$

where there are $N+1$ radial Chebyshev-Gauss-Lobatto points, L azimuthal Fourier points and M axial Fourier points. The remarks made in Section 5.3.1 with respect to the radial and axial directions also apply here. In addition, in the azimuthal direction there are L equidistant points defined by

$$\phi_j = \frac{2\pi}{L} j \qquad \text{for} \quad j = 0, ..., L-1 \tag{32}$$

If wavy vortex flow of a particular azimuthal wavenumber l_{az} is to be simulated, the azimuthal span can be redefined as $0 \leq \phi \leq 2\pi/l_{az}$ and azimuthal periodicity can be used to extend the solution to $0 \leq \phi \leq 2\pi$. This would reduce the overall computational cost. In this case, there are L equidistant points in the azimuthal direction defined by

$$\phi_j = \frac{2\pi}{l_{az} L} j \qquad \text{for} \quad j = 0, ..., L-1 \tag{33}$$

and the factor $\exp(il\phi)$ in Equation (31) is replaced with $\exp(il_{az}l\phi)$

The numerical method for the solvers will be now be described with respect to definition in Equation (31).

7.3.2 Poisson solver for pressure

The Poisson equation for the pressure $P(z, \phi, r)$ at each time step, has the form

$$(r+\gamma)\frac{\partial P}{\partial r} + (r+\gamma)^2\frac{\partial^2 P}{\partial r^2} + \frac{\partial^2 P}{\partial \phi^2} + (r+\gamma)^2\frac{\partial^2 P}{\partial z^2} = F(z, \phi, r) \tag{34}$$

where the Neumann boundary conditions have the form

$$\frac{\partial P}{\partial r} = \alpha(z, \phi) \qquad \text{at } r = -1 \tag{35}$$

$$\frac{\partial P}{\partial r} = \beta(z, \phi) \qquad \text{at } r = 1 \tag{36}$$

and periodic boundary conditions are applied in the axial and azimuthal directions.

For each l, where $-L/2 \leq l \leq L/2 - 1$, Equation (34) in matrix form in spectral space can be written as

$$P(DC + D^2C^2) - l^2P - m^2PC^2 = F \tag{37}$$

where $-M/2 \leq m \leq M/2 - 1$.

The $(N+1) \times (N+1)$ matrices D, D^2, C and C^2 are defined in Sections 5.3.2 and 5.3.3. The $M \times L \times (N+1)$ matrices P and F contain the spectral coefficients P_{mln} and F_{mln}, which are complex numbers in general.

A discrete Fourier-Fourier approximation of a function $\alpha(z, \phi)$ is

$$\alpha(z, \phi) = \sum_{m=-M/2}^{M/2-1} \sum_{l=-L/2}^{L/2-1} \alpha_{ml} \exp(il\phi) \exp(imz) \tag{38}$$

where the spectral coefficients α_{ml} are complex numbers in general.

The spectral form of the boundary conditions can be written as:

$$\sum_{n=0}^{N} n^2 P_{R,mln} = \beta_{R,ml} \tag{39}$$

$$\sum_{n=0}^{N}(-1)^{n+1}n^2P_{R,mln} = \alpha_{R,ml} \tag{40}$$

$$\sum_{n=0}^{N}n^2P_{I,mln} = \beta_{I,ml} \tag{41}$$

$$\sum_{n=0}^{N}(-1)^{n+1}n^2P_{I,mln} = \alpha_{I,ml} \tag{42}$$

for $-M/2 \leq m \leq M/2-1$ and $-L/2 \leq l \leq L/2-1$. The subscripts R and I denote real and imaginary components, respectively.

Adding and subtracting Equations (39) and (40) we get:

$$\sum_{n=0,\ n\ odd}^{N}n^2P_{R,mln} = \frac{1}{2}(\beta_{R,ml}+\alpha_{R,ml}) = \eta_{R,ml} \tag{43}$$

$$\sum_{n=0,\ n\ even}^{N}n^2P_{R,mln} = \frac{1}{2}(\beta_{R,ml}-\alpha_{R,ml}) = \theta_{R,ml} \tag{44}$$

Adding and subtracting Equations (41) and (42) we get:

$$\sum_{n=0,\ n\ odd}^{N}n^2P_{I,mln} = \frac{1}{2}(\beta_{I,ml}+\alpha_{I,ml}) = \eta_{I,ml} \tag{45}$$

$$\sum_{n=0,\ n\ even}^{N}n^2P_{I,mln} = \frac{1}{2}(\beta_{I,ml}-\alpha_{I,ml}) = \theta_{I,ml} \tag{46}$$

In the matrix Equation (37) we substitute Equation (43) and (45) to eliminate the complex coefficients $P_{m,l,N-1}$ and Equation (44) and (46) to eliminate the complex coefficients $P_{m,l,N}$, for $-M/2 \leq m \leq M/2-1$ and $-L/2 \leq l \leq L/2-1$. Subsequently we obtain the matrix equation

$$P(BC+B^2C^2) - l^2P - m^2PC^2 = f \tag{47}$$

where now P is the portion $-M/2 \leq m \leq M/2-1$, $-L/2 \leq l \leq L/2-1$, $0 \leq n \leq N-2$ of its original definition. The matrices C and C^2 are the portions $0 \leq p \leq N-2$,

$0 \leq q \leq N-2$ of its original definitions. The matrices B and B^2 are both $(N-1)\times(N-1)$ and are defined in Section 5.3.3.

The matrix f has real and imaginary components

$$f_R = F_R - Q_R C - S_R C^2 \tag{48}$$

and

$$f_I = F_I - Q_I C - S_I C^2 \tag{49}$$

where Q_R, Q_I, S_R and S_I are $M \times L \times (N-1)$ matrices with components

$$Q_{R,mln} = \begin{cases} \frac{2}{(N-1)c_n}\eta_{R,ml} & \text{for } n \text{ even} \\ \frac{2}{Nc_n}\theta_{R,ml} & \text{for } n \text{ odd} \end{cases} \tag{50}$$

$$Q_{I,mln} = \begin{cases} \frac{2}{(N-1)c_n}\eta_{I,ml} & \text{for } n \text{ even} \\ \frac{2}{Nc_n}\theta_{I,ml} & \text{for } n \text{ odd} \end{cases} \tag{51}$$

$$S_{R,mln} = \begin{cases} \frac{N^2-n^2}{Nc_n}\theta_{R,ml} & \text{for } n \text{ even} \\ \frac{(N-1)^2-n^2}{(N-1)c_n}\eta_{R,ml} & \text{for } n \text{ odd} \end{cases} \tag{52}$$

$$S_{I,mln} = \begin{cases} \frac{N^2-n^2}{Nc_n}\theta_{I,ml} & \text{for } n \text{ even} \\ \frac{(N-1)^2-n^2}{(N-1)c_n}\eta_{I,ml} & \text{for } n \text{ odd} \end{cases} \tag{53}$$

Equation (47) represents a system with $M\times L\times(N-1)$ equations in the $M\times L\times(N-1)$ complex unknowns, P_{mln}. The solution is determined by taking

$$P_{R,ml} = f_{R,ml}[BC + B^2C^2 - l^2 I_{N-1} - m^2C^2]^{-1} \tag{54}$$

and

$$P_{I,ml} = f_{I,ml}[BC + B^2C^2 - l^2 I_{N-1} - m^2C^2]^{-1} \tag{55}$$

for $-M/2 \leq m \leq M/2-1$ and $-L/2 \leq l \leq L/2-1$. The matrices $P_{R,ml}$, $P_{I,ml}$ and $f_{R,ml}$, $f_{I,ml}$ are the $(m,l)^{th}$ row of the real and imaginary component elements of P and f respectively.

As it stands, the $(N-1) \times (N-1)$ matrix $[BC + B^2C^2 - l^2 I_{N-1} - m^2 C^2]$ is not invertible for $l = 0$, $m = 0$. In this instance, it was decided to set the element $[BC + B^2C^2 - l^2 I_{N-1} - m^2 C^2]_{0,0}$ to a constant (unity) for the case $l = 0$, $m = 0$. The solution for $P(z, \phi, r)$ will be accurate to a constant, which itself does not play a role in the Navier-Stokes equations since it is the pressure gradient that is required. Once the P_{mln} are calculated for $-M/2 \leq m \leq M/2-1$, $-L/2 \leq l \leq L/2-1$ and $0 \leq n \leq N-2$, the P_{mln} for $-M/2 \leq m \leq M/2-1$, $-L/2 \leq l \leq L/2-1$ and $n = N-1, N$ can be determined using Equations (43) to (46). A Fourier-Fourier-Chebyshev inverse transform of P_{mln} will then give the solution for $P(z, \phi, r)$.

7.3.3 Coupled Helmholtz solver for radial and azimuthal component of velocity

The two coupled Helmholtz equations for the radial component of velocity $U(z, \phi, r)$ and azimuthal component of velocity $V(z, \phi, r)$ have the form

$$\begin{aligned}(r+\gamma)\frac{\partial U}{\partial r} + (r+\gamma)^2\frac{\partial^2 U}{\partial r^2} + \frac{\partial^2 U}{\partial \phi^2} - 2\frac{\partial V}{\partial \phi} \\ + \quad (r+\gamma)^2\frac{\partial^2 U}{\partial z^2} - \left(\frac{Re}{\Delta t}(r+\gamma)^2 + 1\right) U = F(z, \phi, r)\end{aligned} \tag{56}$$

and

$$\begin{aligned}(r+\gamma)\frac{\partial V}{\partial r} + (r+\gamma)^2\frac{\partial^2 V}{\partial r^2} + \frac{\partial^2 V}{\partial \phi^2} + 2\frac{\partial U}{\partial \phi} \\ + \quad (r+\gamma)^2\frac{\partial^2 V}{\partial z^2} - \left(\frac{Re}{\Delta t}(r+\gamma)^2 + 1\right) V = G(z, \phi, r)\end{aligned} \tag{57}$$

where the Dirichlet boundary conditions have the form

$$U(z, \phi, -1) = \alpha(z, \phi) \tag{58}$$

$$U(z, \phi, 1) = \beta(z, \phi) \tag{59}$$

$$V(z, \phi, -1) = \alpha(z, \phi) \tag{60}$$

$$V(z, \phi, 1) = \beta(z, \phi) \tag{61}$$

and periodic boundary conditions are assumed in the axial and azimuthal directions.

For each l, where $-L/2 \leq l \leq L/2 - 1$, Equations (56) and (57) in matrix form in spectral space can be written as

$$U(DC + D^2C^2) - l^2U - 2ilV - m^2UC^2 - U\left(\frac{Re}{\Delta t}C^2 + I_{N+1}\right) = F \tag{62}$$

and

$$V(DC + D^2C^2) - l^2V + 2ilU - m^2VC^2 - V\left(\frac{Re}{\Delta t}C^2 + I_{N+1}\right) = G \tag{63}$$

where $-M/2 \leq m \leq M/2 - 1$.

In Equations (62) and (63), the letter i refers to the imaginary component of a complex number. The matrices U and V contain the Fourier-Fourier-Chebyshev spectral coefficients of their corresponding velocity functions. The matrices C and C^2 are defined in Section 5.3.3. The matrices D and D^2 are defined in Section 5.3.4. I_{N+1} is the $(N+1) \times (N+1)$ identity matrix.

Applying a Fourier-Fourier transform to the boundary conditions, in spectral form we have:

$$\sum_{n=0}^{N} U_{R,mln} = \beta_{R,ml} \tag{64}$$

$$\sum_{n=0}^{N}(-1)^n U_{R,mln} = \alpha_{R,ml} \tag{65}$$

$$\sum_{n=0}^{N} U_{I,mln} = \beta_{I,ml} \tag{66}$$

$$\sum_{n=0}^{N}(-1)^n U_{I,mln} = \alpha_{I,ml} \tag{67}$$

and

$$\sum_{n=0}^{N} V_{R,mln} = \psi_{R,ml} \tag{68}$$

$$\sum_{n=0}^{N}(-1)^n V_{R,mln} = \chi_{R,ml} \tag{69}$$

$$\sum_{n=0}^{N} V_{I,mln} = \psi_{I,ml} \tag{70}$$

$$\sum_{n=0}^{N}(-1)^n V_{I,mln} = \chi_{I,ml} \tag{71}$$

where the subscripts R and I denote real and imaginary components respectively.

Adding and subtracting Equations (64) and (65) we get:

$$\sum_{n=0,\ n\ even}^{N} U_{R,mln} = \frac{1}{2}(\beta_{R,ml} + \alpha_{R,ml}) = \eta_{R,ml} \tag{72}$$

$$\sum_{n=0,\ n\ odd}^{N} U_{R,mln} = \frac{1}{2}(\beta_{R,ml} - \alpha_{R,ml}) = \theta_{R,ml} \tag{73}$$

Adding and subtracting Equations (66) and (67) we get:

$$\sum_{n=0,\ n\ even}^{N} U_{I,mln} = \frac{1}{2}(\beta_{I,ml} + \alpha_{I,ml}) = \eta_{I,ml} \tag{74}$$

$$\sum_{n=0,\ n\ odd}^{N} U_{I,mln} = \frac{1}{2}(\beta_{I,ml} - \alpha_{I,ml}) = \theta_{I,ml} \tag{75}$$

Also, doing the equivalent for V gives:

$$\sum_{n=0,\ n\ even}^{N} V_{R,mln} = \frac{1}{2}(\psi_{R,ml} + \chi_{R,ml}) = \delta_{R,ml} \tag{76}$$

$$\sum_{n=0,\ n\ odd}^{N} V_{R,mln} = \frac{1}{2}(\psi_{R,ml} - \chi_{R,ml}) = \zeta_{R,ml} \tag{77}$$

$$\sum_{n=0,\ n\ even}^{N} V_{I,mln} = \frac{1}{2}(\psi_{I,ml} + \chi_{I,ml}) = \delta_{I,ml} \tag{78}$$

$$\sum_{n=0,\ n\ odd}^{N} V_{I,mln} = \frac{1}{2}(\psi_{I,ml} - \chi_{I,ml}) = \zeta_{I,ml} \tag{79}$$

Using Equations (73) and (75) we eliminate the complex coefficients $U_{m,l,N-1}$ and using Equations (72) and (74) we eliminate the complex coefficients $U_{m,l,N}$. Similarly, using Equations (77) and (79) we eliminate the complex coefficients $V_{m,l,N-1}$ and using Equations (76) and (78) we eliminate the complex coefficients $V_{m,l,N}$.

Equations (62) and (63) then become

$$U(BC + B^2C^2) - l^2U - 2ilV - m^2UC^2 - U\left(\frac{Re}{\Delta t}C^2 + I_{N-1}\right) = f \tag{80}$$

and

$$V(BC + B^2C^2) - l^2V + 2ilU - m^2VC^2 - V\left(\frac{Re}{\Delta t}C^2 + I_{N-1}\right) = g \tag{81}$$

where U and V are portions $M \times L \times (N-1)$ of their original definitions. The matrices are the $(N-1)\times(N-1)$ portion of their original definitions. I_{N-1} is the $(N-1)\times(N-1)$ identity matrix. The $(N-1) \times (N-1)$ matrices B and B^2 are defined in Section 5.3.4.

The matrix f has real and imaginary components

$$f_R = F_R - Q_RC - S_RC^2 \tag{82}$$

and

$$f_I = F_I - Q_I C - S_I C^2 \tag{83}$$

where Q_R, Q_I, S_R and S_I are $M \times L \times (N-1)$ matrix with components

$$Q_{R,mln} = \begin{cases} \frac{2(N-1)}{c_n}\theta_{R,ml} & \text{for } n \text{ even} \\ \frac{2N}{c_n}\eta_{R,ml} & \text{for } n \text{ odd} \end{cases} \tag{84}$$

$$Q_{I,mln} = \begin{cases} \frac{2(N-1)}{c_n}\theta_{I,ml} & \text{for } n \text{ even} \\ \frac{2N}{c_n}\eta_{I,ml} & \text{for } n \text{ odd} \end{cases} \tag{85}$$

$$S_{I,mln} = \begin{cases} \frac{N(N^2-n^2)}{c_n}\eta_{R,ml} & \text{for } n \text{ even} \\ \frac{(N-1)((N-1)^2-n^2)}{c_n}\theta_{R,ml} & \text{for } n \text{ odd} \end{cases} \tag{86}$$

$$S_{I,mln} = \begin{cases} \frac{N(N^2-n^2)}{c_n}\eta_{I,ml} & \text{for } n \text{ even} \\ \frac{(N-1)((N-1)^2-n^2)}{c_n}\theta_{I,ml} & \text{for } n \text{ odd} \end{cases} \tag{87}$$

Similarly, the $M \times L \times (N-1)$ matrix g has real and imaginary components

$$g_R = G_R - E_R C - H_R C^2 \tag{88}$$

and

$$g_I = G_I - E_I C - H_I C^2 \tag{89}$$

where E_R, E_I, H_R and H_I are $M \times L \times (N-1)$ matrices with components

$$E_{R,mln} = \begin{cases} \frac{2(N-1)}{c_n}\zeta_{R,ml} & \text{for } n \text{ even} \\ \frac{2N}{c_n}\delta_{R,ml} & \text{for } n \text{ odd} \end{cases} \tag{90}$$

$$E_{I,mln} = \begin{cases} \frac{2(N-1)}{c_n}\zeta_{I,ml} & \text{for } n \text{ even} \\ \frac{2N}{c_n}\delta_{I,ml} & \text{for } n \text{ odd} \end{cases} \tag{91}$$

$$H_{R,mln} = \begin{cases} \frac{N(N^2-n^2)}{c_n}\delta_{R,ml} & \text{for } n \text{ even} \\ \frac{(N-1)((N-1)^2-n^2)}{c_n}\zeta_{R,ml} & \text{for } n \text{ odd} \end{cases} \tag{92}$$

$$H_{I,mln} = \begin{cases} \frac{N(N^2-n^2)}{c_n}\delta_{I,ml} & \text{for } n \text{ even} \\ \frac{(N-1)((N-1)^2-n^2)}{c_n}\zeta_{I,ml} & \text{for } n \text{ odd} \end{cases} \tag{93}$$

Equations (80) and (81) are in the form

$$UA - 2ilV = f \tag{94}$$

$$VA + 2ilU = g \tag{95}$$

where here U, V, f and g denote the $(m,l)^{th}$ row of respective elements.

The $(N-1) \times (N-1)$ matrix A depends on the indices m and l:

$$A = BC + B^2C^2 - (1+l^2)I_{N-1} - \left(\frac{Re}{\Delta t} + m^2\right)C^2 \tag{96}$$

Firstly, the special case $l = 0$ results in an uncoupled pair of equations with real and imaginary spectral components for U and V as

$$U_R = f_R A^{-1} \qquad\qquad U_I = f_I A^{-1} \tag{97}$$

$$V_R = g_R A^{-1} \qquad\qquad V_I = g_I A^{-1} \tag{98}$$

For the case $l \neq 0$ we have

$$U_R = \left(g_I - \frac{1}{2l} f_R A\right) T^{-1} \qquad\qquad U_I = -\left(g_R + \frac{1}{2l} f_I A\right) T^{-1} \tag{99}$$

$$V_R = \frac{1}{2l}\left(U_I A - f_I\right) \qquad\qquad V_I = \frac{1}{2l}\left(f_R - U_R A\right) \tag{100}$$

where

$$T = 2lI_{N-1} - \frac{1}{2l}A^2 \tag{101}$$

Once the complex U_{mln} and V_{mln} are calculated for $0 \leq n \leq N-2$, the values for $n = N-1, N$ can be determined using Equations (72) to (79). A Fourier-Fourier-Chebyshev inverse transform of U_{mln} and V_{mln} will give the solution for $U(z,\phi,r)$ and $V(z,\phi,r)$.

7.3.4 Helmholtz solver for axial component of velocity

The Helmholtz equation for the axial component of velocity $W(z,\phi,r)$ has the form

$$\begin{aligned}(r+\gamma)\frac{\partial W}{\partial r} + (r+\gamma)^2\frac{\partial^2 W}{\partial r^2} + \frac{\partial^2 W}{\partial \phi^2} \\ + \quad (r+\gamma)^2\frac{\partial^2 W}{\partial z^2} - \frac{Re}{\Delta t}(r+\gamma)^2 W = F(z,\phi,r)\end{aligned} \tag{102}$$

where the Dirichlet boundary conditions have the form

$$W(z,\phi,-1) = \alpha(z,\phi) \tag{103}$$

$$W(z,\phi,1) = \beta(z,\phi) \tag{104}$$

and periodic boundary conditions are assumed in the axial and azimuthal direction.

Equation (102) in matrix form in spectral space can be written as

$$W(DC + D^2C^2) - l^2W - m^2WC^2 - \frac{Re}{\Delta t}WC^2 = F \tag{105}$$

The matrices D, D^2, C and C^2 in Equation (105) are the same as those defined in Equation (62). The matrix W contains the complex spectral coefficients W_{mln} of the axial velocity.

The spectral form of the boundary conditions can be written as:

$$\sum_{n=0}^{N} W_{R,mln} = \beta_{R,ml} \tag{106}$$

$$\sum_{n=0}^{N} (-1)^n W_{R,mln} = \alpha_{R,ml} \tag{107}$$

$$\sum_{n=0}^{N} W_{I,mln} = \beta_{I,ml} \tag{108}$$

$$\sum_{n=0}^{N} (-1)^n W_{I,mln} = \alpha_{I,ml} \tag{109}$$

for $-M/2 \leq m \leq M/2-1$ and $-L/2 \leq l \leq L/2-1$.

Adding and subtracting Equations (106) and (107) we get:

$$\sum_{n=0,\ n\ even}^{N} W_{R,mln} = \frac{1}{2}(\beta_{R,ml} + \alpha_{R,ml}) = \eta_{R,ml} \tag{110}$$

$$\sum_{n=0,\ n\ odd}^{N} W_{R,mln} = \frac{1}{2}(\beta_{R,ml} - \alpha_{R,ml}) = \theta_{R,ml} \tag{111}$$

Adding and subtracting Equations (108) and (109) we get:

$$\sum_{n=0,\ n\ even}^{N} W_{I,mln} = \frac{1}{2}(\beta_{I,ml} + \alpha_{I,ml}) = \eta_{I,ml} \tag{112}$$

$$\sum_{n=0,\ n\ odd}^{N} W_{I,mln} = \frac{1}{2}(\beta_{I,ml} - \alpha_{I,ml}) = \theta_{I,ml} \tag{113}$$

In the matrix Equation (105) we substitute Equations (111) and (113) to eliminate the complex coefficients $W_{m,l,N-1}$ and Equations (110) and (112) to eliminate the complex coefficients $W_{m,l,N}$, for $-M/2 \leq m \leq M/2-1$ and $-L/2 \leq l \leq L/2-1$. Subsequently we obtain the matrix equation

$$W(BC + B^2C^2) - l^2W - m^2WC^2 - \frac{Re}{\Delta t}WC^2 = f \tag{114}$$

The matrices B, B^2, C and C^2 are the same as those defined for Equation (80). The matrix W contains the $M \times L \times (N-1)$ portion of its original definition. The matrix f has real and imaginary components

$$f_R = F_R - Q_R C - S_R C^2 \tag{115}$$

and

$$f_I = F_I - Q_I C - S_I C^2 \tag{116}$$

where Q and S are $M \times L \times (N-1)$ matrices with components

$$Q_{R,mln} = \begin{cases} \frac{2(N-1)}{c_n}\theta_{R,ml} & \text{for } n \text{ even} \\ \frac{2N}{c_n}\eta_{R,ml} & \text{for } n \text{ odd} \end{cases} \tag{117}$$

$$Q_{I,mln} = \begin{cases} \frac{2(N-1)}{c_n}\theta_{I,ml} & \text{for } n \text{ even} \\ \frac{2N}{c_n}\eta_{I,ml} & \text{for } n \text{ odd} \end{cases} \tag{118}$$

$$S_{R,mln} = \begin{cases} \frac{N(N^2-n^2)}{c_n}\eta_{R,ml} & \text{for } n \text{ even} \\ \frac{(N-1)((N-1)^2-n^2)}{c_n}\theta_{R,ml} & \text{for } n \text{ odd} \end{cases} \tag{119}$$

$$S_{I,mln} = \begin{cases} \frac{N(N^2-n^2)}{c_n}\eta_{I,ml} & \text{for } n \text{ even} \\ \frac{(N-1)((N-1)^2-n^2)}{c_n}\theta_{I,ml} & \text{for } n \text{ odd} \end{cases} \tag{120}$$

Equation (114) represents a system with $M \times L \times (N-1)$ equations in the $M \times L \times (N-1)$ complex unknowns, W_{mln}, determined from

$$W_R = f_R A^{-1} \qquad\qquad W_I = f_I A^{-1} \tag{121}$$

where

$$A = BC + B^2C^2 - l^2 I_{N-1} - m^2 C^2 - \frac{Re}{\Delta t} C^2 \tag{122}$$

for $-M/2 \leq m \leq M/2 - 1$ and $-M/2 \leq l \leq M/2 - 1$, where W_R, W_I and f_R, f_I are the $(m,l)^{th}$ rows of the real and imaginary component elements of W and f respectively. I_{N-1} is the $(N-1) \times (N-1)$ identity matrix. Once the W_{mln} are calculated for $0 \leq n \leq N-2$, the W_{mln} for $n = N-1, N$ can be determined using Equations (110) to (113). A Fourier-Chebyshev inverse transform of W_{mln} will give the solution for $W(z, \phi, r)$.

7.4 Preprocessing calculations

The arrays B and B^2 are calculated once for Dirichlet boundary conditions and once for Neumann boundary conditions in a preprocessing step.

Then we calculate and store:

(1) $M \times L$ inversions of the $N-1 \times N-1$ array Q for the Poisson solver.

(2) M inversions of the $N-1 \times N-1$ array A, and $M \times (L-1)$ inversions of the $N-1 \times N-1$ array T, for the coupled Helmholtz solver for the radial and azimuthal components of velocity.

(3) $M \times L$ inversions of the $N-1 \times N-1$ array A for the Helmholtz solver for the axial component of velocity.

These three sets of inversions are done once, in a preprocessing step.

7.5 Numerical tests of wavy vortex flow.

The three-dimensional code was validated by comparing exponential growth rates for wavy vortex flow. Using the three-dimensional code, the real and imaginary components of the exponential growth rate for a wavy vortex flow simulation are shown in Table 7.1 to converge to their referenced values as the timespacing is reduced.

In the exponential stage of growth, the complex amplitude $A(t)$ has a solution of the form:

$$A(t) = A(0)\exp(\sigma_R t)\exp(i\sigma_I t) \tag{123}$$

where σ_R and σ_I are the real and imaginary components of the growth rate. The amplitude has a real component, $A_R(t)$ and an imaginary component, $A_I(t)$.

Estimates for σ_R were made by using

$$\sigma_R = \frac{1}{\Delta t}\log_e\left(\frac{|A(t+\Delta t)|}{|A(t)|}\right) \tag{124}$$

where

$$|A(t)| = \sqrt{A_R^2(t) + A_I^2(t)} \tag{125}$$

Estimates for σ_I were made by using

$$\sigma_I = \frac{1}{\Delta t}\left(\cos^{-1}\left(\frac{A_R(t+\Delta t)}{|A(t+\Delta t)|}\right) - \cos^{-1}\left(\frac{A_R(t)}{|A(t)|}\right)\right) \tag{126}$$

The amplitudes for each mode were determined from the radial component of velocity evaluated at the radial centre of the gap. Fourier-Fourier transforms in the z and ϕ directions gave $A_R(t)$ and $A_I(t)$ as functions of mode indices m and l.

Figure 7.1 demonstrates second order accuracy for the scheme with $(J_e = 2, J_p = 1)$ and $\theta = 0.0125$, as the slopes for σ_R and σ_I are about two. In other words, $\sigma - \sigma_t$ is proportional to $(\Delta t)^2$, where σ_t refers to the values of the real or imaginary components of growth rate from Marcus (1984a). The scheme with $(J_e = 2, J_p = 1)$ and $\theta = 0.5$ has a slope of two for σ_R but a slope of one for σ_I, hence it is giving second-order time-accuracy for σ_R and first-order time-accuracy for σ_I.

Consider now the simulation to steady state for a wavy vortex flow with $Re = 167$, $\lambda = 2.54$, $\eta = 0.877$ and $l_{az} = 5$. Using a $16 \times 16 \times 17$ grid, $\Delta t = 0.05$ and $\theta = 0.5$ a value of $\sigma_I = 0.30097$ was obtained for the fundamental frequency of the flow, which converts to the value 2.146 Ω_{in}. This is in reasonable agreement with the value of 2.16 Ω_{in} from the computations by Moser, Moin and Leonard (1983) and the value 2.11 Ω_{in} from the experiments of Coles (1965).

Figure 7.2 shows contours of axial velocity in an unwrapped z versus ϕ plane for the azimuthal span $0 \leq \phi \leq 2\pi/5$. Figure 7.3 shows velocity vector plots in the z versus r plane taken at $\phi = \frac{j}{16}\frac{2\pi}{5}$ for $j = 0, ..., 15$. These figures highlight the fact that, unlike Taylor vortex flow, in wavy vortex flow fluid can move between the counter-rotating vortices.

The code was run on a high performance computer, a Silicon Graphics Indy R10000 Workstation. The previous run to steady state took about 4 CPU hours (at 0.36 CPU seconds per time step). In comparison, on a Silicon Graphics Indy R5000 Workstation it took 2.16 CPU seconds per time step, which is six times slower for the grid size chosen.

	l_{az}	4
	η	0.877
	μ	0
	Re	238.2
	$\Gamma = \lambda$	2.3603251
	σ_R, σ_I from Marcus (1984a)	0.067241 , 0.28430
$\theta = 0.5$	$\Delta t = 0.225$	0.067517 , 0.28164
	$\Delta t = 0.2$	0.067430 , 0.28188
	$\Delta t = 0.15$	0.067297 , 0.28239
	$\Delta t = 0.1$	0.067218 , 0.28296
$\theta = 0.0125$	$\Delta t = 0.225$	0.067761 , 0.28464
	$\Delta t = 0.2$	0.067645 , 0.28456
	$\Delta t = 0.15$	0.067455 , 0.28442
	$\Delta t = 0.1$	0.067322 , 0.28432

Table 7.1: A growth rate test for 3D code using a $16 \times 16 \times 17$ grid.

The three-dimensional code has been validated and shown to have second-order time-accuracy for the appropriate choice in the weighting parameter θ. The successful simulation of wavy vortex flow makes it possible to undertake a future study into the effect of nonaxisymmetric modes on state selection in Taylor vortex flow. In particular, modes with azimuthal periodicity, that ultimately lead to a transition to wavy vortex flow when the Reynolds number is sufficiently high.

8 Conclusions And Recommendations For Future Work

8.1 Conclusions

Following the successful numerical treatment of driven cavity flow, a two-dimensional code for Taylor vortex flow based on spectral methods and operator splitting was developed and validated for second-order time accuracy.

The numerical method was extended to three dimensions to simulate Taylor-Couette flow in general. The code was validated against wavy vortex flow and was also shown to give second-order time accuracy.

The Poisson and Helmholtz solvers in these codes were based on the Tau spectral method. In cylindrical coordinates there was a difficulty that was overcome, this being the treatment in spectral space of the coefficients proportional to $1/r$ and $1/r^2$. The equations were firstly rewritten to have factors proportional to r and r^2. These factors had matrix operators in spectral space which were derived analytically.

From the two-dimensional code, results of the behaviour of the amplitude of the modes with ramp time were obtained. A linear model was shown to describe the behaviour of the amplitude of the modes in their independent stage of growth. It was shown that the ramp provides an additional time delay in the growth of the mode which is mode-dependent. This time delay has a shortest-to-longest ordering of the modes corresponding to the lowest-to-highest ordering of the critical Reynolds number of each mode. As the time delay is proportional to the ramp time, progressively longer ramp times result in a change of the ordering of the time taken for each mode to begin self-interaction. Then for a particular ramp time, the mode which has sufficient time to self-interact will become preferred. For sufficiently long ramp times, the critical wavelength mode always has time to self-interact because the other modes have a significantly greater delay time from reaching a finite amplitude.

The nonlinear effects in the results were accounted for using coupled nonlinear amplitude equations. The amplitude equations for each mode accounted for several features:

(i) the initial independent stage of growth where the log of the amplitude varies quadratically with time during the Re ramp and linearly with time for constant Re. This was modelled using linear amplitude terms.

(ii) the three-wave resonance effects causing rapid regions of acceleration for lower amplitude modes prior to the saturation of the preferred mode. This was modelled using quadratic amplitude terms.

(iii) the self-interaction of each mode. In the equation for each mode, this was modelled using cubic terms containing amplitudes of the same mode.

(iv) the coupling or interaction between different modes. In the equation for each mode, this was modelled using cubic terms containing amplitudes of different modes.

The nonlinear amplitude equations provide a model of the behaviour of the amplitude of the modes with ramp time, and the change in preferred mode with ramp time.

The use of amplitude equations implies we can conceptualise the phenomenon of nonuniqueness using a dynamical systems approach. Consider the situation for sudden starts and variable initial conditions. If the coefficients in the amplitude equations satisfy certain conditions, then the N-mode system is nonunique. Such conditions can be considered as conditions for nonuniqueness. Then, in an N-dimensional phase space spanned by the amplitude of each mode, we have N stable equilibrium points. These would represent a discrete set of N stable Taylor vortex flow states spanning the Eckhaus stable band. Which Taylor vortex flow state is preferred depends on the initial conditions.

Consider now the situation of fixed initial conditions and variable ramp time. As the ramp time is lengthened, the structure of the integral curves in the phase space diagram is deformed so that the integral curves from the same initial conditions go to different stable states.

When the ramp time is sufficiently long, it was observed that the Taylor vortex flow with the critical wavelength was always preferred. The integral curves in the phase plane have deformed to the situation where all curves lead to the state with the critical wavelength.

This means that we have progressed from the sudden starts situation which exhibits

nonuniqueness, to the long ramp time situation which exhibits uniqueness.

8.2 Recommendations for future work

Consider the amplitude equation suggested in Section 6.7, namely

$$\frac{d|A_i|}{dt} = \sigma_i(t)|A_i| - l_i|A_i|^3 - \sum_{j=1,j\neq i}^{N} \alpha_{ij}|A_i|.|A_j|^2 + \sum_{j,q} \beta_{jq}|A_j|.|A_q| \tag{1}$$

The growth rates $\sigma_i(t)$ are defined as

$$\sigma_i(t) = K_i(Re(t) - Re_{c,i}) \tag{2}$$

where

$$Re(t) = \begin{cases} Re_i + \frac{Re_f - Re_i}{T}t & \text{if } t \leq T \\ Re_f & \text{if } t > T \end{cases} \tag{3}$$

and the values for K_i and $Re_{c,i}$ for each mode i can be predetermined from a graph of instantaneous growth rate versus instantaneous Reynolds number, plotted from the results of the numerical simulation for a sufficiently long ramp time.

It is now of interest to test how well Equation (1) fits the $|A_i(t)|$ from the numerical simulation. A computer program has been written that applies a least squares approximation with user supplied basis functions. One can select the basis functions to correspond to the terms in the amplitude equation. Using the values for $|A_i(t)|$ from the numerical simulation, values for $\frac{d|A_i|}{dt}$ can be calculated. The routine would make a polynomial approximation of each $\frac{d|A_i|}{dt}$ based on the functions $|A_i|$, $|A_i|^3$, $|A_i|.|A_j|^2$ and $|A_j|.|A_q|$. Thus, the output of the routine would give the values for the coefficients l_i, α_{ij} and β_{jq} such as to provide a least squares fit.

The success of the approach would require careful judgement and trials of the appropriate terms to account for the nonlinear effects from the most significant amplitudes of the modes. For example, consider the amplitude results for $T = 49.81$. An initial suggestion for the amplitude equations for mode 11, 10, 12 and the first harmonic of 11 can involve

those modes alone.

Once the coefficients are calculated for a particular ramp time, it is then of interest to see how well the amplitude model duplicates the behaviour of the amplitude of the modes observed from the numerical simulation at other ramp times.

A simple datafitting application can be illustrated to the results of $|A_i(t)|$ for $T = 0$. The quadratic terms were neglected for simplicity. Only the top two modes were considered, that is, modes 12, 11. The model considered was:

$$\frac{d|A_{11}|}{dt} = \sigma_{11}|A_{11}| - l_{11}|A_{11}|^3 - \alpha_{11,12}|A_{11}|.|A_{12}|^2 \tag{4}$$

$$\frac{d|A_{12}|}{dt} = \sigma_{12}|A_{12}| - l_{12}|A_{12}|^3 - \alpha_{12,11}|A_{12}|.|A_{11}|^2 \tag{5}$$

Figure 8.1 shows that the fit is very good in the linear stage of growth. The coefficients were estimated to be $\sigma_{11} = 1.76$, $l_{11} = 305.42$, $\alpha_{11,12} = 376.09$, $\sigma_{12} = 1.76$, $l_{12} = 434.87$ and $\alpha_{12,11} = 281.63$. However, deviations of the fit from the true amplitudes are noticeable where mode 12 overtakes mode 11. Thus more nonlinear terms need to be included to improve the fit. The next step would be to include coupling to mode 13 as well as allowing for three-wave resonance effects with the first harmonics of each mode.

Following this study, we wish to undertake an investigation into the effect of nonaxisymmetric modes on state selection in Taylor vortex flow. Using the three-dimensional code for Taylor-Couette flow modes that exhibit azimuthal periodicity as well as axial periodicity can be simulated. Such modes ultimately lead to the transition to wavy vortex flow when the Reynolds number is sufficiently high. This work would then lead to a study of state selection in wavy vortex flow. Again, coupled nonlinear amplitude equations could be used to explain the behaviour of the amplitude of the modes.

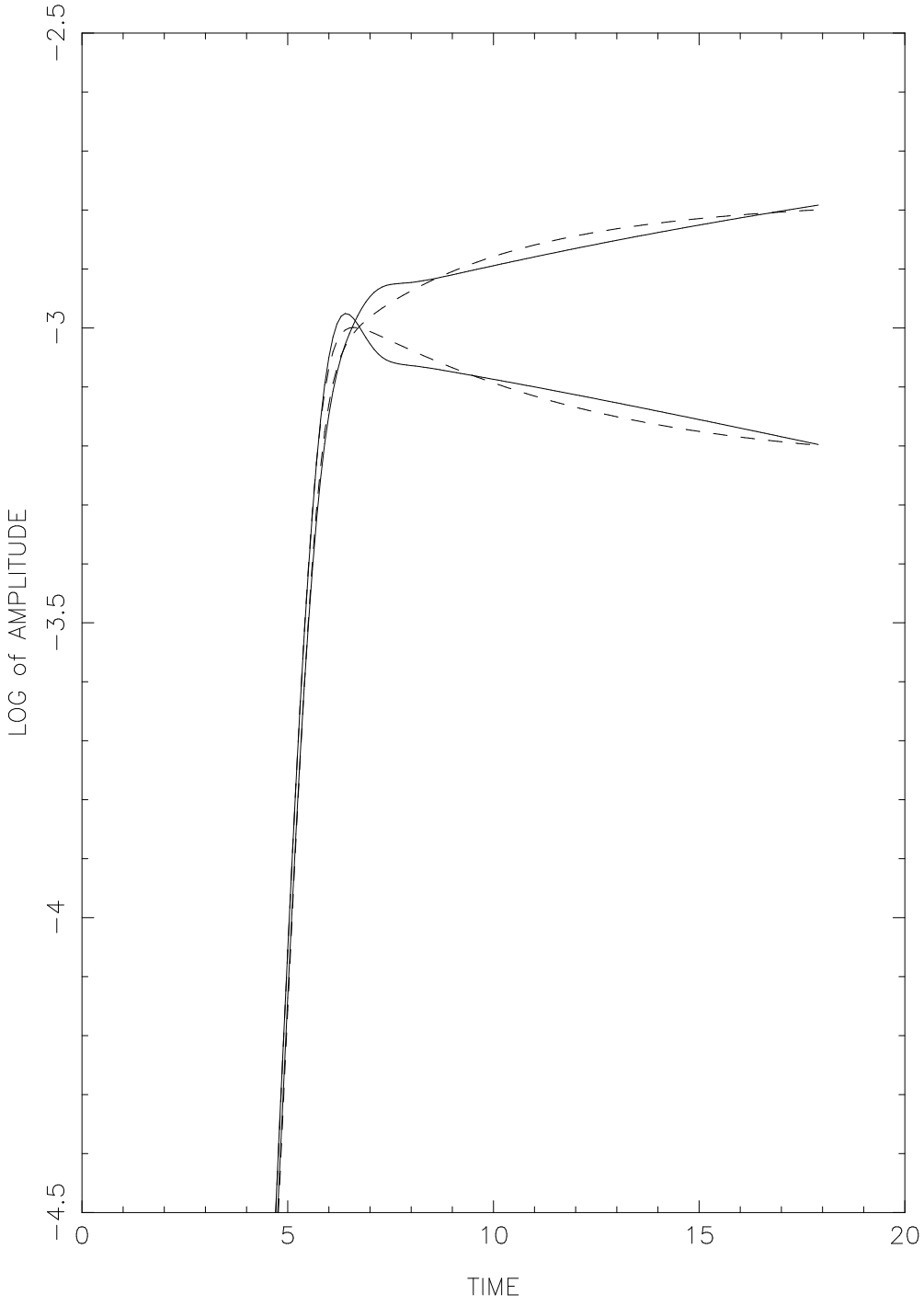

Figure 8.1: Least squares fits for modes 12 (the preferred mode) and 11.

———— amplitude from numerical simulation for $T = 0$

– – – – – least squares fit

9 Appendix

9.1 Publications resulting from this work

10 References

Abarbanel, D.D., Rabinovich, M.I. and Sushchik, M.M. 1993 Introduction to nonlinear dynamics for physicists. World Scientific Lecture Notes in Physics – Vol. 53. Continental Press. Singapore.

Acheson, D.J. 1990 Elementary Fluid Dynamics. Clarendon Press. Oxford.

Ahlers, G., Cannell, D.S., Dominguez-Lerma, M.A. and Heinrichs R. 1986 Wavenumber selection and Eckhaus instability in Couette-Taylor flow. *Physica D*, **23**, 202-219.

Alonso, C.V. and Macagno E.O. 1973 Numerical integration of the time-dependent equations of motion for Taylor vortex flow. *Computers and Fluids* **1**, 301-316.

Andereck, C.D., and Baxter, G.W. 1988 An overview of the flow regimes in a circular Couette system. In *Propagation in systems far from equilibrium*, pp.315-324.

Andereck, C.D., Liu, S.S., and Swinney, H.L. 1986 Flow regimes in a circular Couette system with independently rotating cylinders. *J. Fluid Mech.* **164**, 155-183.

Azuma, H., Ogawara, K. and Iida, S. 1992 Unsteady 3-Dimensional calculation of the flow between concentric rotating cylinders. *JSME International Journal*, Series II, **35**, No. 2, 165-173.

Benjamin, T.B. 1978 Bifurcation phenomena in steady flows of a viscous fluid. I. Theory. *Proc. R. Soc. Lond.* A **359**, 1-26.

Benjamin, T.B. 1978 Bifurcation phenomena in steady flows of a viscous fluid. II. Experiments. *Proc. R. Soc. Lond.* A **359**, 27-43.

Benjamin, T.B. and Mullin, T. 1982 Notes on the multiplicity of flows in the Taylor experiment. *J. Fluid Mech.* **121**, 219-230.

Brandstater, A. and Swinney, H.L. 1987 Strange attractors in weakly turbulent Couette-Taylor flow. *Phys. Rev.* A **35**, No. 5, 2207-2220.

Burkhalter, J.E. and Koschmieder, E.L. 1973 Steady supercritical Taylor vortex flow. *J. Fluid Mech.*, **58**, part 3, 547-560.

Burkhalter, J.E. and Koschmieder, E.L. 1974 Steady supercritical Taylor vortices after sudden starts. *Phys. Fluids* **17**, No. 11, 1929-1935.

Canuto, C., Hussaini, M.Y., Quarteroni, A. and Zang, T.A. 1988 *Spectral Methods in Fluid Dynamics.* Springer.

Chandrasekhar, S. 1961 *Hydrodynamic and Hydromagnetic Stability.* Oxford University Press.

Chen, J-C. and Neitzel G.P. 1982 Strong stability of impulsively initiated Couette flow for both axisymmetric and non-axisymmetric disturbances. *J. Appl. Mech.* **49**, 691-696.

Chen, J-C., Neitzel G.P. and Jankowski D.F. 1987 Numerical experiments on the stability of unsteady circular Couette flow with random forcing. *Phys. Fluids* **30**, 1250-1258.

Coles, D. 1965 Transition in circular Couette flow. *J. Fluid Mech.*, **21**, 385-425.

Coughlin, K.T. and Marcus, P.S. 1991 Vortices in quasiperiodic Taylor-Couette flows. In *Lectures in Applied Mathematics, Vol. 28, Vortex Dynamics and Vortex Methods*, American Mathematical Society, Providence, Rhode Island, (ed. C.R. Anderson and C. Greengard). 119-129.

Coughlin, K.T. and Marcus, P.S. 1992 Modulated waves in Taylor-Couette flow. Part 1. Analysis. *J. Fluid. Mech.*, **234**, 1-18.

Coughlin, K.T. and Marcus, P.S. 1992 Modulated waves in Taylor-Couette flow. Part 2. Numerical simulation. *J. Fluid. Mech.*, **234**, 19-46.

Dang-Vu, H. and Delcarte, C. 1993 An accurate solution of the Poisson equation by the Chebyshev collocation method. *J. Comp. Phys.* **104**, 211-220.

Davey, A. 1962 The growth of Taylor vortices in flow between rotating cylinders *J. Fluid Mech.* **14**, 336-368.

De Roquefort, T.A. and Grillaud, G. 1978 Computation of Taylor vortex flow by a transient implicit method. *Computers and Fluids* **6**, 259-269.

Diprima, R.C. and Eagles, P.M. 1977 Amplification rates and torques for Taylor-vortex flows between rotating cylinders. *Phys. of Fluids*, **20**, 2, 171-175.

Diprima, R.C. and Rogers, E.H. 1969 Computing problems in nonlinear stability. *Phys. of Fluids* Supplement II, High-speed computing in fluid dynamics, 155-165.

Diprima, R.C. and Swinney, H.L. 1981 Instabilities and transition in flow between concentric rotating cylinders. In *Hydrodynamic Instabilities and the Transition to Turbulence* (ed. H.L. Swinney and J.P.Gollub), p.139. Springer.

Dominguez-Lerma, M.A., Cannell, D.S., and Ahlers, G. 1986 Eckhaus boundary and wavenumber selection in rotating Couette-Taylor flow. *Phys. Rev. A* **34**, 4956-4970.

Donnelly, R.J., 1991 Taylor-Couette flow: the early days. *Physics Today*, November, 32-39.

Drazin, P.G. and Reid, W.H. 1989 Hydrodynamic Stability. Cambridge University Press.

Eagles, P.M. 1971 On stability of Taylor vortices by fifth-order amplitude expansions. *J. Fluid Mech.* **49**, 529-550.

Eagles, P.M. 1977 On the stability of slowly varying flow between concentric cylinders. *Proc. R. Soc. Lond. A* **355**, 209-224.

Eckhaus, W. 1965 Studies in Non-Linear Stability Theory. Springer. Berlin.

Elson, T.P., 1979 Velocity profiles of concentric flow between coaxial rotating cylinders with a stationary lower boundary. *Chemical Engineering Science* **34**, 373-377.

Fenstermacher, P.R., Swinney, H.L. and Gollub, J.P. 1979 Dynamical instabilities and the transition to chaotic Taylor vortex flow. *J. Fluid Mech.* **94**, 103-128.

Ghia, U., Ghia K.N. and Shin C.T. 1982 High-Re Solutions for Incompressible Flow Using the Navier-Stokes Equations and a Multigrid Method. *J. Comp. Phys.* **48**, 387-411.

Gorman, M., and Swinney, H.L. (1982). Spatial and temporal characteristics of modulated waves in the circular Couette system. *J. Fluid Mech.* **117**, 123-142.

Gottlieb, D. and Orszag, S.A. 1977 Numerical Analysis of Spectral Methods. SIAM.

Greenspan, H.P. (1990) The theory of rotating fluids.

Haidvogel, D.B. and Zang, T. 1979 Accurate solutions of Poisson's equation by expansion in Chebyshev polynomials. *J. Comp. Phys.* **30**, 167-180.

Hussaini, M.Y. and Voigt, R.G. Eds, 1990 Instability and Transition, Vol. 1. Springer-Verlag.

Ives, K.J. and Bhole, A.G. 1975 Study of flowthrough Couette flocculators – I. Design for uniform and tapered flocculation. *Water Research* **9**, 1085-1092.

Ives, K.J. and Bhole, A.G. 1977 Study of flowthrough Couette flocculators – II. Laboratory studies of flocculation kinetics. *Water Research* **11**, 209-215.

Karniadakis, G. E., Israeli M., and Orszag S. A. 1991 High-order splitting methods for incompressible Navier-Stokes equations. *J. Comp. Phys.* **97**, 414-443.

Kim, J. and Moin P. 1985 Application of a Fractional-Step Method to Incompressible Navier-Stokes Equations. *J. Comp. Phys.* **59**, 308-323.

Kogelman, S. and Diprima, R.C. 1970 Stability of spatially periodic supercritical flows in hydrodynamics. *Phys. Fluids*, **13**, 1-11.

Kohuth K.R. and Neitzel G.P. 1988 Experiments on the stability of an impulsively initiated circular Couette flow. *Exp. Fluids* **6**, 199-208.

Koschmieder, E.L. 1993 Benard cells and Taylor vortices. Cambridge Monographs on Mechanics and Applied Mathematics. Cambridge University Press.

Ku, H.C., Hirsh, R.S. and Taylor, T.D. 1987 A pseudospectral method for solution of the three-dimensional incompressible Navier-Stokes equations. *J. Comp. Phys.* **70**,439-462.

Landau, L.D. 1944 On the problem of turbulence. *C.R. Acad. Sci. U.R.S.S.* **44**, 311-314.

Leonard, A. and Wray A. 1982 A new numerical method for the simulation of three-dimensional flow in a pipe. In *Eighth International Conference on Numerical Methods in Fluid Dynamics, Aachen.* 335-342.

Liu, D.C.S. and Chen, C.F. 1973 Numerical experiments on time-dependent rotational Couette flow. *J. Fluid Mech.* **59**, pt 1, 77-95.

Marcus, P.S., Orszag, S.A. and Patera, A.T. 1982 Simulation of cylindrical Couette flow. In *Proceedings of the Eighth International Conference on Numerical Methods in Fluid Dynamics.* 371-376.

Marcus, P.S. 1984a Simulation of Taylor-Couette flow. Part 1. Numerical methods and comparison with experiment. *J. Fluid Mech.* **146**, 45-64.

Marcus, P.S. 1984b Simulation of Taylor-Couette flow. Part 2. Numerical results for wavy-vortex flow with one travelling wave. *J. Fluid Mech.* **146**, 65-113.

Meyer, K.A. 1967 Time-dependent numerical study of Taylor vortex flow. *Phys. Fluids* **10**, No. 9, 1874-1879.

Meyer-Spasche, R. and Keller, H.B. 1980 Computations of the axisymmetric flow between rotating cylinders. *J. Comp. Phys.* **35**, 100-109.

Moser, R.D., Moin, P. and Leonard, A. 1983 A spectral numerical method for the Navier-Stokes equation with applications to Taylor-Couette flow. *J. Comp. Phys.* **52**, 524.

Nakaya, C. 1974 Domain of stable periodic vortex flows in a viscous fluid between concentric circular cylinders. *J. Phys. Soc. Japan* **36**, 1164-1173.

Neitzel, G.P. 1982a Marginal stability of impulsively initiated Couette flow and spin decay. *Phys. Fluids* **25**, 226-232.

Neitzel, G.P. 1982b Stability of circular Couette flow with variable inner cylinder speed. *J. Fluid Mech.* **123**, 43-57.

Neitzel, G.P. 1984 Numerical computation of time-dependent Taylor-vortex flows in finite geometries. *J. Fluid Mech.* **141**, 51-66.

Neitzel, G.P., Kirkconnell, C.S. and Little L.J. 1995 Transient, nonaxisymmetric modes in the instability of unsteady circular Couette flow. Laboratory and numerical experiments. *Phys. Fluids* **7** (2), 324-334.

Ning L., Ahlers G. and Cannell, D.S. 1990 Wave-number selection and travelling vortex waves in spatially ramped Taylor-Couette flow. *Phys. Rev. Lett.* **64**, 11, 1235-1238.

Orszag, S.A. and Kells, L.C. 1980 Transition to turbulence in plane Poiseuille and plane Couette flow. *J. Fluid Mech.* **96**, part 1, 159-205.

Patera, A.T. and Orszag, S.A. 1980 Transition and turbulence in planar channel flows. In *Seventh International Conference on Numerical Methods in Fluid Dynamics.* 329-335.

Patera, A.T. and Orszag, S.A. 1981 Finite-amplitude stability of axisymmetric pipe flow. *J. Fluid Mech.* **112**, 467.

Rand, D. 1982 Dynamics and symmetry. Predictions for modulated waves in rotating fluids. *Arch. Rat. Mech. Anal.* **79**, 1-38.

Riecke, H. and Paap, H.-G. 1986 Stability and wave-vector restriction of axisymmetric Taylor vortex flow. *Phys. Rev. A* **33**, 547-553.

Roberts, P.H. 1965 Experiments on the stability of viscous flow between rotating cylinders: Appendix. *Proc. Roy. Soc.* A **283**, 531-46.

Rudman, M.J. 1995 Mixing in the wavy vortex regime of Taylor-Couette flow. *Proceedings of the Twelfth Australasian Fluid Mechanics Conference*, The University of Sydney, Volume 1, 291-294.

Schlüter, A., Lortz, D. and Busse, F. 1965 On the stability of steady finite amplitude convection. *J. Fluid Mech.*, **23**, 129-44.

Shen, J. 1991 Hopf Bifurcation of the Unsteady Regularized Driven Cavity Flow. *J. Comp. Phys.* **95**, 228-245.

Segel, L.A. 1962 The non-linear interaction of two disturbances in the thermal convection problem. *J. Fluid Mech.*, **14**, 97-114.

Snyder, H.A. 1969 Wave-number selection at finite amplitude in rotating Couette flow. *J. Fluid Mech.* **35**, 273-298.

Street, C.L. and Hussaini, M.Y. 1991 A numerical simulation of the appearance of chaos in finite-length Taylor-Couette flow. *Appl. Numer. Math.* **7**, 41-71.

Stuart, J.T. 1960 Non-linear effects in hydrodynamic stability. *Proc. Tenth Inter. Cong. Appl. Mech. Stresa: Elsevier.*

Stuart, J.T. 1960 On the non-linear mechanics of wave disturbances in stable and unstable parallel flows. Part 1. The basic behaviour in plane Poiseuille flow. *J. Fluid Mech.* **9**, 353-370.

Stuart, J.T. 1986 Taylor-Vortex flow: A dynamical system. *Siam Rev.* **28**, No. 3, 315-342.

Stuart, J.T. and DiPrima, R.C. 1978 The Eckhaus and Benjamin-Feir resonance mechanisms. *Proc. Roy. Soc. London A* **362**, 27-41.

Taylor, G.I. 1923 Stability of a viscous liquid contained between two rotating cylinders. *Phil. Trans. R. Soc. Lond.* A **223**, 289-343.

Voigt, R.G., Gottlieb, D. and Hussaini, M.Y. 1984 Spectral methods for partial differential equations. SIAM.

Watson, J. 1960 On the non-linear mechanics of wave disturbances in stable and unstable parallel flows. Part 2. The development of a solution for plane Poiseuille flow and for plane Couette flow. *J. Fluid Mech.* **9**, 371-389.

Weisshaar, E., Busse, F.H. and Nagata, M. 1991 Twist vortices and their instabilities in the Taylor-Couette system. *J. Fluid Mech.*, **226**, 549-564.